



Verification and science simulations with the Instrument Performance Simulator for JWST - NIRSpec

Bernhard Dorner

► To cite this version:

Bernhard Dorner. Verification and science simulations with the Instrument Performance Simulator for JWST - NIRSpec. Other. Université Claude Bernard - Lyon I, 2012. English. NNT : 2012LYO10066 . tel-00738070

HAL Id: tel-00738070

<https://theses.hal.science/tel-00738070>

Submitted on 3 Oct 2012

HAL is a multi-disciplinary open access archive for the deposit and dissemination of scientific research documents, whether they are published or not. The documents may come from teaching and research institutions in France or abroad, or from public or private research centers.

L'archive ouverte pluridisciplinaire **HAL**, est destinée au dépôt et à la diffusion de documents scientifiques de niveau recherche, publiés ou non, émanant des établissements d'enseignement et de recherche français ou étrangers, des laboratoires publics ou privés.

N° d'ordre 66-2012

Année 2012

THESE DE L'UNIVERSITE DE LYON

Délivrée par

L'UNIVERSITE CLAUDE BERNARD LYON 1

ECOLE DOCTORALE PHYSIQUE ET ASTROPHYSIQUE

DIPLOME DE DOCTORAT

(arrêté du 7 août 2006)

soutenue publiquement le 10 Mai 2012

par

M. Bernhard DORNER

TITRE :

**Verification and science simulations with the Instrument
Performance Simulator for JWST/NIRSpec**

Directeur de thèse :
M. Bruno GUIDERDONI

JURY : M. Roland BACON
M. Peter JAKOBSEN
M. Niranjan THATTE
M. Santiago ARRIBAS
Mme. Anne EALET
M. Pierre FERRUIT
M. Jean-François GONZALEZ
M. Hans-Walter RIX

Abstract

The James Webb Space Telescope (JWST), a joint project by NASA, ESA, and CSA, is the successor mission to the Hubble Space Telescope. One of the four science instruments on board is the near-infrared spectrograph NIRSpec. To study the instrument performance and to create realistic science exposures, the Centre de Recherche Astrophysique de Lyon (CRAL) developed the Instrument Performance Simulator (IPS) software. Validating the IPS functionality, creating an accurate model of the instrument, and facilitating the preparation and analysis of simulations are key elements for the success of the IPS. In this context, we verified parts of the IPS algorithms, specifically the coordinate transform formalism, and the Fourier propagation module. We also developed additional software tools to simplify the scientific usage, as a target interface to construct observation scenes, and a dedicated data reduction pipeline to extract spectra from exposures. Another part of the PhD work dealt with the assembly of an as-built instrument model, and its verification with measurements from a ground calibration campaign. For coordinate transforms inside the instrument, we achieved an accuracy of 3–5 times better than the required absolute spectral calibration, and we could reproduce the total instrument throughput with an absolute error of 0–10% and a relative error of less than 5%. Finally, we show first realistic on-sky simulations of a deep field spectroscopy scene, and we explored the capabilities of NIRSpec to study exoplanetary transit events. We determined upper brightness limits of observable host stars, and give noise estimations of exemplary transit spectra.

Vérification et simulations scientifiques avec le simulateur des performances de l'instrument JWST/NIRSpec

Résumé

Le télescope spatial James Webb (JWST) est le successeur du télescope spatial Hubble (HST). Il est développé en collaboration par les agences spatiales NASA, ESA et CSA. Le spectrographe proche infrarouge NIRSpec est un instrument du JWST. Le Centre de Recherche Astrophysique de Lyon (CRAL) a développé le logiciel de simulation des performances (IPS) de NIRSpec en vue de l'étude de ses performances et de la préparation de poses synthétiques réalistes. Dans cette thèse, nous vérifions certains algorithmes de l'IPS, en particulier ceux traitant des transformations de coordonnées et de la propagation en optique de Fourier. Nous présentons ensuite une interface simplifiée pour la préparation de « scènes » d'observation et un logiciel de traitement de données permettant d'extraire des spectres à partir de poses synthétiques afin de faciliter l'exploitation des simulations. Nous décrivons comment nous avons construit et validé le modèle de l'instrument par comparaison avec les données de calibration. Pour les transformations de coordonnées, le modèle final est capable de reproduire les mesures avec une précision 3 à 5 fois meilleure que celle requise

pour la calibration spectrale. Pour la transmission globale notre précision est de 0–10% dans l’absolu et meilleure que 5% en relatif. Finalement, nous présentons la première simulation d’une observation de type « champ profond spectrographique » et nous explorons comment NIRSpec pourra être utilisé pour observer le transit de planètes extra-solaires. Nous déterminons en particulier la luminosité maximale des étoiles hôtes pouvant être observées et quels peuvent être les rapports signal sur bruit attendus.

Résumé substantiel

Le télescope spatial James Webb (JWST) est souvent présenté comme le successeur du télescope spatial Hubble (HST). Mission majeure de la communauté astronomique, il est développé en collaboration par les agences spatiales américaine (NASA), européenne (ESA) et canadienne (CSA) et son lancement est prévu pour la fin de la décennie. Le spectrographe proche infrarouge NIRSpec, un des quatre instruments du JWST, est réalisé par EADS Astrium pour le compte de l’ESA.

Dans le cadre d’un contrat avec EADS Astrium, le Centre de Recherche Astrophysique de Lyon (CRAL) a développé le logiciel de simulation des performances (IPS) de NIRSpec en vue de l’étude de ses performances et de la préparation de poses synthétiques réalistes reproduisant calibrations et observations scientifiques. La vérification des algorithmes, la mise en place d’un modèle réaliste de l’instrument et la mise à disposition des scientifiques d’une interface simplifiée pour la préparation et le traitement des simulations d’observations sont des éléments clés pour la réussite de l’IPS. C’est dans ce contexte que se situe cette thèse.

Ainsi, dans une première partie nous décrivons la vérifications de certains algorithmes de l’IPS, plus spécifiquement ceux traitant des transformations de coordonnées et de la propagation en optique de Fourier. Nous présentons ensuite une interface simplifiée pour la préparation de « scènes » d’observation et un logiciel de traitement de données permettant d’extraire des spectres à partir de poses synthétiques afin de faciliter l’exploitation des simulations, ces deux outils ayant été développés dans le cadre de la thèse. Nous décrivons comment nous avons construit et validé le modèle de l’instrument par comparaison avec les données de sa première campagne de calibration au sol. Nous insistons sur les étapes suivies pour ajuster les transformations de coordonnées et les transmissions. Pour les transformations de coordonnées, le modèle final est capable de reproduire les mesures avec une précision 3 à 5 fois meilleure que celle requise pour la calibration en longueur d’onde de l’instrument. En ce qui concerne la transmission globale de l’instrument cette précision est de 0–10% dans l’absolu et meilleure que 5% en relatif.

Pour terminer, nous présentons les premières simulations réalistes d’une observation de type « champ profond spectrographique », basé sur des objets avec des spectres simulés. Au cours de la préparation de la scène de simulation, nous avons trouvé des aspects importants pour la sélection des galaxies à grand redshift, qui auront un impact sur le fonctionnement de l’instrument et l’exploitation des données.

Par ailleurs, nous explorons les capacités de NIRSpec à observer le transit de planètes extra-solaires devant leur étoile. Nous déterminons la luminosité maximale des étoiles hôtes pouvant être observées, et étudions les différentes sources de bruit dans ces observations. Parmi les autres effets instrumentaux, nous analysons spécifiquement le bruit issu des erreurs de pointage du télescope, mais seul le bruit de lecture des détecteurs s'avère être un facteur important. Nous dérivons des expressions pour le signal sur bruit atteignable, et montrons les performances attendues de NIRSpec pour observer des exoplanètes connues, et plus particulièrement le « Jupiter chaud » HD189733b et la « super Terre » GJ1214b. Enfin, nous confirmons que NIRSpec sera capable de mesurer les grandes caractéristiques atmosphériques d'une planète ayant une taille comme la Terre, qui orbite dans la zone habitable autour une étoile naine proche de la classe M4.5. Toutes les simulations scientifiques démontreront les capacités qu'offrira NIRSpec en orbite.

Discipline

Astrophysique

Keywords

Instrumentation, optics, performance simulation, NIRSpec, JWST

Mots-cles

Instrumentation, optique, simulation de performance, NIRSpec, JWST

Intitule et adresse du laboratoire

CRAL - Centre de Recherche Astrophysique de Lyon

Observatoire de Lyon

9, avenue Charles Andre

69561 Saint Genis Laval cedex

The Stars are Indifferent to Astronomy
Peter Caws

Acknowledgments

I would like to thank everyone who contributed to this thesis, both by scientific and social support. During 3.5 years in such a big project that makes a lot of people, but in particular, I want to thank...

...Pierre Ferruit for initiating and directing this work, having always an open ear for my problems, and the help and support in many thinkable and unthinkable ways,

...Bruno Guiderdoni for taking over the supervision and supporting me during the second half of the thesis,

...Peter Jakobsen and Niranjana Thatte for refereeing this thesis, Roland Bacon for acting as president of the jury, and Santiago Arribas, Anne Ealet, Jean-François Gonzalez, and Hans-Walter Rix for joining the committee,

...the CRAL scientific informatics team consisting of Laure Piqueras, Emeline Legros, Aurélien Jarno, Pierre-Jaques Legay, Arlette Pécontal, Dominique Dubet, and Aurélien Pons for all their help in professional matters, but also during settling in and with general issues outside of CRAL,

...the NIRSpec team at EADS/Astrium, in particular Jess Köhler and Jean-François Pittet, Werner Hupfer, Xavier Gnani, Markus Melf, Peter Mosner, and Ralf Ehrenwinkler for their warm welcome and continuous support,

...Stephan Birkmann, Torsten Böker, Guido de Marchi, Giovanna Giardino, and Marco Sirianni for their enthusiasm and for integrating me into the work of the ESA JWST science team,

...the other students of the ELIXIR network for lots of fun times, especially Joki for chases during lunchtime and Cami for the great collaboration,

...Jeff Valenti for his experienced advice and great cooperation,

...Stéphane Charlot for leading the ELIXIR network and all his encouragement,

...the ESA JWST project team, especially Maurice te Plate for bringing me to the instrument in the first place, and the continued support during the PhD,

...all other members of CRAL for their kindness and for making this such an enjoyable place to work,

...and finally my parents and other relatives, who gave me all the freedom and support to get this far.

The research leading to these results has received funding from the European Community's Seventh Framework Program (FP7/2007–2013) under grant agreement nr. PITN-GA-2008-214227 – ELIXIR. This research has made use of the Exoplanet Orbit Database and the Exoplanet Data Explorer at exoplanets.org.

Contents

List of Figures	xv
List of Tables	xix
1 Introduction	1
1.1 The James Webb Space Telescope	1
1.2 Overview of the NIRSpec instrument	2
1.3 Optical layout of JWST and NIRSpec	4
1.4 The NIRSpec Instrument Performance Simulator	6
1.5 Goal and structure of this thesis	9
2 IPS software verification	11
2.1 Introduction	11
2.2 Revision of coordinate transforms	11
2.2.1 General formalism	11
2.2.2 Derivation of transform parameters	14
2.2.3 Slit tilt implementation	15
2.3 Revision of Fourier propagation	17
2.3.1 General application	17
2.3.2 Geometrical orientation	17
2.3.3 Single propagation steps	19
2.3.4 Implementation for NIRSpec	20
2.3.5 Sampling of PSFs and wavefront errors	22
2.3.6 Required sampling for NIRSpec	24
3 NIRSpec model description	27
3.1 Model data overview	27
3.2 Subsystem and telescope data	27
3.3 NIRSpec as-built optical model	31
3.3.1 Motivation	31
3.3.2 Model description	32
3.3.3 Model verification and transformation to cold	33
3.3.4 Relation between wavefronts and coordinate transforms	37

3.3.5	Data extraction for the IPS model	39
4	Science software tools	43
4.1	Science data interface	43
4.1.1	Motivation	43
4.1.2	Object positioning	44
4.1.3	Object input file types	46
4.1.4	Object separation criteria	48
4.1.5	Technical implementation	49
4.2	Spectrum extraction pipeline	50
4.2.1	Purpose and scope	50
4.2.2	Software implementation	50
4.2.3	Spectrum extraction operations	52
5	NIRSpec model verification	61
5.1	Motivation	61
5.2	Instrument geometry	62
5.2.1	Initial data and manual tuning	62
5.2.2	Model optimization	64
5.2.3	GWA tilt sensor integration in extraction	73
5.3	Test of IPS with tuned instrument model	75
5.4	Calibration Light Source spectra	76
5.5	Instrument efficiency	79
5.5.1	Filter transmissions	79
5.5.2	Grating efficiencies	81
5.5.3	Overall instrument throughput	83
5.5.4	IFU throughput	86
5.6	Limitations of simulations	87
6	NIRSpec science simulations	91
6.1	Multi-object deep field	91
6.1.1	Introduction	91
6.1.2	Observation scene creation	91
6.1.3	Galaxy shapes	92
6.1.4	Galaxy spectra	97
6.1.5	Exposure simulation	98
6.1.6	Spectrum extraction	101
6.1.7	Results and discussion	103
6.2	Exoplanetary transits	106
6.2.1	Introduction	106
6.2.2	Host star brightness limits	108
6.2.3	Noise from pointing jitter	110

6.2.4	Effective integration times	113
6.2.5	Signals and noise	114
6.2.6	Simulations of HD189733b	120
6.2.7	Simulations of GJ1214b	123
6.2.8	Simulations of an Earth-sized planet in the habitable zone . . .	126
7	Conclusion and outlook	129
A	Additional images	131
A.1	Verification of the as-built optical model	131
A.1.1	Measured wavefront errors at the FPA	131
A.1.2	Simulated wavefront errors at the FPA	133
A.1.3	Wavefront error residuals at the FPA	134
A.2	NIRSpec model data	136
A.2.1	Wavefront error maps	136
A.2.2	Efficiencies	138
B	Publications	145
B.1	Overview	145
B.2	Verification of the IPS with demonstration model data	146
B.3	First simulation of a JWST/NIRSpec observation	158
C	Acronyms	163
	Bibliography	165

List of Figures

1.1	Image of the JWST	2
1.2	JWST OTE optical scheme	4
1.3	JWST field of view allocation	5
1.4	NIRSpec paraxial layout	6
1.5	NIRSpec schematic drawing	7
1.6	Image of the NIRSpec FM1	8
2.1	Scheme of the coordinate transform formalism	12
2.2	Coordinate transform behavior outside fit region	15
2.3	Spectrum derivatives on the detector	16
2.4	FFT matrix pixel indexing	17
2.5	Axis orientations in Fourier transforms	18
2.6	Pupil and field orientations in NIRSpec optical planes	21
2.7	Measured and simulated PSF at MSA	22
3.1	Exemplary NIRSpec component efficiency curves	28
3.2	JWST OTE model wavefront error	32
3.3	Measured wavefront errors at MSA	33
3.4	Residuals of wavefront errors at MSA without optimization	34
3.5	Model wavefront errors at MSA and residuals	35
3.6	MIRR positions for optical measurements at the FPA	36
4.1	Scheme pf the simple input FOV	45
4.2	NIPPLS spectrum extraction workflows	51
4.3	Schemes of pixel grids in spectrum rectification	56
5.1	CLS SR1 source spectrum	62
5.2	Spectrum data of SLIT_A_200_2 with CLS SR1 and G140H	63
5.3	Spectrum data of SLIT_A_200_2 with CLS Argon and G140H	64
5.4	G140H B_200 CLS flatfield spectrum	66
5.5	G140H B_200 CLS flatfield trace data	66
5.6	Extracted spectrum of SLIT_A_200_2 with CLS Argon and G140H	68
5.7	Extracted spectrum of SLIT_B_200 with CLS Argon and PRISM	69
5.8	Model fit residuals with R2700 and MIRROR data	70

5.9	Total model fit residuals	71
5.10	Residuals of Argon lines with G140H	72
5.11	Residuals of Argon lines with G140H and GWA tilt	74
5.12	Drawing of the CLS	76
5.13	CLS PSB output spectra comparison	78
5.14	CLEAR filter spectra with PRISM	80
5.15	Relative transmission of F170LP measured and simulated	81
5.16	Ratio of G235M and G235H spectrum and model data	82
5.17	Ratio of IPS data to measured, R2700 gratings	83
5.18	Ratio of IPS data to measured with tuned model	84
5.19	Ratio of IPS data to measured, relative IFU spectra	87
5.20	Scheme of the NIRSpec MULTIACCUM readout	89
6.1	Evolution of galaxy sizes with redshift	93
6.2	Sizes of galaxies in MOS simulation scene	94
6.3	Sérsic profile curves with $n = 1$	95
6.4	Integrated intensity of elliptical Sérsic sapes	96
6.5	Galaxy contour images with MSA slitlet overlay.	96
6.6	Parameters of MOS simulation scene objects.	98
6.7	Exposure of the MOS simulation	100
6.8	Images of two spectrum extraction steps	102
6.9	Comparison of input and extracted galaxy spectra	104
6.10	Scheme of exoplanetary transit events	107
6.11	Map of losses in the A_1600 slit with G235H	111
6.12	Photometric drift noise in the A_1600 slit with G235H	112
6.13	Input spectrum of HD189733	120
6.14	Maximum electron rate for HD198733	121
6.15	SNR of primary transit of HD198733b	122
6.16	SNR of atmospheric height of HD198733b	123
6.17	SNR of emitted flux of HD198733b	123
6.18	Input spectrum of GJ1214	124
6.19	SNR of atmospheric height of GJ1214b	125
A.1	Measured wavefront errors at FPA center	131
A.2	Measured wavefront errors at FPA $+x$ -side	132
A.3	Measured wavefront errors at FPA $-x$ -side	132
A.4	Simulated wavefront errors at FPA center	133
A.5	Simulated wavefront errors at FPA $+x$ -side	133
A.6	Simulated wavefront errors at FPA $-x$ -side	134
A.7	Wavefront errors residuals at FPA center	134
A.8	Wavefront errors residuals at FPA $+x$ -side	135
A.9	Wavefront errors residuals at FPA $-x$ -side	135

A.10 IPS model FORE and COL wavefront errors	136
A.11 IPS model CAM wavefront errors at FPA center	137
A.12 IPS model CAM wavefront errors at FPA $+x$ -side	137
A.13 IPS model CAM wavefront errors at FPA $-x$ -side	138
A.14 IPS model mirror throughput	138
A.15 IPS model FWA element efficiencies	139
A.16 IPS model GWA element efficiencies	141
A.17 IPS model detector QE	143
A.18 IPS model IFU throughput	143

List of Tables

1.1	NIRSpec basic characteristics	3
2.1	Minimum required wavefront sampling	25
3.1	Differences in raytracing coordinates	38
4.1	Science input interface object file types	47
4.2	Spatial source separation criteria	49
4.3	Spectral source separation criteria	49
5.1	Model fit residuals on the detector	72
5.2	Ratio of simulated and expected electron rates	75
6.1	Limiting minimal magnitudes of stellar spectra	110
6.2	Mean drift noise in short exposures in the A_1600 slit	113
6.3	Exposure parameters for observations of GJ1214	125
6.4	Exposure parameters for observations of G1214 put at 10 pc	127
6.5	SNR of atmospheric features of an Earth-sized planet orbiting a M4.5 dwarf	128

For NASA, space is still a high priority.

Dan Quayle



Introduction

1.1 The James Webb Space Telescope

Ideas and plans for a successor mission to the Hubble Space Telescope (HST) already date back to the early 1990s. In the wake of discoveries made with the HST, the astronomical community realized the need and potential of follow-up observations in the infrared (IR) wavelength range, especially to enable the research of redshifted objects, and to peek through dust clouds surrounding stars and star-forming regions.

These considerations led to the project of the James Webb Space Telescope (JWST, Gardner et al., 2006), a cooperation between the National Aeronautics and Space Administration (NASA), the European Space Agency (ESA), and the Canadian Space Agency (CSA). It is a large near- and mid-infrared space observatory with a primary mirror diameter of about 6.5 m (see Figure 1.1), and passively cooled to less than 50 K. The JWST will be placed in an orbit around the Sun-Earth Lagrange point L2 with an Ariane 5 launch foreseen in 2018. The observatory will carry a package of four science instruments: A Near-IR Camera (NIRCam, Horner and Rieke, 2004), a Near-IR Spectrograph (NIRSpec, Bagnasco et al., 2007), a Near-IR Imaging Slitless Spectrograph (NIRISS, former TFI, Doyon et al., 2010), and a Mid-IR Instrument (MIRI, Wright et al., 2010). The three near-infrared instruments will observe in a wavelength range of 0.6 to 5 μm , while MIRI is sensitive between 5 and 27 μm . The scientific objectives of the JWST mission can be split up into four themes:

- The end of the dark ages: first light and reionization
- The assembly of galaxies
- The birth of stars and protoplanetary systems
- Planetary systems and the origins of Life

In combination with NIRISS, there is also the Fine Guidance Sensor (FGS) to track the telescope pointing.

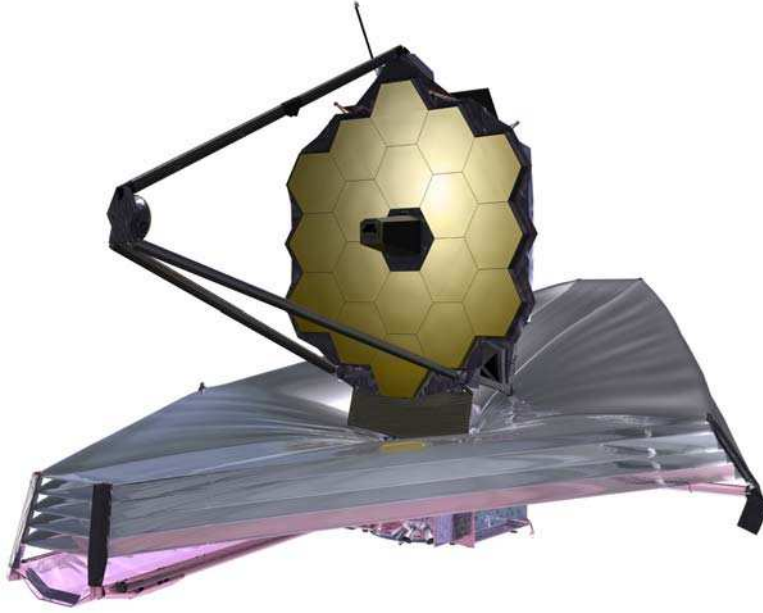


Figure 1.1: Image of the James Webb Space Telescope (credit: NASA).

1.2 Overview of the NIRSpec instrument

The primary science driver for NIRSpec is the spectroscopy of high-redshift galaxies out to $z = 6$ and beyond, where the end of the dark ages and begin of the reionization era is assumed. A second objective is the study of the evolution and assembly of galaxies throughout the ages. Therefore, the instrument has been designed as a multi-object spectrograph with the goal to observe at least 100 objects simultaneously. This capability is offered by a MicroShutter Array (MSA), consisting of four configurable grid masks for individual target selection (Kutyrev et al., 2008), covering a Field Of View (FOV) of at least 9 arcmin^2 . In addition, NIRSpec harbors an Integral Field Unit (IFU, Closs et al., 2008) with a small FOV to resolve single objects in both spatial and spectral dimensions. And lastly there are five FiXed SLits (FXSL) with different widths for high-contrast long-slit spectroscopy. Especially one of them (SLIT_A_1600) has gained scientific importance, as it offers the spectral analysis of exoplanetary transit events, and thus the characterization of exoplanets.

NIRSpec is sensitive across a spectral range of 0.6 to $5 \mu\text{m}$, more than three wavelength octaves, which therefore is divided into three main scientific bands. In each of them, two dedicated gratings provide a spectral resolution of $R = \lambda/\Delta\lambda \approx 1000$ and $R \approx 2700$. The complete wavelength span can also be observed with a

Table 1.1: *NIRSpec basic characteristics*

Feature	Value and explanation
Spectral range	0.6 μm –5.0 μm
Field of view	$> 9 \text{ arcmin}^2$
Spectral resolutions	$R \approx 100$ (low) $R \approx 1000$ (medium) $R \approx 2700$ (high)
Spectral bands (gratings)	Band I (1.0 μm –1.8 μm) Band II (1.7 μm –3.0 μm) Band III (2.9 μm –5.0 μm) Band 07 (0.7 μm –1.2 μm)
Filters	CLEAR (complete range) F100LP (1.0 μm –5.0 μm , long-pass) F170LP (1.7 μm –5.0 μm , long-pass) F290LP (2.9 μm –5.0 μm , long-pass) F070LP (0.7 μm –5.0 μm , long-pass) F110W (0.99 μm –1.2 μm , target acquisition band-pass) F140X (0.8 μm –2 μm , target acquisition band-pass) OPAQUE (closed, internal calibration and pupil reference)
MSA elements	Four quadrants of 365 \times 171 microshutters, width 200 mas
Fixed slits	SLIT_A_200_1, SLIT_A_200_2, SLIT_B_200: width 200 mas SLIT_A_400: width 400 mas SLIT_A_1600: square aperture, width 1600 mas
IFU	30 slices, widths 100 mas, lengths 3 arcsec
GWA elements	PRISM ($R \approx 100$) G140M, G235M, G395M: gratings $R \approx 1000$, bands I-III G140H, G235H, G395H: gratings $R \approx 2700$, bands I-III TAM: Target Acquisition Mirror
Detectors	2 Mercury-Cadmium-Telluride (MCT) Sensor Chip Arrays (SCAs), each 2048 \times 2048 pixels of 18 μm \times 18 μm (100 \times 100 mas ²), labeled 491 (blue side) and 492 (red side)

prism at low resolution ($R \approx 100$). A list of all filters and dispersers and other details is given in Table 1.1.

NIRSpec is largely manufactured from Silicon Carbide (SiC), a ceramic which is very lightweight yet stiff, has a small thermal expansion, and is able to be optically

polished. Only some subsystems employ other materials as Invar and Aluminum. NIRSpec will be operated at a temperature of about 35 K.

1.3 Optical layout of JWST and NIRSpec

The JWST observatory consists of an Optical Telescope Element (OTE), and an Integrated Science Instrument Module (ISIM). The OTE primary mirror is assembled from 18 partially deployed hexagonal segments. The telescope optics has an effective focal length of 131.4 m and delivers a $f/20$ beam to the instruments at the curved exit focal surface (OTE Image Plane, OTEIP, see Figure 1.2). The field of view is split up into different regions for the science instruments and the FGS (Figure 1.3). JWST has an off-axis telescope, therefore a master chief ray has been defined serving as reference origin for the FOV coordinates. NIRSpec has a field allocation rotated clockwise by 41.5° , defined by nine field points F1–F9. The spectral direction is tangential to the symmetry axis of the telescope optics.

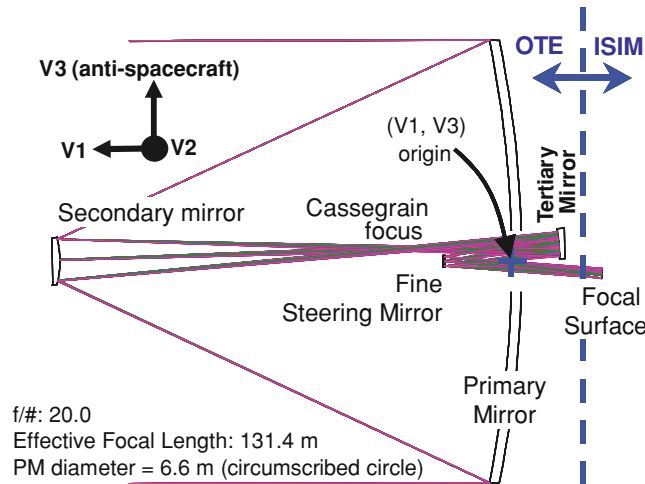


Figure 1.2: Optical layout of the JWST telescope (from Gardner et al., 2006).

At the OTEIP, the NIRSpec Field Stop (FS) constrains the observable sky area. The light is then picked up by the two coupling mirrors COM1 and COM2 and guided to the optical bench. The general optical design consists of three major blocks, all employing Three-Mirror Anastigmats (TMAs) (te Plate et al., 2005). Figure 1.4 shows the paraxial representation of the optical train with the different modules and key components. A design drawing of NIRSpec with the light path can be seen in Figure 1.5.

The FORE optics re-images the OTEIP onto the slit plane at the MSA with an adjusted scale, a telecentric beam, and flattened focal surface. The nominal f-number

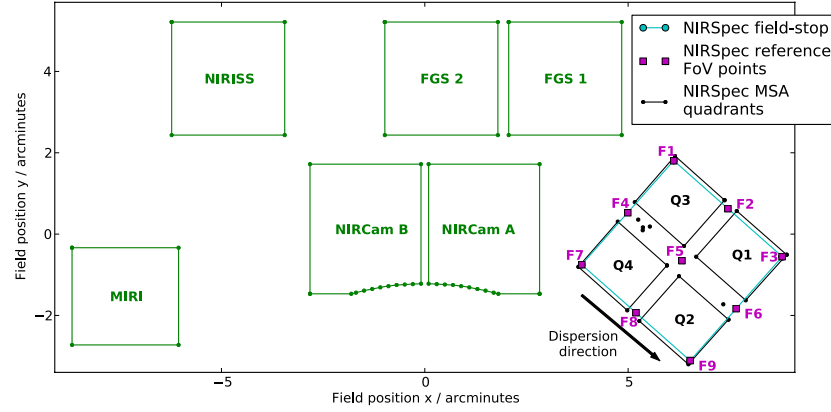


Figure 1.3: Field of view allocation of the JWST instruments and elements of the NIRSpec slit plane on the sky. The area for NIRSpec is rotated clockwise by 41.5° and defined by the nine points F1–F9.

is converted to $f/12.5$. In the pupil plane, the Filter Wheel Assembly (FWA) is located, carrying the filters listed in Table 1.1. Before reaching the MSA, the light also passes through the Refocusing Mirror Assembly (RMA), which allows the adaption of the focus without displacing the beam laterally.

The COLimator optics (COL) projects the light from the slits onto the Grating Wheel Assembly (GWA), where a pupil plane is located. The GWA is equipped with eight elements described in Table 1.1 and allows the selection of disperser band and resolution, or mirror for imaging. Finally, the CAMera optics (CAM) focuses the (dispersed) beam onto the two detectors in the Focal Plane Array (FPA) with a f -number of $f/5.6$.

The IFU entrance aperture is located in the MSA plane, but normally obscured by the MSA magnet arm. IFU and MSA observations are exclusive as their spectra share the detector area, so all shutters have to be closed during IFU operations, and the IFU has to be blocked for MOS exposures. The IFU optics are split into an IFU FORE part, which re-images and -scales the MSA plane onto the slicer, and an IFU POST part, which picks up the 30 image parts, and creates a virtual slit image for each slice at the MSA plane. The rest of the light path is similar to the other observation modes. More details of the optical properties are given by Closs et al. (2008).

For the internal calibration, NIRSpec is equipped with a CALibration Assembly (CAA), which hosts a series of lamps for different flatfield and spectral calibration illuminations. The beam of the CALibration optics (CAL) is coupled into the nominal NIRSpec path by putting the OPAQUE filter, that also acts as a shutter for external light.

One part of the ground support equipment is the Calibration Light Source (CLS, Bagnasco et al., 2008). This is the primary tool for the absolute radiometric and

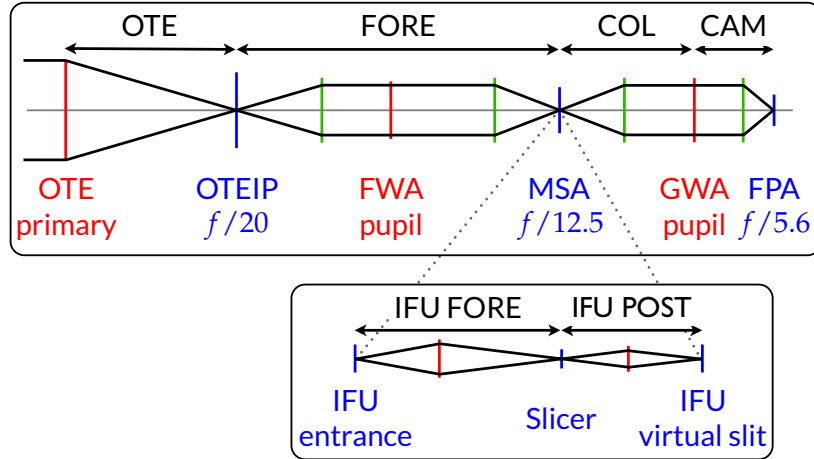


Figure 1.4: Paraxial layout of the NIRSpec optical train with the main modules and nominal focal ratios. Pupil stops are red, focal planes blue. The system pupil stop is the OTE primary mirror, the system field stop is located at the OTEIP. The IFU optics is coupled into the beam at the MSA focal plane.

spectral calibration of NIRSpec during the ground calibration campaigns. It consists of a lightbox with filament lamps and a set of four filter wheels, which carry different attenuators and spectral filters to generate appropriate illuminations for the flatfield and spectral calibration. In addition, there is an Argon emission line source and a laser diode for accurate spectral reference. All the sources are fed into a large integrating sphere, whose exit aperture mimics the JWST pupil. A Field Stop Mask (FSM) can be placed at the NIRSpec entrance for a flatfield illumination, as well as a PinHole Mask (PHM) to calibrate the geometrical distortion. The latter has a grid of small holes (diameters typically $< 8 \mu\text{m}$) which create quasi point-like sources in the OTEIP, and also allow the characterization of the polychromatic PSF of the instrument.

In spring 2011, the first NIRSpec flight model (FM1, Figure 1.6) has successfully undergone cryogenic testing and calibration. Due to hardware issues, a second assembly of the components is currently under way (FM2), and will likely be completed towards the end of 2012.

1.4 The NIRSpec Instrument Performance Simulator

Early in the development of NIRSpec, the need for an instrument simulator was realized, given the inherent complexity of a multi-object spectrograph, with all other operation modes on top. In the frame of the project, the Centre de Recherche Astrophysique de Lyon (CRAL) has developed the NIRSpec Instrument Performance

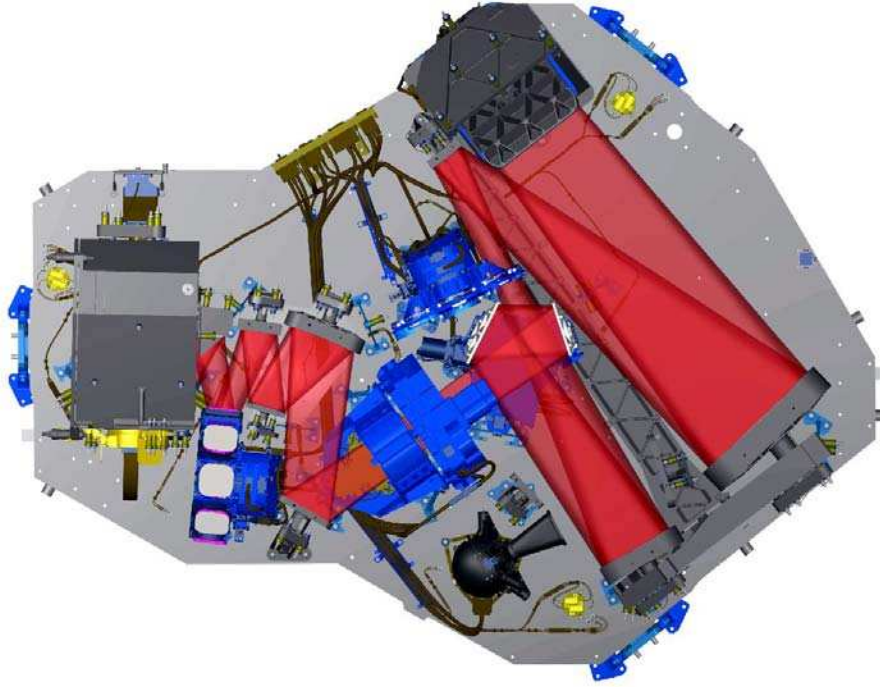


Figure 1.5: NIRSpec schematic drawing with light path, top view. The light enters at top right, passes through the FORE optics, the filter wheel, the RMA, and reaches the MSA slit plane. Proceeding through the collimator, it arrives at the grating wheel, then passes the camera, ending up at the detector (hidden in the CAM housing). (Credit: EADS/Astrium)

Simulator (IPS) software (Gnata, 2007; Piqu  ras et al., 2008, 2010). Its primary functions are to assess the instrument specifications, verify the performance, and do end-to-end simulations of calibration and scientific exposures. Besides, it serves to create realistic input data for processing tools, as the Instrument Quick Look Analysis and Calibration software (IQLAC, Gerssen et al., 2008) or the final NIRSpec data reduction pipeline.

To simulate the propagation of light, the instrument is divided into optical modules, mostly defined by the single TMAs (COM + FORE, COL, CAM, CAL, OTE, IFU FORE, IFU POST), and the functional parts as filters, slits, and dispersers. The IPS uses a novel approach combining Fourier optics for the diffractive effects, geometrical coordinate transforms between the key optical planes, and simple efficiency calculations for the radiometry. These elements produce noiseless electron rates as a first main simulation product. The data contains the number of electron per second in each detector pixel, without any photon or readout noise, separate for each disperser order.



Figure 1.6: Fully assembled NIRSpec flight model 1 without the instrument cover (credit: EADS/Astrium).

In a second stage, the readout process is simulated. All detectors in JWST use a sampling up the ramp-technique, where the signal in each pixel is probed non-destructively during the integration time. In the IPS, the electron rates for each pixel are collapsed over the orders, dark current is applied, and all the noise contributions added (Poisson, readout, etc.). The currently integrated signal is then put into a readout frame, and depending on the parameters, the frames are averaged to groups and written into the readout cube file.

In order to reduce the calculation time of electron rates, the sources are split into three spatial and spectral categories, each of them simulated differently. The spatial types are point sources (spatially unresolved), background sources (spatial variations on scales much larger than the instrument Point Spread Function, PSF), and extended sources (in between). The spectral types are continuum spectra (spectral variations on scales much larger than a resolution element), unresolved emission lines and absorption lines associated with a continuum, and spectrally resolved (in between).

Point sources are always completely Fourier-propagated for each required wavelength. For the other source types, there is a collection of pre-calculated PSFs for the step up to the slit plane, and for the spectrograph from slit to detector. They can be created with a single wavefront error map for the whole module, or with a grid of 3×3 maps covering the relevant fields. From them, the locally valid PSF is then interpolated. Background sources are projected to the detector, the slit mask is applied, and they are convolved with the spectrograph PSF. Extended sources are

similarly processed, but convolved with the PSF at the slit plane before applying the slit mask.

In the case of emission and absorption lines, this is done for the single given wavelength only. With continuum spectra, the spectrograph PSF is collapsed in spectral direction before being interpolated to the local wavelengths. Besides, the sampling along the spectral direction on the detector is reduced to full pixels. The spectrally resolved spectra are always using the full 2D PSF for each oversampled wavelength step on the detector.

1.5 Goal and structure of this thesis

The goal of this thesis is to demonstrate the verification of the IPS, the instrument model and the instrument itself, and show first scientific simulations of NIRSpec observations.

In order to assure correct and accurate simulation results, one has to differentiate between two sources of errors: The intrinsic design of functions and algorithms in the software, and the data used in the instrument model.

The first can be partially checked by simulations with controlled inputs and models, which allow an independent calculation of the expected results. This approach has been taken in the acceptance tests required before the software delivery. However, they may not be sensitive to wrong assumptions in the software design, and effects caused by realistic model data.

The second type of errors can be mitigated by assembling the instrument model from measured and as-built subsystem data where possible. Nevertheless, this is not always feasible, the data may be inaccurate, and the interplay with other model data can cause unforeseen effects. To verify the software functions as well as the models, it is necessary to compare simulations with theoretical results and with real instrument measurements. A first set of them for the NIRSpec FM1 is available from the cryogenic calibration campaign, taken in spring 2011.

The final purpose of the IPS is to provide realistic simulations of in-orbit observations. Naturally, a complex instrument also yields a complex simulator, and to facilitate the scientific application, it is necessary to create a simple way to use external source data. Besides, the IPS outputs are electron rates or raw data cubes, which need to be processed before any scientific analysis.

With the necessary tools and data prepared, it is then possible to produce accurate on-sky simulations, and analyze them easily. This enables a in-depth assessment and verification of NIRSpec's capabilities for different science cases. Besides, it shows the characteristics and quality of the data that could be expected from the instrument.

This thesis describes the different steps in the model preparation and verification process, along with software tools for science data input and output data processing, and presents first simulations of on-sky observations. The structure is split into the

following parts: In chapter 2 we revise two specific IPS algorithms, and in chapter 3 we describe the data of the as-built instrument model. We present two software tools to facilitate the usage of the IPS in chapter 4. In chapter 5 we demonstrate how we verified the instrument model by comparing simulations with calibration data, and finally in chapter 6 we show the simulation and analysis of two scientific observation types: a multi-object scene, assembled from high-redshift galaxies, and exoplanetary transit events.

The work was embedded in the NIRSpec project environment, and makes use of various other existing efforts, most notably the IPS software. For clarity, we repeat essential characteristics of the simulator in chapter 2, in detail the algorithm for coordinate transforms in the instrument. Using this concept, we re-implemented the slit tilt effect based on the presented analysis. Also the general algorithm of the Fourier propagation and the coupling with physical parameters was established during the software design, however it had never been verified with the real orientations and the process of stepping through the instrument principal planes. In the end, the corresponding code was fully revised with the new considerations from this thesis.

The assembly of an as-built instrument model described in section 3.2 was largely a team effort, especially as it was part of the deliverable package in the IPS project. However, the work leading to the optical as-built model presented in section 3.3, originates solely from this thesis. It only uses the existing alignment model from Astrium as a starting point, and was done independently of officially required activities.

Finally, the development of the auxiliary software, the verification of the instrument model data, and the scientific simulations are fully original work, contributions from collaborators are marked accordingly.

*If debugging is the process of removing bugs,
then programming must be the process of
putting them in.*

Edsger Dijkstra

2

IPS software verification

2.1 Introduction

As mentioned in section 1.4, the IPS consists of several modules to model different physical processes (Piqueras et al., 2008). The basic considerations for the design of the algorithms can be found in Gnata (2007). However, some points had not been defined in detail, and other effects were only apparent once realistic simulations were run. Two major issues are the geometrical coordinate transforms, especially the effect of the slit tilt, and the orientation and sampling of wavefront errors and PSFs. We therefore review two simulation elements, the implementation of coordinate transforms in section 2.2, and the Fourier propagation in section 2.3. Independent of these major points, there was always close support of the software development team during the IPS project, for various issues ranging from user interaction, finding and isolating errors in the computations, and testing so far unused functionality.

2.2 Revision of coordinate transforms

2.2.1 General formalism

Transform formulas

The coordinate transforms in the IPS use a paraxial transform between the principal planes, and on top a 2D distortion polynomial (Figure 2.1). The paraxial part of a forward coordinate transform is defined by the magnification factors along the output axes γ_x and γ_y , the rotation angle of the coordinate system ϑ , and the absolute position of the input and output frame origin in the local coordinates (x_{0in}, y_{0in}) and (x_{0out}, y_{0out}) . From the input coordinates (x_{in}, y_{in}) , the paraxial output coordinates

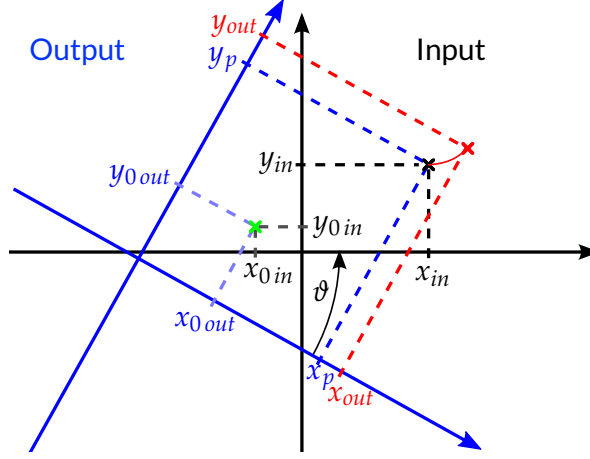


Figure 2.1: Scheme of the coordinate transform formalism. The transform is a rotation of the input point (x_{in}, y_{in}) around the center with the coordinates (x_{0in}, y_{0in}) and (x_{0out}, y_{0out}) in the input and output planes (green), and a scaling along the output axes, giving the paraxial output coordinates (x_p, y_p) . The distortion is added as a 2D-polynomial yielding the output coordinates (x_{out}, y_{out}) (red). The rotation angle ϑ is measured anti-clockwise from the output axes to the input axes.

(x_p, y_p) are then calculated by

$$\begin{aligned} x_p &= \gamma_x \cdot [(x_{in} - x_{0in}) \cos(\vartheta) + (y_{in} - y_{0in}) \sin(\vartheta)] + x_{0out} , \\ y_p &= \gamma_y \cdot [-(x_{in} - x_{0in}) \sin(\vartheta) + (y_{in} - y_{0in}) \cos(\vartheta)] + y_{0out} . \end{aligned}$$

The optical distortion is applied in the form of a 2D polynomial of order n , so the final output coordinates of the transform (x_{out}, y_{out}) are

$$\begin{aligned} x_{out} &= \sum_{i=0}^n \sum_{j=0}^{n-i} a_{i,j}(\lambda) x_p^i y_p^j , \\ y_{out} &= \sum_{i=0}^n \sum_{j=0}^{n-i} b_{i,j}(\lambda) x_p^i y_p^j . \end{aligned}$$

The transmissive filters in the FORE cause a chromatic aberration, which is sufficiently fitted by first-order wavelength-dependent polynomial coefficients

$$\begin{aligned} a_{i,j}(\lambda) &= \alpha_{xi,j} \lambda + \beta_{xi,j} , \\ b_{i,j}(\lambda) &= \alpha_{yi,j} \lambda + \beta_{yi,j} . \end{aligned}$$

Other optical modules are only reflective, and their transforms therefore exhibit no chromatic dependence.

A backward transform is done in the reverse order. At first, the distortion is removed and the paraxial coordinates calculated:

$$\begin{aligned} x_p &= \sum_{i=0}^n \sum_{j=0}^{n-i} c_{i,j}(\lambda) x_{out}^i y_{out}^j , \\ y_p &= \sum_{i=0}^n \sum_{j=0}^{n-i} d_{i,j}(\lambda) x_{out}^i y_{out}^j , \end{aligned}$$

where

$$\begin{aligned} c_{i,j}(\lambda) &= \rho_{x i,j} \lambda + \sigma_{x i,j} , \\ d_{i,j}(\lambda) &= \rho_{y i,j} \lambda + \sigma_{y i,j} . \end{aligned}$$

Then the input coordinates are

$$\begin{aligned} x_{in} &= \frac{1}{\gamma_x} (x_p - x_{0out}) \cos(\vartheta) - \frac{1}{\gamma_y} (y_p - y_{0out}) \sin(\vartheta) + x_{0in} , \\ y_{in} &= \frac{1}{\gamma_x} (x_p - x_{0out}) \sin(\vartheta) + \frac{1}{\gamma_y} (y_p - y_{0out}) \cos(\vartheta) + y_{0in} . \end{aligned}$$

The presented approach is adjusted to the instrument in two ways: First, the polynomial order can be set to $1 \leq n \leq 5$ as this corresponds to the requirement for the design. Second, we also exploit the fact that there is no nominal rotation in the area where distortion occurs. The only place rotating the coordinates is between COM1 and COM2, which both are flat mirrors right after a focal surface, and do not change the optical behavior. Therefore it is allowed to put the rotation in the paraxial approximation, and adding the distortion in a single step.

Transform coordinates

The paraxial description of the optical modules is based on the nominal entrance and exit focal lengths. They can be different in both axes, so that in total four parameters $f_{in x,y}$, $f_{out x,y}$ are present. For modules between a focal and pupil plane or reverse, one of the focal length types is ignored.

In an image plane, the coordinates are the physical positions in the local reference frame. For the transform between two image planes (as in the FORE), the magnification factors γ_x and γ_y correspond to the ratio of the focal lengths:

$$\gamma_x = \frac{f_{out x}}{f_{in x}} , \quad \gamma_y = \frac{f_{out y}}{f_{in y}} . \quad (2.1)$$

In a pupil plane, the coordinates are angular values of the ray direction. Often they are given as direction cosines $\Gamma_{x,y,z}$, but we use a vector with unitary z-component

of the form

$$\begin{pmatrix} x \\ y \\ 1 \end{pmatrix} = \begin{pmatrix} \Gamma_x/\Gamma_z \\ \Gamma_y/\Gamma_z \\ \Gamma_z/\Gamma_z \end{pmatrix}$$

Between an image plane and a pupil plane, the magnification factors are then

$$\gamma_x = \frac{1}{f_{in\ x}}, \quad \gamma_y = \frac{1}{f_{in\ y}}, \quad (2.2)$$

and between a pupil plane and an image plane

$$\gamma_x = f_{out\ x}, \quad \gamma_y = f_{out\ y}. \quad (2.3)$$

2.2.2 Derivation of transform parameters

The transform parameters are calculated from raytracing data of the NIRSpec model in the ZEMAX® optical design software. For a set of wavelengths, a grid of points covering the field of interest is traced through each optical module, and the input and output coordinates are recorded. A priori the paraxial parameters are unknown, and a distortion fit is done with dummy paraxial values, the center coordinates (x_{0in}, y_{0in}) , (x_{0out}, y_{0out}) are set to the center of the data grid. Nevertheless, this fit yields a valid transform calculation, which can be used to derive the paraxial parameters.

With the assumption that locally a paraxial approximation can be used, the parameters are related to the local derivatives as follows:

$$\begin{aligned} \frac{\partial x_{out}}{\partial x_{in}} &= \gamma_x \cos(\vartheta), & \frac{\partial x_{out}}{\partial y_{in}} &= \gamma_x \sin(\vartheta), \\ \frac{\partial y_{out}}{\partial x_{in}} &= -\gamma_y \sin(\vartheta), & \frac{\partial y_{out}}{\partial y_{in}} &= \gamma_y \cos(\vartheta). \end{aligned} \quad (2.4)$$

The derivatives can be calculated numerically for the center point, and by taking care of the signs, the magnifications and rotation of the average paraxial approximation are obtained with $\gamma_y \geq 0$ and $\vartheta \in [-\pi, \pi]$. The new parameters are then put into the transform, and a second distortion polynomial fit is performed, now based on a correct paraxial description.

From the new magnification factors, one can also derive the actual effective focal lengths with Equations 2.2, or 2.3. In the case of the FORE, where the transform is directly from focal to focal plane, another distortion fit is established between the OTEIP and FWA pupil plane to determine the effective entrance focal lengths. Then, the exit focal lengths are calculated with the module magnification and Equation 2.1.

The described approach harbors the danger that the polynomials are only valid inside the grid area. Calculating a coordinate transform outside the defining grid

can lead to problematic results and has to be avoided, as it is evident in Figure 2.2. A partial solution is to slightly oversize the raytracing grids on the expected used area, or to choose a first order polynomial fit, which is more robust in the outside region. However, this corresponds to a paraxial system and is usually not sufficient to fit the optical distortion with the required accuracy, therefore it is only applicable in few cases.

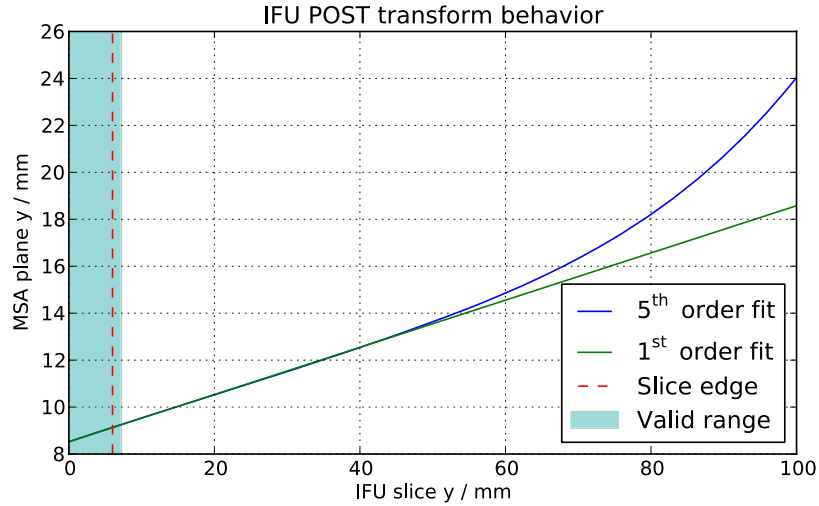


Figure 2.2: Behavior of the IFU POST coordinate transform for a slice at $x = 0$ (slice center). The polynomial was fitted over a grid extended to $y = 7.2$ mm, beyond the slice edge located at $y = 6$ mm. The fifth order polynomial yields unrealistic distortion when using points farther away. A first order fit corresponds to a paraxial transform and is more robust in the outside region, but may generally not be sufficient to fit the distortion of the optics with the desired accuracy.

2.2.3 Slit tilt implementation

The previously illustrated recipe is capable of producing very accurate coordinate transforms for the OTE and inside NIRSpec. In all modules except the FORE optics, there is no or very little rotation, and no chromatic dependence of the coefficients. However, in combination with the dispersing element in the spectrograph, another effect occurs: the tilt of the slit image in the spectra.

In imaging mode, the spectrograph transform from slits to the detector can locally be approximated by a paraxial system. A slit itself may be rotated in the MSA plane by ϑ_{rot} , so that the spatial axis along the slit y_{slit} and the MSA y_{MSA} are not collinear. The slit image will then be rotated by the angle $\vartheta_{FPA} + \vartheta_{rot}$. Assuming paraxial systems, ϑ_{FPA} is the sum of the rotations in the collimator and camera

$\vartheta_{FPA} = \vartheta_{COL} + \vartheta_{CAM}$, and can be derived from the tilt of the MSA x -axis with

$$\vartheta_{FPA} = \vartheta_x = \arctan \left(\frac{\partial y_{FPA}}{\partial x_{MSA}} / \frac{\partial x_{FPA}}{\partial x_{MSA}} \right),$$

which is the same angle for the MSA y -axis

$$\vartheta_y = \arctan \left(\frac{\partial x_{FPA}}{\partial y_{MSA}} / \frac{\partial y_{FPA}}{\partial y_{MSA}} \right).$$

The local orientations are more complex in spectrographic mode, where the off-plane design of NIRSpec causes a curvature of the spectral lines (Schroeder, 2000, chapter 14). The curvature radius is very large compared to the length of a single slit, therefore it can be approximated with a slit tilt as shown in Figure 2.3. The single transforms for COL and CAM remain valid, but when including the disperser, the partial derivatives are not orthogonal any more, i.e. $\vartheta_x \neq \vartheta_y$. The slit tilt is a shear along the projected MSA x -axis by an angle ϑ_{slit} , which can be calculated as the difference between the tilts of the y - and x -axes to $\vartheta_{slit} = \vartheta_y - \vartheta_x$. On the FPA, the image of the slit is finally tilted by $\vartheta_y + \vartheta_{rot}$.

In the IPS this has consequences for all simulation types described in section 1.4, especially for continuum spectra. By collapsing the PSF in the FPA x -direction, all position information along this axis is lost and the resulting spectra would be straight in the FPA y -direction. The rotations of the distortion ϑ_x and the slits ϑ_{rot} are typically much smaller than the slit tilt. Therefore the collapsed vector is rebinned along the x -direction with a shear rate of $\Delta x_{FPA} = \Delta y_{FPA} \sin(\vartheta_y + \vartheta_{rot})$, where Δy_{FPA} is measured from the slit center trace location.

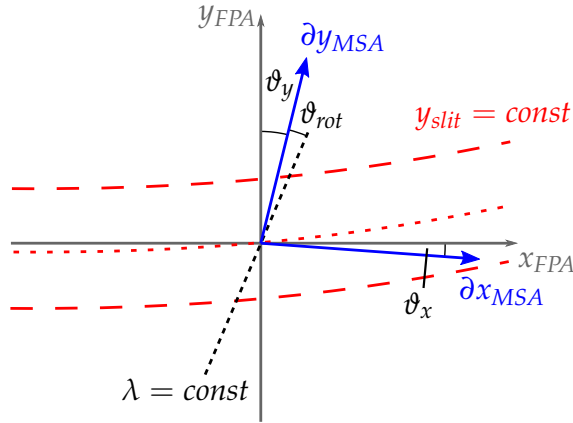


Figure 2.3: Scheme of the spatial derivatives and tilt angles on the detector. The slit is rotated by ϑ_{rot} in the MSA plane. The derivatives along the MSA axes ∂x_{MSA} and ∂y_{MSA} are not orthogonal. The spectra are curved due to the distortion, and the image of the slit is tilted by $\vartheta_y + \vartheta_{rot}$ due to the off-plane spectrograph.

The PSFs for point sources are directly calculated on an oversampled grid of the detector pixels. To mimic a slit tilt, the slit mask is rotated by the angle relative to the orientation on the FPA $\vartheta_y + \vartheta_{rot}$. Extended and background sources are projected onto the oversampled detector grid, and masked there with the slit shape. This mask is sheared in x with $\Delta x_{FPA} = \Delta y_{FPA} \sin(\vartheta_{slit})$ to introduce the slit tilt, and rotated by $\vartheta_x + \vartheta_{rot}$ to account for the geometrical rotation.

2.3 Revision of Fourier propagation

2.3.1 General application

The principle of propagating a wavefront from a pupil plane to an image plane and back is well known, and if the Fraunhofer approximation is valid, it can be numerically done with a Fast Fourier Transform (FFT) (Goodman, 1996). However, the relations between the orientation in physical coordinates in the optics and data arrays in the software require a careful definition of the algorithm and associated data input and output routines. NIRSpec has an unusual and rotated pupil shape, therefore the PSFs have a distinct appearance. Hence the PSF shape is an easy way to visually verify simulations with measurements, even though the absolute impact of a wrongly oriented PSF may be small.

2.3.2 Geometrical orientation

When using a FFT with a complex 2D array of the shape $N \times N$ (FFT matrix, N even), the zero frequency component is associated with the center of a pixel. In the

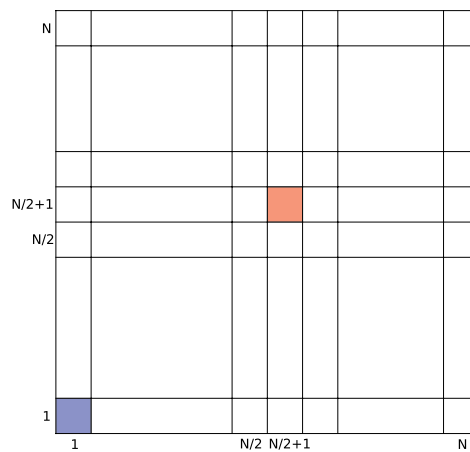


Figure 2.4: Pixel indexing of a FFT matrix. The zero frequency is in pixel $(1, 1)$ for the FFT calculation, while it is moved to $(N/2 + 1, N/2 + 1)$ for physical applications.

standard FFT output, this pixel is located in the corner of the array with index $(1, 1)$ (we use indices starting at 1). To enable the physical application of pupil apertures and wavefront error (WFE) maps, which generally have the coordinate frame center in the array center, the FFT matrix has to be transformed to put the zero frequency at pixel $(N/2 + 1, N/2 + 1)$, and back for the FFT transform (see Figure 2.4). We generally assume the zero frequency pixel to be in the center of the matrix.

The physical extent and orientation can be defined by auxiliary parameters. We associate a FFT matrix with the pixel step sizes of the array $\Delta x, \Delta y$ and the physical position of the corner pixel $(1, 1)$, (x_0, y_0) . In similar fashion, the model data as wavefront errors and pupil masks have their own physical coordinates. If they are provided in the instrument reference frames, and the FFT propagation keeps track of the physical coordinates, one obtains the PSFs with the correct orientation.

By default, the x - and y -axes in a Cartesian system span the input plane, while the z -axis points downstream along the propagation of the light (Figure 2.5). After a Fourier transform, the axes in the output plane are collinear to the input plane. For a propagation from pupil to pupil via image plane, an inverse FFT (iFFT) \mathcal{F}^{-1} and a FFT \mathcal{F} are done sequentially. In the mathematical definition, the coordinate systems remain collinear, while in the real optical system, the pupil content is flipped. In the IPS algorithm, this effect has to be traced by adjusting the physical parameters in the FFT matrix, and not flipping the array contents, which would otherwise move the pixels to wrong frequency coordinates.

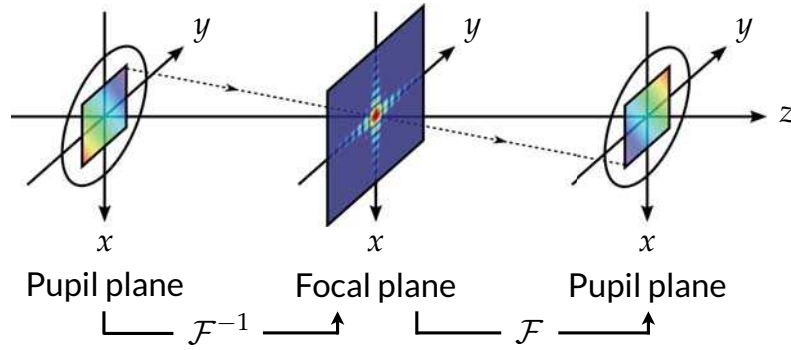


Figure 2.5: Orientations of the coordinate axes in the Fourier propagation from pupil to pupil via focal plane. The planes are spanned by x and y , z points along the propagation of the light. The propagation is calculated by an inverse and a forward Fourier transform \mathcal{F}^{-1} and \mathcal{F} . Mathematically the coordinates stay collinear, while the pupil is flipped optically.

2.3.3 Single propagation steps

Pupil to focal plane

If there is no previous propagation step, the complex FFT matrix in the pupil plane $A_p(i, j)$ is initialized with 1 everywhere. The origin is in pixel $(N/2 + 1, N/2 + 1)$. The physical step size $\Delta x_p, \Delta y_p$ has to be chosen for appropriate sampling of the pupil and PSF. In subsection 2.3.5 we describe this adjustment in detail. The physical position of pixel $(1, 1)$ is given as

$$x_{0p} = -\frac{N}{2\Delta x_p}, \quad y_{0p} = -\frac{N}{2\Delta y_p}.$$

At a specific wavelength λ , a wavefront error map $W(x, y)$ is then applied by interpolating the data at the physical coordinates of the FFT matrix pixels $(x_{i,j}, y_{i,j})$, and changing the phase with

$$A'_p(i, j) = A_p(i, j) \cdot \exp\left(2\pi i \frac{W(x_{i,j}, y_{i,j})}{\lambda}\right).$$

In similar fashion, a pupil intensity mask $I(x, y)$, $0 \leq I(x, y) \leq 1$ is applied by changing the amplitude as

$$A''_p = A'_p(i, j) \cdot I(x_{i,j}, y_{i,j}).$$

The WFE map does not influence the amplitude of the complex matrix, and therefore has to cover the same area of the pupil mask. Otherwise, no wavefront error is applied outside the available area while the intensity may be not zero. This can lead to wrong PSFs consisting of a combination of a degraded part with aberrations and an ideal PSF without.

The complex amplitude in the focal plane is the inverse Fourier transform of the pupil

$$A_f = \mathcal{F}^{-1}(A''_p),$$

and the pixel step size is now

$$\Delta x_f = \frac{\lambda f_{out x}}{\Delta x_p N}, \quad \Delta y_f = \frac{\lambda f_{out y}}{\Delta y_p N} \quad (2.5)$$

with the exit focal lengths of the optical module $f_{out x}, f_{out y}$. Like before, the coordinate of the corner pixel is

$$x_{0f} = -\frac{N}{2\Delta x_f}, \quad y_{0f} = -\frac{N}{2\Delta y_f}.$$

Focal to pupil plane

The Fourier propagation starting at a focal plane is only reasonable if there is a complex matrix A_f present from a previous pupil-to-focal propagation. The amplitude in the pupil plane is then the FFT of the focal plane:

$$A_p = \mathcal{F}(A_f).$$

As mentioned in subsection 2.3.2, the optical pupil is now rotated by 180° , while the Fourier matrix is not. Therefore the step and start values have to be inverted:

$$\Delta x_p = -\frac{\lambda f_{in x}}{\Delta x_f N}, \quad \Delta y_p = -\frac{\lambda f_{in y}}{\Delta y_f N},$$

$$x_{0p} = -\frac{N}{2\Delta x_p}, \quad y_{0p} = -\frac{N}{2\Delta y_p}.$$

This does not change the data, but relates the array correctly to the local coordinates. If another propagation step to a focal plane is necessary, the PSF there will be oriented the right way.

2.3.4 Implementation for NIRSpec

The Fourier algorithm uses the system of optical modules in the IPS (section 1.4). They are characterized with their pupil diameter D , and nominal entrance and exit focal lengths for both axes. These can be calculated with the scheme presented in subsection 2.2.2.

To define the orientations at the principal optical planes, we used the official NIRSpec optical model, where the reference frames in pupils and focal planes are given (Figure 2.6). We then put together the steps for a FFT-based propagation from one plane to the next, including the coordinate flips and rotations. We also noted the orientation of the z -axis, and how a wavefront with positive phase is oriented locally. This is important to correctly add the single WFE maps at different steps. We tested the newly assembled Fourier module using pupil masks with unique features to detect the orientations of pupils and PSFs. Comparing with a Python-based implementation, we could successfully reproduce the results in the IPS.

To verify the scheme with real instrument data, we used measurements taken during the NIRSpec Demonstration Model (DM) test campaign (Böker et al., 2010). With a pinhole mask at the NIRSpec field stop location, and the detector at the slit plane, the broadband PSFs of the FORE optics were recorded. In this configuration, the FWA stop defines the system pupil. In the DM, the stop is an oversized shape of the OTE primary boundaries, similar to the mask shown in Figure 2.6(b) without the three spider arms.

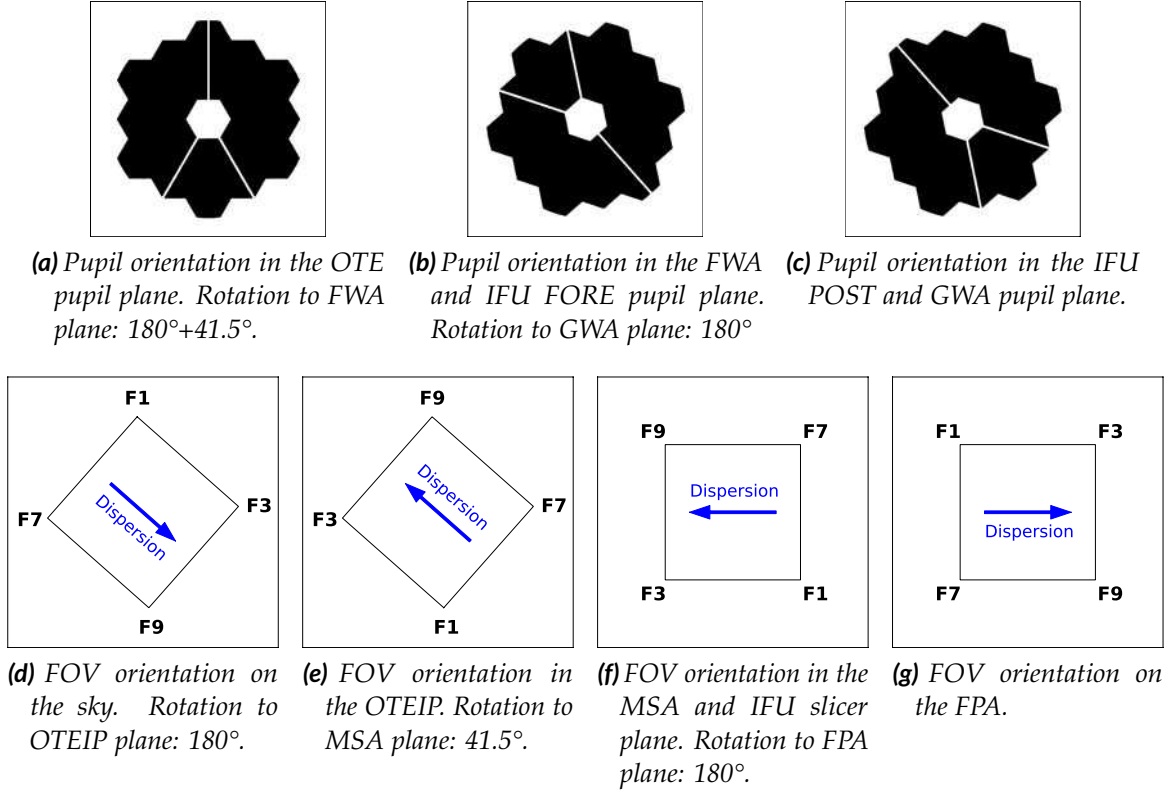


Figure 2.6: NIRSpec pupil and field orientation in various key optical planes with the projected dispersion direction. The local physical axes are x to the right, y up. The z -axis points downstream except for the MSA and FPA planes. To move to the next plane, the data has to be rotated counterclockwise with the given angle.

One PSF example, reconstructed from dithered data as in Dorner et al. (2010, see section B.2), is shown in Figure 2.7(a). It is the polychromatic PSF of a pinhole in the spectrum range $0.9\text{--}1.9\,\mu\text{m}$. At this wavelengths, the FORE optics is already diffraction limited, therefore the PSF is purely determined by the pupil stop shape. Clearly visible is the six-spoke diffraction pattern caused by the hexagon-like outer edge of the FWA stop.

For a comparison we simulated the monochromatic PSF of the FORE at $1.5\,\mu\text{m}$ shown in Figure 2.7(b). The orientation of the diffraction spikes is the same, confirming correct handling of the stop masks and FFT matrices. As the measured PSF contains contributions from longer wavelengths, the simulated PSF size is slightly smaller, but generally matches in the extension and decay of the diffraction features.

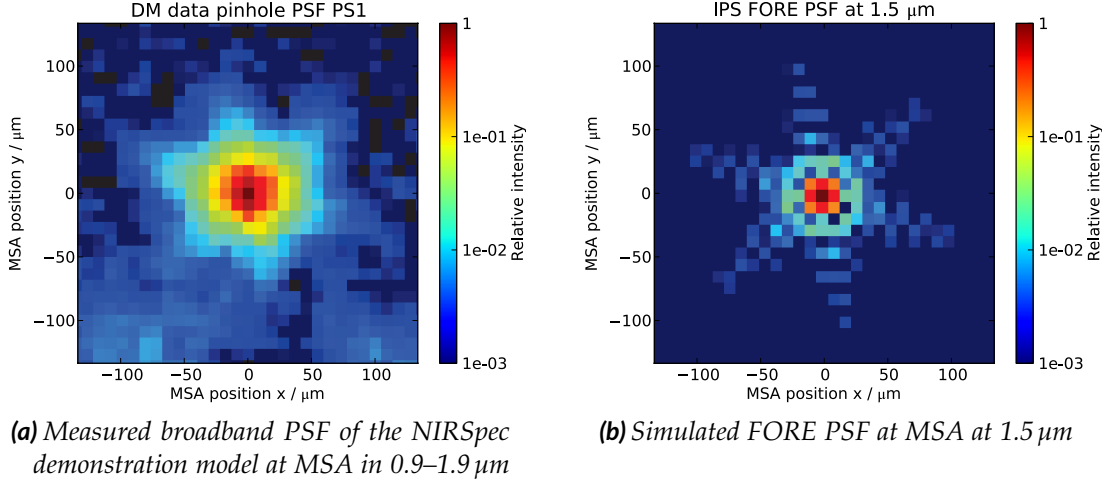


Figure 2.7: PSFs of the NIRSpec FORE optics. (a): Measured in the NIRSpec demonstration model. (b): simulated with the IPS. The diffraction pattern is rotated alike. The PSF size is similar, the measured PSF is slightly larger as it contains contributions from longer wavelengths.

2.3.5 Sampling of PSFs and wavefront errors

Space domain

The physical pixel sizes of the FFT matrices are directly linked to each other (Equation 2.5). It is therefore necessary to establish a relation between the sampling of the PSF and the WFE maps. Considering only one dimension, we get

$$\Delta x_f = \frac{\lambda f_{out x}}{\Delta x_p N} = \frac{\lambda f\#}{N} \cdot \frac{D}{\Delta x_p} = \frac{\lambda f\#}{N} \cdot n_p ,$$

where $f\# = f/D$ is the focal ratio of the optical module, and n_p the number of pixels sampling the pupil in the FFT matrix.

In a PSF, the smallest structure present is of the size of the Airy disc, which has the radius $r_{Airy} = 1.22\lambda f\#$. This also applies to speckles in aberrated systems. The sampling of the PSF can then be characterized by the number of pixels within one Airy radius, n_x :

$$n_x = \frac{1.22\lambda f\#}{\Delta x_f} = 1.22 \frac{N}{n_p} .$$

This means that the sampling of the PSF only depends on the sampling of the pupil area and the size of the FFT matrix, independent of any optical parameters, and vice versa.

The pre-computed PSFs for non-pointlike sources are created with a constant n_x . Thus the physical step size of these PSFs is different at the detector and the slit, and

varies spectrally as

$$\Delta x_f = \frac{1.22\lambda f\#}{n_x}.$$

In the case of point sources, the Fourier propagation is done for each PSF individually. To avoid spatial interpolation, the final PSF is sampled with the selected detector oversampling, and the initial step size is calculated accordingly. Therefore, Δx_f is constant, Δx_p changes with wavelength, and so do n_x and n_p .

Frequency domain

In the PSF matrix, the pixel indices with respect to the origin are $-\frac{N}{2}, -\frac{N}{2} + 1, \dots, -1, 0, 1, \dots, \frac{N}{2} - 2, \frac{N}{2} - 1$ with the PSF being centered at 0. The spatial frequency coordinates of the pixels are

$$-\frac{N/2}{N\Delta x_p}, -\frac{N/2+1}{N\Delta x_p}, \dots, -\frac{1}{N\Delta x_p}, 0, \frac{1}{N\Delta x_p}, \dots, \frac{N/2-2}{N\Delta x_p}, \frac{N/2-1}{N\Delta x_p}.$$

The minimum spatial frequency resolved in the pupil is

$$k_{min} = \frac{1}{D} = \frac{1}{n_p \Delta x_p},$$

and the maximum frequency

$$k_{max} = \frac{n_p/2}{D} = \frac{1}{2\Delta x_p}.$$

The index corresponding to the minimum frequency i_{min} is given as

$$\frac{i_{min}}{N\Delta x_p} = \frac{1}{n_p \Delta x_p}$$

and so

$$i_{min} = \frac{N}{n_p}.$$

The smallest reliable structure in the PSF extends then from $-i_{min} \dots i_{min}$, which is similar to the number inside the Airy radius n_x . Therefore the minimum reliable sampling in the PSF corresponds as expected to the Airy disc, which by definition is the smallest possible structure.

The index corresponding to the maximum frequency i_{max} is then

$$i_{max} = \frac{N\Delta x_p}{2\Delta x_p} = \frac{N}{2}.$$

This shows that the large-scale structure in the PSF array is reliable out to the edges.

2.3.6 Required sampling for NIRSpec

Pre-computed PSFs

For a reasonable PSF sampling, the default values are $N = 2048$ and $n_x = 6$, which give $n_p = 416$. The pre-computed PSFs are stored keeping only the central $N/2$ -sized array to prevent aliasing effects in the outer matrix area during the convolution of the detector images. At short wavelengths, the large relative WFE creates a large halo of scattered light in the PSF matrix. When cutting the central part, some intensity is lost and not recovered, as the final PSFs are normalized to total intensity of 1. This effect is stronger with smaller Δx_f and therefore larger n_x . The default parameters are a tradeoff between calculation speed, resolution of the PSF, the wavefront map, and errors in the normalization, but can be changed during the IPS model creation if the user considers other values as more appropriate.

When cutting the central part of the PSF matrix, it is important to have correct values out to $\pm N/4$. According to section 2.3.5, the wavefront data then needs to be resolved with $n_{WFE} \geq n_p/2 = 208$. n_p remains as before, it only defines the size of the pupil in pixels, not the real resolution of the data.

Point source propagation

The default FFT matrix size is $N = 2048$, the oversampling factor 30, and $\Delta x_f = 0.6 \mu\text{m}^1$. A very important aspect for point sources is the calculation of the slit losses. Especially to assess the photometric stability of exoplanetary transit observations, this has to be done with high accuracy. It means that the PSFs at the slit plane need to be valid at least out to the slit edges.

Considering a slit with the aperture size x_s, y_s being centered on the PSF, it covers

$$N_{Sx} = \frac{x_s}{\Delta x_{fMSA}}, \quad N_{Sy} = \frac{y_s}{\Delta y_{fMSA}}$$

pixels. For simplicity, we do the calculation for one dimension. In the extreme case, where $N_{Sx} = N$, the PSF matrix needs to be valid out to the edges, which requires the wavefront error to be resolved with

$$n_{WFE} = \frac{N \Delta x_{fMSA}}{\lambda f \#_{FORE out}} = \frac{x_s}{\lambda f \#_{FORE out}}$$

pixels. In Table 2.1 we show exemplary values of n_{WFE} for different slit types and a shutter pattern. For a centered PSF to be accurate out to the slit edges at short wavelengths, the WFE diameter needs to be $n_{WFE} \geq 193$.

¹It is possible to change the parameters for an electron rate computation by setting the oversampling to 10, 20, or 40, and the point source FFT matrix size to 1024 or 4096, depending if the focus of the simulation is on speed or resolution of PSF and WFE structures.

Table 2.1: Minimum required wavefront sampling for valid PSF data in different slit apertures.

Name, axis	Slit aperture x_S or y_S / mm	n_{WFE}	
		$\lambda = 0.6 \mu\text{m}$	$\lambda = 5 \mu\text{m}$
1x5 shutters, y	1.01	135	17
SLIT_A_200_1, y	1.27	169	21
SLIT_A_400, y	1.45	193	24
SLIT_A_1600, x	0.631	85	11
SLIT_A_1600, y	0.620	83	10

With the fixed PSF pixel size, the sampling in the GWA pupil plane is

$$\Delta x_{pGWA} = \frac{\lambda f_{CAM}}{\Delta x_f N} ,$$

and the spatial sampling in the MSA plane

$$\Delta x_{fMSA} = \frac{\lambda f_{COL}}{\Delta x_{pGWA} N} = \Delta x_f \frac{f\#_{COL}}{f\#_{CAM}} .$$

The sampling in the FWA pupil, where the Fourier propagation usually starts, is then

$$\Delta x_{pFWA} = \frac{\lambda f_{FOREout}}{\Delta x_{fMSA} N} .$$

The nominal focal ratios of the collimator and the FORE at the MSA are equal, therefore

$$\Delta x_{pFWA} = \Delta x_{pGWA} .$$

The sampling of the PSF and the pupils is then

$$n_{xMSA} = n_x ,$$

and because the nominal pupil diameters at FWA and GWA are equal

$$n_{pFWA} = n_{pGWA} .$$

With the camera focal ratio $f\# = 5.6$, the PSF sampling ranges from $n_x = 6.8 \dots 57$, the pupil sampling from $n_p = 365 \dots 44$ for the wavelengths $\lambda = 0.6 \dots 5 \mu\text{m}$. This is well balanced to sufficiently resolve both the PSFs at short wavelengths, and the wavefront errors at long wavelengths.

A satellite has no conscience.

Edward R. Murrow

3

NIRSpec model description

3.1 Model data overview

Most of the data needed for the instrument model has been provided in reports or data packages for subsystems. To obtain accurate instrument simulations, we used these measured data wherever possible. Nevertheless, there is a fundamental difference between proving compliance with requirements and preparing data for an instrument simulator. Sometimes only key statistical properties are relevant, e.g. the Root Mean-Square (RMS) of a wavefront error, or curves are only shown as a plot and not given in digital values. Besides, to reproduce the instrument output, simulations generally need to be done on ranges larger than the region defined for requirements.

In the following, we list the single data types for the instrument and calibration equipment in section 3.2. We describe the sources and potentially applied adjustments, and give a brief indication about the reliability. We also explain a more interesting case in detail in section 3.3, the simulation of wavefront errors and geometrical distortion with a dedicated optical model. However, the final set is only a collection of independent data, which has to be verified as a whole using calibration exposures. This is done later in chapter 5.

3.2 Subsystem and telescope data

Mirror reflectivities

The manufacturers have provided measurements of the reflectivities for each of the mirrors in the instrument at ambient conditions. If necessary, the data has been smoothed to reduce noise and extrapolated to a range of 0.5–6 μm . In line with the official sensitivity calculations, we scaled the throughput values by 0.995 to account for measurement uncertainties. The metallic coatings in NIRSpec exhibit

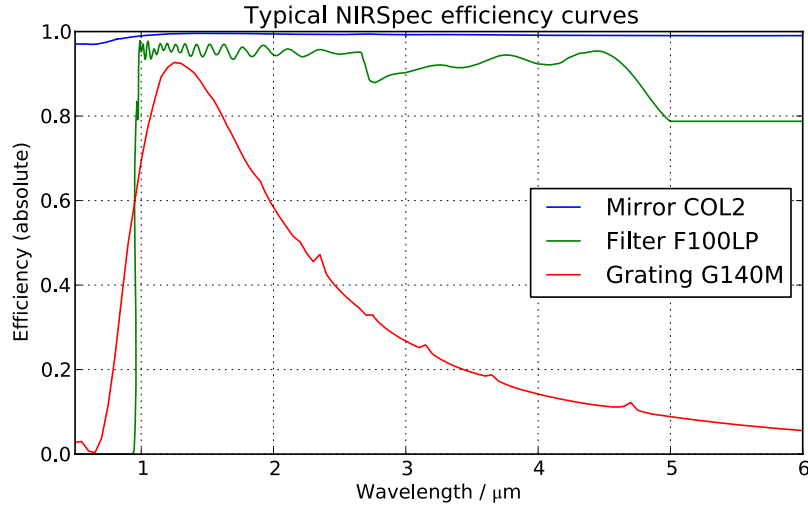


Figure 3.1: Exemplary NIRSpec component efficiency curves for a single mirror (COL2, blue), a long-pass filter (F100LP, green) and the first order of a medium resolution grating (G140M, red) in band I. The data has been extrapolated to 6 μm .

an efficiency improvement when changing to cryogenic conditions. From sample measurements at ambient and cold temperatures we derived a correction curve, and multiplied all the data with half the value. One mirror efficiency example for COL2 is shown in Figure 3.1, the combined data for all mirrors in the appendix in Figure A.14.

Filters

The transmission curves for each filter have been measured at cryo, mostly combining two independent measurements overlapping between 1.3 and 3.3 μm . Values were extracted from plots of the overall spectral range, and zoomed into the science, transmission, and rejection regions. The curves were adjusted to match in the common overlap region, and extrapolated to cover 0.5–6 μm . One long-pass filter example (F100LP) is plotted in Figure 3.1.

The filter pupil masks were constructed from design shapes of the tri-contagon stop for the long- and bandpass filters, and a circular shape for the CLEAR. Cryogenic test results of the wavefront error in transmission showed only small RMS values between 4–12 nm. The RMS of the WFE of the instrument is 4–10 \times higher, and has to be compared via the sum of the squares. Therefore the impact of the filters on the wavefront is considered negligible.

GWA elements

We used ambient measurements of the grating groove densities, the change to cryogenic temperature is considered negligible. The tilt angles of the dispersers were set to the nominal values, and so was the internal PRISM angle. The PRISM is made from CaF_2 , for which there is a Sellmeier description of the refractive index at cold conditions. Its parameters are somewhat uncertain, and the resulting prism dispersion has to be verified. This relation is used not only in the diffraction formula, but also to calculate the prism efficiency of the uncoated front side, combined with a measurement of the metallic rear side coating. Here, the impact of an uncertain diffraction index curve is negligible.

The efficiencies of the gratings were computed for the orders 0 to -7 with theoretical models based on the surface parameters (groove densities, design blaze angles, coating) for orthogonal and parallel polarized light¹. These two contributions can be very different (Palmer, 2005, chapter 9), and were averaged equally. The resulting curve for the first order of the medium-resolution grating G140M is plotted in Figure 3.1. However, this data has not been confirmed by measurements, and is therefore a primary target for tuning in the instrument model. Even more so as the incident angle on the gratings is not zero, and NIRSpec polarizes the light internally to some extent due to slant incidence on the mirrors.

For all the elements on the GWA, there are cryogenic wavefront error measurements in face-on reflection, which were scaled to an angular incident beam including the element tilt angles. In case of the PRISM, the map only covers the nominal beam, and was extrapolated radially to the full aperture. The PRISM pupil mask was calculated from the design aperture tilted to the beam incidence. For gratings and the TAM, the WFE maps cover the full apertures, and a pupil mask was derived from their extent, again respecting the surface tilt.

Microshutters and fixed slits

The geometry of the MSA quadrants and the shutter aperture has been measured at cold, as well as the positions and sizes of the fixed slits. Visible contrast maps resolving sub-shutter structures are available for the quadrants, but need to be confirmed in the infrared during the cryogenic test campaign.

Integral field unit

The wavefront error of the IFU optics was tested in cold conditions. For each path corresponding to one of the slices there is a single wavefront error map available. These maps contain the complete aberrations from IFU entrance to exit, and therefore a combination of the IFU FORE- and POST-optics. The contribution of the IFU FORE

¹M. te Plate, priv. comm.

is the same for all maps, so we created a mean WFE map from all 30 measurements, and defined it as the IFU FORE-aberration. Naturally it contains mostly low-order errors, some of them also originating from common POST optics design features. In order not to concentrate the low-order aberrations in the FORE part, and thus unrealistically degrading the PSF at the slicer, we scaled it to a total RMS of 65 nm, which is in line with the design WFE allocation. The maps for the single POST optical paths were then created by subtracting the FORE map from each measured WFE.

The throughput of the IFU was provided as a combination of several reflectivity measurements and microroughness contribution in two parts across the spectral range. The data has been averaged and scaled to remove discontinuities, and extrapolated to 0.5–6 μm . The single measurements are somewhat scattered, so the final data is not very reliable and has to be verified.

From the IFU design model, we extracted coordinate transforms for the IFU FORE and each IFU POST part. The raytracing grids were oversized on the IFU entrance in the MSA plane, which itself is oversized with respect to the slicer. For each slice, a grid covering an extended area around the aperture was traced through the POST optics. The distortion has been fitted with a first order polynomial, which is sufficient for the design geometry. Therefore we expect no problems in the transforms should a point be calculated outside the valid area as described in subsection 2.2.2. Originating from the design only, the transform parameters need to be verified, also to include alignment errors of the whole subsystem inside NIRSpec.

Detectors

The positions of the two detector arrays was set to the design values, symmetrical to the y -axis. From experience with the NIRSpec demonstration model, the FPA geometry is a primary candidate for model tuning. Data obtained during subsystem testing allowed the derivation of spectral flatfields, an average efficiency curve, and a gain value for each detector. The efficiencies were extrapolated to 0.5–6 μm with an artificial cutoff at 5.5 μm , as shown in the appendix in Figure A.17. Combined with the flatfield maps we constructed radiometric response cubes for the conversion of photons to electrons. Unfortunately, the currently installed detectors suffer from degradation over time, therefore the flatfields and efficiencies have to be treated with caution.

Internal calibration assembly

For the exit aperture we set the design shape. The angular intensity distributions of the flatfield modes have been measured, and one arbitrary map was used for the other ones. The output spectra were modeled by the manufacturer based on measurements of the flatfield lamps and a simulation of the integrating sphere,

and are likely not very accurate. Besides, the lamp currents were only selected after the first cryo test with NIRSpec. We keep using the initial data, but it is only approximate and will have to be adjusted to the final settings and measurements of the lamps.

Ground calibration sources

Eventually, the Calibration Light Source outputs have been calibrated to absolute radiometric levels. Due to the faintness of the nominal filter settings, this was done in two steps. At first, the spectrum of the brightest filter wheel combination was measured at the CLS exit, and at the lightbox alone. The ratio was used to establish a transfer function for the integrating sphere. Secondly, all the nominal source settings were measured at the lightbox level. The final output of the CLS was then calculated by combining these spectra with the transfer function. The claimed accuracy of the output spectra is about 10% absolute, nonetheless they remain a candidate for tuning of the CLS model.

JWST telescope

An optical model of the telescope is included in the NIRSpec Zemax design models. It is based on the NASA OTE definition, and does not reflect any as-built characteristics. We created a coordinate transform between sky to OTEIP from raytracing data, and set the focal length and pupil diameter to the nominal values. For the wavefront error we used an artificial map created by te Plate et al. (2007). It is constructed from a statistical budget and mimics a realistic realization of the different contributions from inter- and intra-segment deformations with a total RMS of 140 nm (see Figure 3.2). The perimeter of this map was also used to create the corresponding OTE pupil mask.

3.3 NIRSpec as-built optical model

3.3.1 Motivation

The key model data for the Fourier propagation are the wavefront error maps. The IPS assumes them to be concentrated in the pupil plane, which allows to separate the contributions from the mirrors and the elements on the FWA and GWA. During the ambient alignment, the WFE maps are measured with Shack-Hartmann Sensors (SHS) in the MSA, COL pupil, and FPA plane on a 5×5 Image Point Array (IPA, Schmoll et al., 2008)². These data mostly serve to characterize the WFE RMS, and have a resolution of $n_{WFE} \approx 22 \dots 40$ points in diameter, depending

²Source number 8 was not working and is missing in the grid.

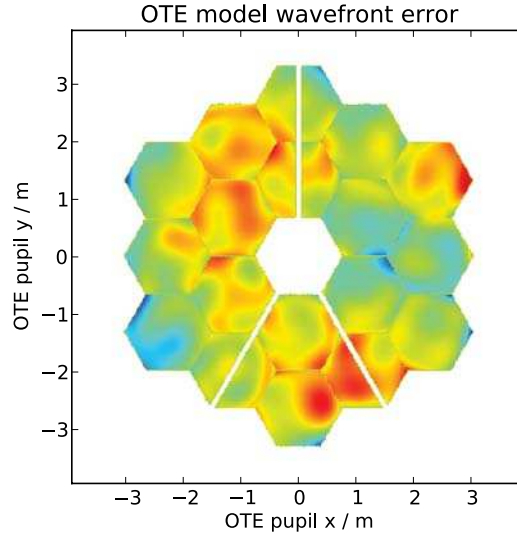


Figure 3.2: *Simulated JWST OTE wavefront error map, RMS: 140 nm.*

on the measurement plane. As shown in subsection 2.3.6, this is insufficient for the generation of accurate PSFs.

In the following, we describe how an as-built optical model of NIRSpec was verified with the wavefront measurements, and used to create finely sampled wavefront maps. In the same way, the design geometry may be good as a starting point, but the final aligned optics can have different characteristics, so we generated realistic coordinate transforms with the as-built model.

3.3.2 Model description

The as-built optical model is a Zemax file that EADS/Astrium used during instrument integration to optimize the positions of the subassemblies. The components are aligned following the model description, and the optical performance (WFE and distortion) is measured at the MSA, COL pupil, and FPA plane. Possible deviations from the model prediction are recorded, and a second alignment step is taken to match the measured performance with the simulated one. This way, the ZEMAX file does not describe the physical locations of the subsystems, but mimics the optical behavior of the real instrument. More specifically, it represents a "warm all-SiC" design, as if all the components were made from SiC, and the instrument is at ambient conditions. To correct the different thermal expansion coefficients of the parts made from other materials, at the very end the subsystems are pre-aligned with a calculated offset to arrive at the optimal location when cooled down.

The core of this model are as-built descriptions of the FORE and the spectrograph optics with COL and CAM, provided by the manufacturer. The shapes of the single

TMA mirrors were measured with an interferogram, and divided into an aspheric surface description and residual surface maps. The mirror data was then put into a model of the TMAs, which was fitted to reproduce optical characterization results. These building blocks have been combined to a single optical model representing the as-built NIRSpec at ambient conditions.

3.3.3 Model verification and transformation to cold

To a certain extent, the model is intrinsically verified in the alignment process, when the subsystems were moved to match the measured distortion with the model output. Apart from the geometry, the optimization included a minimization of the average measured wavefront error in the field of view. However, that influence is not reflected in the model, as the wavefront errors were not used for the alignment prediction. To verify this particular model output we therefore compared the simulated wavefront errors with the measurements in the finally determined focal planes.

Verification of the FORE

At first we checked the results of the FORE optics at the image plane of the MSA. The SHS measurements are shown in Figure 3.3. We created a separate as-built model at ambient conditions to simulate the SHS data by removing all objects after the MSA

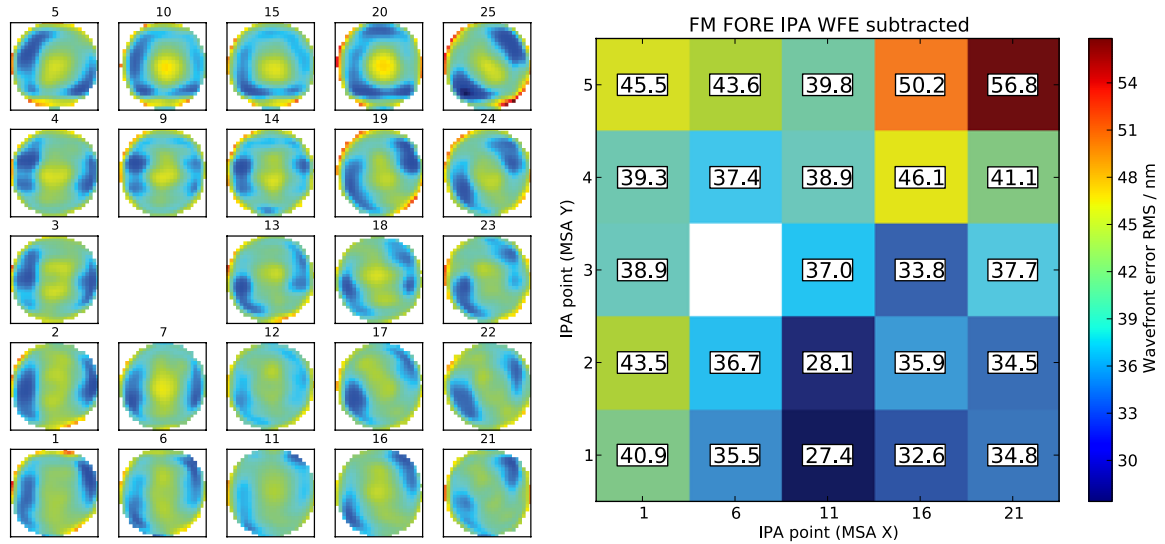


Figure 3.3: Measured wavefront errors of the FORE optics at the MSA plane at ambient. Left: WFE maps. Right: WFE RMS, mean: 39 ± 6.4 nm. The maps are oriented in FWA coordinates, the arrangement is in MSA coordinates.

plane. Besides that, we inserted the interferometric mirror surface maps, which had not been included in the original model during alignment. For all SiC-based mirrors we used the data supplied by the manufacturer, while for the RMA mirrors we put surface deformations measured by Astrium at ambient. The WFE maps were then extracted in ZEMAX with a size of 63×63 pixel at the location of the IPA sources.

To better match the resolution with the measured data, we smoothed the simulated wavefront maps. For verification we then created the difference of both, displayed in Figure 3.4. With the MSA plane at the nominal position, they generally showed a small defocus. The RMS of the 24 residual maps is 52.4 ± 9.5 nm, larger than the measurement itself. Apart from that, the structures in the pupil were well met (not shown). We then optimized the MSA z -position and x - and y -rotation in the model by fitting the RMS of the individual wavefront errors to the measured values.

The optimization run ended with the MSA plane moved by -0.145 mm in z and tilted by -0.039° and 0.082° in x and y . The model then reproduced the measurements very well, both in shape and RMS values (Figure 3.5(a) and (b)). The mean difference of the individual RMS values is 0.5 ± 4.8 nm, proving that the model fit was working correctly. The residual maps (Figure 3.5(c)) are very flat with an RMS of 21.4 ± 6.0 nm (Figure 3.5(d)). They mostly show features at the pupil edges, where the comparison is problematic. While the Zemax data strictly refers to the coordinates in the stop, the measured shape at the MSA can be slightly deformed. The SHS then looks for a circle fitting inside the recorded data, and hence may not cover exactly the same area.

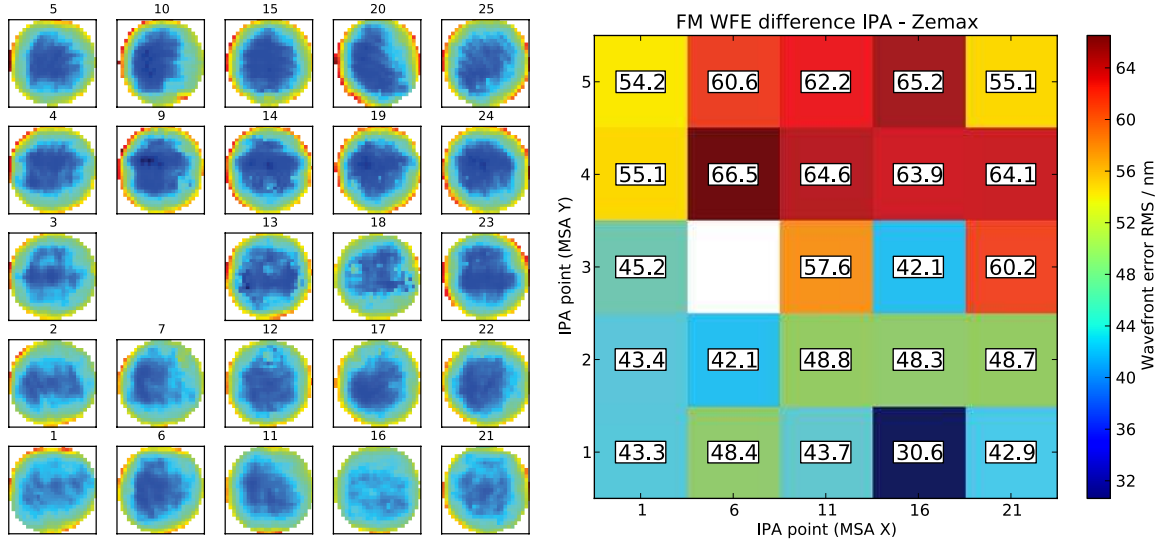


Figure 3.4: Difference of the measured and simulated wavefront errors at MSA before model optimization. Left: WFE map residual. Right: RMS of residual, mean: 52.4 ± 9.5 nm. There is a global defocus visible, the residual RMS is larger than the measured one.

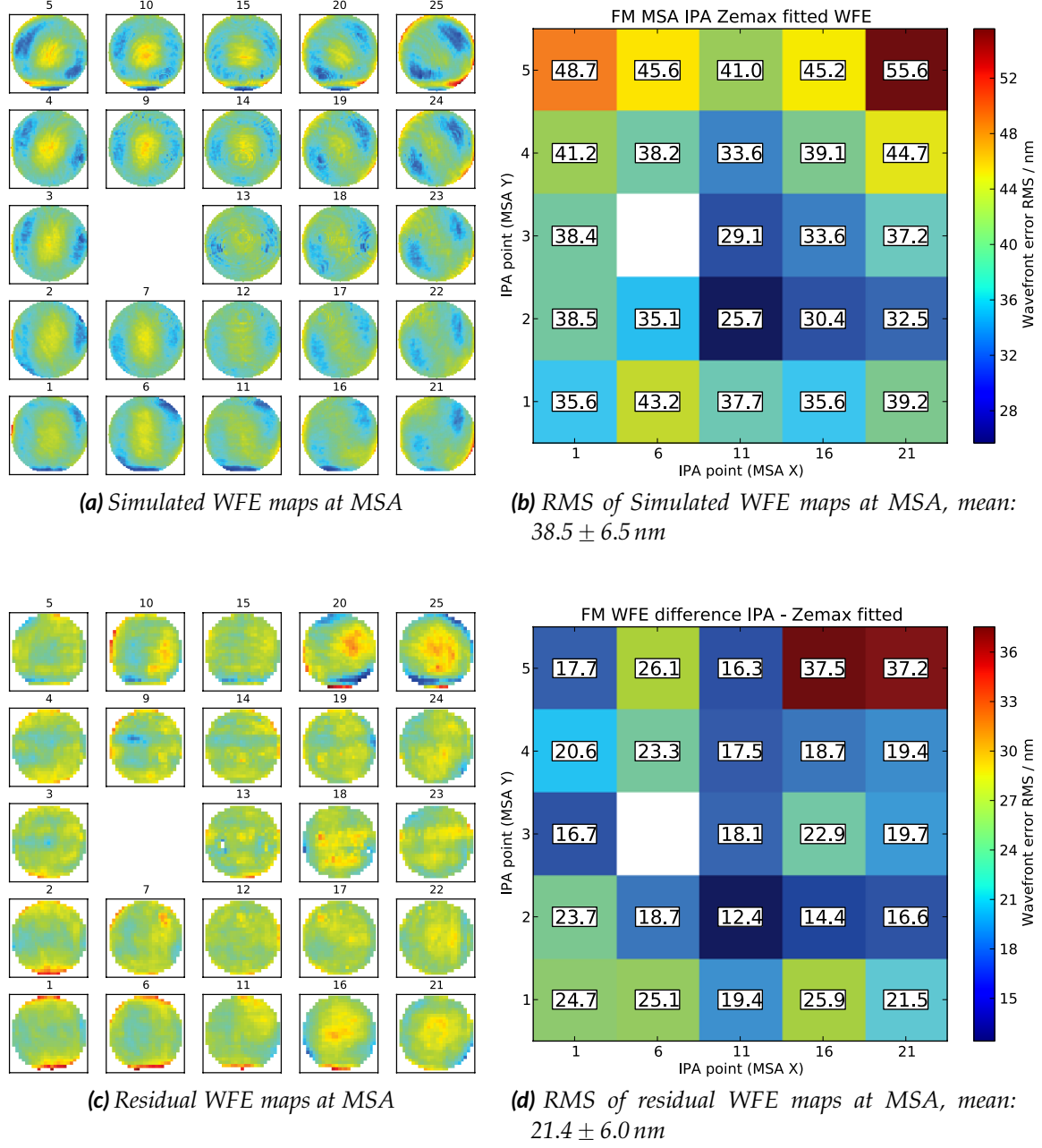


Figure 3.5: Simulated and residual wavefront errors at MSA after model optimization. (a): Model WFE maps. (b): Model WFE RMS. (c): WFE map residual. (d): RMS of residual. The shapes of the measured maps are reproduced very well, the residuals are very flat and mostly show features at the pupil boundaries.

In addition, only partly illuminated SHS lenses at the edges can produce wrong local tilts. Apart from the boundaries, the quality of the simulation is determined by the optical model itself, and the mirror surface maps.

Statistically, wavefront RMS values can be compared using their squared values. In the case of the MSA, the residual is then $21.4^2/39^2 = 30\%$ of the measured value. Given that the differences are dominated by the pupil edges, the model delivers sufficiently realistic WFE maps. Even more so, in the case of on-sky simulations, the FORE WFE is combined with the OTE WFE to compute the PSF at the slits. The FORE alone has exceptional optical quality, and is diffraction limited at $0.52\ \mu\text{m}$. Adding the OTE, the RSS value at MSA is $145.3\ \text{nm}$, the diffraction limit is at $1.9\ \mu\text{m}$. The residual fraction in the total wavefront error is then 2.2% , which is negligibly small. We therefore conclude that the WFE maps extracted from the as-built model are representative.

Verification of the spectrograph

In similar fashion we verified the wavefront error at the detector focal plane. In the measurement setup, a relay mirror (MIRR) was placed at the GWA plane for an imaging configuration. In this mode, the nominal FOV covers only the central part of the FPA. To characterize the optics in the full detector area that will record the spectra, the MIRR could be tilted around the y -axis. The measurements have been taken in several steps as depicted in Figure 3.6: Number 1 without a MIRR tilt, number 3 with the MIRR tilted by $+1.9^\circ$ (covering the $+x$ -FPA side), and number 5 with the MIRR tilted by -1.9° (covering the $-x$ -FPA side). Although the FPA positions of the three configurations partially overlap each other, they do not simultaneously probe the same optical path through the collimator and camera. The measured IPA data in the detector focal plane are shown in the appendix in Figure A.1 for step 1, Figure A.2 for step 3, and Figure A.3 for step 5, the overall RMS is about $90\ \text{nm}$.

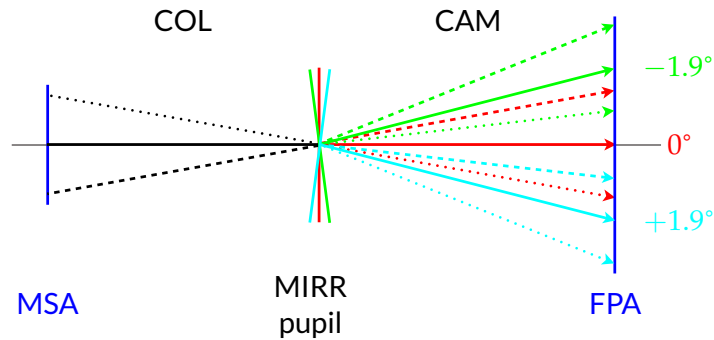


Figure 3.6: MIRR positions to measure the optical characteristics at the FPA. The MIRR is either centered (red) or tilted by $\pm 1.9^\circ$ (cyan, green) to cover the complete FPA area. For each configuration the light passes through different positions in the COL and CAM.

In the Zemax file, there are three configurations for the different MIRR tilt angles. As for the MSA, we optimized the FPA z -position and x - and y -rotation by minimizing the difference between the measured and model output RMS values for each IPA source in each MIRR configuration. After fitting, the FPA plane was moved by -0.024 mm in z and tilted by -0.014° and 0.0013° in x and y . The remaining difference of the RMS numbers are -5.6 ± 9.7 nm (step 1), 2 ± 12 nm (step 3), and -3 ± 13 nm (step 5), giving a sufficient confidence of the model fit. In general the simulated wavefront errors again look like the measured ones (see Figures A.4, A.5, and A.6). One obvious discrepancy is a shift of features in the center in y -direction between the SHS and ZEMAX arrays, possibly caused by non-matching pupil shapes as seen at the MSA. This is also evident in the residuals (Figures A.7, A.7, and A.9), where a large-scale aberration in y dominates the images.

In the IPS, the contributions of the COL and CAM are handled separately. As seen in Figure 3.6, each measured wavefront combines two different paths through both modules. The reproduction of the maps is equally good for all three steps, therefore we infer that the optical model of COL and CAM are independently verified without specifically analyzing data at the COL exit pupil.

Comparing the residual RMS values again to the measurements, the average fraction is 29%, or 8.5% including the OTE wavefront. With the telescope added, the instrument is diffraction limited at $2.2 \mu\text{m}$ at the detector. At this wavelength, the first Airy-ring of a PSF has the size of 1.7 pixels. At shorter wavelengths, where the wavefront error influence on the PSF increases, the sampling becomes too low to detect any small-scale structure, while at longer wavelengths, the PSF has almost an ideal shape. Given the small relative residual and the detector sampling, the model is considered to provide sufficiently accurate wavefront data.

Transformation to cold

Having verified the wavefront results, we transformed the model to cryogenic conditions. As explained in subsection 3.3.2, the description assumes all-SiC components. Its thermal expansion coefficient is known, and uniformly applied to all physical dimensions. The aspheric terms of the mirrors have been scaled with the factor respecting their units, as well as the ambient surface maps in amplitude and size. The RMA mirrors made from BK7 glass show a strong deformation with temperature, so we used surface interferograms measured in cryogenic conditions for their shape.

3.3.4 Relation between wavefronts and coordinate transforms

In the end, the verification of coordinate transforms will be done with centroids from spatially resolved images of pinholes or slits. This means that the PSFs from the Fourier propagation need to have a centered centroid, and the data from the raytracing needs to refer to the PSF centroid. To first order, this can be achieved

by removing the wavefront tilt, and to create the coordinate transforms from spot diagram centroids. While the first is done routinely and fast, the second would need extensive raytracing, which is generally slow in the complex as-built models.

To enable a faster creation of the distortion grids, we compared raytracing results of single chief rays and full spot diagrams, with and without mirror surfaces. The test was done with an as-built model of the NIRSpec demonstration model and the respective mirror data, but is also applicable to the flight model. We created distortion data at the MSA plane on a 11×11 grid covering the full FOV with $N = 121$ points. The spot centroid position with mirror surface maps served as the reference positions (x_r, y_r) , and the difference to each of the three other positions was characterized with the mean radial error

$$\Delta r = \frac{1}{N} \sum_{i=1}^N \Delta r_i = \frac{1}{N} \sum_{i=1}^N \sqrt{(x_i - x_{ri})^2 + (y_i - y_{ri})^2}$$

and its standard deviation

$$\sigma_r = \sqrt{\frac{1}{N} \sum_{i=1}^N \Delta r_i^2} = \sqrt{\frac{1}{N} \sum_{i=1}^N (x_i - x_{ri})^2 + \frac{1}{N} \sum_{i=1}^N (y_i - y_{ri})^2}.$$

The results are listed in Table 3.1. At the MSA, 2 μm correspond approximately to 5 mas, which is the required accuracy of the coordinate transforms. The mirror surface interferograms hardly influence the spot diagram position ($\Delta r = 1.76 \mu\text{m}$), but rather enlarge the spot sizes by 50–100% (not shown). This is in line with the design of the as-built model, where the low-frequency surface shapes are put in the mirror description, while the surface maps contain the high-frequency components which mostly cause straylight and an enlargement of the geometrical spot. On the other hand, when excluding the maps and tracing only the chief ray, the difference

Table 3.1: Radial differences of raytracing data in the as-built NIRSpec demonstration model at the MSA plane. The positions are obtained with or without the interferometric mirror surface maps, and referenced to the spot diagram centroids with surface data. 2 μm correspond approximately to 5 mas.

Extraction mode	Radial difference / μm		
	Min	Max	Mean and scatter
Centroid, no surface maps	0.11	2.95	1.76 ± 0.67
Chief ray, no surface maps	0.22	3.67	2.32 ± 0.86
Chief ray, surface maps	0.78	40.0	12.3 ± 7.1

is not much larger ($\Delta r = 2.32 \mu\text{m}$). The spot diagrams equalize the small surface perturbations, and the single ray reaches the same position following the aspheric mirror shapes. When including the surface maps for a single ray trace, there are large deviations in case it hits a local tilt on one of the mirrors.

We therefore decided to create the distortion data from chief ray tracing without the interferometric surface maps, which provides transforms almost as accurate as required. On the other hand, the wavefront errors can be extracted with the real mirror surfaces and tilt-subtracted.

3.3.5 Data extraction for the IPS model

Coordinate transforms

During the verification of the as-built model described before in subsection 3.3.3, we modified the position of the image planes at MSA and FPA. These changes are however very small, and monitoring the centroid of the spot diagrams we found the impact on the positions to be only a few micrometers. Given also that the coordinates extracted from Zemax should serve as a best-knowledge starting point for the instrument model, the impact on them is considered negligible. Eventually the coordinate transforms can be verified with cryogenic test data, hence we performed the raytracing with optimized image plane positions.

For the nominal NIRSpec optics, we used the as-built model at cryogenic conditions without the mirror surface maps and with a mirror at the GWA element location. The FORE transform was constructed from a 41×41 grid covering the field stop area. The COL distortion was retrieved from a 45×41 grid, enlarged in MSA x to cover the area of the IFU virtual slits, for which some of the nominal mirror apertures had to be removed. The CAM was probed with rays injected directly at the CAM entrance on a 61×41 grid, enlarged in x to cover the full FPA area, which extends farther than the imaging FOV. The final coordinate transforms were constructed following the recipe in subsection 2.2.2.

Even though these distortion data is more realistic than the design, it needs to be verified with calibration measurements. The thermal behavior of the optics may be different, some subsystem elements are not made from SiC, and can behave in another way than the prediction in the model.

Wavefront errors

The IPS is capable of simulating field-dependent wavefront errors by using nine maps on a 3×3 -grid of positions for the FORE, IFU FORE, COL, CAM, and CAL modules. With the as-built model we could create the WFE data at the MSA, the COL pupil, and the FPA. By subtraction of the arrays, we finally obtained the single module WFE of the FORE, COL, and CAM.

For the FORE, we took the as-built model at cryo with the fitted position of the MSA plane, and applied the cryogenic surface maps to the mirrors. The system stop at the FWA was set to a 64 mm circular diameter without an aperture mask to cover the maximum design pupil. All the wavefront maps were extracted at the nominal FOV positions F1–F9 with a size of 255×255 pixels and automatically tilt subtracted.

With the enlarged pupil there is vignetting where the beam extends over some of the model mirror apertures and no surface map data is available. To fill the missing areas we performed a natural-neighbor extrapolation. The method sorts the pixels radially and sets them iteratively to the mean value of the known neighbors. The procedure maintains the aberrations at the pupil edge, which usually are rather large. Therefore the extrapolated area can considerably increase the RMS of the final map. However, this has no impact on sky source simulations, as the system stop is defined by the OTE pupil and smaller than the originally extracted WFE area. Also the FORE PSF from OTEIP to MSA is little affected, the FPA pupil stop masks most of the extrapolated regions.

The full FORE wavefront maps are shown in the appendix in Figure A.10(a), the data inside the projected OTE stop and their RMS in Figure A.10(b) and A.10(c). In the OTE pupil the RMS at cold is only 36 ± 6 nm, which means the FORE alone is diffraction limited at $0.48 \mu\text{m}$.

For the creation of the spectrograph PSFs, the IPS uses the full aperture of the GWA elements. They are oversized to encompass the light diffracted outwards at the slits, and considerably larger than the nominal pupil. To reduce the need of extrapolation of the wavefront data, we enlarged the pupil area in the model by removing the filter element apertures, and setting the stop size to 91 mm. This way the wavefront maps were only limited by the apertures of the mirrors.

After deleting all surfaces following the COL pupil, we simulated the WFE there in the nine field points. In order to obtain the aberrations of the COL alone, we also re-created the wavefront data at the MSA with the larger pupil configuration, and subtracted them from the maps at the COL pupil. The resulting data is shown in Figure A.10(d), masked with the aperture of the PRISM, which is the largest one of the GWA elements. Restricted to the OTE pupil (Figure A.10(e)), the mean RMS is 82 ± 18 nm (Figure A.10(f)).

To extract the wavefronts at the FPA, we again used the model with the complete optics and the fitted detector position. The tilt angle of the MIRR in the ambient setup is not sufficient to reach out to the nominal FPA edges, therefore we selected a tilt of $\pm 2^\circ$ for the mirror at the GWA for the two extreme positions. From every wavefront we then subtracted the corresponding one at the COL pupil to obtain the aberration in the CAM. The data for each step masked with the PRISM are shown in Figure A.11(a), A.12(a), and A.13(a). In the OTE aperture (Figure A.11(b), A.12(b), and A.13(b)), the RMS are 60 ± 13 nm, 69 ± 19 nm, and 71 ± 18 nm, respectively. Upon closer inspection, it is obvious that the two outer positions overlap with the

center one, and the wavefronts and RMS values in the two common columns are almost the same (compare e.g. step 1 F1 and F2 with step 5 F2 and F3). Considering that the data originate from similar FPA positions, but different COL paths and therefore different total WFE maps, this is a confirmation that the method works well.

For the IPS model input, we selected the nine maps at the extreme positions and the center one, which are step 5 F1, F4, F7, step 1 F2, F5, F8, and step 3 F3, F6, F9. The RMS of these maps is 79 ± 19 nm, slightly larger than the individual averages, as the outer positions have a larger RMS value and dominate in the selection.

Finally, with the as-built model it is possible to extract the wavefront maps at arbitrary field locations. If simulations are done in a very specific area in the field of view, it is better to create a dedicated model with the real local wavefront errors to avoid time-consuming interpolation in the field, and have a more accurate PSF. This is the case for exoplanetary transits, which will only be observed in the square aperture, and require a good knowledge of the PSF at the slit. Consequently we repeated the WFE extraction for the FORE and COL at the field position of the SLIT_A_1600, and set up a separate model for the observation of planetary host stars. The spectra are still spread in the CAM, therefore its data are set as above. Similarly, one could create another model for the IFU with the FORE wavefront data at the IFU entrance location.

*Complexity is a sign of technical immaturity.
Simplicity of use is the real sign of a well design
product whether it is an ATM or a Patriot missile.*

Daniel T. Ling

4

Science software tools

4.1 Science data interface

4.1.1 Motivation

The IPS is designed as a full-scale end-to-end simulator of all kinds of NIRSpec observations. Depending on the input characteristics, spatial and spectral samplings can be adjusted to reduce the calculation time without impacting the result. Therefore, a separation in different source types had been established (section 1.4). Spatially, there is a individual treatment of

- large extended background objects with variations on scales much larger than the instrument PSF size,
- point-like sources,
- and spatially resolved objects, i.e. showing variations on scales similar to the PSF size.

In the spectral domain, the IPS distinguishes

- continuum spectra, which vary on scales larger than the spectral resolution element, and associated unresolved absorption lines,
- spectrally unresolved emission lines
- and resolved spectral features.

All these kinds can be combined to a total of 3×3 distinct source types.

The IPS uses a universal and rather complex definition of source input files. To simplify the interface with the science community, we defined a reduced set of

file types, which serve as an intermediate layer for the preparation of simulation scenarios.

In addition, the generic IPS source files are directly placed in their respective plane. This means that the position of scientific objects is defined on the sky in the NIRSpec FOV coordinates, as it would be in a fully realistic scenario. To simulate a certain observation on the other hand, it is more practical to put the sources at a defined location relative to a slit or IFU slice. In reality this will be performed by target acquisition before the actual observation, but it is completely unfeasible in the simulation, and the goal here is not to mimic the full in-orbit operation¹.

Calculating the position of a slit on the sky is an easy task with the instrument model, however the general user will neither have access to the data, nor the appropriate tools. Therefore we developed an interface to put targets relative to slits, shutters, IFU slices, or on the sky. The final IPS input data can then be created by an operator from the simple data files and their positioning information, using parameters from the instrument model for the simulation.

4.1.2 Object positioning

As just mentioned, for the construction of a defined simulation scenario it is easier to place the objects directly into shutters or slits, instead of rather blindly on the sky. The NIRSpec FOV is off-axis and rotated in the JWST standard coordinates, therefore we defined an "input field of view", where the x - and y -coordinates are approximately along the NIRSpec spectral and spatial directions. The nominal coordinates are rotated counterclockwise by 41.5° and centered on the location of the F5 point (see Figure 4.1). This also corresponds to the appearance on the detector.

In our scheme, there are three ways to specify the position of an object:

- **Sky coordinates:** The location is given by the x - and y -position in the input FOV. The coordinates are treated as rectangular. If a projection from RA/DEC is necessary, it has to be done externally.
- **MSA plane coordinates:** The object is placed in a shutter or fixed slit aperture. For shutters, the necessary data is the quadrant number and shutter indices. In the simple FOV, the indexing starts at the lower left corner of each quadrant, i increasing in the spectral and j in the spatial dimension. The fixed slits can be assigned directly by their name. In each case, the object can be finely placed by giving a relative offset within the aperture (-0.5 to 0.5). However, larger values are possible to move it outside, or behind a MSA bar.²
- **IFU slicer coordinates:** The position is set inside an IFU slice by giving its number 1–30. The slice indices start at the $-x$ -side of the FOV, and increase in

¹Although it is possible and one of the purposes of the IPS

²In the current geometry, the shutter pitch corresponds to about ± 0.68 in i and ± 0.58 in j .

the spectral direction. A fine placement is possible by giving the offset within the slice aperture (-0.5 to 0.5). It is worth noting that the edge between slice 15 and 16 is located at the center of the slicer.

All position information is contained in a specific scene file. Objects defined by the same input file can be listed multiple times with different locations. For each entry a rotation angle and scaling factor has to be set. The angle is defined as rotating the object counterclockwise with respect to the input FOV axes around its specified location. The scaling is directly applied to the source data when creating the IPS input. This way it is possible to create a scene with template objects used multiple times with different orientations and intensities. If a source is of the "large uniform background"-type covering the full FOV with a single spectrum (see following part), the position and rotation data is ignored, and the IPS input is automatically created

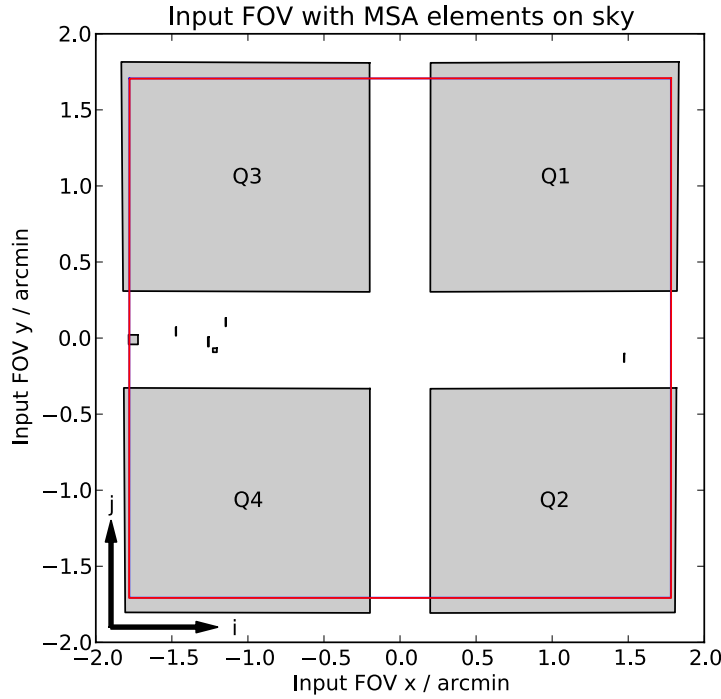


Figure 4.1: Simple input FOV for NIRSpec in sky coordinates. It is the nominal FOV rotated 41.5° counterclockwise and centered on the F5 point. The dispersion direction is to the right, spatial is up and down. The shutter indices i and j for each MSA quadrant (large grey areas) start at the lower left. The red polygon is the projection of the field stop to the FOV. At each edge, about 12 shutters are obscured and not usable for observations. The apertures visible between the quadrants are from left to right: IFU entrance, SLIT_A_200_2, SLIT_A_400, SLIT_A_1600, SLIT_A_200_1, and SLIT_B_200 on the far right. The IFU slices are oriented vertically, the numbering is similar to the MSA i indices.

to extend over the full FOV. However, it has to be listed somewhere in the scene file to be included at all.

For objects positioned in the MSA quadrants, it is necessary to specify an associated shutter pattern. It is assumed that observations are always done with one shutter open in the spectral direction, and a few ones open in the spatial direction. The available options are a slitlet "1×3", "1×5", or "1×7", with 3, 5, or 7 open shutters, where the central one is the reference for the target location. Besides it is possible to open the complete column in both spatially neighboring quadrants, or no shutters for obscured targets, which may leak through the MSA due to its limited contrast. This information can also be supplied for targets placed in sky coordinates. Then the central shutter of the pattern is selected as the closest one to the target, even if it is outside of the quadrants.

Compared with real observations, there are two major differences to the described input scheme: First, it is not equivalent to an observation preparation tool. The interface allows to set up a scene with specific object positions in the apertures, but does not optimize the FOV placement and orientation for a set of targets. Second, we do not take failed shutters into account which can not be opened, or are stuck in open position. A chosen arrangement may therefore not be feasible in orbit, and it places even tighter constraints on the optimization of the observation. For the real operations, the Astronomer's Proposal Tool developed at the Space Telescope Science Institute includes a MSA preparation function to perform these tasks, but this is much more complex and beyond our scope. However, it produces the list of shutter indices and relative offsets, which then can be used in the simple interface to build a scene for simulations.

4.1.3 Object input file types

The actual source input files are split into three types: A single spectrum, an image with a spectrum, and a data cube. They correspond to common types of scientific object data, and their content is listed in Table 4.1. Internally they employ the separation scheme of the IPS, so the spatial and spectral types are set by keywords in the file header. In the following, we briefly describe the three types and their application with object data.

Single spectrum file: The file contains a single spectrum with wavelength and spectral flux. The source type can either be point-like, or a large uniform background source covering the full FOV. For point sources, it is possible to add a position offset, by which the source is moved with respect to the location defined in the scene description. Uniform background sources are assumed to extend over the complete FOV, and are not influenced by any position data. The spectrum type can be chosen

from continuum, emission lines, and resolved. With a continuum spectrum, an optional list of unresolved absorption lines can be supplied.

Image & spectrum file: The input file describes a spatially extended object with a 2D intensity image, and a single spectrum. In the creation of the IPS object, the spectrum is put at the locations of the image pixels and scaled with their value. The position information for the image can be supplied as coordinate vectors for a rectangular system, or as 2D-maps with individual coordinates for each pixel. The type of the image is either extended background or spatially resolved. The spectrum type can be chosen from continuum, emission lines, or resolved. With a continuum spectrum, an optional list of unresolved absorption lines can be supplied.

Data cube: This file type contains a 3D data cube with the third dimension corresponding the spectral direction, made for spatially and spectrally varying objects. The spatial pixel coordinates are either given by vectors for a rectangular system, or as 2D-maps with individual values. The spectral coordinates are defined by a wavelength vector. The type of the spatial variations is either extended background or spatially resolved. The spectrum type can be chosen from continuum, emission lines, or resolved.

Table 4.1: Science input interface object file types. Each of them contains different spatial and spectral data. Extended sources are either of spatially resolved or background type. The spectra are one of the types used in the IPS.

Object file	Source type	Source data	Additional data
Single spectrum	Point or large background source	• Spectrum table	• Optional position offset • Optional list of absorption lines for continuum spectra
Image & spectrum	Extended source	• Intensity image • Spectrum table	• Image pixel coordinates as vectors or 2D-maps • Optional list of absorption lines for continuum spectra
Data cube	Extended source	• 3D data cube	• Cube spectral coordinate vector • Cube spatial coordinates as vectors or 2D-maps

4.1.4 Object separation criteria

Spatial domain

The spatial classification for the objects contains the following types:

- Point sources,
- spatially resolved sources,
- background sources with variations in the FOV,
- and large spatially uniform background sources in the full FOV.

The differentiation between them depends on the instrument parameters and the spatial variation scale of the sources. For very accurate simulations, to be considered as a point source, an object needs to be smaller than about $1/10^{\text{th}}$ of a detector pixel, which nominally is 0.01 arcsec. To treat a source as a background type, its spatial features need to vary on a scale much larger than the instrument PSF. We typically use 20 detector pixels, or 2 arcsec. Large uniform background sources can only be used if the spectrum has no or negligible variations in the FOV. In all other cases, the object needs to be declared as spatially resolved. If the simulation fidelity is less important in the spatial domain, these thresholds can be weakened to some extent. If possible, it is advantageous to try a simulation in a non-spatially resolved way, which heavily reduces the computation time of the electron rates. The criteria are also listed in Table 4.2, along with the corresponding input file types to use.

Spectral domain

In the spectral dimension the types are the same as in the IPS. The relevant parameter for an unresolved feature is the Full Width at Half Maximum (FWHM) of an emission line or the equivalent width of an absorption line, while to distinguish between resolved and continuum spectra, it is the scale of the spectral variations. They need to be compared to the spectral resolution $R(\lambda)$, which strongly depends on the observation mode, band, and wavelength. For simplification, only the spectral resolutions modes are differentiated for the criteria. Generally, features smaller than $1/10^{\text{th}}$ of a pixel can be treated as unresolved. The corresponding wavelength interval is $\Delta\lambda_{\min} = \frac{\lambda}{2.2R(\lambda) \cdot 10}$ and is shortest for $\lambda = 5 \mu\text{m}$ for the PRISM, and $\lambda = 1.8 \mu\text{m}$ for the gratings. The threshold for the continuum type is the maximum size of a resolution element, and therefore $\Delta\lambda_{\max} = \frac{\lambda}{R(\lambda)}$ with $\lambda = 1.5 \mu\text{m}$ for the PRISM, and $\lambda = 2.9 \mu\text{m}$ for the gratings. The criteria for each resolution mode and their corresponding spectrum type are listed in Table 4.3.

4.1.5 Technical implementation

The input files utilize the FITS format. The detailed structures are described in an interface control document, where we also state the data units, and necessary header keywords. We developed the installable Python package "pyIPStargets", which contains modules for each object type and the positioning file. These do not only handle data input and output, but also provide functions to verify the data and file integrity. Besides, they offer methods to create the actual IPS input data, making use of the respective classes for this files. The package contents are fully documented inline and with html pages, including exemplary scripts for the usage. Of course, the simple input files can also be created with every program that writes FITS files, as long as they conform to the defined format.

Table 4.2: *Spatial source separation criteria, corresponding source and object file types.*

Size or variation scale	Source type	Object file
Source size < 0.01"	Point source	Single spectrum
0.01" < variation < 2"	Spatially resolved source	Image & spectrum or data cube
Variation scale > 2"	Background source	Image & spectrum or data cube
Uniform in FOV	Large background source	Single spectrum

Table 4.3: *Spectral source separation criteria and corresponding spectrum types.*

Spectral resolution			Spectrum type
R100	R1000	R2700	
FWHM / eq. width < 0.83 μ m	FWHM / eq. width < 69 pm	FWHM / eq. width < 26 pm	Unresolved line
Variation scale > 44 nm	Variation scale > 4 nm	Variation scale > 1.5 nm	Continuum
	— Other spectra —		Resolved

4.2 Spectrum extraction pipeline

4.2.1 Purpose and scope

The final output of the IPS are raw data cubes, which contain the signal sampled up the ramp during the readout. To derive a count rate map from this data, special tools are necessary and have been developed by Astrium (the IQLAC software, Gerssen et al., 2008), and by ESA. They perform the ramp fitting, variance calculation, quality flag application, and remove detector signatures. The output is a processed file with count rate, variance, and quality values for each detector pixel.

However, this format is not suitable for scientific analysis. Due to NIRSpec's multi-object capability, the spectral and spatial coordinates of a pixel depend on the wavelength and the position in the MSA plane. No other tools were available to extract spectra and transform them to regular sampling, therefore we created the NIRSpec IPS Pipeline Software (NIPPLS).

It is a framework for spectrum extraction, primarily aimed at processing data generated with the IPS, and utilizes the instrument model geometry information from the simulation. This has the advantage that the extraction is done with a virtual perfectly calibrated instrument. In addition, existing software and functions for the model data provided a basis for the pipeline development. Finally, by implementing a calibrated instrument model, it is also possible to process real measured data with high accuracy.

The spectrum extraction workflow is shown in Figure 4.2. It starts with count rate maps, and provides all necessary functions to arrive at a rectified and calibrated data product. Available steps are to apply a flatfield, locate the spectra of different slits on the detector, rectify them to regular 2D coordinates, subtract background spectra, and produce the final calibrated output. This can be a 2D spectrum, 1D collapsed spectrum, or IFU cube assembled from 2D spectra of slices. All variances and quality flags are propagated throughout the analysis. The software is designed in a modular way, allowing a flexible composition of the processing methods, and external modification of the data before continuing the internal calculations. However, it also offers high-level methods to perform a standard extraction of science data, similar to classical long-slit data reduction.

4.2.2 Software implementation

The NIPPLS is written in Python, with a main class for the pipeline. It contains all the functions for the processing, as well as the default high-level methods, and many auxiliary methods for data handling. In a second layer, there are classes for pipeline model data: a general one for the instrument, and single ones for different subsystem data. They make use of the low-level classes for IPS model files, but also contain generic functions for specific calculations as system-level coordinate

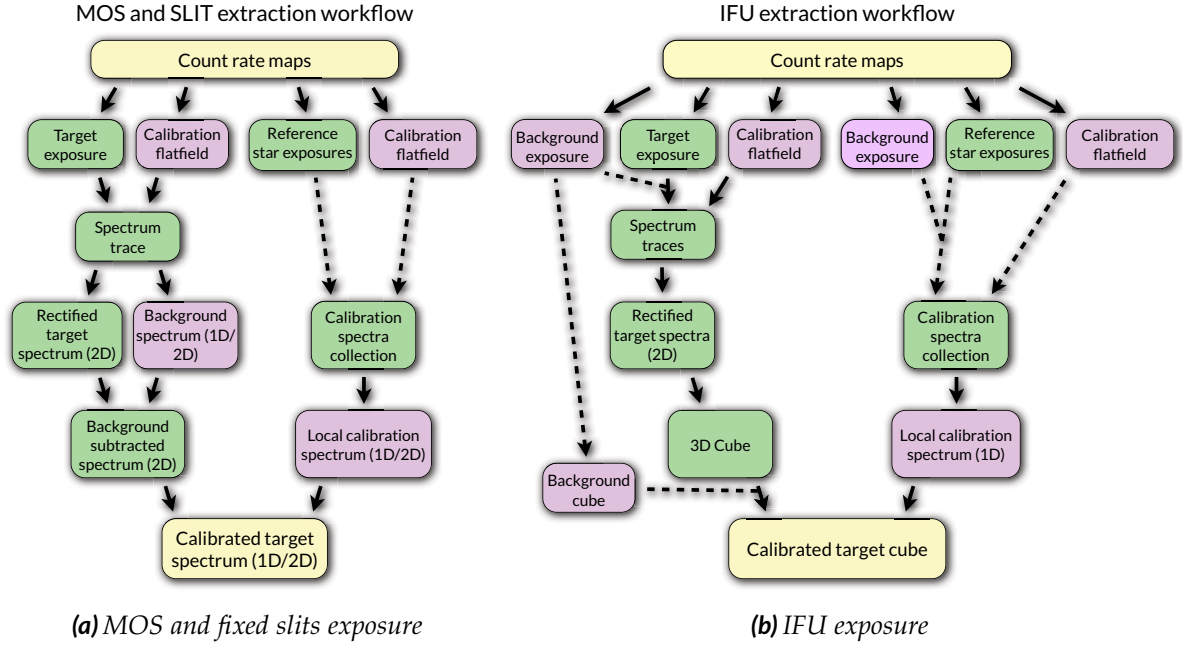


Figure 4.2: Standard NIPPLS spectrum extraction workflows, (a): for MSA shutters and fixed slits, (b): for IFU cubes. The processing starts with count rate maps, and produces rectified and calibrated output data, propagating variances and quality flags.

transforms or index conversions. This can be for example the direct transform from MSA to FPA coordinates, or conversions between positions in the MSA in shutter indices and absolute physical values. Lastly, there are dedicated classes for all the data types, ranging from processed detector data to 1D spectra with file handling, plotting, and basic data processing methods.

As NIRspec is a complex instrument, the configuration of the extraction is rather extensive. The available parameters contain

- the type of the exposure (MOS, SLIT, IFU),
- IDs of slits with targets and background data,
- usable quality flags,
- optional spatial and spectral intervals for data extraction and sampling,
- an optional flatfield exposure file,
- units of the spatial spectrum axis (arcsec on sky or relative to slit aperture),
- and finally the instrument model for the exposures.

They have to be set before any extraction can be done. We tried to reduce the necessary configuration to a minimum, therefore many parameters are optional and have sensible default values, e.g. the spectral range is automatically set to the nominal interval of the disperser band. When using the data input interface for the simulation scene, with the pyIPStargets package it is possible to create a list of shutters and slits from the object positioning file. It then can be used for the slit and shutter ID selection in the pipeline configuration.

The single extraction methods are described in the following part, most of them have been completed and tested. Missing is only the detailed implementation of the final calibration with different positions in the apertures.

4.2.3 Spectrum extraction operations

The different methods deal with pixel-based data, rectified 2D or 1D spectra, or IFU cubes. All data is composed of count rates c/C , variances v/V , and bitwise quality flags q/Q . Lower case letters denote pixel-based values, while upper case letters are for rectified data (spectral power or intensity). Pixel indices are given by i, j , spectral coordinates are in wavelength λ and the spatial coordinate y . IFU cubes also have a spatial coordinate x , which is parallel to the dispersion direction in the slicer plane.

When processing data from a readout, the count rates are measured and contain noise, while the variances are only estimated from the measured rate value. As the mean count rate is unknown, the variance is an approximation, which becomes worse at low SNR pixels. However, it is the only way this data can be derived, and in the following c and v are simply the values from the processed detector image.

Flatfield correction

Input: Count rate map

Output: Flatfielded count rate map

To flatfield the target exposure, the detector count rate map is divided by an exposure with a flatfield lamp, typically from the CAA. If the individual Signal to Noise Ratio (SNR) of the flatfield data is at least 10, the new pixel values are calculated as

$$c' = \frac{c_{data}}{c_{flatfield}}, \quad v' = \left(\frac{v_{data}}{c_{data}^2} + \frac{v_{flatfield}}{c_{flatfield}^2} \right) * c'^2, \quad q' = \text{bitwise_or}(q_{data}, q_{flatfield}).$$

If $SNR_{flatfield} < 10$, the pixels are left unchanged, and the quality bit 512 is set, indicating "no flatfield correction":

$$c' = c_{data}, \quad v' = v_{data}, \quad q' = \text{bitwise_or}(q_{data}, 512).$$

These pixels are not usable for science.

Spectrum subarray extraction

Input: Count rate map

Output: Subset of count rate map of the spectrum trace area

For a given slit, the pipeline calculates the spectrum trace on the detector and cuts the respective area. If the spectrum spreads over both detectors, there are two subarrays, one from each SCA. The data is stored in a "spectrum window" object. The pipeline also determines the coordinates $\lambda_{i,j}$ and $y_{i,j}$ at each pixel center, or sets them to invalid values if they are too far outside of the projected slit aperture. The individual pixel data is left unchanged.

1D irregular spectrum creation

Input: Spectrum trace subarrays

Output: 1D spectrum collapsed along detector columns or in wavelength bins

To enable a quick spectrum extraction, there is the possibility to directly create 1D spectra from the spectrum trace subarrays. It usually has an irregular wavelength sampling. There are various options for the extraction type:

- "sum": Sum the trace pixels along the detector columns, using only those with the selected quality flags:

$$c'_i = \sum_j c_{i,j}, \quad v'_i = \sum_j v_{i,j}, \quad q'_i = \text{bitwise_or}_j(q_{i,j}).$$

The quality flags of the selected pixels are propagated in each column. The pixel row index and spectral coordinates are the weighted mean:

$$j'_i = \frac{\sum_j j c_{i,j}}{\sum_j c_{i,j}}, \quad \lambda'_i = \frac{\sum_j \lambda_{i,j} c_{i,j}}{\sum_j c_{i,j}}, \quad y'_i = \frac{\sum_j y_{i,j} c_{i,j}}{\sum_j c_{i,j}}.$$

- "mean": Calculate the mean of the pixels in each detector column, using only those with the selected quality flags:

$$c'_i = \frac{1}{n_j} \sum_j c_{i,j}, \quad v'_i = \frac{1}{n_j^2} \sum_j v_{i,j}, \quad q'_i = \text{bitwise_or}_j(q_{i,j}),$$

where n_j is the number of pixels selected in a single column. The quality flags of the pixels are propagated in each column. The pixel row index and spectral coordinates are the weighted mean:

$$j'_i = \frac{\sum_j j c_{i,j}}{\sum_j c_{i,j}}, \quad \lambda'_i = \frac{\sum_j \lambda_{i,j} c_{i,j}}{\sum_j c_{i,j}}, \quad y'_i = \frac{\sum_j y_{i,j} c_{i,j}}{\sum_j c_{i,j}}.$$

- "median": Calculate the median in each detector column, using only pixels with the selected quality flags. The variance is derived via the variance of the mean (see before) and the statistical relation (see Weisstein)

$$\frac{v_{mean}}{v_{median}} = \frac{4N}{\pi(2N+1)} ,$$

where N calculates as $N = \frac{1}{2}(n_j - 1)$ from the number of selected pixels in the column n_j . Hence we get

$$c'_i = \text{median}_j(c_{i,j}), \quad v'_i = \frac{\pi}{2(n_j^2 - n_j)} \sum_j v_{i,j} , \quad q'_i = \text{bitwise_or}_j(q_{i,j}).$$

If $n_j = 1$, the variance is set to the value of the single pixel. The quality flags of the pixels are propagated in each column. The pixel row index and spectral coordinates are the weighted mean of the selected pixels:

$$j'_i = \frac{\sum_j j c_{i,j}}{\sum_j c_{i,j}} , \quad \lambda'_i = \frac{\sum_j \lambda_{i,j} c_{i,j}}{\sum_j c_{i,j}} , \quad y'_i = \frac{\sum_j y_{i,j} c_{i,j}}{\sum_j c_{i,j}} .$$

- "row": Extract a single spectrum row at a spatial coordinate y_r . The output data are the values of the pixels in a column at j_r where $y_{i,j} - y_r$ is minimal:

$$c'_i = c_{i,j_r} , \quad v'_i = v_{i,j_r} , \quad q'_i = q_{i,j_r} .$$

If they are not selected due to bad quality flags, c'_i and v'_i are set to 0. The pixel row index and spectral coordinates are accordingly

$$j'_i = j_r , \quad \lambda'_i = \lambda_{i,j_r} , \quad y'_i = y_{i,j_r} .$$

- "max": Extract the maximum values in the columns. The output data are the values of the pixels in a column at j_{max} where $y_{i,j}$ is the maximum in a column:

$$c'_i = c_{i,j_{max}} , \quad v'_i = v_{i,j_{max}} , \quad q'_i = q_{i,j_{max}} .$$

If they are not selected due to bad quality flags, c'_i and v'_i are set to 0. The pixel row index and spectral coordinates are accordingly

$$j'_i = j_{max} , \quad \lambda'_i = \lambda_{i,j_{max}} , \quad y'_i = y_{i,j_{max}} .$$

- "meantrace": Calculate the mean of the pixels in wavelength intervals, using only pixels with the selected quality flags. The spectral intervals are determined from the wavelengths of the center trace pixels at j_{trace} where $y_{i,j} \approx 0$. The bin edges are the column boundaries at the trace

$$\lambda_{i,edge} = \frac{1}{2}(\lambda_{i,j_{trace}} + \lambda_{i+1,j_{trace}}).$$

Let \mathcal{T} be the set of pixels in $[\lambda_{i,edge}, \lambda_{i+1,edge}]$ containing $n_{\mathcal{T}}$ pixels, then the output data is

$$c'_i = \frac{1}{n_{\mathcal{T}}} \sum_{i,j \in \mathcal{T}} c_{i,j}, \quad v'_i = \frac{1}{n_{\mathcal{T}}} \sum_{i,j \in \mathcal{T}} v_{i,j}, \quad q'_i = \text{bitwise_or}(q_{i,j \in \mathcal{T}}).$$

The pixel indices and spectral coordinates are the weighted mean of the selected pixels in each interval:

$$i'_i = \frac{\sum_{\mathcal{T}} i c_{i,j}}{\sum_{\mathcal{T}} c_{i,j}}, \quad j'_i = \frac{\sum_{\mathcal{T}} j c_{i,j}}{\sum_{\mathcal{T}} c_{i,j}}, \quad \lambda'_i = \frac{\sum_{\mathcal{T}} \lambda_{i,j} c_{i,j}}{\sum_{\mathcal{T}} c_{i,j}}, \quad y'_i = \frac{\sum_{\mathcal{T}} y_{i,j} c_{i,j}}{\sum_{\mathcal{T}} c_{i,j}}.$$

Spectrum rectification

Input: Spectrum trace subarrays

Output: Rectified 2D spectrum in regular spectral and spatial coordinates

Optical distortion in the spectrograph, slit tilt, and varying spectral dispersion cause a deformation of the spectra on the detector. Therefore the data is rectified to a grid with regular spectral and spatial coordinate axes. The coordinate start and step values are automatically set to reasonable values, or can be chosen manually e.g. to unify the axes for the IFU cube assembly. To preserve the spectral resolution, the default spectral step size is the minimum spectral extension of a pixel found in the trace, or the approximate size of a pixel corresponding to the nominal NIRSpec scale. For spectra of targets on the sky, the default spatial step is 0.1 arcsec, while for coordinates relative to the slit length, it is the minimum of the average pixel extension in each trace column.

In general, the spectra are curved and tilted on the detector, while the detector pixels are similarly distorted in the output coordinates, as shown in Figure 4.3. The rectification is done by projecting the input pixels with the indices i, j into the regular output grid with coordinates λ, y . For an output pixel, there is a set of overlapping input pixels \mathcal{P} . Each of them has a count rate $c_{i,j}$, variance $v_{i,j}$ and quality flag $q_{i,j}$.

We used the Drizzle algorithm by Fruchter and Hook (2002) as a starting point and adapted it to our specific needs. In general there is only one input array for a spectrum, so the input pixels are not shrunk. At first, the spectral coordinates (λ, y) of the input pixel corners are calculated. Neglecting the spectrum curvature on this

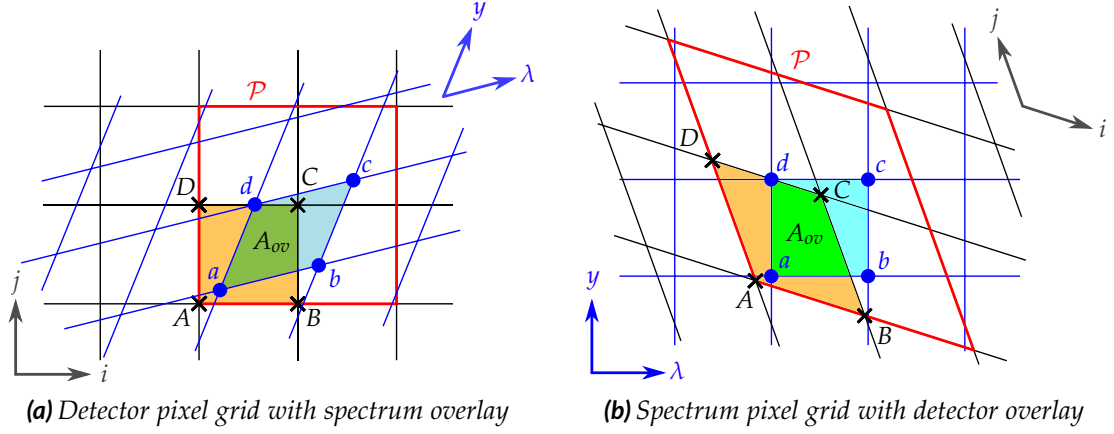


Figure 4.3: (a): Pixel grids in the detector data (rectification input). (b): Pixel grids in the spectrum data (rectification output). For each output pixel $\square abcd$ (blue dots) there is a set of overlapping input pixels \mathcal{P} (red polygon). The overlap with one of them ($\square ABCD$, black crosses) has the surface A_{ov} in spectrum units.

small scale, the pixels are treated as 4-corner polygons. An input pixel $\square ABCD$ has the surface A_{in} (in spectrum units), and an output pixel $\square abcd$ the surface A_{out} . Let

$$s_{i,j}^2 = \frac{1}{A_{in}}$$

be the scaling factor. The overlap of the input and output pixel $\square ABCD \cap \square abcd$ has the surface A_{ov} , and the input pixel fraction is then

$$a_{i,j,\lambda,y} = \frac{A_{ov}}{A_{in}}.$$

To track the coverage of an output pixel, we define the fill fraction

$$f_{i,j,\lambda,y} = \frac{A_{ov}}{A_{out}}.$$

The input pixel weights $w_{i,j}$ are set to 0 if pixels are rejected by quality flag selection or lack spectral coordinates, and 1 otherwise.

For an output pixel, the overlapping input pixels \mathcal{P} are identified, and the output weights W , surface brightness C , variance V , quality flag Q , and fill fraction F are calculated as

$$\begin{aligned} W_{\lambda,y} &= \sum_{i,j \in \mathcal{P}} w_{i,j} a_{i,j,\lambda,y} , \\ C_{\lambda,y} &= \frac{\sum_{i,j \in \mathcal{P}} c_{i,j} w_{i,j} a_{i,j,\lambda,y} s_{i,j}^2}{\sum_{i,j \in \mathcal{P}} w_{i,j} a_{i,j,\lambda,y}} , \end{aligned} \quad (4.1)$$

$$V_{\lambda,y} = \frac{\sum_{i,j \in \mathcal{P}} v_{i,j} w_{i,j}^2 a_{i,j,\lambda,y} s_{i,j}^4}{(\sum_{i,j \in \mathcal{P}} w_{i,j} a_{i,j,\lambda,y})^2}, \quad (4.2)$$

$$Q_{\lambda,y} = \text{bitwise_or}(\{q_{i,j} w_{i,j}\}_{i,j \in \mathcal{P}}),$$

$$F_{\lambda,y} = \sum_{i,j \in \mathcal{P}} f_{i,j,\lambda,y} w_{i,j}.$$

By scaling only with the input pixel surface, the output C and V are per units of spectral and spatial length. Additional quality flags of an output pixel are set if there was no, insufficient, or incomplete coverage ($F_{\lambda,y} = 0$, $F_{\lambda,y} < 0.5$, or $F_{\lambda,y} < 0.999$).

While we put $a_{i,j}$ in the variance calculation, the original Drizzle code employs $a_{i,j}^2$. This is mathematically correct, but it leads to an unwanted behavior in the noise propagation. Fruchter and Hook (2002) already noted that the pure Drizzle output underestimates the noise on large scales, as it neglects the covariance terms introduced when splitting the data of an input pixel over multiple output pixels. We compensated this effect by properly increasing the variance in a single output pixel ($a_{i,j} \leq 1$), which conserves the total noise level when integrating over multiple output pixels. This can be shown when comparing SNR values of the data before and after rectification. The total SNR of an input spectrum is

$$SNR_1 = \frac{\sum_{i,j} c_{i,j}}{\sqrt{\sum_{i,j} v_{i,j}}},$$

and of the output spectrum

$$SNR_2 = \frac{\sum_{\lambda,y} C'_{\lambda,y} A_{out}}{\sqrt{\sum_{\lambda,y} V'_{\lambda,y} A_{out}^2}}.$$

In our case, A_{out} is constant. Using Equation 4.1 and 4.2,

$$SNR_2 = \frac{\sum_{\lambda,y} \frac{\sum_{i,j \in \mathcal{P}} c_{i,j} w_{i,j} a_{i,j,\lambda,y} s_{i,j}^2}{\sum_{i,j \in \mathcal{P}} w_{i,j} a_{i,j,\lambda,y}}}{\sqrt{\sum_{\lambda,y} \frac{\sum_{i,j \in \mathcal{P}} v_{i,j} w_{i,j}^2 a_{i,j,\lambda,y} s_{i,j}^4}{(\sum_{i,j \in \mathcal{P}} w_{i,j} a_{i,j,\lambda,y})^2}}}.$$

Assuming a complete coverage ($F_{\lambda,y} = 1$) with no bad pixels ($w_{i,j} = 1$), and a locally constant input pixel size in \mathcal{P} , it is

$$\sum_{i,j \in \mathcal{P}} w_{i,j} a_{i,j} = 1.$$

If input and output data cover continuously the same total area, the double summation over output pixels and a distinct subset of input pixels fractions can be

transformed into a summation over the input only, so that

$$SNR_2 = \frac{\sum_{i,j} c_{i,j} s_{i,j}^2}{\sqrt{\sum_{i,j} v_{i,j} s_{i,j}^4}} .$$

This is the step where we neglect the covariances of the output pixels, and the original Drizzle data would predict a too high SNR. In our case, if the input pixel size $1/s_{i,j}^2$ is constant, $SNR_2 = SNR_1$.

This is approximately valid for grating spectra with a linear dispersion. The spectral size of input pixels of the PRISM varies by 4–5× from minimum to maximum. Nevertheless, a verification with prism spectra in different FOV positions and defined input data showed relative differences of only 10^{-5} in integrated count rates and signal to noise ratios.

1D spectrum creation

Input: Rectified 2D spectrum

Output: 1D spectrum collapsed in spatial dimension

Another option for the end product is the creation of a 1D collapsed spectrum from the 2D spectrum. The processing along the spatial dimension can be selected from the following methods:

- "collapse": Collapse the spectrum along the spatial dimension, using only pixels with the selected quality flags, and multiply it with the spatial pixel extension Δy :

$$C'_\lambda = \Delta y \sum_y C_{\lambda,y} , \quad V'_\lambda = \Delta y^2 \sum_y V_{\lambda,y} , \quad Q'_\lambda = \text{bitwise_or}_y(Q_{\lambda,y}).$$

By default, the quality flags are propagated in each wavelength bin.

- "mean": Calculate the mean in each wavelength bin, using only pixels with the selected quality flags, and multiply with the spatial pixel extension Δy :

$$C'_\lambda = \frac{\Delta y}{n_\lambda} \sum_y C_{\lambda,y} , \quad V'_\lambda = \frac{\Delta y^2}{n_\lambda^2} \sum_y V_{\lambda,y} , \quad Q'_\lambda = \text{bitwise_or}_y(Q_{\lambda,y}),$$

where n_λ is the number of pixels selected in a single wavelength bin. By default, the quality flags are propagated in each bin.

- "median": Calculate the median in each wavelength bin, using only pixels with the selected quality flags, and multiply with the spatial pixel extension Δy .

The variance is derived via the variance of the mean, as shown before in the 1D irregular spectrum creation:

$$C'_\lambda = \Delta y \text{ median}_y(C_{\lambda,y}), \quad V'_i = \frac{\pi \Delta y^2}{2(n_\lambda^2 - n_\lambda)} \sum_\lambda V_{\lambda,y}, \quad Q'_\lambda = \text{bitwise_or}_y(Q_{\lambda,y}),$$

where n_λ is the number of pixels selected in a single wavelength bin,. If $n_\lambda = 1$, the variance is set to the value of the single pixel multiplied with the squared spatial pixel size. By default, the quality flags are propagated in each bin.

- "rebin": Rebin the spectrum in the spatial dimension over an interval using only pixels with the selected quality flags. Pixel fractions Δy_y covered by the interval are correctly taken into account:

$$C'_\lambda = \sum_y C_{\lambda,y} \Delta y_y, \quad V'_\lambda = \sum_y V_{\lambda,y} \Delta y_y^2, \quad Q'_\lambda = \text{bitwise_or}_y(Q_{\lambda,y}).$$

By default, the quality flags are propagated in each wavelength bin.

Background spectrum creation

Input: Rectified 2D background spectra

Output: Rectified 2D or 1D background spectrum

For each slit with a source, there are corresponding areas to extract the background spectrum. In the case of the MSA, this are neighboring shutters in the minislit. The final background spectrum can be constructed as a 2D spectrum from the mean of the 2D background shutter spectra, or as a 1D spectrum from the median of the 2D background spectra (see previous processing step). For fixed slits, the background is extracted from regions next to the target area in the same slit as a median 1D spectrum. By default, the spectral and spatial axes are chosen to match the target spectrum to avoid additional rebinning. The background data of an IFU exposure is either a count rate map of a dedicated observation, or a second cube extracted from it. At the moment, the subtraction it not automated in the pipeline but can easily be done externally.

Background subtraction

Input: Rectified 2D and background spectrum

Output: Rectified 2D spectrum with background spectrum subtracted

The previously generated background spectrum is subtracted from the 2D target spectrum. If the background is in 2D format, the new data is

$$C' = C_{data} - C_{bg}, \quad V' = V_{data} + V_{bg}, \quad Q' = \text{bitwise_or}(Q_{data}, Q_{bg}).$$

If it is a 1D spectrum, the values are divided by the spatial pixel size of the target spectrum Δy :

$$C' = C_{data} - \frac{C_{bg}}{\Delta y}, \quad V' = V_{data} + \frac{V_{bg}}{\Delta y^2}, \quad Q' = \text{bitwise_or}(Q_{data}, Q_{bg}).$$

The subtraction in the IFU is possible on count rate map level or cube level, but has to be done externally at the moment. With the modular pipeline design, it is possible to include it in the general workflow of a processing script, but it will likely be offered as automatic step in the future.

IFU cube assembly

Input: Rectified 2D spectra of IFU slices

Output: IFU datacube assembled from slice spectra

With the assumption that there is negligible distortion in the spatial x -direction of the IFU FOV, the spectra of the IFU slices can simply be stacked to create an IFU cube. The step size Δx is automatically set to the average slice width. By default, Δy in the 2D spectrum rectification is set to the same value, so the cube has quadratic spatial pixels. The spectra are divided by Δx to convert them to spectral surface brightness.

Spectrum flux calibration

Input: Rectified 1D or 2D spectrum or IFU cube of the target

Output: Calibrated spectrum in photons/s/m²/μm on sky

For an absolute flux calibration of sky exposures, typically a reference point source with a known spectrum F_{cal} in photons/s/m²/μm is observed with high SNR and extracted in a standard way. This is done at different locations in the FOV and in the local slit apertures to create a map of reference spectra. Depending on the target characteristics, a spatial interpolation is done to derive a calibration spectrum C_{cal} . The absolute flux of the target is then

$$F_{target} = F_{cal} \frac{C_{target}}{C_{cal}} (\cdot \Delta x)(\cdot \Delta y), \quad V_{F_{target}} = \left(\frac{V_{target}}{C_{target}^2} + \frac{V_{cal}}{C_{cal}^2} \right) * F_{target}^2,$$

$$Q_{F_{target}} = \text{bitwise_or}(Q_{target}, Q_{cal}),$$

respecting the spatial units of the target spectrum if necessary.

This approach is not yet fully implemented in NIPPLS. The current version only allows defined test cases, calibrating spectra with a single point source spectrum. However, the default algorithm is available and tested, and the extension to more complex spatial patterns is planned for future development.

*Research is what I am doing
when I don't know what I am doing.*

Wernher von Braun

5

NIRSpec model verification

5.1 Motivation

Although the NIRSpec model described in chapter 3 has been composed from the latest subsystem measurements where possible, when put together it is not guaranteed to replicate the final instrument. For some data, the validity is unknown as no measurement error was stated in the test reports. Besides, the characteristics may have changed between the individual testing and the cryogenic instrument calibration. For the efficiencies, this can be due to contamination, or unforeseen degradation over time. The alignment may suffer from uneven deformations during the cooldown, and its intrinsic accuracy of some tens of microns. In addition, the as-built model, from where the coordinate transforms have been extracted, is not perfectly matching the instrument behavior. All in all, we need to verify the NIRSpec model as a whole, and also the interplay of the model data and the IPS itself.

This exercise has several benefits: Tuning single subsystem characteristics offers a much deeper insight into the instrument than simple global performance verification. Besides, the model can provide important input for the data processing, e.g. for the spectral calibration, or the throughput model which is planned for the official NIRSpec extraction pipeline (Beck, 2009). Finally, for proper scientific simulations, we need an instrument model as close as possible to reality.

For the verification, we used NIRSpec data from the cryogenic test and calibration campaign of the first flight model FM1, which was held in February 2011. It provides various sequences of test exposures for different aspects of the instrument calibration. Unfortunately, the MSA was not operational during the test, and exposures were only taken through the fixed slits and the IFU. All the data has been pre-processed by the ESA ramp-fitting pipeline, and is available in the form of count rate maps, their variance, and quality flags. Further data extraction and processing has been performed inside the NIPPLS framework. It not only provides the spectra, but also allows non-standard operations which may be necessary for the model fitting. In

addition, it is intrinsically coupled with the instrument model, which then can be optimized within the same processing environment.

5.2 Instrument geometry

5.2.1 Initial data and manual tuning

The starting point for the instrument model was the data illustrated in chapter 3, which is briefly repeated here. The essential characteristics for the instrument geometry had been derived from the as-built optical model, while for the IFU we had used the design optical model. To calculate a full coordinate transform from slit to detector, we also needed the disperser parameters. They were as-built values for the grating groove densities, and design numbers for their nominal tilt angles. The refractive index of the PRISM was based on a theoretical curve for cryogenic conditions. The FPA geometry had been set to the nominal positions without any rotation.

A first manual adjustment of the model was done with flatfield exposures of the rare-earth spectral reference filter (SR1, Figure 5.1). The spatial position of the spectrum trace could be determined from the continuum, while the absorption lines provided a spectral reference. We iteratively changed the alignment tilt angles of the disperser elements (small deviations to their nominal orientation), and the position of the second detector 492. The spatial location was controlled with the images of the slit traces by matching the projection of the model trace with the measurement, as exemplary shown for the slit A_200_2 in Figure 5.2(a). The spectral coordinates

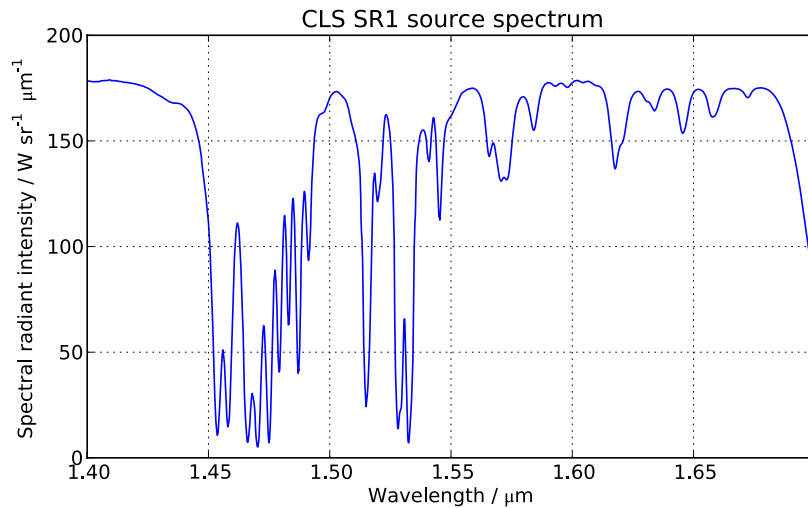


Figure 5.1: Spectrum of the CLS SR1 source at the CLS exit aperture. It is composed of a continuum, attenuated by a band-pass and an Erbium absorption line filter.

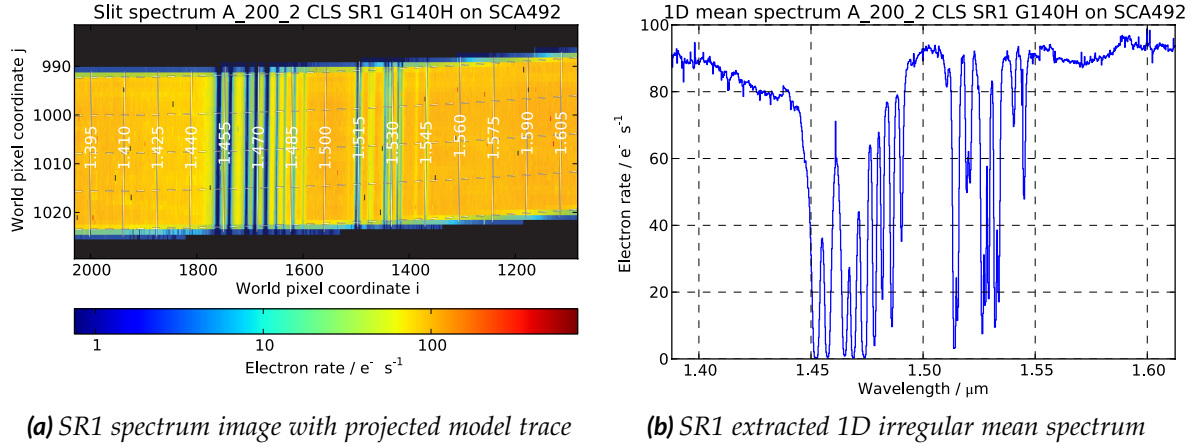


Figure 5.2: Spectrum data of the SLIT_A_200_2 in a CLS SR1 exposure with the grating G140H. (a): Spectrum electron rates on the detector 492 after manual model adjustment, other spectra are masked out. The projected trace is overplotted in white and matches the measurement very well. (b): Extracted 1D irregular mean spectrum. The absorption features between 1.45 μm and 1.55 μm seen in Figure 5.1 are clearly identifiable and allow a precise adjustment of the spectral direction.

were verified by comparing the 1D irregular mean spectrum with the CLS filter absorption lines (Figure 5.2(b)). This was repeated for all dispersers, where for the band II and III we used higher orders of the spectra falling into the nominal wavelength range. To complete the model for the fixed slits, we tuned the TAM alignment with the images of the slits in another flatfield exposure.

In order to include the IFU but not disturb the previous adjustments, we could only change its specific geometry. The free parameter here was the position of the virtual slits in the MSA plane. Comparing with imaging data and SR1 spectra, we matched the position of the measurements with the model predictions.

The accuracy of the tuned data was checked with spectra of Argon emission lines, one example is shown in Figure 5.3(a). We extracted the 1D irregular mean spectrum (Figure 5.3(b)), and visually compared the position of prominent lines with the absolute reference from the source data. In the case of the gratings we found average residuals of less than 3 nm, while for the PRISM they were in the range of 10–40 nm. Both values correspond to a few detector pixels due to the different resolutions. In the spatial direction, the traces were matching typically with 1 detector pixel.

The achieved accuracy is sufficient as a first-order tuning, and usable for extraction of approximate spectra, as it was done during the FM1 test campaign. It is also enough for realistic scientific simulations, given that the instrument will be assembled anew and with other detectors, and the final geometry in orbit will be different due to gravity release effects.

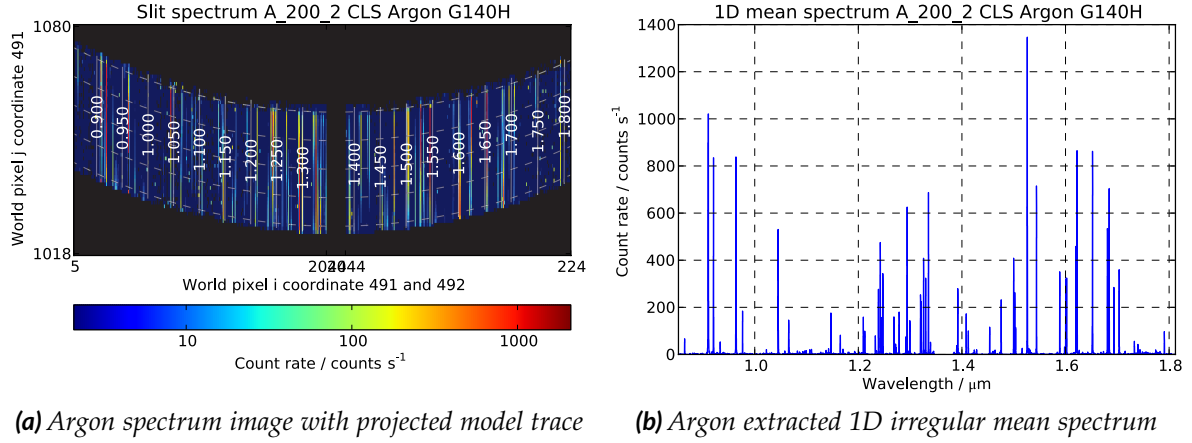


Figure 5.3: Spectrum data of the SLIT_A_200_2 in a CLS Argon exposure with the grating G140H. (a): Spectrum count rates, other spectra are masked out. The projected trace is overplotted in white. (b): Extracted 1D irregular mean spectrum. For verification, the position of some prominent emission lines were visually compared to the absolute reference values.

5.2.2 Model optimization

Although in the preceding analysis we could match the spectral and spatial directions with a sufficient accuracy for simulations, there was still room for further improvement to reduce the residuals. Besides, the process of manually adjusting single parameters, and especially verifying the model with several Argon lines in multiple slit- and IFU spectra and for each disperser turned out very tedious. At the time this work was conducted it was already certain that the detector would be replaced with another model for the second cryogenic campaign, which will make it necessary to repeat the tuning. Therefore we decided to automatize and extend the data extraction, and optimize the model in a fitting process. This way we could include much more parameters with the prospect of significantly reducing the residuals, while establishing a workflow for the same analysis with new calibration measurements.

For an optimization with a merit function we needed absolute reference points in the slit and the detector plane. In the MSA we chose the measured positions of the fixed slits. On the detector, we needed to determine the exact positions of the Argon emission lines in pixel indices. With the known wavelengths, it is then possible to minimize the error when calculating coordinate transforms from MSA to FPA and reverse. However, there was no automatic spectrum extraction available that could return the required data, and the NIPPLS used the instrument model that we wanted to optimize. Therefore we did the analysis in two steps, which were not relying on the absolute knowledge of the instrument.

We used the exposures taken during a so-called "combo"-run, where different sources were recorded for a single disperser, without moving the grating wheel. This way, the geometrical configuration in the spectrograph was constant for this disperser, and the information of different spectra can be combined. The data in the band III and with the PRISM were background subtracted using exposures without the source. To mitigate the influence of the MSA, which harbored some not fully closed shutters, we subtracted the non-IFU data from each IFU exposure to remove the other spectra.

We analyzed the data for all fixed slits except the A_1600, which was largely saturated in the flatfield exposures, and all IFU slices. For the PRISM, the detector was only partially read out targeting the IFU spectra, so apart from them we could only use the B_200 and a small fraction of the A_200_2 data.

Spatial reference data

In the first part, we took the flatfield continuum exposures to measure the spatial location of the traces, as exemplary shown in Figure 5.4 for the B_200 slit with the disperser G140H. This was done by determining the centroid index $j_{Centroid}$ in each detector column i_{Trace} within a range 10% larger than the nominal slit width. The oversizing in spatial direction is necessary to obtain a meaningful center of gravity. If the range was smaller than the slit width and only pixels within the spectrum were selected, the value would just resemble the center of the interval itself.

Upon closer inspection, some contamination from the neighboring slit A_1600 is visible at the top left. Unfortunately the slits are located not very far apart in spatial direction, and a wrong initial model can include parts of the adjacent spectrum. This is especially pronounced here where the other one is 8× brighter and leaks into the separating pixels. We therefore visually inspected each flatfield image, and restricted the spectral range for the centroids to areas without disturbance from other slits.

To eliminate the effects of bad pixels and the QE variations, we fitted a low-order polynomial to the pixel index pairs $(i_{Trace}, j_{Centroid})$ using only the columns without any rejected pixels, giving a function $j_{Trace}(i_{Trace})$ for each slit and disperser. The polynomial is drawn as a black line in Figure 5.4, while the corresponding index data is plotted in Figure 5.5. The blue values are the single measured centroids of the columns, and the red line is the initial prediction of the model. The deviation on the left side is mainly caused by the contamination by neighboring spectra and not a real effect. The fitted 4th-order polynomial is drawn in green and restricted to the range where the trace data is valid. The model already closely matches the polynomial curve, but is offset up to 1 pixel towards the right, so there is still room for improvement.

The IFU flatfield spectra were processed the same way, creating trace polynomials for each slice. Due to their larger spacing, neighbor contamination was less an issue.

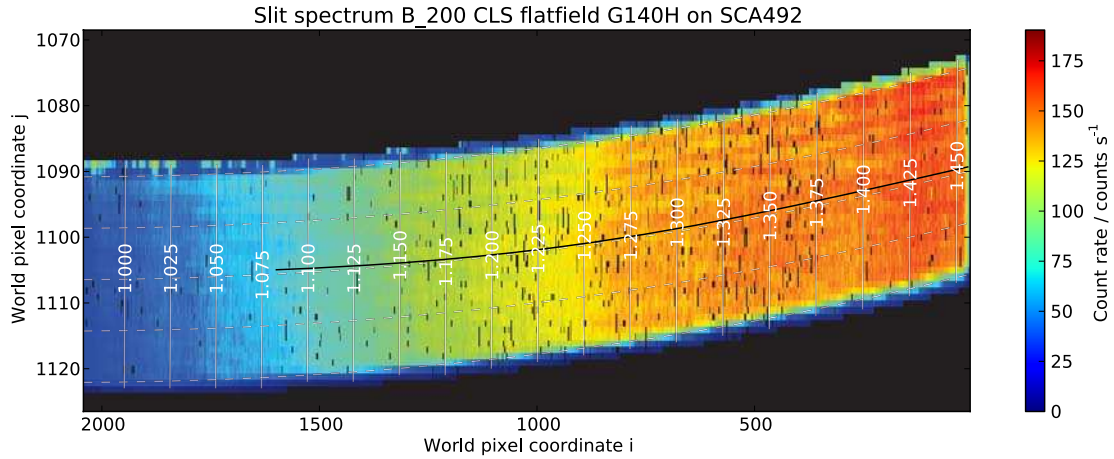


Figure 5.4: Spectrum of the SLIT_B_200 in a CLS flatfield continuum exposure with the grating G140H. Neighboring spectra are masked out, but some contamination is visible at the upper left edge. The projected model trace is overplotted in white, the polynomial fit of the column centroids in black. To avoid disturbance by other spectra, the valid range of the centroid data is reduced. The model trace is slightly offset from the measured values, especially towards the right.

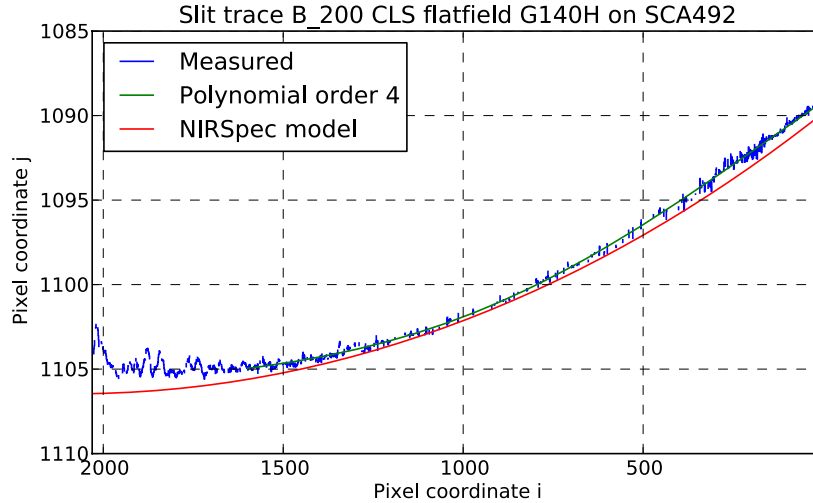


Figure 5.5: Trace data of the SLIT_B_200 in the CLS flatfield continuum exposure with the grating G140H shown in Figure 5.4. The blue values are the measured centroids in the detector columns which contain no bad pixels. The green line is the 4th-order polynomial fit of the centroids in the range without contamination by other spectra. The model trace in red is offset from the measurements at the right, while the deviation on the left is caused by erroneous centroid data.

However, towards the edges of the detectors the number of bad pixels increased considerably and reduced the valid trace range of the outer slice spectra.

Obviously the initial model guess for the slit spectrum locations is essential to obtain reliable centroid data for the fixed slits. If there would be an offset of several pixel, the proximity of the spectra would render an automated data extraction much more difficult. Therefore, the manual adjustment described in subsection 5.2.1 is a very important step and has to be done with care. If the resulting model is not yet accurate enough, one may also consider intermediate fitting of the disperser angles only in the spatial direction by matching the slit center traces. This way, the influence of local offsets in centroids may be reduced if only one parameter is adjusted at a time.

Finally, we also added the slit image positions (i_{IMA}, j_{IMA}) to the spatial reference data. They were determined from exposures of the fixed slits and IFU virtual slits with the MIRROR, and measured as the centroids in both detector coordinates.

Spectral reference data

To obtain absolute references in the spectral direction, we again used the Argon emission line spectra. Although the source mostly provides lines in the range of 0.7–1.5 μm , they are present in higher orders in the other NIRSpec bands. The wavelengths of the lines are very precisely known, and the prominent ones can be easily identified in the spectra.

Performing a standard extraction with NIPPLS, after rectification we obtained the regular 1D spectra, as shown in Figure 5.6(a) for the G140H grating in the A_200_2 slit. Depending on the disperser, we manually picked a set of 7–23 isolated lines, and fitted them individually with a Gaussian profile. One example can be seen in Figure 5.6(b). The center of the line is the wavelength as predicted by the model λ_{Model} . From the instrument model trace, we could calculate the spectral pixel index i_{Trace} , and with the trace polynomial, we derived the spatial index j_{Trace} . The real wavelength of the line λ_{ref} is known, thus we finally obtained a set of reference positions tuples ($i_{Trace}, j_{Trace}, \lambda_{ref}$) which give absolute spectrum positions on the detector for each disperser, slit, and IFU slice.

Again, it is necessary to point out that the initial model needs to be already very accurate. First, in the presence of a slit tilt, the calculation of the reference positions is only an approximation. The model trace may be off in spatial direction, and to reach the polynomial curve with the same wavelength we would need to translate along the tilted spectral line, not the detector column. In our case, the RMS of the spatial trace offset was typically less than half a pixel, and the slit tilt does not exceed 8° for the gratings. Hence the error in the spectral index i_{Trace} was smaller than $1/14^{\text{th}}$ of a pixel, or $1/31^{\text{th}}$ of a resolution element. Compared with the required absolute spectral calibration for NIRSpec of $1/8^{\text{th}}$ of a resolution element, this is negligible. Second, smaller offsets between the expected and real positions of the

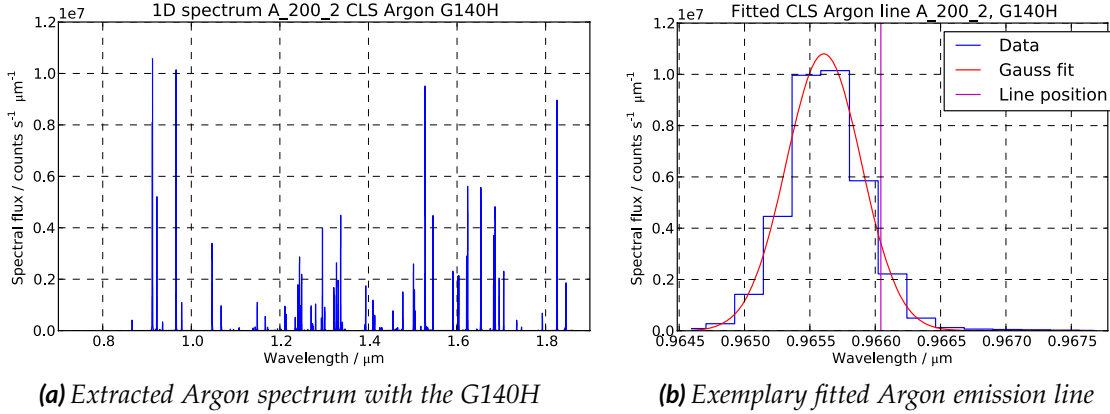


Figure 5.6: Extracted spectrum of the SLIT_A_200_2 in a CLS Argon exposure with the grating G140H. (a): 1D spectrum of the Argon lines. To derive absolute references, we individually fitted the position of isolated ones. (b): Exemplary fitted emission line at $\lambda_{ref} = 0.96604 \mu\text{m}$ (purple line). The Gauss fit (red) provides the predicted model wavelength $\lambda_{Model} = 0.96561 \mu\text{m}$.

lines somewhat simplify the fitting process. This can also be achieved by once fitting the GWA element tilt in the spectral direction and iterating the data extraction procedure.

As already mentioned, for the PRISM the exposures were targeting the IFU spectra, and there was only little coverage of the fixed slits. Analysis was further complicated by the very low resolution, especially around $1.5 \mu\text{m}$, which made single lines indistinguishable (see Figure 5.7(a)). Beyond $3.2 \mu\text{m}$ there are no lines any more, so we picked 7 between 1.7 and $3.13 \mu\text{m}$, which partially were overlapping with other ones. As they were fitted individually, we added a linear component to the Gauss function, and carefully selected the fit interval, as exemplary shown in Figure 5.7(b). This way we could at least obtain a few reference points for the PRISM, which however have a reduced fit reliability, and cover only a small range in the spectrum.

The reference positions of the slit images are independent of the wavelength, and were simply added to the list of spectrum positions with the central wavelength of the imaging band-pass filter ($i_{IMA}, j_{IMA}, \lambda_{ref}$).

Model optimization and residuals

To optimize the model we compared coordinate transforms in the spectrograph between different planes. The calculations are influenced by the following model characteristics:

- Geometry of the MSA, and IFU POST coordinate transforms,

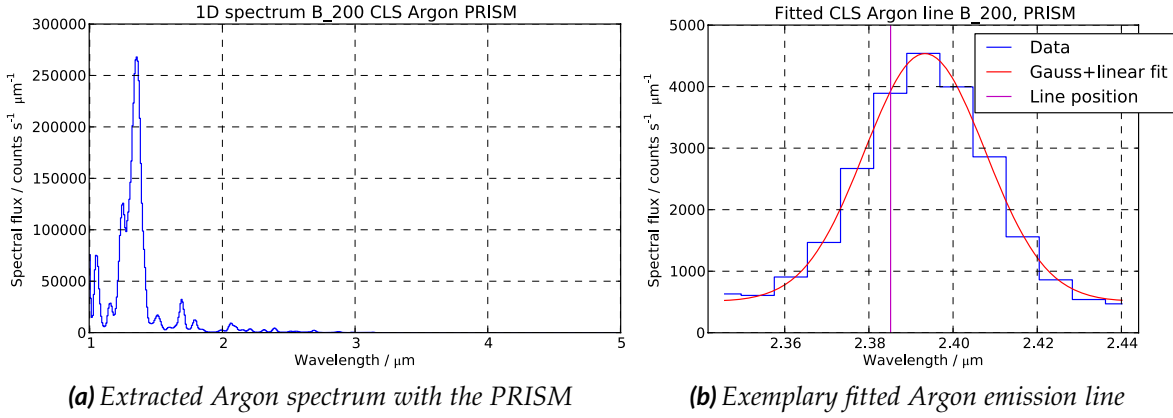


Figure 5.7: Extracted spectrum of the SLIT_B_200 in a CLS Argon exposure with the PRISM. (a): 1D spectrum of the Argon lines. The low resolution blends the individual lines at wavelengths below $1.5 \mu\text{m}$ and makes them indistinguishable. Above, there are only few lines, partially overlapping each other, from which we fitted the position of 7 of them. (b): Exemplary fitted emission line at $\lambda_{\text{ref}} = 2.3851 \mu\text{m}$ (purple line). The fit was done with a Gaussian and a linear function (red). The predicted model wavelength is $\lambda_{\text{Model}} = 2.3933 \mu\text{m}$.

- COL and CAM coordinate transforms,
- GWA element alignment,
- FPA geometry.

At the start we decided on absolute references to constrain the parameters and avoid unrealistic fit results, which were

- the measured fixed slit positions,
- setting the MIRROR the alignment angles to 0.

This way we established the MIRROR orientation in the exposures as the absolute GWA reference. The slit images then land at a certain point in the FPA plane, which can only change with the COL and CAM distortion, and the detectors are forced to remain at this location.

In the first optimization run we computed the forward coordinate transform through the spectrograph at the reference wavelengths λ_{ref} . Starting at the center of the slits and IFU slices, we obtained the detector pixel indices $(i_{\text{Model}}, j_{\text{Model}})$, and compared them to the measured values $(i_{\text{Trace}}, j_{\text{Trace}})$. The tuned model parameters were

- position of the detectors,

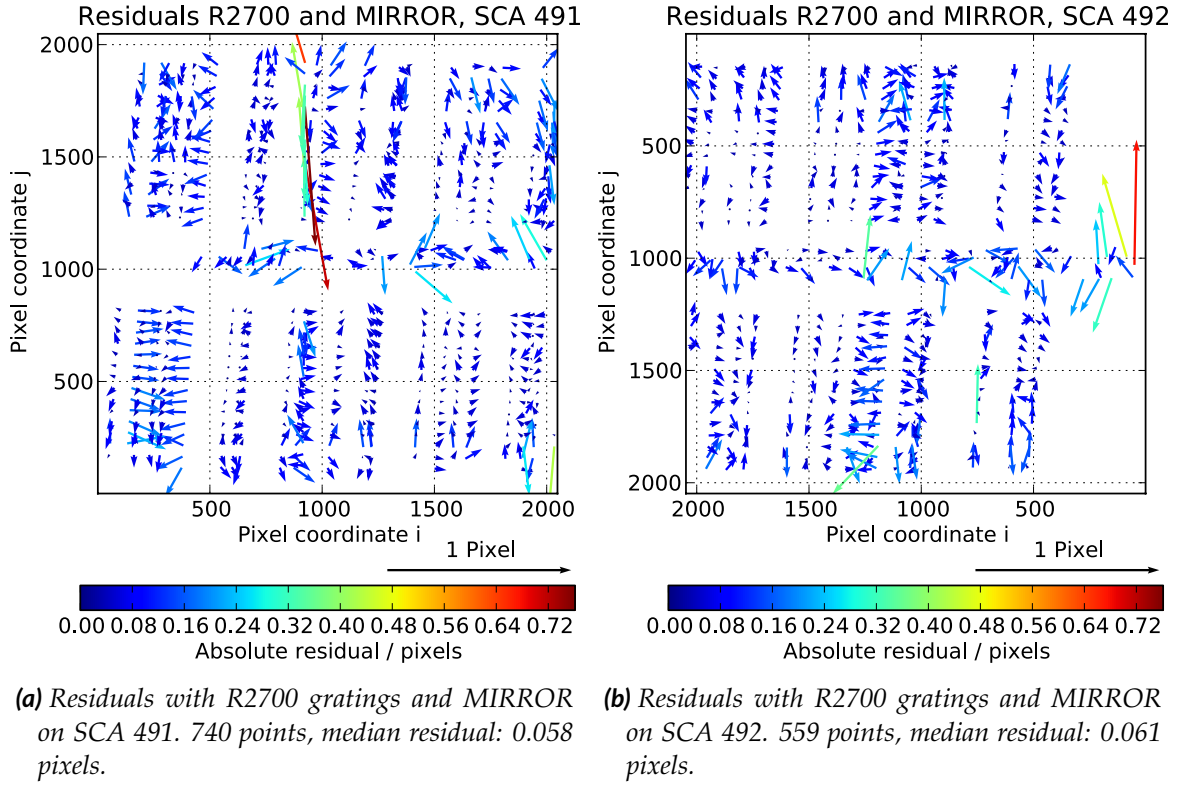


Figure 5.8: Model fit residuals with the FXSL and IFU data of the high-resolution gratings and the MIRROR (equal size and color scale). The median residual is 0.059 or $1/17^{\text{th}}$ of a pixel from 1299 reference points. (a): Residuals on SCA 491. The large values originate from the IFU virtual slit images. (b): Residuals on SCA 492. At the right edge there are too few points to influence the fit, and the residuals are larger.

- CAM magnification factor and low-order distortion (up to 2nd order),
- R2700-disperser tilt angles,
- COL x -distortion 1st order,
- IFU virtual slit positions.

As we were changing the distortion of the optics, we did not use all measured spectra right away. To retain a balance in the FOV, we only included the data of the high-resolution mode, which is almost equally distributed over both detectors (740 points on SCA 491, 559 points on SCA 492). The R1000-data is mostly located on the left detector 491, and the distortion fit then would be dominated by the behavior on this side. To constrain the global geometry of the spectrograph, we added the slit image positions as fundamental reference points. Finally, we ran a least-squares fit to minimize the residuals.

The residuals on both detectors are plotted in Figure 5.8. From the 1299 available reference points, the overall median residual is 0.059 pixels, which corresponds to $1/17^{\text{th}}$ of a detector pixel.

We then did a second model fit, now optimizing the disperser angles of the R1000 gratings and the PRISM, without changing the optics again. The total residuals of all dispersers are shown in Figure 5.9. The combined median of the residuals is $1/14^{\text{th}}$ of a pixel, the values for single instrument modes are listed in Table 5.1. In general the fit works very well, especially for the gratings where the residuals are almost $4\times$ smaller than the required spectral instrument calibration.

They are only larger for the PRISM, where a lower quality of the line fits reduces the accuracy of the reference points. Besides, there is some uncertainty in the refractive index, which has a big influence on the dispersion. However, given that we could only extract a hand full of lines with small reliability, we did not tune this model parameter. In any case, the achieved residuals are sufficiently small for realistic simulations.

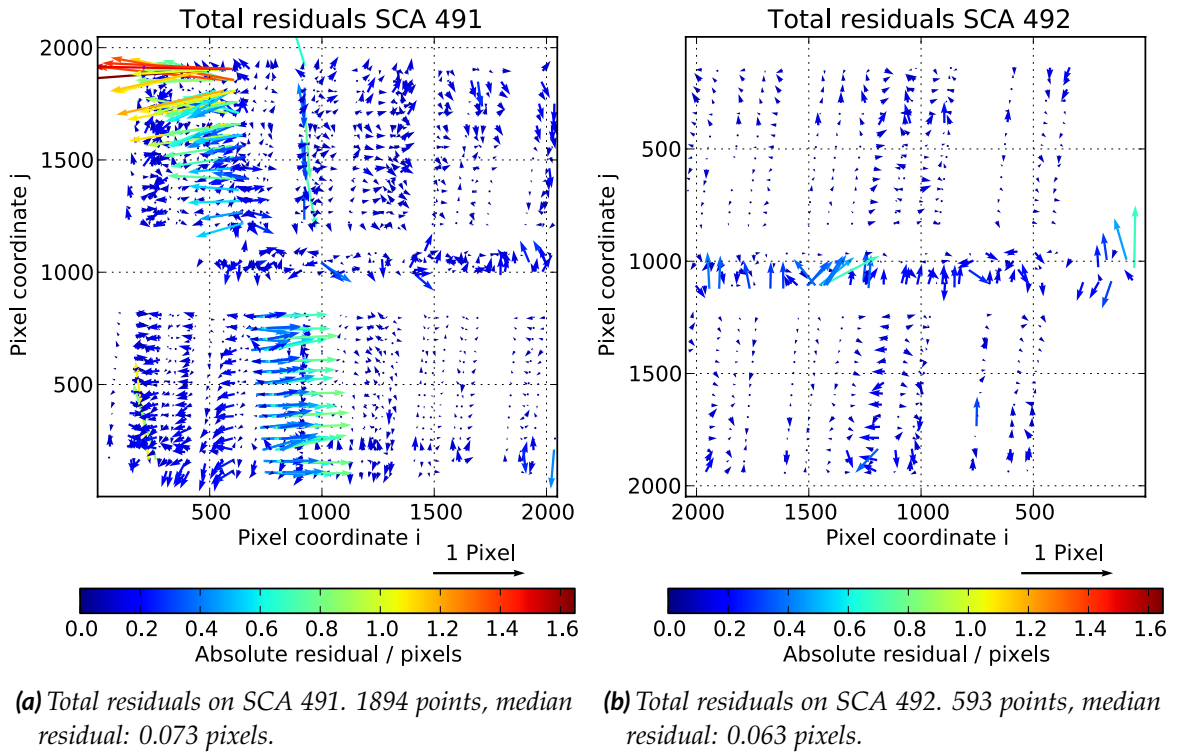


Figure 5.9: Total model fit residuals with the FXSL and IFU data (equal size and color scale). The median residual is 0.071 or $1/14^{\text{th}}$ of a pixel from 2487 reference points. (a): Residuals on SCA 491. The diagonal large values originate from the PRISM spectra. (b): Residuals on SCA 492. Compared to Figure 5.8, the arrow length is reduced.

Table 5.1: Residuals of the model fit in the transforms from slits to detector. They are generally smaller than the required absolute spectral knowledge of $1/4^{\text{th}}$ of a pixel.

Dispersers	Number of reference points	Median residual in fraction of a pixel
Gratings	2233	1/15
PRISM	219	1/4
MIRROR	35	1/5.6
Total	2487	1/14

To keep the model consistent, we also fitted the backward coordinate transforms in the COL and CAM optics. This is equally necessary for the calculation of spectral coordinates of a detector pixel, and ultimately for the spectrum extraction. Again, we used only the R2700 and MIRROR reference data, and optimized the same type of distortion parameters in the COL and CAM transform as done in the forward direction with a least-squares fit. The quality was evaluated by extracting the same Argon lines as in the creation of the reference data. The residuals are $1/10^{\text{th}}$ – $1/18^{\text{th}}$ of a pixel with the gratings (e.g. Figure 5.10), and $1/2$ – $1/10^{\text{th}}$ of a pixel with the PRISM.

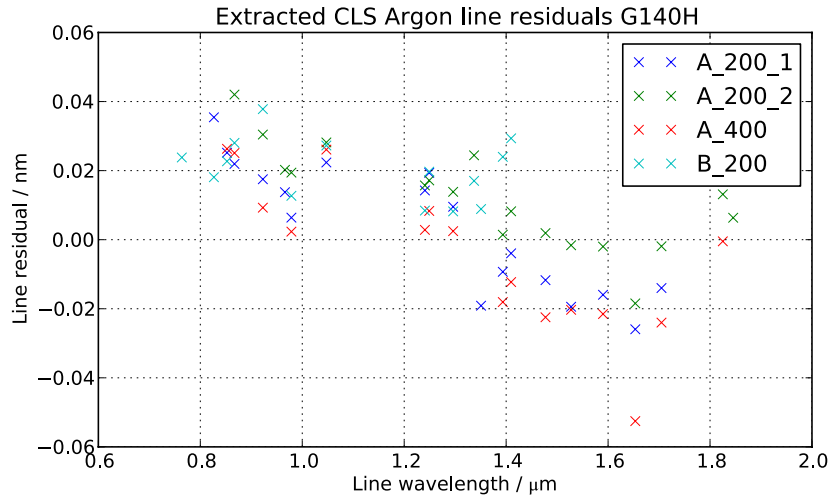


Figure 5.10: Residuals of the extracted CLS Argon lines in the fixed slits with the grating G140H. The mean is 0.008 nm with a RMS of 0.019 nm, which is $1/31^{\text{th}} \pm 1/12^{\text{th}}$ of a pixel in this mode.

Model fit evaluation

In general, the residuals of the forward and the backwards transforms are small compared to the required absolute spectral knowledge. Especially the fit of the gratings worked very well, the model being typically 3–5× more accurate. The PRISM and MIRROR still deliver a sufficient precision for simulations and data extraction.

Upon closer inspection of the residuals, some limitations of the approach and the model become obvious. First, the slit A_1600 was not used as a reference for the spectra, and now has a systematic trace offset of 0.2 pixel in spatial direction. As the IFU virtual slits could move freely, the distortion of the CAM in y was only constrained by the other four fixed slits traces. Nevertheless we fitted it up to the second order, therefore the A_1600 fixed slit is not necessarily met very well.

For similar reasons, the residuals for the IFU are mostly horizontal, as the virtual slit positions were optimized in both directions, while the spectral one is much more constrained by the spectra and therefore the CAM distortion.

The lower fit quality for the PRISM is due to uncertain line references, and a limited coverage of the spectral band. This did not allow any adjustment of the refractive index, which has a large influence on the dispersion calculation.

In the forward residual plots (Figure 5.8 and Figure 5.9), there is a wave-like pattern visible in x -direction. Here the CAM distortion seems to require tuning of even higher orders. A second check by fitting combinations of many more Argon lines by Birkmann et al. (2011) revealed a similar behavior.

With data taken only through the fixed slits and the IFU, the COL is largely unconstrained. Therefore we only adjusted one linear parameter in x to accommodate the spacing between the A- and B-slits, and let the IFU positions free. To finally tune the COL distortion, we need to wait for data with the MSA, which will be taken in the second calibration campaign.

As it finally turned out, apart from changing the detector, NIRSpec will also be re-integrated on a new optical bench, and the optimization process will have to be repeated. Following the recipe from above with minor changes in the parameter selection, and including the MSA data, the chance of reaching a similar accuracy as now is very high. Additionally, we will be able to verify the FORE distortion by analyzing pinhole mask data through the open MSA, which are not yet available.

5.2.3 GWA tilt sensor integration in extraction

There is one more constraint in the model caused by an instrumental effect: The GWA has a limited positioning repeatability, which means that the tilt angles of the dispersers are not the same after turning the wheel and returning to the same configuration. In the data of the first cryo campaign, de Marchi et al. (2011) looked at the displacement of images on the detector after moving the wheel to other

positions. This test had been done at two operating temperatures (31 K and 45 K). As it turned out, only the spectral dimension is affected, and they were able to establish a relation between the image shifts, and the reading of the position sensors in the GWA for both temperatures.

We used the calibrated sensor curves, and added a function in the spectrum extraction to calculate the GWA tilt from the sensor value in the exposure header. Using this information, and the sensor value from the exposures in the model optimization, we can compute the actual GWA element tilt and put it into the NIPPLS instrument model.

We verified the approach by extracting the Argon lines from a G140H exposure at 45 K which had a large GWA tilt compared to the reference data in the model, taken at 31 K. The sensor value corresponded to an image shift of about 1 pixel in the FPA. The residuals of the line fitting are shown in Figure 5.11. There is a systematic offset of 0.014 nm with an RMS of 0.018 nm. Compared to the residuals with the reference exposure in Figure 5.10, the RMS is similar, and the offset is about the same size, much smaller than the image displacement.

Hence we conclude that with the GWA tilt sensor data and the optimized instrument model, we can use the NIPPLS to extract the spectra from all data in the first calibration campaign with high accuracy. Besides, with the sensor calibration for the two temperatures, we automatically correct for thermal deformations in the spectrograph, whether they originate from the GWA alone or not.

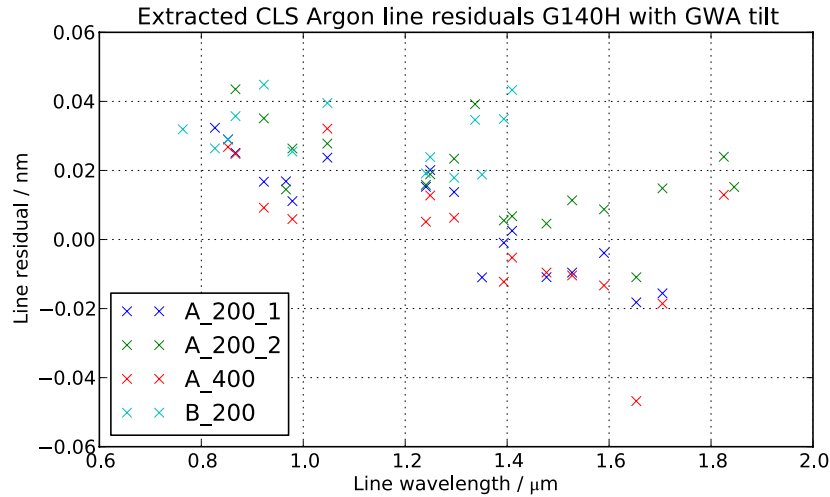


Figure 5.11: Residuals of the extracted CLS Argon lines with the grating G140H in an exposure with different GWA positioning. The mean is 0.014 nm with a RMS of 0.018 nm, which is $1/17^{\text{th}} \pm 1/13^{\text{th}}$ of a pixel in this mode. The systematic offset is about the same size as its RMS.

5.3 Test of IPS with tuned instrument model

Before delivery, the IPS had to go through Acceptance Test Procedures (ATP), which verified the overall functionality and details of the computation. One test was checking the level of electron rates by putting defined sources, and simulating the exposure with a special test instrument model. This was a simplified version of NIRSpec which partly mimicked its characteristics, but with paraxial optics and flat efficiencies. That way, the expected electron rate in each pixel could be derived, and compared to the result in the simulation. Obviously, the tests were passed and the IPS provided correct exposures.

We repeated similar tests with the tuned instrument model. The general optical parameters are not very different to the ATP, but now include distortion, and most noticeably, an off-plane spectrograph with a slit tilt. To enable the external calculation of expected electron rates, we also used constant efficiencies.

We put different source types on the sky at the locations of the fixed slits, and simulated the exposures with the realistic instrument geometry. The theoretical pixel values were calculated from the source rate, the instrument efficiency, the aperture size of the OTE, and the spatial extent of a resolution element on the sky (slit width, 1 detector pixel high). We extracted the 1D irregular row spectrum from the electron rates at the center of each slit, which also contains the data of a single pixel row. The simulated spectra were then corrected with the slit efficiency caused by the diffraction losses, which was not included in the external calculation. Finally, we calculated the ratio of the total electron rates in the IPS and the expected values. The numbers from the 200 mas wide slits are shown in Table 5.2.

Obviously, there are large errors of more than 30% in the calculation of the electron rates when using a realistic instrument model. One possible cause is the slit tilt, which may disturb the spatial and spectral integration of the source on the detector. Unfortunately we were not yet able to resolve the issue due to constraints in time and resources.

Table 5.2: *Ratio of the electron rates in the IPS and expected values, using a realistic instrument model. The data are from simulations of continuum and spectrally resolved sources in the 200 mas-wide fixed slits.*

Source type	Ratio IPS / expected in %		
	R1000	R2700	PRISM
Point-like	100	100	110
Background	100	93	130
Extended	67	64	88

This has major consequences for the simulations. All analysis relying on absolute knowledge of the electron rates are affected, e.g. noise levels are wrong, as well as the absolute radiometric calibration of the instrument when using the IPS as a comparison. At least, the offsets seem systematic for all exposure types, so a manual correction of the electron rates is possible. However, different source types need to be simulated separately in order to apply the correction for each of them, and the electron rates need to be combined afterwards.

5.4 Calibration Light Source spectra

The second important characteristics that is verified during the ground calibration is the efficiency of the instrument. The CLS (Bagnasco et al., 2008) serves as the radiometric reference, and has been calibrated to absolute levels. By comparing the exposures to the known input spectra, it is possible to characterize the throughput of the instrument. To exclude possible errors, we did some sanity checks on the CLS spectra with exposures from the campaign.

The CLS (Figure 5.12) consists of two major parts: A lightbox with the source and filters, and an integrating sphere with an exit port mimicking the JWST pupil. The spectra created in the lightbox are fed into the integrating sphere, and an almost perfectly uniform illumination is reached at the exit port.



Figure 5.12: Drawing of the ground Calibration Light Source. In the lightbox on the top, a filament lamp provides the source spectrum, which is altered by passing through four filter wheels. The lightbox output enters the large integrating sphere, whose exit port can be seen at the front (orange). The aperture has a mask mimicking the JWST OTE pupil (red). (Credit: MSSL)

The source for the spectra is a filament lamp emitting a broad-band continuum spectrum. In the lightbox, there are four Filter Wheels (FW) which allow the modification of the source spectrum to create various continuum and spectral references. Two of them carry spectral filters and some attenuators (FW 1 and 2), while FW 3 and 4 are used to adjust the global intensity levels. Due to their design, the individual attenuation factors depend on the setting of the other wheels. In the preparation of the test campaign, it was decided to obtain an absolute radiometric calibration of the CLS in all modes with their particular configuration of the filter wheels. To find suitable positions for FW 3 and 4, their attenuations had been measured in different combinations, and the final positions were determined from the required source brightness. One constraint was that FW 4 can only be moved manually, and needs to be at the same position at all times.

The calibration was done in two steps: At first, the output spectrum of the CLS at the exit port CLS_{raw} was measured. Due to its faintness, this could only be done in the brightest source mode ("PSB"), with all the filter wheels in the lightbox in their "open" position, including FW 3 and 4. The same filter configuration was also used to measure the spectrum at the lightbox exit itself $LB_{PSB_{open,open}}$, where the subscripts denote the positions of FW 3 and 4. From these two curves, a transfer function T was established, describing the efficiency of the integrating sphere:

$$T = \frac{CLS_{raw}}{LB_{PSB_{open,open}}}.$$

Second, the wheels were set to their nominal positions, and all the spectral modes were measured at the lightbox exit, giving the single spectra $LB_{nom,nom}$. The calibrated CLS exit spectra were then derived by multiplying the lightbox curves with the transfer function to

$$CLS_{nom,nom} = LB_{nom,nom} \cdot T.$$

Between the CLS calibration and the NIRSpec testing it was discovered that three modes needed an adjustment of the FW 3 position to deliver the required intensities. To preserve the calibration, exposures were done during the campaign with the nominal FW 3 position, and the new lightbox configuration. One of them was the PSB mode, and we obtained data with FW 3 in the calibrated position $NIRS_{PSB_{nom,nom}}$ and the new one $NIRS_{PSB_{open,nom}}$ with FW 3 open.

We corrected the count rate maps with the known detector QE to reduce the pixel-to-pixel noise, and extracted the 1D spectra of the fixed slits A_200_1 and A_200_2. Dividing the curves, we derived the ratio of the two CLS spectra, and fitted a low-order polynomial to it. This is the attenuation factor of FW 3 when FW 4 is in nominal position:

$$FW3_{open \rightarrow nom,nom} = \frac{NIRS_{PSB_{nom,nom}}}{NIRS_{PSB_{open,nom}}}.$$

During the CLS calibration, the attenuation of FW 4 was measured while all other wheels were set to open, and the factor $FW4_{open,open \rightarrow nom}$ is known. We then tried to reproduce the nominal output spectrum of the PSB mode $PSB'_{nom,nom}$ by multiplying the raw CLS spectrum with these two attenuations

$$PSB'_{nom,nom} = CLS_{raw} \cdot FW4_{open,open \rightarrow nom} \cdot FW3_{open \rightarrow nom,nom}$$

and calculated the ratio with the spectrum given by the CLS manufacturer $PSB_{nom,nom}$

$$R_{CLS} = \frac{PSB_{nom,nom}}{PSB'_{nom,nom}}.$$

The two spectra are plotted in Figure 5.13 in blue and green, as well as the ratio in red (scale on the right y -axis). Obviously, the curves differ by a significant amount, the data from the CLS calibration is about $0.82\times$ too low. Explicitly writing the ratio

$$R_{CLS} = \frac{CLS_{raw} \cdot LB_{PSB_{nom,nom}}}{CLS_{raw} \cdot FW4_{open,open \rightarrow nom} \cdot FW3_{open \rightarrow nom,nom} \cdot LB_{PSB_{open,open}}},$$

the measurement of CLS_{raw} cancels out, and the error must be caused by other values. Given that the FW 4 attenuation $FW4_{open,open \rightarrow nom}$ was measured with an integrating photometer, it is considered reliable, and so is $FW3_{open \rightarrow nom,nom}$ which comes from NIRSpec exposures. The only realistic possibilities are erroneous measurements of the lightbox spectra.

To reconstruct the true CLS output, we assume that the raw CLS spectrum is correct, despite the difficulties in the measurement. Besides, even if the nominal

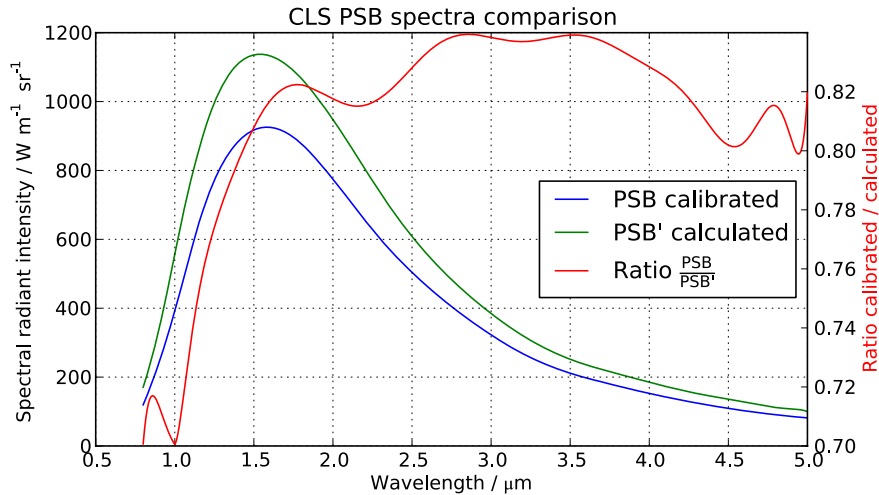


Figure 5.13: CLS PSB output spectra as calibrated (blue) and calculated with NIRSpec data (green). The ratio of both is about 0.82 (red).

lightbox level measurements may be wrong, we presume that they are correct relative to each other. We then re-created the single CLS output spectra from the existing data by rescaling them with the inverse ratio:

$$\begin{aligned} CLS'_{nom,nom} &= \frac{1}{R_{CLS}} \cdot CLS_{nom,nom} \\ &= CLS_{raw} \cdot FW4_{open,open \rightarrow nom} \cdot FW3_{open \rightarrow nom,nom} \cdot \frac{LB_{nom,nom}}{LB_{PSB_{nom,nom}}} \cdot \end{aligned}$$

In addition, for the other two modes that needed an adjustment of FW 3, we multiplied the spectra with the ratio extracted from the NIRSpec exposures of both settings.

This way we constructed a new model of the CLS with correct spectra. In any case, we need to rely on the absolute CLS output spectrum CLS_{raw} , which is the only available reference. The absolute accuracy of the spectra was estimated to 10% by the manufacturer, but may very well be only 15% given the discovered inconsistency in the initial calibration.

5.5 Instrument efficiency

5.5.1 Filter transmissions

After tuning the model geometry for spectrum extraction and correcting the calibration source, we could go on and analyze the transmission data of NIRSpec. The first subsystem we looked at was the filter wheel. In the test campaign we obtained exposures with the PRISM and a flatfield continuum source for each one of the transmissive filters. We subtracted background exposures where available, and corrected the count rates with the measured QE of the detector. The spectra were extracted in the range 0.5–5.5 μm from all fixed slits except the A_1600, rectified, and collapsed to 1D.

When looking at the spectra of the CLEAR filter, we found an inconsistency of the count rates of the A_200-slits and the B_200 slit between 4.5 and 5.5 μm . Differences of the spectra could only be caused by their position in the field and the local scale, an incorrect QE map, or some other field-dependent throughput variation. While the latter can be excluded, and the first would affect the spectra as a whole, it is likely that the efficiency data of the detectors had changed since the characterization. The chips in the installed FPA were already known to degrade with time, hence we decided to manually adjust the average QE data of SCA 492, where the B_200 spectrum was recorded. The old and new detector curves are shown in the appendix in Figure A.17. Afterwards, the spectra of the small slits are approximately matching, as it can be seen in Figure 5.14.

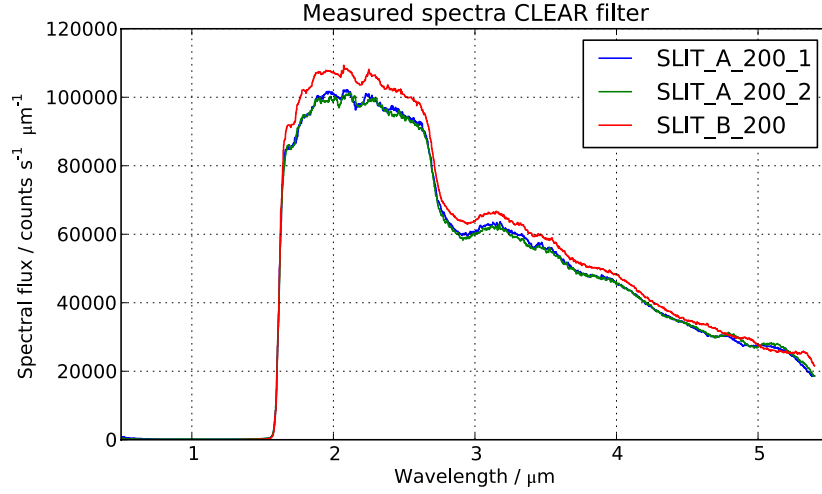


Figure 5.14: Continuum spectra of the CLEAR filter with the PRISM in the 200 mas fixed slits. The data was QE-corrected and extracted to regular 1D spectra. Around 5 μm we needed to tune the detector QE to keep the curves consistent.

To mitigate the influence of any absolute transmission, we calculated the ratio of each filter spectrum to the CLEAR one, and obtained relative transmission values. The throughput of the uncoated CLEAR filter had been calculated from the refractive index of the CaF_2 substrate at operating temperature. Although its limited knowledge causes problems with the exact PRISM dispersion, the influence on the transmission curve is small, and we could use the model CLEAR curve as an absolute reference.

The spectral resolution of the PRISM is rather poor, especially in the range 1–2 μm , where some of the filters show small-scale features (e.g. the F100LP plotted in Figure 3.1). In the measurement this leads to a smoothing of the relative transmission, and taking this as the reference we would remove unresolved throughput variations. Therefore we simulated the same exposures with the IPS, which imitates the PRISM spectra, and extracted the data in similar way. To further reduce the noise in the data, we smoothed them with a moving mean. Some corrections of the model curves are necessary, as it can be seen in the example of the F170LP in Figure 5.15. While in the cuton region (Figure 5.15(b)) there is an offset, the small features are not resolved by the PRISM, which becomes obvious when comparing the IPS curve (red) to the pure model ratio (green). The absorption feature at 2.7 μm on the other hand is fully real and needs to be adjusted in the model.

By dividing the filter ratios in the measurements with the simulations, we could derive a correction factor for the model. We multiplied the model filter curve with this factor, and finally obtained calibrated filter transmissions, while preserving their

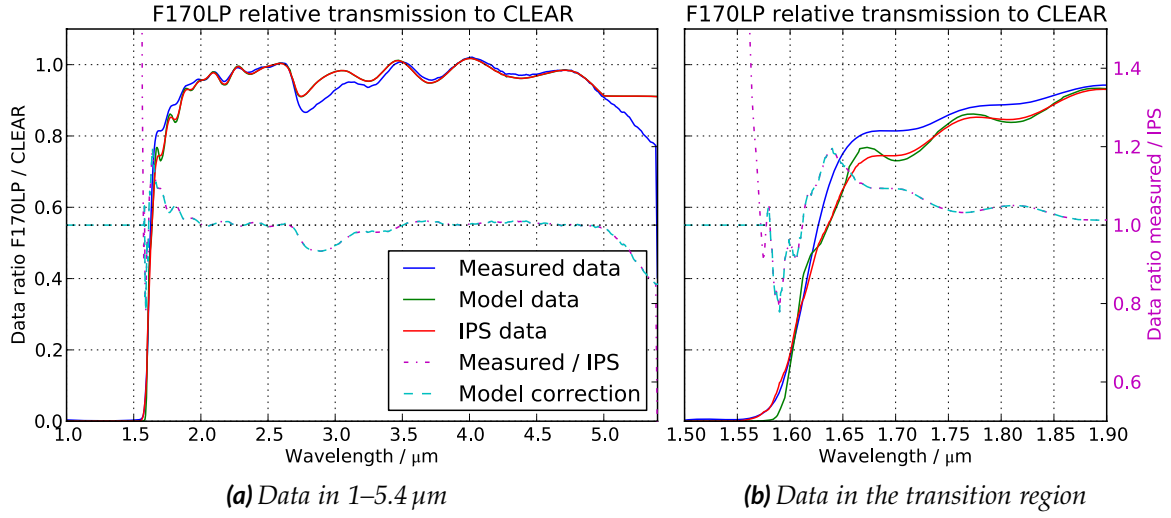


Figure 5.15: Comparison of relative F170LP transmission from NIRspec measurements (blue), filter characterization data (green) and IPS simulations (red). (a): Full spectral range. The feature at $2.7\ \mu\text{m}$ is missing in the model. In the transition region (b), the PRISM does not resolve the small scales. We calculated the ratio between the measured and simulated curves (magenta), and applied a correction to the model filter throughput (cyan).

behavior on small scales. The initial and tuned curves for all filters are shown in the appendix in Figure A.15.

5.5.2 Grating efficiencies

In a second process we analyzed flatfield continuum exposures of the nominal filter and disperser combinations in band 0.7, I, II, III, and the PRISM, focussing on the efficiencies of the GWA elements. By default, we corrected the count rate maps with the detector QE, extracted, rectified, and collapsed the spectra of all fixed slits. The data of the A_1600 was partly saturated, but provided valuable results in the valid regions.

We analyzed the data set in two ways: First, we calculated the ratio of the R1000 and R2700 spectra for each band, as exemplary shown for band II in Figure 5.16. This is directly equivalent to the ratio of the grating efficiencies, apart from errors in the spatial detector QE data. All other parameters are similar in the exposures, and the rectification corrects the different spectrum lengths. Compared to the ratio of the model grating data, we could identify features in the curves, which are not present in the measured data (e.g. at $1.85\ \mu\text{m}$), and vice versa (e.g. at $2.6\ \mu\text{m}$).

This is not surprising given that the efficiencies originate from theoretical calculations, and had never been verified. The sharp features especially in the R2700-

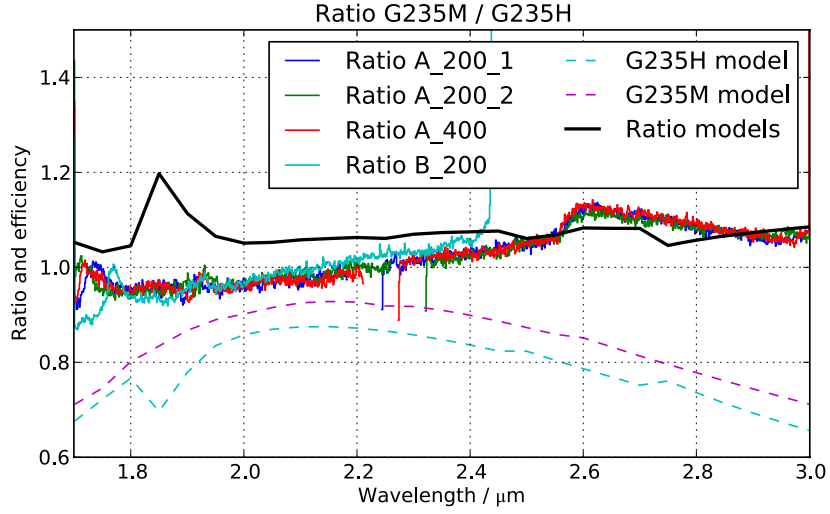


Figure 5.16: Ratio of the R1000 and R2700 spectra in band II in fixed slits, the initial grating model efficiencies (dashed) and their ratio (black). The resonance at $1.85\ \mu\text{m}$ in G395H is not seen in the measured data, while at $2.6\ \mu\text{m}$ a feature is not predicted by the model. The overall match is good, although there is an offset growing towards shorter wavelengths. The peaks at $1.75\ \mu\text{m}$ can not be modeled by a single feature, and are likely field-dependent resonances.

gratings are caused by polarization resonances. In the model, parallel and orthogonal contributions had been averaged equally, while the light in NIRSpec is partially polarized due to grazing incidence on the mirrors. Therefore, differences between the measurements and the simulations were not unexpected.

The second check was comparing the absolute levels of simulations to the measurements. We generated exposures in the IPS with the tuned CLS spectra, filters, and detector QE, and corrected the simulated electron rate maps with the factors in section 5.3. We applied the gain and created noiseless count rate maps directly from the electron rates, adding an average dark current and pixel-to-pixel crosstalk. The spectra of the fixed slits were processed the same way as the measurements, and we calculated the ratio of simulated spectra to the measured ones. The curves of the R2700-gratings can be seen in Figure 5.17. Not all variations are caused by the gratings, especially the different behavior of the slits at longer wavelengths. This effect is discussed in the next part.

By visually comparing the ratios of the resolutions, and the ratios with the simulations, we determined characteristics in the efficiencies which were manually tuned. While the former plots gave an indication at which wavelengths we needed to change the grating data, the simulation comparison provided information if it was the R1000 or R2700 curve, e.g. if overlaps between two neighboring bands were incorrect, as in the transition band II–III at $2.9\ \mu\text{m}$.

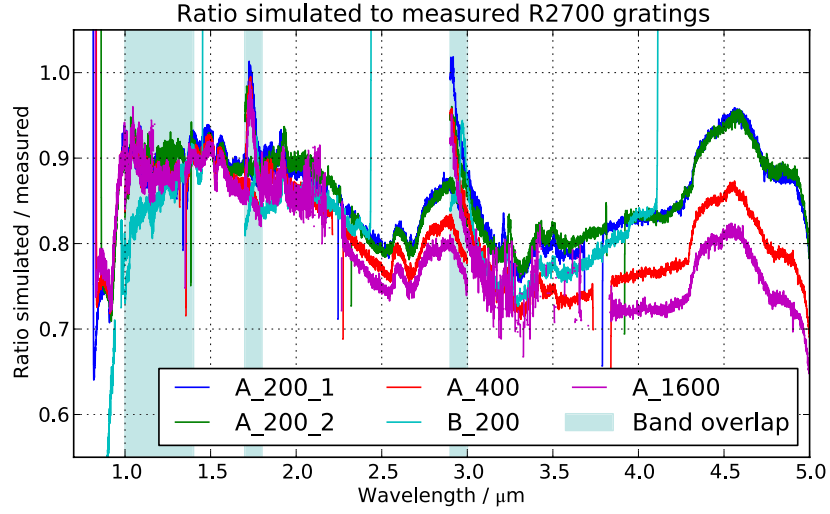


Figure 5.17: Ratios of simulated to measured spectra in the fixed slits for the R2700 gratings. The overlap regions of the bands are marked, and allow a check of the filter curves (band 0.7–I), or the grating efficiencies (band I–II and II–III). In general the ratios are about 0.8, the different behavior of the fixed slits is discussed in the following part.

In the end, we tuned the efficiencies of all gratings except G140M (R1000, band I). Mostly we slightly changed already existing resonance features, but the curves of the other two R1000 dispersers were also generally scaled to a lower level. However, the measured data was restricted to the nominal wavelength ranges, therefore we could not correct any particular aspects outside that range. Besides, we only had reliable data for the first order, and all others were left unchanged. The final data of the instrument model is shown in the appendix in Figure A.16 with the initial and tuned curves of the first order. All in all the corrections were small, confirming a good quality of the simulated model data. The PRISM efficiency curve, based on the CaF_2 transmission and a metallic coating, needed no adjustment.

5.5.3 Overall instrument throughput

As a final test, we evaluated the the total transmission of the NIRSpec model. Once again, we used the ratio of the simulations to the measurements, now with the complete tuned model data. We plotted the curves separately for the R2700 (Figure 5.18(a)), R1000 (Figure 5.18(b)), PRISM (Figure 5.18(c)), and all combined (Figure 5.18(d)). For each one, we derived the mean ratio from the spectra, and its RMS in the wavelength range 1–5 μm .

The data of all bands and modes are consistent, although they originate from configurations with different dispersers, filters, and sources. Only the fixed slits differ in the long wavelengths, the small ones being systematically simulated with

higher count rates. This may be due to wrong sized in the MSA model, or an incorrect calculation of the diffraction losses in the IPS.

The peaks visible in the R2700-data are caused by the influence of the shadow mask at the detector edges and were not flagged in the extraction. This effect is not simulated, and will probably be mitigated by the design of the new FPA. Below $1\text{ }\mu\text{m}$ the curves drop rapidly and the simulation quality decreases, possibly caused by uncertainty in the CLS input spectrum. The large feature at $2.7\text{ }\mu\text{m}$ is similar to

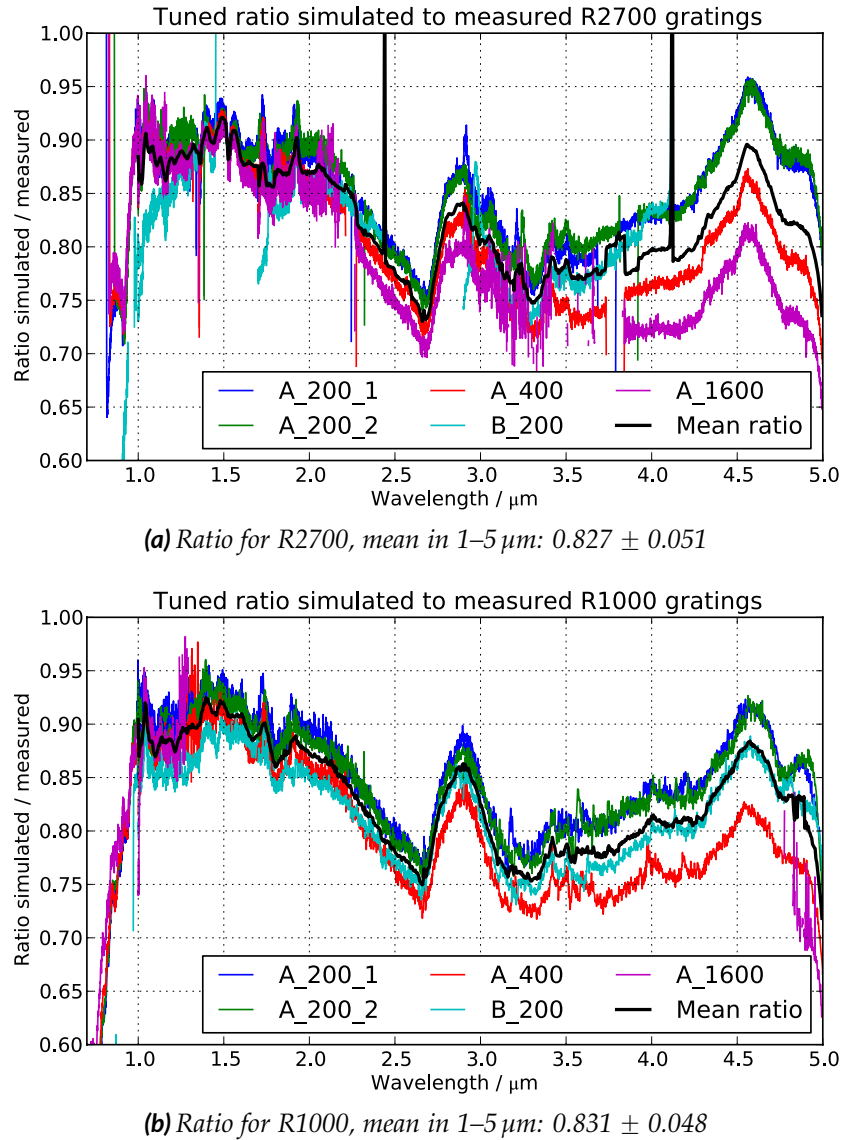
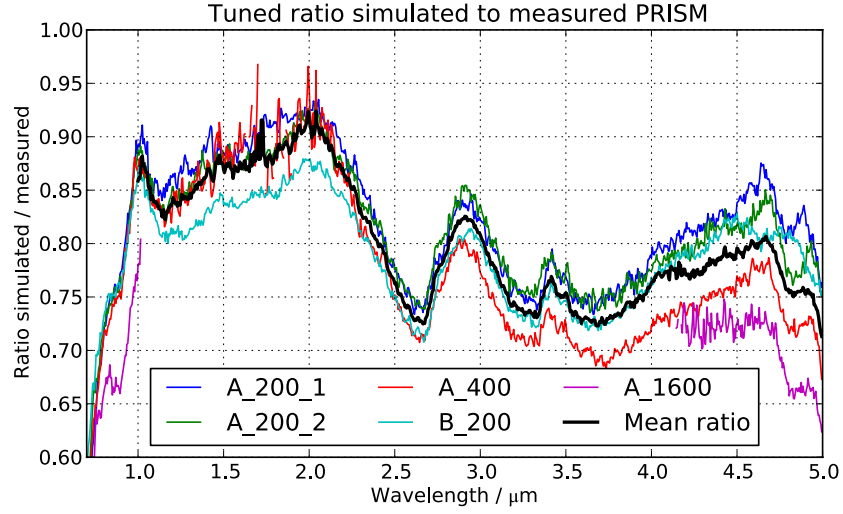
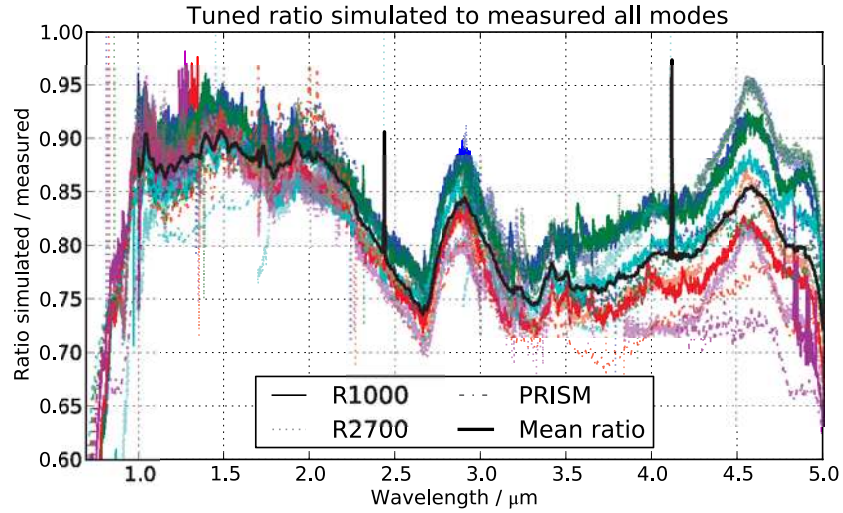


Figure 5.18: Ratios of simulated to measured spectra in the fixed slits after model tuning for different disperser types, and all combined. (a): R2700 gratings, (b): R1000 gratings. Continued on next page.



(c) Ratio for PRISM, mean in 1–5 μm : 0.801 ± 0.056



(d) Ratio for all modes, mean in 1–5 μm : 0.819 ± 0.049 . Slit color coding as in other plots.

Figure 5.18: Ratios of simulated to measured spectra in the fixed slits after model tuning for different disperser types, and all combined. (c): PRISM, (d): All modes combined. All bands and modes are consistent and hardly distinguishable, the fixed slits differ in the long wavelengths, probably due to incorrect sizes or wrong treatment of the diffraction losses. The peaks in the R2700-data are caused by influence of the shadow mask at the detector edges. Below 1 μm the simulation quality decreases, possibly caused by uncertainty in the source spectrum. The average mean ratios are calculated in the range 1–5 μm , and is 0.819 ± 0.049 for all modes combined.

ones corrected in the filter curves. However, we decided not to modify the model, as there was no clear indication which data to change. It may as well be contamination

in the CLS, by which the measured values are smaller than expected, and the ratio curves are boosted.

The average mean ratio of all modes in the range 1–5 μm is 0.82 ± 0.05 . Looking at the single throughputs of the instrument model (Appendix A.2.2), we could not identify a single component where the offset of 18% could be compensated. Neither the mirrors, nor any of the filters, dispersers, or detector curves allow an adjustment by this amount without exceeding 1 or violating the preceding relative consistency checks.

We therefore conclude that the error in the absolute level is mostly caused by the uncertain input spectra. Assuming an offset of 15% in the calibration of the CLS, the NIRSpec model is wrong by only a few percent. All in all, we estimate simulations with the as-built model to be accurate on absolute levels with an RMS of 5%, as seen in the variation of the mean ratio. Should the error in the CLS be smaller, we would underestimate the electron rates by up to 10%.

5.5.4 IFU throughput

The very last step of the model verification was to check the throughput of the IFU. To mitigate errors in the source data and absolute transmission of other elements, we once again compared relative curves from measurements and simulations. The measured data was from a PRISM flatfield continuum exposure, where the IFU and the fixed slits were recorded simultaneously. We corrected the detector QE, extracted, rectified, and collapsed the spectra of each slice between 0.5 and 5.5 μm . As it can be seen in Figure 5.18, the simulations of the fixed slits are inconsistent towards longer wavelengths. We therefore chose the A_400 slit as an average reference, and extracted the spectrum as well. In the IPS we simulated the same exposure scene, created a noiseless count rate map by adding gain, dark current, and crosstalk, and processed the data the same way.

Calculating the ratio of the IFU slice to the A_400 slit data, we obtained the relative overall throughput of the IFU, including the effect of relative slit aperture sizes. We divided the simulated by the measured relative transmission, and calculated the mean ratio. The curves of all slices are shown in Figure 5.19.

In general, the original IFU model underestimates the throughput. While the measured data is approximately constant across the slices, the levels in the simulation are increasing from slice 1 to 30 (bottom to top on detector), which results in the spread of the curves of about 15%. The detector QE is already corrected, so it is not caused by variations of the large-scale flatfield. One possibility is an incorrect source integration in the IPS, as already seen in section 5.2.2 for the fixed slits. We did not study this further and preferred to wait for a fix of the electron rate level computation. Besides, the model data originated from measurements of coating reflectivities and microroughness contributions, which were not continuous in the

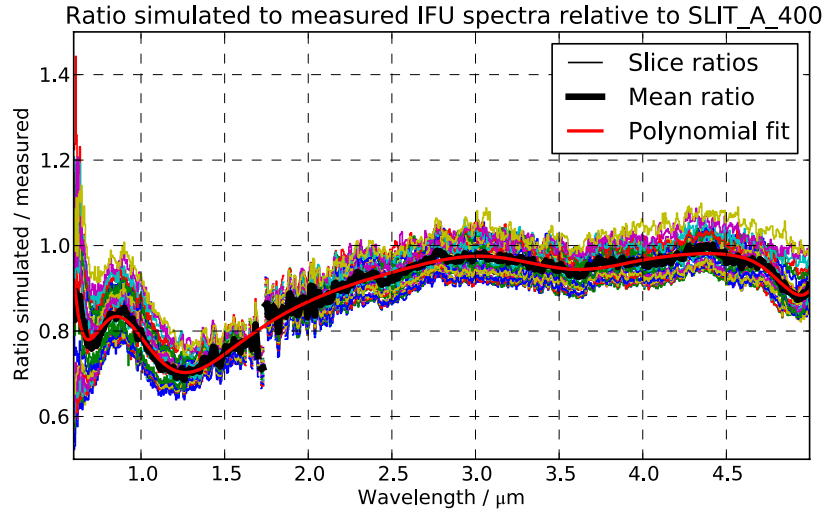


Figure 5.19: Ratios of simulated to measured spectra of the IFU slices relative to the slit A_400. The simulated data varies from slice to slice, while the measurements are almost constant. The local RMS of the mean curve is 3–5%. The model generally underestimated the IFU transmission.

spectral range and not very reliable. No dedicated measurement of the end-to-end transmission of each slice had been made.

Until issues in the IPS are solved, we refrained from modifying the individual curves, especially because there is no such effect in the measurements. Instead we fitted a low-order polynomial to the mean ratio, corrected the model throughput data accordingly, and accepted a larger error for the simulations. The initial and tuned curves of the IFU are plotted in the appendix in Figure A.18. In the end, with this correction the simulated IFU spectra have the same radiometric accuracy as stated in the previous section for the fixed slits, with an increased relative error of about $\sqrt{5\%^2 + 5\%^2} = 7\%$.

5.6 Limitations of simulations

During the preceding work we already encountered some limitations of the simulation approach and the models. To give a final picture, we will summarize them once again and discuss their relevance.

Optical simulation

First of all, the IPS does not simulate all optical effects in the instrument. Most notably, there is no treatment of straylight which can originate from scattered light, grating orders outside the nominal field, or diffraction at slit edges. The

measurements in the FM1 campaign show a feature in the high-resolution spectra, which was traced back to reflections of the 0 order. The location of the reflection is known, and the hardware will be modified to remove the effect. There also were other ghosts caused by the MSA structure, and a protecting baffle will be installed. Other than that, we spotted no significant straylight in the exposures. Given that all discovered effects will be mitigated with changes in the hardware, we assume that a missing simulation has no influence on the validity of the data.

Apart from diffraction-based throughput at the slits and the GWA aperture, we assume a uniform instrument reflectivity in the FOV. This assumption is valid as the beam footprint usually covers large areas on the mirrors (except on COM1 and the fold mirror after the MSA) and the coating reflectivities have no spatial dependence. However, there is no treatment of the polarization-induced effects on the gratings. We found isolated peaks in the measured curves (Figure 5.16) which were neither at a constant wavelength, nor spatial position on the detector, and may be the result from field-dependent resonances. They are limited to a small spectral interval ($< 0.1 \mu\text{m}$) and have relative amplitudes of $< 10\%$. Hence we do not consider them a significant limitation.

The overall transmission data of the instrument model itself is accurate to 10% pessimistic. The uncertainty could only be reduced if the CLS spectra were calibrated with smaller errors. The remaining variations in the comparison (Figure 5.18) were not traceable to a specific subsystem, and may either be the measurement errors in the instrument, of the calibration source. We assume a relative uncertainty of 5% from the RMS of the mean ratio between the simulated and measured data.

In the comparison we also saw an inconsistent behavior of the fixed slits with different sizes at long wavelengths. Having not found this effect in the verification of the IPS in section 5.3, it may be caused by incorrect slit widths in the MSA model, or a wrong calculation of the diffraction losses. The resulting error is included in the general model uncertainty. The ambiguity could be resolved with exposures through the MSA shutters from the next calibration campaign, which have more reliable aperture data.

Unfortunately it is still the IPS which causes the largest error. Depending on the source type, the electron rates are wrong by $\pm 30\%$ when using the real instrument model. This effect is at least systematic, and the electron rates can be corrected manually. However it requires different source types to be simulated separately, and is a severe restriction on the usefulness of the IPS. We hope to be able to correct the computation in the near future.

Detector readout

The simulation of the readout process in the IPS also turned out to be too simple. The NIRSpec detectors use a MULTIACCUM sampling technique (Rauscher et al., 2007), where the value of each pixel is read non-destructively, and the data is written

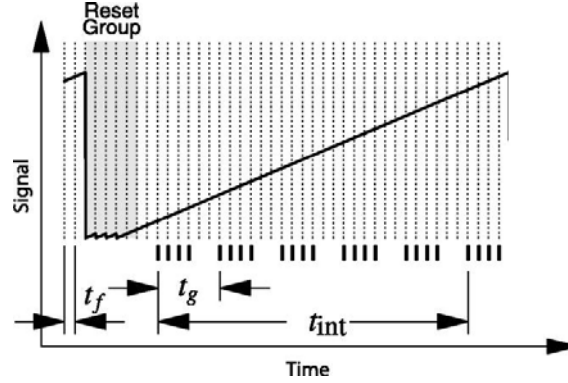


Figure 5.20: Scheme of the readout process in the NIRSPEC MULTIACCUM sampling. One integration provides the raw data cube consisting of n_g group arrays, each averaged from n_f frames. The frames are read out during the time t_f , one group takes t_g to complete. The effective integration time is t_{int} . Before the readout the detector is reset. Between the groups there may be dropped frames. (From Rauscher et al., 2007)

into a frame, which takes the frame time t_f . The on-board electronics then averages n_f frames in a group, and writes the n_g groups into the raw data data cube (see Figure 5.20).

Although the IPS correctly generates the raw data cube with contributions of the Poisson and readout noise, it only uses an average readout noise value for the detectors. Besides, it misses the important contribution of a $1/f$ noise which was discovered after the design of the software was settled. Consequently, the simulated readout data is not as noisy as in reality.

Another missing feature in the simulations are new types of bad pixels. The IPS only puts hot and dead ones, while in the testing other kinds appeared, as "open" (distributing the charge to neighbors) or "telegraph" (fluctuating values), which are not included in the readout simulation.

In addition, the ramp fitting tools to create count rate maps now use a processing approach which does not match the simulation of the IPS any more. Considering that the simple readout effects and noise contributions can also be added analytically, we did not generate the readout cubes with the IPS. At the moment, we are not interested in the raw data, but the final count rate maps. Instead of having to fit the count rates to the readout, we generated fake processed files directly from noiseless electron rate maps.

We usually convolved the data with a measured crosstalk kernel. The variances in each pixel were calculated with an analytical formula from the electron rates and the dark current rate (Rauscher et al., 2007, Eq. 1), while using an average readout noise, and the exposure parameters t_f , n_f , and n_g . If desired, we added the equivalent noise to the electron rates with a Gaussian distribution. Known bad pixels in the

detector data were flagged, and this way we obtained gain and linearity corrected count rate maps, which are similar to a simulation by the IPS and a matching ramp fitting.

There is still one important difference: In reality, the variances are estimated from the fitted count rates, which are already noisy. Especially for pixels with low rates, this may lead to a wrong variance value. In the fake processed data, the variance is correctly calculated from the noiseless electron rate, and the noise is added later on.

Another limitation of this approach are missing cosmic rays and their effect on the variance. When generating the raw data cube, the IPS randomly adds cosmic rays as sudden jumps in the signal with a user-defined rate. The ramp can still be fitted in parts without the cosmic influence, but this increases the variance. However, at the moment there is no processing tool available for NIRSpec data which handles cosmic rays. Hence it would be useless to simulate the effect in the readout anyway, and we assume a perfect correction in our simple processed data.

In the end, for bright sources, and under the assumption that the additional noise contributions can be removed by the processing tools, the direct creation of processed data is equivalent, and not different from simulations with the IPS. Nevertheless, we are not able to model all readout effects in their full wealth.

*It's the best simulation you can get,
unfortunately.*

John Pike



NIRSpec science simulations

6.1 Multi-object deep field

6.1.1 Introduction

The primary science case for NIRSpec is the spectroscopy of galaxies throughout the ages, up to very high redshift. This will be done with deep field exposures in multi-object mode, where the objects are selected in the FOV by configuring the MSA accordingly.

For the simulation of this observation type, we needed a realistic arrangement of galaxies at different redshifts, and proper spectra for the objects. Using the input data interface from section 4.1, we could easily create a typical sky scene. With the verified instrument model, we then simulated the exposures, as well as dedicated observations of fake reference stars for the absolute photometric calibration. Extracting and processing all data in the NIPPLS, we obtained the calibrated spectrum of each galaxy including variances.

We describe how the input scene was constructed from real observation data in subsection 6.1.2. Following, we explain in subsection 6.1.3 which spatial shapes were set for the objects, including the consequences that arise for the observation planning when assuming extended targets. In subsection 6.1.4 we demonstrate how we attributed a spectrum from a catalog of simulated high-redshift galaxy data to each object. After creating the exposure as described in subsection 6.1.5, we extract the spectra in subsection 6.1.6 and finally show the results in subsection 6.1.7, followed by a discussion.

6.1.2 Observation scene creation

One of the most deeply imaged areas on the sky is the Hubble Ultra-Deep Field (UDF, Beckwith et al., 2006; Thompson et al., 2005), whose source catalogs are

publicly available¹. Coe et al. (2006) analyzed the data and derived photometric redshifts for the detected objects, making their data public as well². We used a MOS sky scene for the MSA, where targets from the UDF catalog have been selected when falling into a shutter aperture. This arrangement had been constructed the following way³:

- Selecting objects in the catalog from Coe et al. (2006) with $z \geq 1$ and one magnitude in i , z , J , or $H \leq 27$ to achieve a reasonable SNR,
- sorting the objects in descending redshift order,
- setting a telescope roll angle to align the UDF area with the MSA FOV,
- iterating over the objects and calculating their position inside a shutter,
- checking if the relative distance in the shutter is < 0.25 , and the MSA row and the neighboring ones do not yet contain an open shutter,
- adding the object to the target list, and opening a "1×3" slitlet in the MSA configuration, if they are not marked as failed closed.

With the last selection it was guaranteed that the objects are within the shutter area where the slit losses are not too high (te Plate et al., 2007), and that there was no overlap of the spectra of different slitlets. This process was a very simple optimization of the observation scene, as it will have to be done in the real operation, although with many more possible parameters. The final list contained 72 targets with their catalog ID, redshift, the MSA shutter indices, and the offset within the shutters.

6.1.3 Galaxy shapes

The available catalogs also contain morphology parameters for most of the galaxies. We used the original data from Beckwith et al. (2006) and Thompson et al. (2005), where half-light radii r_h , ellipticities e , and position angles θ are listed. In case this information was missing, we created the shapes from an analytical size relation.

In the UDF data, Oesch et al. (2010) found a scaling law for r_h with the redshift in $2 \leq z \leq 8$ of

$$r_h(z) = r_0(1 + z)^{-m},$$

where $m = 1.12 \pm 0.17$ and $m = 1.32 \pm 0.52$ for two galaxy brightness samples. For our general calculations, we adopted the mean $m = 1.22$. From their figures, we derived the reference radius to $r_0 \approx 8$ kpc, and used the power law down to $z = 1$.

¹See http://archive.stsci.edu/prepds/udf/udf_hlsp.html

²See <http://acs.pha.jhu.edu/~coe/UDF>

³P. Jakobsen, priv. comm.

To compute the apparent angular size on the sky we took the WMAP7 mean cosmology model from Komatsu et al. (2011). In Figure 6.1 we show the absolute and the apparent half-light radii curves for $z = 1 \dots 8$. r_h does not drop below 0.1 arcsec, which is in agreement with values of Y-band dropouts from Bunker et al. (2010). Defining the galaxy core to be inside r_h , we see that NIRSpect will generally sample it with 2–6 pixels. This also means that the objects are significantly larger than a shutter width of 2 pixels.

Specifically for our scene, we obtained the galaxy size distribution plotted in Figure 6.2. Where available, we used the values from the catalogs in which we found the data of 61 objects, and the analytical relation for all others. The distribution is fairly consistent with the power law, although there is a clustering of small galaxies at low redshifts. Nevertheless, a significant fraction of the targets is also larger than 0.15 arcsec.

To create a 2D image with the shape of a galaxy, we assumed a Sérsic-type surface brightness distribution. In a radially symmetric case, the profile behaves as

$$I(r) = I_0 \exp(-kr^{1/n}),$$

with the Sérsic index n and the normalization factor k . We set $n = 1$, which is a good description of spiral and dwarf-elliptical galaxies, as expected in the high-redshift observation. The integrated brightness is then

$$I_{int}(R) = \int_0^R \int_0^{2\pi} I_0 \exp(-kr) r dr d\varphi.$$

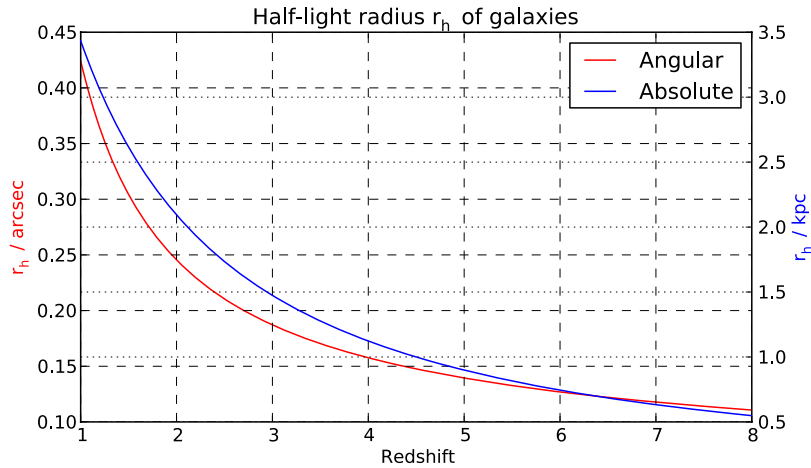


Figure 6.1: Evolution of the half-light radius of galaxies r_h with redshift in absolute and angular units (relation from Oesch et al., 2010).

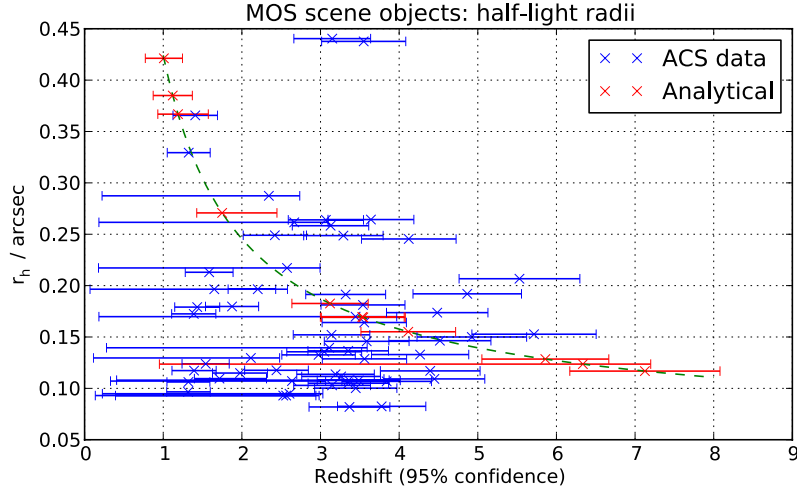


Figure 6.2: Half-light radii of the galaxies in the MOS simulation scene (redshifts: Coe et al. (2006), r_h : Beckwith et al. (2006) or analytical as in Figure 6.1).

The integral is analytically solvable, and with the half-light radius defined by

$$I_{int}(r_h) = 0.5 I_{int}(R \rightarrow \infty)$$

we obtain the relation

$$k r_h = 1.67835.$$

The radial profile can therefore be written as

$$I(r) = I_0 \exp \left(-1.67835 \frac{r}{r_h} \right).$$

We plotted the relative profile $I(r/r_h)/I_0$ and the missing relative integrated intensity $1 - I_{int}(R/r_h)/I_0$ in Figure 6.3. At r_h , the profile has dropped only by 80%, and for a proper background subtraction, it will be necessary to extract the background signal in distances of at least $2 r_h$, where $I/I_0 < 0.05$. The shutter pitch in spatial direction is approximately 0.5 arcsec. A "1×3" slitlet should therefore only be used if $r_h < 0.13$ arcsec. Taking into account the PSF size of about 2 pixels at long wavelengths and a possible offset of the target from the shutter center, the actual brightness in the adjacent background shutters will be even higher.

From the plots we also determined the required extension of the galaxy images. In order to have a smooth fade-out at the edges and to keep enough integrated intensity, we constructed all objects out to $4 r_h$, where the relative intensity has decreased to 10^{-3} , and not more than 1% of the integrated flux is missing.

To introduce the ellipticity, we at first created a radially symmetric 2D image on a Cartesian grid with $r = \sqrt{x^2 + y^2}$ in units of r_h . The coordinates were then rescaled

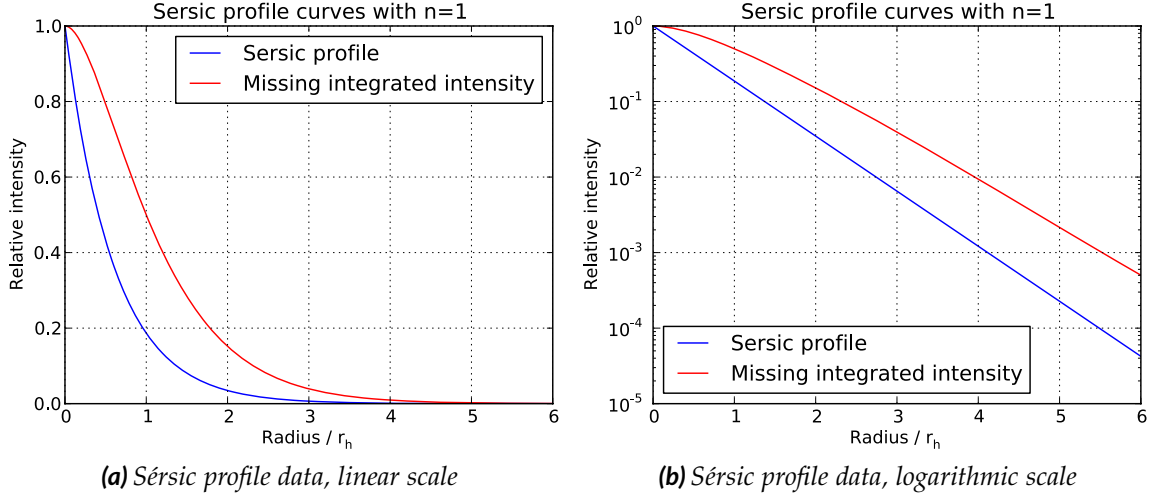


Figure 6.3: Sérsic profile curves with $n = 1$ depending on the half-light radius. The profile drops by 80% at r_h , while the missing integrated intensity decreases much slower.

with the ellipticity from the catalog $e = 1 - a/b$, where the semi-major axis is along the x -axis, and to the real extension:

$$x_{glx} = x \frac{r_h}{\sqrt{1-e}}, \quad y_{glx} = y r_h \sqrt{1-e}.$$

Finally, we set all pixel values outside $4 r_h$ to 0, and the images were normalized to a surface integral of 1.

Stretching the radial profile to an ellipse also changes the radially integrated intensity $I_{int}(R)$. We therefore plotted $I_{int}(R)/I_0$ for shapes with different ellipticities when constructed in the way described before, shown in Figure 6.4. At a given r_h , we overestimate the true size of highly elliptic galaxies, as the half-intensity is reached at larger radius instead. For correction we would need to shrink the galaxy shape to move its real half-light radius to the desired one. However, for ellipticities $e < 0.6$, the error in size is $< 15\%$. Only 5 objects in our sky scene exceed this limit, and we therefore decided not to correct the galaxy profiles.

For the input object collection, we created the 2D shapes with the catalog data. Where missing we set the ellipticity to 0.3 and the position angle to a random number. The sampling was set to 10 pixels within r_h . To study the potential problem of large sizes, we also plotted the images with an overlay of the actual shutter apertures at their position. Two examples at redshifts 1.388 and 4.866 are displayed in Figure 6.5 with the slitlet apertures in white. The objects have sizes of $r_h = 0.173''$ and $0.192''$, and ellipticities $e = 0.423$ and 0.424 respectively. Although not particularly large, the shapes drop only to a level of 10% when reaching the outer shutters, which are meant to extract the background signal.

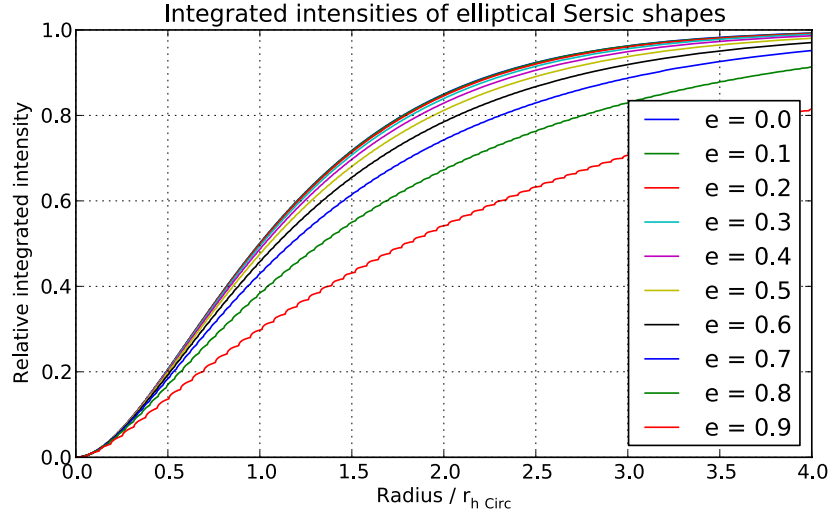


Figure 6.4: Relative integrated intensities for elliptical Sérsic shapes when constructed with the half-light radius of a circular profile $r_{h\text{Circ}}$. Up to $e = 0.6$, the error in the size is $<15\%$.

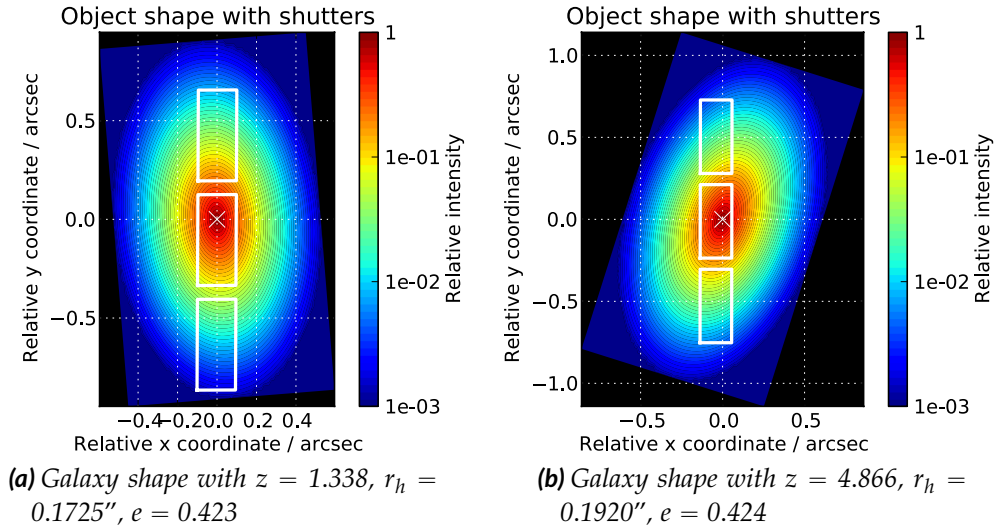


Figure 6.5: Galaxy contour images with a Sérsic profile in logarithmic scale with MSA slitlet overlay. In this examples, the object intensity does not drop to less than 10% in the outer shutters. A background singal extracted there will contain a significant amount of the source.

To obtain clean background spectra, we would need to use more distant shutters in a "1×5" slitlet. However, this collides with the initial scene creation to avoid spectrum overlap. Hence the object selection has always to be done taking into account the shape of the galaxies to select an appropriate shutter pattern.

Despite the encountered effects we continued to work with the existing scene. So far, the IPS has not been able to produce simulations with with extended targets and complex spectra due to inefficient source data and memory management. As a consequence, we only created exposures with the galaxies assumed as point-like sources, where the problem of sizes does not occur. This is however a strong simplification where the targets are much more concentrated, and their shape does not exceed the shutter aperture. In return, they appear brighter in the spectra, resulting in an increase of their SNR.

6.1.4 Galaxy spectra

NIRSpec is meant to record the spectra of these high-redshift targets, which are unknown a priori. To find proper spectra for the simulation objects, we used a catalog of 8000 galaxy models in $z = 0 \dots 8$ from Pacifici et al. (2012). They were calculated with a random distribution of mass, specific star formation rate, gas-phase oxygen abundance, and dust absorption. However, their mass can be scaled arbitrarily, which is equivalent to directly scaling the emitted flux. For all catalog spectra, apparent magnitudes in the same bands as the UDF data had been calculated.

For each object at redshift z_{Obj} we then selected a catalog spectrum by matching the band magnitudes m_X . To include the mass scaling without modifying the spectrum colors, we converted the magnitudes to spectral fluxes with

$$F_{\lambda X} = 10^{10-0.4(m_X+48.6)} \frac{c}{\lambda_X^2},$$

where λ_X is the effective wavelength of the filter band. We selected the spectra in the redshift range $z_{Obj} \pm 0.3$, and calculated a scaling factor w_s for each spectrum from the observed fluxes $F_{Obs X}$, their variances $\Delta F_{Obs X}^2$, and the spectrum fluxes $F_{s X}$:

$$w_s = \sum_X \frac{F_{Obs X} F_{s X}}{\Delta F_{Obs X}^2} / \sum_X \frac{F_{s X}^2}{\Delta F_{Obs X}^2}.$$

Then we set up the merit function

$$\chi_s^2 = \sum_X \frac{(F_{Obs X} - w_s F_{s X})^2}{\Delta F_{Obs X}^2}$$

and picked the catalog spectrum with the minimum value of χ_s^2 .

To examine the agreement between the UDF objects and the chosen spectra, we plotted a color-color diagram of both, shown in Figure 6.6(a). The overall match

between the observed and catalog data is very good, even at higher redshifts where the errors in the UDF data increase. Only for two very red objects with low redshift there is no well matching spectrum, possibly the measured J-color is questionable. To ensure that the constructed input galaxies are not too faint, we also plotted the brightest magnitude of the bands i, z, J, and H, which had been used to pick the objects from the UDF catalog (Figure 6.6(b)). Only three of them are now slightly fainter than 27 mag, all others are bright enough as required. All in all, the parameters of the observed and selected objects are in good agreement, and the created scene is very realistic.

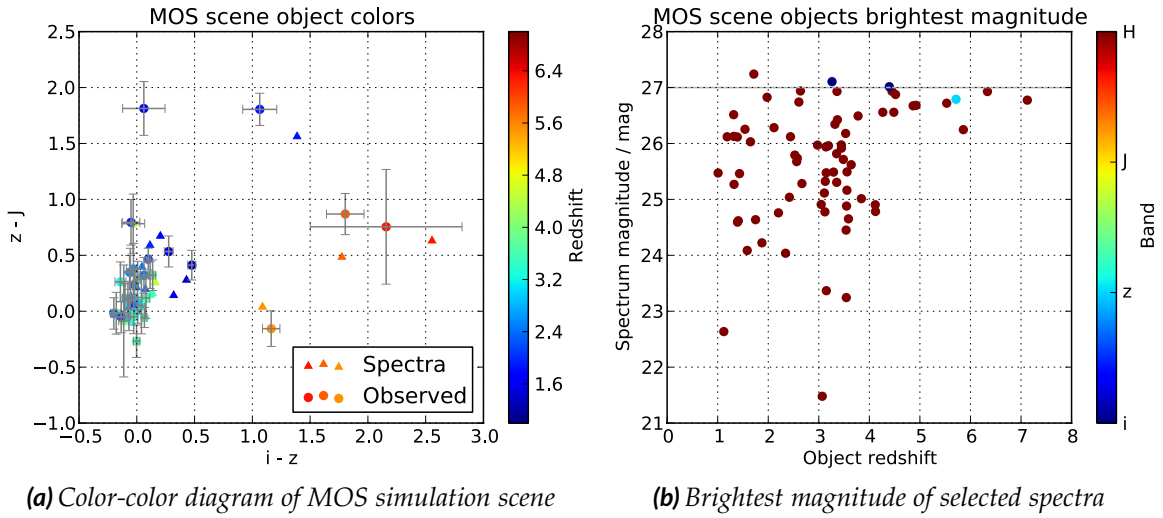


Figure 6.6: Parameters of MOS simulation scene objects. (a): Color-color diagram of the objects in the MOS simulation scene. Circles: Magnitudes as observed with errors. Triangles: Magnitudes of selected spectra from the catalog. In general the parameters match well apart for two very red objects at low redshift. (b): Brightest magnitudes of the selected spectra for the objects. Only three are a little fainter than the initial selection parameter of $m_{[i,z,J,H]} \leq 27$.

6.1.5 Exposure simulation

In the IPS, we assembled the instrument model from the verified as-built data collection. To circumvent a problematic and time-consuming spatial PSF interpolation, we put only a single wavefront error map from the FOV center for the optical modules instead of the field dependent aberrations. We created the electron rate maps using a typical MOS configuration with the CLEAR filter and the PRISM as disperser. The first exposure was done with the UDF targets as point sources with spectrally resolved spectra, and the respective MSA configuration. With the same MSA shutter

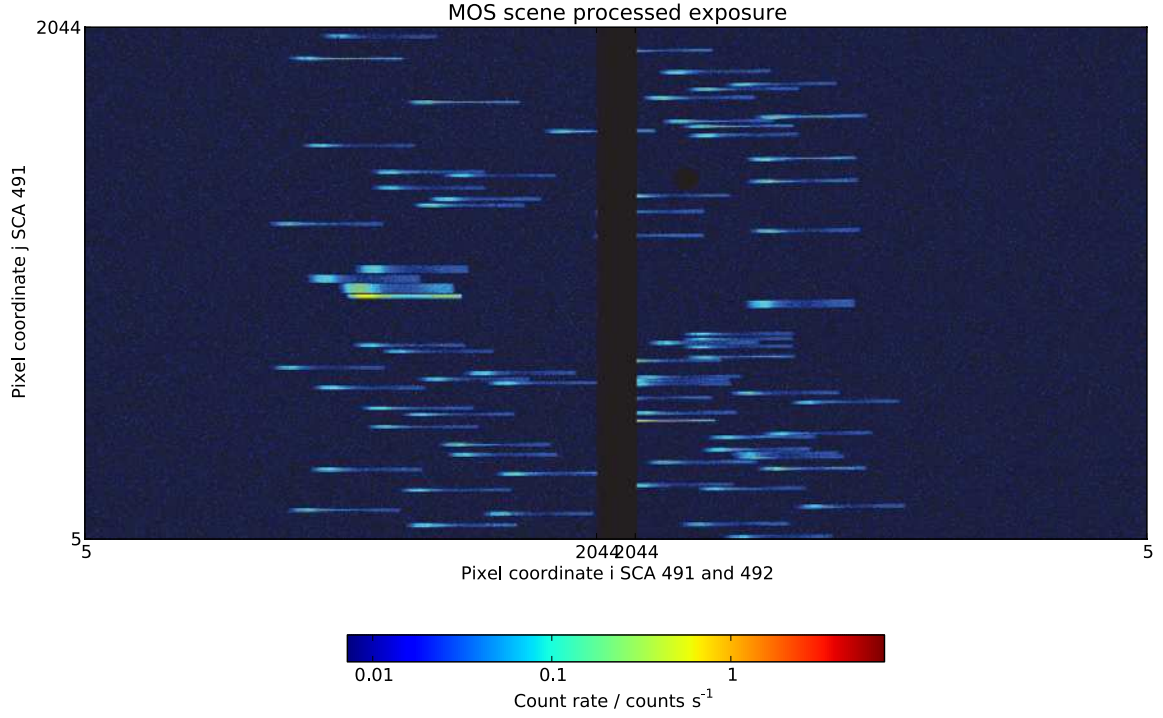
pattern, we also simulated electron rates of the Zodiacal light. We corrected both data sets with the factors found in section 5.3, and added them to a single noiseless electron rate file.

To simulate the readout and create a processed exposure we followed the way described in section 5.6, directly computing the count rates and noise from the electron rates. In the present case, the dark current maps for each detector contained random values with a mean and RMS as in the detector characterization. The pixel-to-pixel crosstalk kernels were also taken from the measurement reports, and the electron rates were convolved with them. The typical exposure configuration of a NIRSpec deep-field observation is a "22×4" MULTIACCUM pattern with $n_g = 22$ groups of $n_f = 4$ frames. We set the single-frame readout noise values to 22 and 19 e^- , which give a total noise for this pattern of about 6 e^- . The variances of the pixels were then calculated for a "22×4" exposure, and written into the fake processed file, along with the signal where we added the noise as random values from a Gaussian distribution of the same variance. Finally, we applied the gain of 1.453 e^-/ADU and 1.339 e^-/ADU for the two detectors to the signal and variances, and flagged bad pixels with the map extracted from the detector QE data.

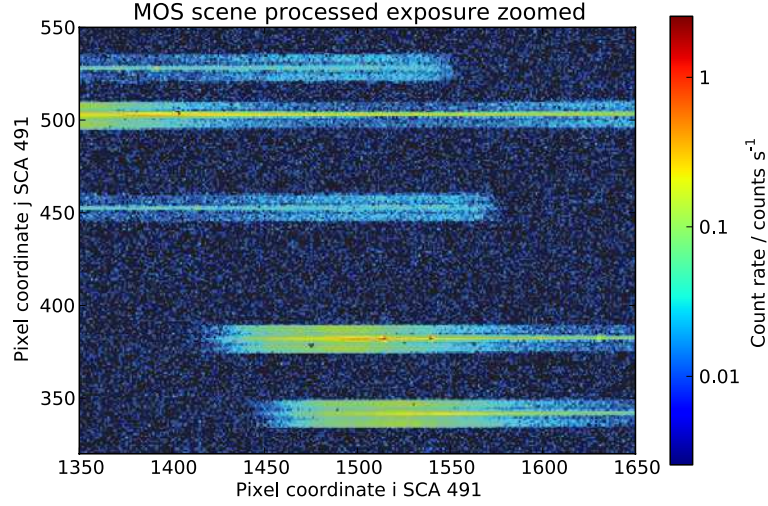
The full count rate maps of both detectors are shown in Figure 6.7(a). In the PRISM mode, the short spectra appear concentrated in the center part of the FPA area. The MSA spectra are located in the top and bottom half, while the always present spectra of the five fixed slits are visible in the center, four on SCA 491 (left array), and one on SCA 492 (right array). In the large overview, the dominant feature is the background radiation of the Zodiacal light, producing spatially extended spectra. Zooming closer into a region on SCA 491 (Figure 6.7(b)), one can discern the single spectra of the shutters, grouped in the "1×3" slitlets. In the central ones, there are the target spectra as thin lines with the continuum slightly above the background level, and some peaks originating from emission lines.

Upon detailed inspection of the scene, five objects are missing, which are close to the edges of the MSA quadrants. Two of them are outside of the detector area, and three are masked by the field stop (compare Figure 4.1). Obviously the field geometry has to be taken into account in the observation planning. Further optimization should be done to avoid spectra falling into the FPA gap (except for R2700, where the spectra spread over both detectors). In our example, significant parts of seven spectra are missing, and 3 are cut at wavelengths below 1 μm .

For the flatfield exposure, we created the electron rates with the instrument in auto-calibration mode using a broadband CAA source spectrum, and the MSA configuration of the sky observation. The CAA data has not been verified and the model is uncertain, therefore we optimized the readout parameters to achieve the best peak SNR level without saturating the detector. During the instrument tests we saw that the saturation level is primarily determined by the Analog-Digital Converter (ADC), and not by the pixel well capacity. Assuming a perfectly linear pixel response,



(a) Full detector count rate maps



(b) Zoom into region on SCA 491

Figure 6.7: Processed exposure of the MOS simulation scene in logarithmic scale. (a): Full image of both detector count rate maps. The MSA spectra are in the top and bottom half, while the fixed slit spectra are visible in the center. (b): Zoom into a region on detector 491. Clearly visible are the slitlet pattern made from three neighboring spectra. The target spectra are visible as thin lines in the center ones with occasional emission lines.

the maximum number of groups (with $n_f = 1$) can then be calculated from the ADC saturation $N_{max} = 65,000$ ADU, the approximate bias level $N_{Bias} = 10,000$ ADU, the gain $g = 1.453 \text{ e}^-/\text{ADU}$, the frame time t_f , and the maximum electron rate e_{max} to

$$n_g = \frac{(N_{max} - N_{Bias}) \cdot g}{t_f \cdot e_{max}}.$$

We determined the maximum electron rate in the flatfield simulation, and corrected it with the IPS error factor of 1.3. In our case we ended up with the maximum number of groups $n_g = 6$, and we created a processed exposure the same way as described before. The peak SNR value in the flatfield finally was then 270.

For an absolute radiometric calibration of the sky exposures, the in-orbit strategy foresees observations of reference stars to create a radiometric response function of the instrument. It is especially important to examine the throughout of the slits, where the diffractive losses increase towards the edges. To simulate the calibration, we created fake reference stars as targets for a special calibration exposure. The star spectrum was artificially set to a constant photon rate of $8 \cdot 10^8$ photons/s/m²/μm. In the IPS, we set the stars at the same location as the galaxies. Treating both as point-like objects, we could directly link the calibration spectra with the target data. We optimized the readout parameters as for the flatfield, and generated a processed exposure file with $n_f = 1$ and $n_g = 23$. The peak SNR of the pixels in the calibration data was then 240.

6.1.6 Spectrum extraction

All the spectrum extraction was done with NIPPLS. The procedure for the target exposure started with flatfielding the count rate maps and cutting the spectrum subarrays for each shutter. One example for a target is shown in Figure 6.8(a) with the shutter trace overlay. This reveals the spectrum curvature, while the strong slit tilt of the PRISM is masked due to the aspect ratio, and only noticeable upon close inspection when comparing the isowavelengths with the detector columns. The data was then rectified, where the spectral step size was determined as the minimum wavelength step in the subarray, and the spatial step was set to 0.1 arcsec. The spectra of the two outer shutters were processed the same way and rectified with similar step sizes. The 2D background data was set as the mean of both. Subtracting it from the center target shutter data, we obtained the pure rectified target spectrum as in Figure 6.8(b).

The overall shape of the extracted spectra is heavily influenced by the flatfield maps. Towards the edges of the spectral range, the CAA spectra drop considerably and produce only low count rates, which in turn boost the flatfielded data. At the short wavelength edge, the CAA signal is so low that these pixels are flagged with "no flatfield correction". The 2D spectrum shows that most of the target signal is

concentrated in the center. The pixels at ± 0.2 arcsec hardly contain any relevant data but rather noise. The objects were put within ± 0.25 of the shutter apertures. At $5\text{ }\mu\text{m}$, the diameter of the first Airy-ring of a PSF on the detector is 3.8 detector pixels. To create the final 1D spectrum it is therefore acceptable to collapse only over the five pixels as seen in the example, which is about the shutter aperture, although some other 2D spectra were constructed with one more row on each side.

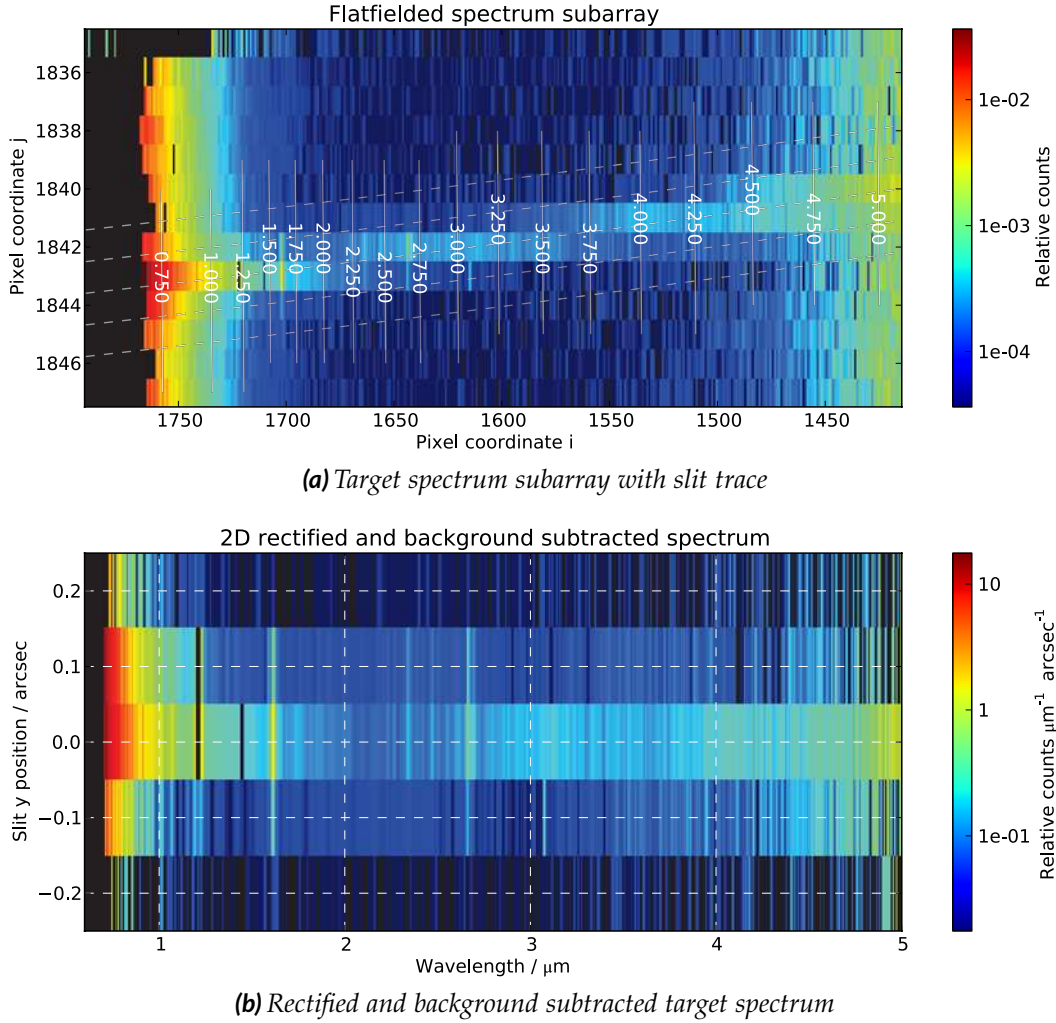


Figure 6.8: Images of two spectrum extraction steps. The high relative values at the spectral range edges are caused by low flatfield count rates, which become unusable at short wavelengths. (a): Spectrum trace subarray after flatfielding. The slit trace is drawn on top as a grid with isowavelengths and the traces of the relative positions $[-0.5, 0.25, 0, 0.25, 0.5]$ in the aperture. The spectrum curvature is evident, while the slit tilt is hard to see due to the aspect ratio. (b): Rectified and background subtracted 2D spectrum. The target spectrum is clearly visible in the center. The pixels at $\pm 0.2''$ hardly contain any signal.

This significantly damps the noise while incorporating the major part of the signal, especially at shorter wavelengths.

Before continuing with the targets, we created the calibration spectra, which were processed the same way as described above. The final 1D calibration data was generated by collapsing the 2D spectra over the interval of $-0.25 \dots 0.25$ arcsec. To reach absolute radiometric levels we then divided the 2D rectified data by the individual calibration spectrum, taking into account the spatial dimension, and multiplied it with the spectrum of the fake reference star. Collapsing the data over $-0.25 \dots 0.25$ arcsec, we finally obtained the 1D absolute target spectra, which also contained all noise and quality flag information.

6.1.7 Results and discussion

The data of a sample of galaxies through the redshift range and with different magnitudes is plotted in Figure 6.9. On the left we always show the input spectrum, and the equivalent level of the Zodiacal light, integrated over the solid angle of a nominal resolution element ($0.2'' \times 0.1''$). On the right the figures contain the extracted spectrum, and the input rebinned to the nominal resolution of the instrument, along with the SNR curve.

Overall, the observability decreases with the brightness of the object over the background. In the single 945 s exposure, the continuum can only be reliably detected from the brighter galaxies to about $mag_H = 25$. Nevertheless it is hard to predict the final data quality only from the HST NICMOS H-band magnitudes, whose filter center wavelength is at $1.61 \mu\text{m}$. Comparing Figure 6.9(a) and 6.9(c), both have almost the same magnitude, with the latter being even a little fainter. However, the brightness of the second object is determined just before the Balmer break, the continuum rises considerably afterwards, and the observation in general yields a higher SNR than for the first object.

Comparing the original and rebinned input, we see that the extracted data often exceeds the peaks of the lines, because the objects were treated as point sources. Hence the size of their PSF on the detector is smaller than the resolution element, which was used to rebin the input, and sharp spectral features are better resolved. It also becomes clear that the PRISM does not resolve emission lines if they are too narrow or too faint (e.g. in Figure 6.9(b)). Should they not be blended by the PRISM resolution, they can on the other hand be detected even at very high redshifts, as seen in Figure 6.9(e). While in this case the continuum is too faint, the lines still stand out with $SNR > 5$. However if there is no emission feature, high-redshift objects will be hard to observe, and definitely need multiple exposures (Figure 6.9(f)).

One particular feature in Figure 6.9(e) is a false emission signal at $4.55 \mu\text{m}$. Upon close inspection it becomes clear that it has no extension as the real emission lines, but is only a single value in the spectrum. It originates from bad pixels in one column of the output, where the source and calibration spectra are the result of

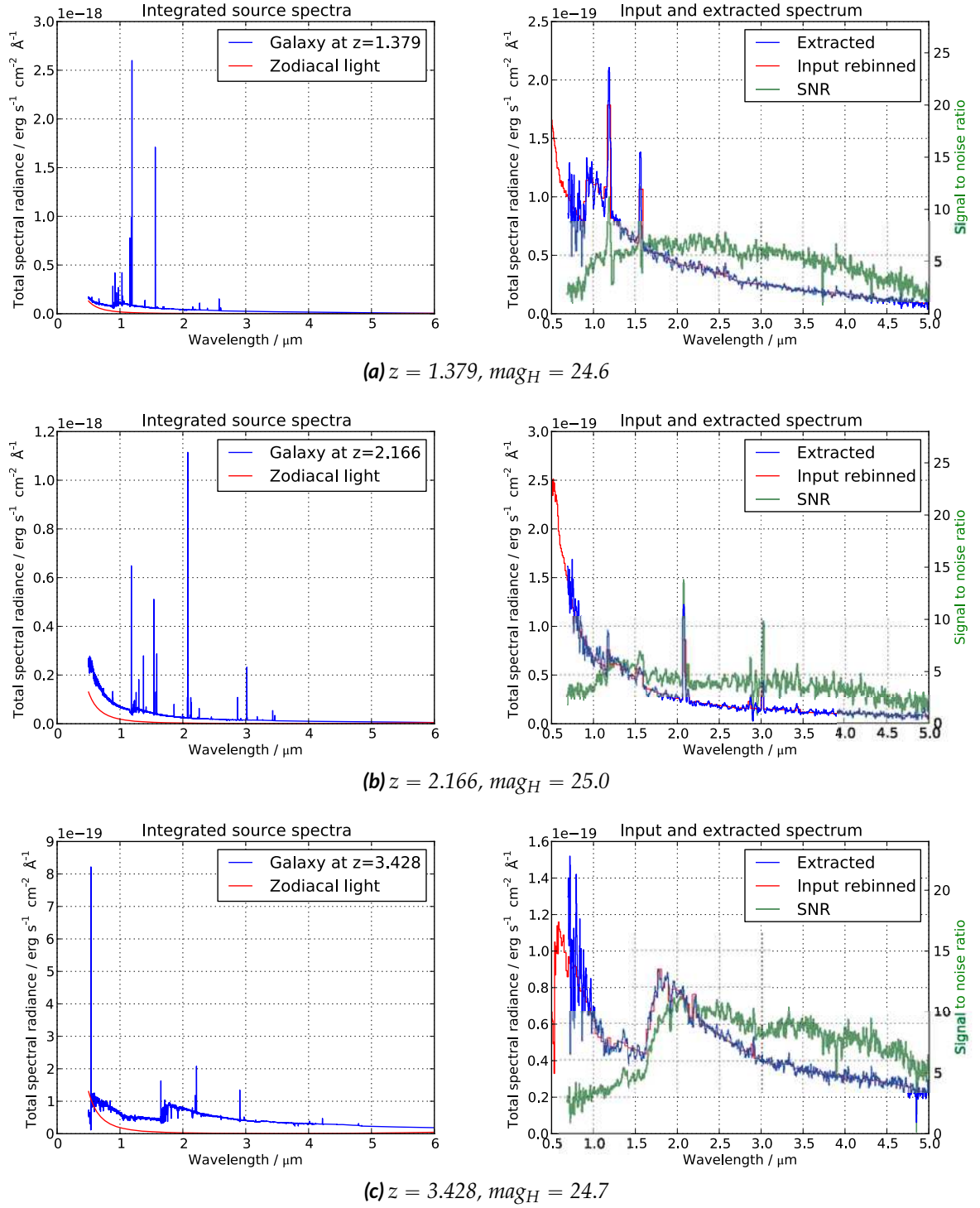


Figure 6.9: Comparison of input and extracted galaxy spectra with different redshifts and magnitudes. Left: input spectrum and equivalent Zodiacal light. Right: Comparison of extracted and rebinned input spectrum at nominal resolution. Continued on next page.

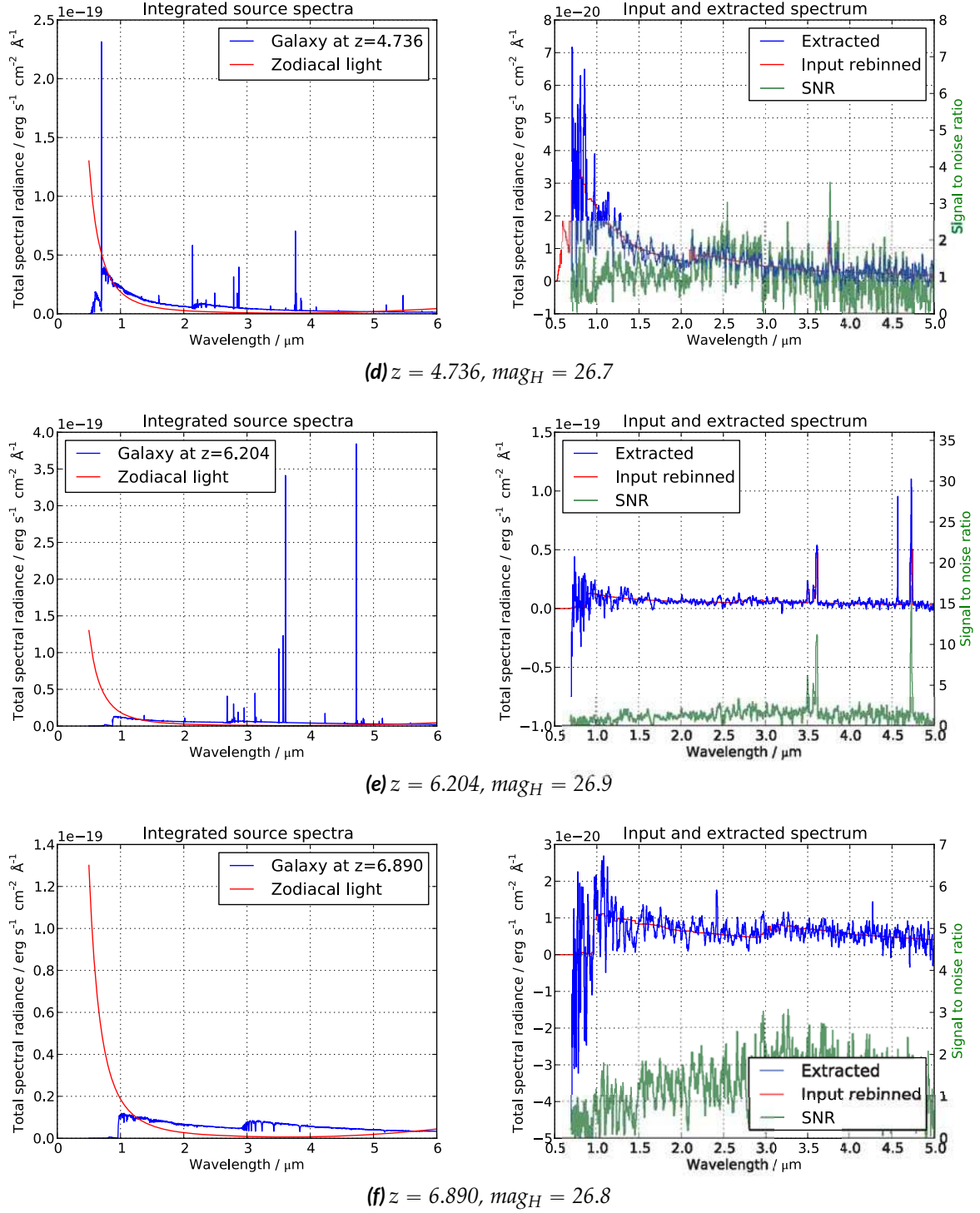


Figure 6.9: Comparison of input and extracted galaxy spectra with different redshifts and magnitudes. Left: input spectrum and equivalent Zodiactal light. Right: Comparison of extracted and rebinned input spectrum at nominal resolution.

the pixels at the spectrum edges. Receiving little signal and having a high noise level, the division of the small numbers cause the peak seen in the result. However, also from the SNR data it becomes clear that there is no real emission present. This emphasizes the need to properly track the variances through the extraction.

Of course, there are possibilities to increase the SNR, as shutter dithering for a better background subtraction, and tuning of the single extraction parameters, e.g. reducing the resolution of the output. Especially between 1–2 μm , the wavelength interval of one detector pixel is up to 4 \times as wide as the final resolution of the rectified data. If it is acceptable to lose resolution towards the red end of the spectrum, the fidelity of the continuum signal could be improved to some extent.

For all these efforts, the IPS is capable of producing realistic exposures, which can be easily constructed with the input interface. Using the NIPPLS framework, one can then study the impact of different extraction techniques, and even plug in non-standard routines, without having to deal with the instrument calibration and its complex geometry.

6.2 Exoplanetary transits

6.2.1 Introduction

Since the discovery of the first extrasolar planets in the 1990s, this scientific domain has grown rapidly. Up to now, there have been 760 planets detected⁴, where 230 of them are transiting their host stars. There are two different types of transits: One where the planet crosses in front of the host star (primary transit), and where the planet passes behind it (secondary eclipse), schematically shown in Figure 6.10. The actual duration of the events depends in the inclination of the orbit and its eccentricity. It is even possible that a planet shows only one type of transit event.

During a primary transit, the stellar light is attenuated by the geometrical obscuration of the planet body, and the change in brightness depends on the ratio of the area of the stellar and planetary disc. Even more subtle differences at different wavelengths can be caused by the filtering of the light in the upper atmosphere of the planet. Shortly before and after a secondary eclipse, in addition to the stellar light one can detect the self-emission of the planet in the infrared, or reflected stellar light in the visible spectral range. When the planet is then hidden behind the star, it leads to a dip in the lightcurve of the system.

The transit effects therefore allow a more detailed study of the planet characteristics, as atmospheric composition or surface structures, by comparing the stellar signal during and out of the transit event. Such observations have successfully been done with HST and Spitzer (Charbonneau et al., 2002, 2005), and even ground based telescopes (Bean et al., 2010).

⁴<http://exoplanet.eu>, as of 29.02.2012

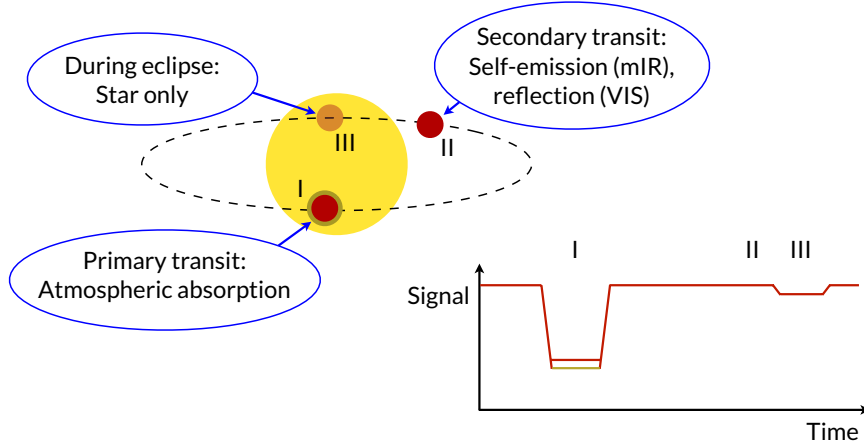


Figure 6.10: Scheme of exoplanetary transit events and a corresponding lightcurve. When the planet passes in front of the star (I), the stellar light is reduced by the geometrical obscuration of the planet body and a potential atmosphere. During the secondary eclipse (III) the planet is invisible, while before and after (II) it contributes to the brightness of the system with self-emitted radiation in the IR, or reflected stellar light in the visible.

The design of NIRSpec was initially not adapted to this kind of exposures, and the large A₁₆₀₀-aperture was introduced after the increasing demand to enable exoplanet spectroscopy. The large size is needed to avoid truncation of the PSF in the slit, and reduce the diffraction pattern at the GWA pupil. This way, the noise introduced by pointing uncertainty diminishes, which is critical to detect the very small brightness differences between the transit phases.

We used the IPS and a special as-built instrument model to explore NIRSpec's capabilities to study exoplanetary systems. First, in subsection 6.2.2 we determine upper magnitude limits of the host stars, which can be observed at all without saturation. Second, in subsection 6.2.3 we simulate in detail the losses caused by the truncation of the PSF in the slit and the diffraction pattern at the disperser, depending on the position of the source inside the aperture. Linking it with the expected pointing of the telescope, we give an estimation of the noise contribution to single exposures. Third, we study the impact of fast detector saturation on the effective exposure times during transit events in subsection 6.2.4, followed by a discussion of the signals and expected noise contributions in subsection 6.2.5. After deriving formulas for the SNR of different transit observations, we simulate the exposures of exemplary known host stars HD189733 and GJ1214, and present the SNR data for the characterization of the planets in subsection 6.2.6 and subsection 6.2.7. Finally, in subsection 6.2.8 we analyze the possibility to detect spectral features of an Earth-sized planet's atmosphere around a close M-dwarf.

For all the simulations in this chapter, we assembled a dedicated instrument model

for the exoplanetary science case. It is largely identical with the one for the MOS deep field described in subsection 6.1.5, apart from two differences: The wavefront errors of the FORE and COL were specifically created at the FOV position of the A_1600 slit. All the stars will be observed in this aperture, which determines the optical path up to the GWA. In the CAM, we also set the nine field-dependent WFE maps to achieve a high fidelity of the PSF at the detector.

Besides, the detector QE was set to a flat 80% efficiency with a cutoff at $5.5\text{ }\mu\text{m}$, matching the requirement. The final NIRSpec detector will be different from the one characterized in the FM1 calibration, but at least the mean QE curve will be similar. We chose a flat spatial distribution to enable an easier calculation of the instrument efficiency without having to use the local QE values. Furthermore, it eliminates pixel-to-pixel variations, which would make the spectra without flatfield correction look very noisy. Assuming an operation scenario where the NIRSpec configuration is not changed during the in- and out-of-transit observation, the spectrum will always fall at the same place on the detector (apart from pointing jitter, which is negligible here). In the following data processing, we calculate ratios of the signal from both event phases, and a local QE then always cancels out. Therefore, the assumption of a uniform detector efficiency has no impact on the conclusions, but simplifies our analysis.

6.2.2 Host star brightness limits

NIRSpec is primarily designed to observe very faint objects in the far distant universe, requiring a high photon collecting power. Planet host stars on the other hand are the complete opposite, being bright, very close, and point-like, leading to high and very concentrated signals. This means that detector saturation can be a serious restriction of the observable stars.

To determine upper brightness limits, we created fake target stars with a constant spectrum in photons/s, which correspond to a known magnitude mag_0 in one of the bands J, K, and L. The pivot wavelengths of these colors 1.25, 2.2, and $3.4\text{ }\mu\text{m}$ lay close to the center of the three scientific bands (1.4 , 2.35 , and $3.95\text{ }\mu\text{m}$), and are representative for them. We simulated exposures of the stars in the A_1600 slit with all NIRSpec gratings without any background, which is negligible in the case of very bright objects. We corrected the electron rates of the PRISM for the IPS error, and multiplied them with $1/0.85$ as an optimistic safety margin to take into account the possible absolute and relative error of the model seen in subsection 5.5.3. We created a noiseless processed exposure file, convolved the detector data with the crosstalk, and divided it with a gain of $1.4\text{ e}^-/\text{ADU}$.

Observations of single stars will be done in window-mode, where only a subarray of the detector is read. The two dimensions Δi and Δj can be configured as powers of 2 between 8 and 2048. From the detector testing, it became clear that in horizontal direction, one wants to include the reference pixels at the detector edges. These

pixels are not sensitive to light, and serve as input for the preprocessing of the readout. Without using their information, the quality of the data is severely limited, therefore we always set Δi to 2048. We saw from the traces that a useful size is $\Delta j = 32$, which is necessary to capture the curved spectra in their full vertical extent. The frame time as the duration of one readout process can be calculated to

$$t_f = (\Delta i + 1) \cdot (\Delta j + 12) \cdot 10^{-5} \text{ s.}$$

For our default values, $t_f = 0.90156 \text{ s}$.

To enable a determination of the count rate, the readout cube has to contain at least two non-saturated groups (compare Figure 5.20). With only one frame per group ($n_f = 1$), the duration of one group readout is equal to t_f . Assuming a perfectly linear detector behavior, the dynamic range of the ADC is about 55,000 ADU. To avoid saturation in the second group, this number of counts must be reached in not less than $2 \cdot t_f$.

After cutting the spectrum subarrays from the processed files, we determined the maximum count rate r_{max} in each detector column. The level of the PRISM data varies strongly due to the changing spectral resolution. To obtain a meaningful value in the photometric band, we restricted the spectral range in this case to intervals of $\pm 0.25 \mu\text{m}$ around the pivot wavelengths. To achieve the maximum allowed count rate, the input spectra would need to be scaled with

$$s = \frac{55,000 \text{ ADU}}{2 \cdot t_f \cdot r_{max}} ,$$

and the limiting magnitude mag_{min} is then

$$mag_{min} = -2.5 \log(s) + mag_0 .$$

In Table 6.1 we show the resulting values for each resolution in the photometric bands. With the gratings, the brightest stars can have magnitudes down to 5.7 in L, while at shorter wavelengths, only fainter stars are observable. The PRISM is also most critical in J, where the spectral resolution leads to very high count rates. If saturation is unproblematic in the range with the highest instrument efficiency (around the band center wavelengths), the limits may be pushed to some extent, but one loses the information in this interval.

In the end, these values can still only be approximate guidelines for now. First of all, the actual saturation limit in the band depends on the shape of the stellar spectrum, while we assumed a constant photon rate. Especially in the PRISM mode with its varying spectral interval, the stellar type of the target will have a strong influence on the brightness limits. Besides, the final efficiency of the telescope and the instrument is unknown. We assumed an OTE throughput as required, while the hardware eventually may be more efficient. On the other hand, we added a (here pessimistic) safety margin on the NIRSpec data. If the actual throughput is as

Table 6.1: Limiting magnitudes of stellar spectra to avoid detector saturation. Values calculated for a 2048×32 detector subarray readout.

Resolution	mag_{min} in band		
	J	K	L
R100	12.2	10.3	8.5
R1000	8.8	7.6	6.7
R2700	7.7	6.6	5.7

predicted by the as-built model, the measured count rates will be only 85% of the currently simulated ones. This would mean a reduction of the limiting magnitudes by 0.18 mag.

Nevertheless, this calculation shows that there is an important restriction on the observability of planet host stars. Especially the (so far) best studied ones are very bright, and may eventually be out of reach for NIRSpec.

6.2.3 Noise from pointing jitter

The ratio of the stellar flux to the signal of a planet hidden in the spectrum is typically $\approx 10^5$. At this level, different effects which otherwise cause no problems in the observation can introduce significant noise terms. One of them is the variation of the signal due to the slit- and diffraction losses, changing with the telescope pointing.

This behavior is caused by two phenomena: First, the PSF is truncated at the MSA aperture, which leads to a loss of intensity. Depending on the shape of the wings, by moving inside the slit the throughput varies by a certain amount. Second, despite the size of the A_1600 slit, there is a diffraction effect, producing an image of the pupil at the GWA where parts of the intensity are drawn outside of the disperser aperture. The pupil plane pattern is sensitive to the absolute position inside the slit, and a movement of the source has an impact on the diffraction losses.

To evaluate the influence of the pointing onto the measurement of small planetary signals, we used the standalone PSF computation in the IPS. We moved the source along each axis on a grid of 11×11 points in the slit with a side length of 35 mas. For a proper spectral sampling of the losses, we did the calculations on a wavelength vector linear in Strehl in the scientific band. This ensured a gradual distribution of intensity from the PSF core to the wings. It also increased the coverage at short wavelengths, where the speckle pattern in the outer regions of the PSF changes faster.

The final spatial sampling of the PSF data was set such that the wavefront errors

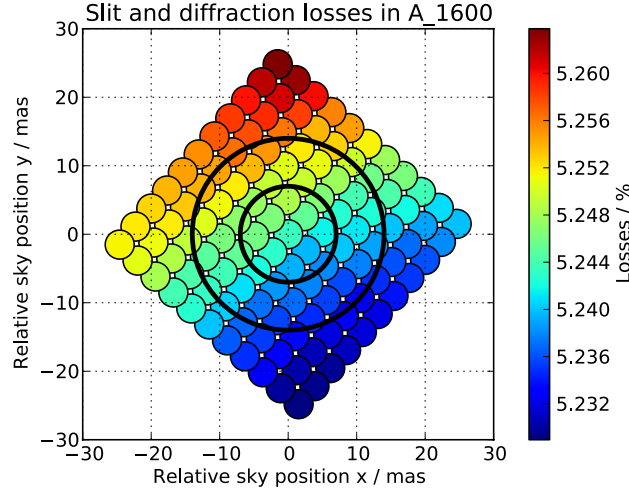


Figure 6.11: Map of combined slit- and diffraction losses in the A_1600 slit for the grating G235H at $2.45\ \mu\text{m}$. The absolute loss level is about 5%, and varies on the grid with about 0.03% peak to valley. For reference, the black circles denote 7 and 14 mas, corresponding to 1 and 2σ of the allowed pointing jitter during 10,000 s.

were resolved with $n_p = 300$. With a FFT matrix size of $N = 2048$ pixels, this resulted in $n_x = 8.3$ pixels in the Airy radius, sufficiently sampling the small-scale structures.

At each position inside the slit and each wavelength, we then simulated the PSF up to the FPA, and extracted the total losses (slit and diffraction) from the file header. One map for the grating G235H at $2.45\ \mu\text{m}$ is shown in Figure 6.11. Although the slit aperture is more than $8\times$ larger than an Airy disc, the losses are still about 5%. The peak to valley variation on the grid is about 0.03%.

The pointing stability of JWST is required to be better than 7 mas (1σ) during a 10,000 s exposure. In Figure 6.11, the black circles mark the 7 and 14 mas distances. As we have seen in the previous part, the brightness of the stars will require short exposures in window mode. This means that we could not directly apply the long-term stability to this situation. While throughout 10,000 s the jitter causes a random distribution of pointing vectors, during one short exposure for the stars it can be described by a simple linear drift by a certain angular distance. We assumed that the spatial variation of the signal depends only on the relative movement inside the slit and not the absolute position, as long as the guiding system keeps the object within the allowed long-term stability limit. The relative noise in one exposure introduced by the movement in a random direction is then the RMS of the throughput on a circle at this radial distance relative to the value in the center. We calculated these variations for angular drifts up to 7 mas, and show one contour map of the G235H grating in Figure 6.12.

The noise values depend strongly on the wavelength. The diffraction pattern of

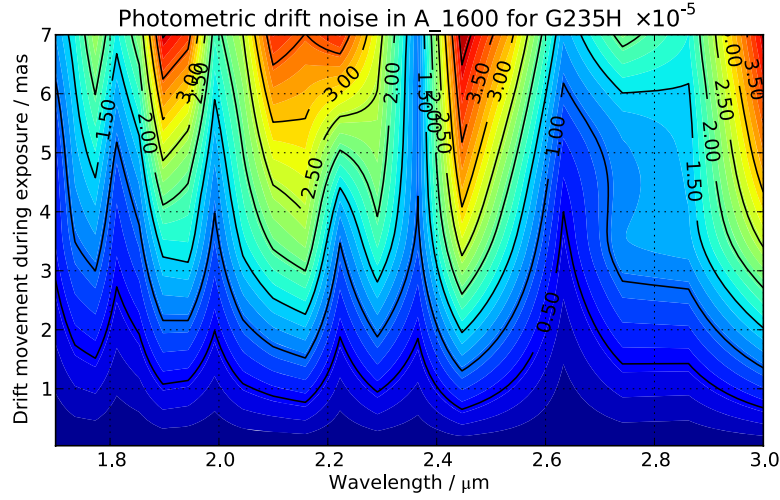


Figure 6.12: Relative photometric noise in the A_1600 slit with G235H introduced by radial drifts in a random direction during one exposure. The variations originate from the actual diffraction pattern of the PSF at MSA and pupil at GWA. Noise below 10^{-5} is only possible with drifts below 1 mas. At 7 mas, the maximum values are about $4 \cdot 10^{-5}$.

the PSF at MSA and the pupil at GWA changes with wavelength, and so do the losses when truncating the intensity. This can lead to abrupt oscillations as between 2.4 and 2.5 μm . To reach a noise floor of 10^{-5} , the drift would have to be less than 1 mas. This is obviously a severe restriction, and unlikely to be achieved. However, at 7 mas, the maximum value is about $4 \cdot 10^{-5}$, and still in the tolerable range.

For an estimation of the noise contribution in the simulations, we adapted the pointing requirement of NIRCcam for timescales of a few seconds, which is 3.5 mas in line of sight and roll stability (Blackmore et al., 2011). Both values are defined relative to the guide star, which is located in the guider FOV (see Figure 1.3). The distances between the NIRCcam and FGS FOV, and the A_1600 and the guider is approximately equal and we used the same numbers for our calculations. While line of sight jitter is a movement in a random direction, roll will cause the spacecraft to rotate around the guide star location. Both effects are independent, and we chose a final drift length of $\sqrt{3.5^2 + 3.5^2} \text{ mas} = 5 \text{ mas}$.

As noted before, the spectral behavior of this noise depends strongly on the diffraction pattern, and therefore the wavefront errors. While we took great care to construct them as accurate as possible for NIRSpec, the OTE data is only an assumption. This is even worse as it provides the dominant part of the WFE (RMS: 140 nm), while the FORE optics RMS is only about 30 nm, which is 5% in quadratic relations. On top of that, the truncation of the PSF and the slit diffraction happens at distances far from the core, where the mid- and high-frequency parts of the wavefront errors are relevant. For the OTE, these contributions are barely modeled,

Table 6.2: Mean relative noise in short exposures of point sources in the A_1600 slit, calculated with a random radial drift of 5 mas for each scientific band. The value for the R100 PRISM is valid over the 0.6–5 μm range.

Resolution	Relative noise $\times 10^{-5}$		
	band I	band II	band III
R100	2.242 (in 0.6–5 μm)		
R1000	1.705	2.017	2.552
R2700	1.622	1.865	2.273

no irregular patterns as manufacturing errors had been introduced. Considering that the NIRSpec FORE WFE maps contain quite a few of these irregular and small-scale features, the PSF at the MSA can be considered representative, but the real speckle pattern is unknown. Therefore we see the obtained loss data as realistic, but not definitive. To avoid stating too large noise in parts of the spectra, we averaged the data at 5 mas drift movement on an equally spaced wavelength vector. The values are shown in Table 6.2, overall the mean noise is in the range $2 \cdot 10^{-5}$, depending on the instrument mode.

6.2.4 Effective integration times

During the discussion of detector saturation in subsection 6.2.2 we already saw that for bright stars, the readout has to be done with only a few groups per exposure. In this case, there is another effect impacting the final SNR: the reduction of the effective exposure time due to readout overheads.

To determine the readout parameters for an exposure, we extracted the maximum count rate r_{max} . As before, the maximum number of groups is then

$$n_g = \text{floor} \left(\frac{55,000 \text{ ADU}}{n_f \cdot t_f \cdot r_{\text{max}}} \right),$$

and stars are only observable if $n_g \geq 2$. Before each exposure the detector is reset with n_r reset frames. During a transit with the duration t_{trans} , the maximum number of exposures possible is therefore

$$n_e = \text{floor} \left(\frac{t_{\text{trans}}}{(t_f \cdot n_f) n_g + t_f \cdot n_r} \right)$$

To minimize the readout overheads, we set $n_f = 1$ and $n_r = 1$.

The count rate fitting is done between the first and the last group, which means that the first group does not contribute to the exposure time. The effective exposure time during one transit is therefore

$$t_{eff} = n_e \cdot t_f \cdot (n_g - 1).$$

Combining the influence of the reset time and the ramp fitting, with a small number of groups the effective exposure time can be much shorter than the actual transit time. The previous formulas can be merged to

$$t_{eff} \leq \frac{n_g - 1}{n_g + 1} \cdot t_{trans} ,$$

and in the extreme case of $n_g = 2$ we see that $t_{eff} \leq 1/3 \cdot t_{trans}$. This has a direct impact on the achievable SNR of the spectra.

6.2.5 Signals and noise

Exposure data

To simulate an exposure, we generated a noiseless fake processed file. The arrays were convolved with the crosstalk kernels, but left in electron rates and not multiplied with the gain. We then determined the maximum possible number of groups from the peak electron rate.

Keeping the original resolution, we extracted the spectra as irregular type "sum" in each detector column. To include the outer parts of the PSF, in spatial direction we added the content of the 16 pixels covering the slit aperture. For a single exposure, the total accumulated electron rate in a column is the stellar signal r_i with the variance σ_i^2 .

For a single event, the average electron rates during the transit phases R are derived from the n_e exposures as

$$R = \frac{1}{n_e} \sum_{i=1}^{n_e} r_i ,$$

and their variance is

$$\sigma_R^2 = \frac{1}{n_e^2} \sum_{i=1}^{n_e} \sigma_i^2 .$$

Transit signals

We set R_i and R_o to the average rates in and out of transit. During a primary transit, the signal to measure is the dip in the lightcurve with relative depth

$$d_p = \frac{R_o - R_i}{R_o} = \frac{\Delta R_p}{R_o} , \tag{6.1}$$

which is equivalent to $R_i = (1 - d_p)R_o$. The loss of the signal of the planet in the secondary eclipse causes a drop relative to the stellar signal by

$$d_s = \frac{R_o - R_i}{R_i} = \frac{\Delta R_s}{R_i}, \quad (6.2)$$

equal to $R_i = (1 + d_s)R_i$.

If the stellar light in the primary transit is filtered by a planetary atmosphere, it causes an additional reduction by d_A on top of the planet signal d_p . Then the rates are related as $R_i = (1 - d_p - d_A)R_p$, and the atmospheric signal alone is

$$d_A = \frac{R_i}{R_o}(1 - d_p). \quad (6.3)$$

d_p can be measured in other spectral regions as for the simple transit.

In all three cases, we take ratios of electron rates in the same detector column. As mentioned before, the usage of a flat QE map in the simulation has no impact on the results, the relative QE variations cancel out.

Background subtraction

To assess the influence of the Zodiacal background, we compared the variance introduced during the background subtraction with the intrinsic variance of the stellar spectrum. The resolution element in the A_1600 slit has the solid angle $d\Omega \approx 0.1 \times 1.6 \text{ arcsec}^2$. Integrating the input spectrum of the spatially extended Zodiacal light over this area, we obtained the spectral photon rate q_{Zod} . Comparing it with the input spectra of the stars in our simulations, the typical levels are $q_{Star}/q_{Zod} \geq 10^5$. In the extraction, the spectra are summed in 16 pixels along the spatial direction, and so is the background. Therefore we can assume a ratio of the count rates $r_{Star}/r_{Zod} \gtrsim 10^4$. This means that the background creates an additional rate on the 10^{-4} level.

When writing the rates in Equation 6.1 and 6.2 as the sum of the star and background, the latter only remains in the denominator. However, this value is then $R_{Star}(1 + 10^{-4})$. While for a precise value of d in the real observation one will want to subtract it, we do not simulate it in the exposure, as it does not contribute significantly to the electron rates.

Instead we evaluate the noise contribution from the background subtraction. In the data processing, this happens as

$$r'_{Star} = r_{Star} + r_{Zod} - r_{Zod},$$

where the first two terms originate from the target exposure, and the third one from the background exposure. The new variance is then

$$\sigma_{Star}^2 = \sigma_{Star}^2 + 2 \cdot \sigma_{Zod}^2.$$

In the input spectrum, only with Poisson noise and summing the Zodiacal light over 16 pixels, this is equivalent to

$$\sigma_{Star}^2 = Q_{Star} + 32 \cdot Q_{Zod} \approx Q_{Star} \cdot (1 + 10^{-4}).$$

The new SNR of the stellar spectrum is therefore

$$\frac{Q_{Star}}{\sigma_{Star}'} = \frac{Q_{Star}}{\sqrt{Q_{Star} \cdot (1 + 10^{-4})}} = \frac{Q_{Star}}{\sigma_{Star}} \cdot \frac{1}{\sqrt{1 + 10^{-4}}} = \frac{Q_{Star}}{\sigma_{Star}} \cdot \frac{1}{1 + 5 \cdot 10^{-5}},$$

i.e. the SNR changes only by a factor of $< 10^{-4}$. Hence we simulated the observations without Zodiacal light and also assumed no impact on the spectrum variance.

A similar reasoning is valid for the dark current, reaching about the same electron rate levels as the sky background. We do not take it into account in the simulation, and as shown here, this has no significant impact on the noise itself.

Pointing jitter

By maximizing n_g , we almost reach saturation in the brightest pixels. As the last group will not be read at exactly the saturation limit, we assume a typical maximum charge of 50,000 ADU or $N_e = 70,000$ electrons. In a photon-noise limited exposure, the relative variance of the accumulated charge is then simply $\sigma_{N_e}^2 = N_e$. The change in signal due to pointing jitter can be seen as a rescaling of N_e with a factor j , giving the new rate

$$N_e' = N_e \cdot j.$$

The jitter has the standard deviation σ_j , listed in Table 6.2. For multiple exposures the jitter fluctuations level out, and the mean is $\bar{j} = 1$. The effect on the variance of N_e' can be expressed with

$$\frac{\sigma_{N_e'}^2}{N_e'^2} = \frac{\sigma_{N_e}^2}{N_e^2} + \frac{\sigma_j^2}{\bar{j}^2}.$$

On average for different exposures, and at best with the maximum $N_e = 70,000$, it is then

$$\frac{\sigma_{N_e'}^2}{N_e'^2} = \frac{1}{70,000} + \sigma_j^2.$$

While the photon noise based term is $1/70,000 = 1.43 \cdot 10^{-5}$, the variance contribution of the jitter noise is considerably smaller with $\sigma_j^2 \approx 4 \cdot 10^{-10}$. For lower electron numbers, the first variance term becomes even more important. Hence it is safe to assume that the pointing uncertainty has no impact on the signal quality of a single exposure.

The drift on longer time scales however affects the averaged exposures. If the mean of the absolute pointing in and out of transit is different, the two rates will be

offset by a certain amount. The relative error introduced here can also be extracted from Figure 6.12 at the appropriate drift distance.

Using n_e spectra, the relative variance of the final rates caused by Poisson noise is $1/70,000 n_e$. With average transit durations of 3000 s and $n_f > 2$, there are less than 1000 exposures per transit phase. Therefore the relative variance is still in the range of 10^{-8} , and considerably higher than the drift term.

Obviously, the A_1600 aperture is designed large enough that pointing uncertainties play no role in high-SNR observations of stars. Neither on short timescales of a few seconds, nor during the length of a single transit event, the PSF truncation and diffraction loss variation cause a significant noise term. In both cases, the dominant factor is always the Poisson noise of the signal. Only when combining 10,000 exposures or more, the relative variances become comparable. If the mean absolute pointing for that many exposures can be kept constant by the guiding system better than 1 mas, the jitter term reduces to levels of less than 10^{-5} .

Readout noise

The total noise of a default NIRSpec integration with $n_f = 4, n_g = 22$ is specified with 6 e⁻ RMS. The noise of a single readout per pixel however is in the range of $\sigma_{read} = 20$ e⁻. In the case of high electron levels and close to saturation, for better noise performance it is advantageous to use a Correlated Double Sampling (CDS) technique instead of ramp fitting. There, the data of the first group is subtracted from the last one, and the count rate is determined by division with the effective integration time. For a single pixel, the final readout noise is then $\sigma_{CDSi} = \sqrt{2} \sigma_{read}$.

To cover the full slit aperture and include diffracted light, the spectra are extracted as the sum of $n_{pix} = 16$ detector pixels in spatial direction. The readout noise of one spectral element is then $\sigma_{CDS} = \sqrt{2 n_{pix}} \sigma_{read}$. Assuming saturation in the column, there is a maximum possible number of electrons of about 70,000 e⁻ in a spectral element, which is also the variance due to Poisson noise. Compared to the variance of the readout $\sigma_{CDS}^2 \approx 12,800$, it becomes clear that even in the most photon-noise dominated case, the readout noise contributes significantly to the final noise of the extracted spectrum. In all following calculations we used $n_{pix} = 16$, and the readout noise σ_{read} of 22 and 19 e⁻ for SCA 491 and 492 respectively.

Other instrumental effects

Other noise originating from jitter could be caused by varying signals due to detector intra-pixel sensitivity variations. However, the detectors of NIRSpec do not show such a behavior. The type of sensitivity changes inside a pixel is rather a redistribution of electrons to neighboring pixels, not leading to a loss of signal, but merely a reduction of spectral resolution. A pointing stability of 5 mas is equal to a

movement of $1/20^{\text{th}}$ of a pixel, hence we considered the effect negligible for now and did not simulate it in the examples shown here.

In similar fashion, the movement of the PSF on the detector caused by the jitter also leads to a redistribution of electrons, but not to an actual loss. When summing along the columns, the effect is eliminated in one dimension, and causes a reduction of the spectral resolution of the averaged electron rates. With the small drift length the effect is small and we did not simulate this behavior either.

Finally, the telescope of the observatory and the ISIM structure holding the instruments show deformations with thermal changes. This leads to a change of the wavefront error of the OTE, and so the PSF in NIRSpec. The structural change mostly influences the low spatial frequencies of the WFE (Lightsey et al., 2004), and therefore only the region close to the PSF core. Farther outside, where the PSF is truncated in the slit and the diffraction occurs, the speckle pattern remains unchanged. Thus we expect no variation of the slit and diffraction losses caused by the WFE drift.

The change in WFE also leads to a change of the PSF core height. The actual impact is wavelength dependent, nevertheless, on the scale of a few pixels, it can be considered equal for all PSFs. Looking at one specific detector pixel, the alteration of the PSF core causes a redistribution of the signal to the neighbors. On the other hand, the spectra is affected the same way locally, and the pixel will receive amounts of light from its neighbors as well. The absolute level depends however on the actual local signal, and cannot be modeled with simple assumptions. Besides, without knowing the real OTE WFE and its detailed temporal behavior, an evaluation of the impact on the noise is not possible. Lacking this information, we did not take into account any WFE drift in the simulations.

Noise of transit signals

In the previous parts we showed that apart from the readout noise, other instrumental, detector, and sky phenomena do not contribute significantly to the SNR of the stellar spectra, if we integrate large numbers of electrons. We can therefore safely describe the variance of the extracted spectra only with Poisson noise and the readout noise of the data extraction.

The total number of electrons in one detector column is $N_i = r_i t_i$, where $t_i = t_f(n_g - 1)$ is the effective exposure time for a single exposure. The Poisson noise is then $\sigma_P = \sqrt{N_i}$, and the readout noise in a CDS exposure $\sigma_{CDS} = \sqrt{2 n_{pix}} \sigma_{read}$, when summing n_{pix} pixels in a column. For the variance of a single integration we get

$$\sigma_{N_i}^2 = \sigma_P^2 + \sigma_{CDS}^2 = N_i + 2 n_{pix} \sigma_{read}^2 ,$$

and for the variance of the electron rate

$$\sigma_i^2 = \frac{\sigma_{N_i}^2}{t_i^2} = \frac{r_i}{t_i} + \frac{2 n_{pix} \sigma_{read}^2}{t_i^2} .$$

Averaging the data of n_e exposures during a transit phase, the variance of the final count rate is then

$$\sigma_R^2 = \frac{1}{n_e^2} \sum_{i=1}^{n_e} \sigma_i^2 = \frac{R}{t_{eff}} + \frac{2 n_e n_{pix} \sigma_{read}^2}{t_{eff}^2}.$$

When calculating the transit depth as in Equation 6.1, the SNR can be written as

$$\frac{d_p}{\sigma_{d_p}} = \sqrt{\frac{\sigma_{\Delta R}^2}{\Delta R^2} + \frac{\sigma_{R_o}^2}{R_o^2}}^{-1},$$

and after transformations we get

$$\frac{d_p}{\sigma_{d_p}} = \sqrt{\frac{d_p^2 R_o^2 t_{eff}^2}{(d_p^2 - d_p + 2) R_o t_{eff} + (d_p^2 + 2) 2 n_e n_{pix} \sigma_{read}^2}}.$$

Under the condition that the transit depths are at most a few percent, we can approximate $(d_p^2 - d_p + 2) \approx 2$ and $(d_p^2 + 2) \approx 2$. Therefore, the SNR of the primary transit depths is

$$\frac{d_p}{\sigma_{d_p}} = \frac{d_p R_o t_{eff}}{\sqrt{2(R_o t_{eff} + 2 n_e n_{pix} \sigma_{read}^2)}}. \quad (6.4)$$

The signal can be interpreted as the difference in electrons in the transit phase, while the noise is composed of the shot noise of the stellar light and the total readout noise of the exposures. The factor 2 in the variance originates from the observations in and out of transit. In similar fashion, we obtain the SNR of the secondary eclipse

$$\frac{d_s}{\sigma_{d_s}} = \frac{d_s R_i t_{eff}}{\sqrt{2(R_i t_{eff} + 2 n_e n_{pix} \sigma_{read}^2)}}. \quad (6.5)$$

When observing a transiting planet of radius r_{Planet} with an atmosphere, the latter causes an additional obscuration by filtering the stellar light at certain wavelengths, depending on its composition and thermal structure. This is equivalent to an enlargement of the planetary radius, and for simplification the absorption can be assumed as an opaque annulus around the planet with an effective height h , while $h \ll r_{Star}$ (Kaltenegger and Traub, 2009, in the following called KT09). The complete relative dip in the lightcurve is then the ratio of the equivalent planetary disc and the stellar disc:

$$d = \frac{\pi(r_{Planet} + h)^2}{\pi r_{Star}^2} \approx \frac{r_{Planet}^2}{r_{Star}^2} + \frac{2 r_{Planet} h}{r_{Star}^2} = d_p + d_A.$$

In analogy to the considerations above, the SNR of the atmospheric feature alone is

$$\frac{d_A}{\sigma_{d_A}} = \frac{d_A R_o t_{eff}}{\sqrt{2(R_o t_{eff} + 2 n_e n_{pix} \sigma_{read}^2)}} = \frac{2 r_{Planet} h R_o t_{eff}}{r_{Star}^2 \sqrt{2(R_o t_{eff} + 2 n_e n_{pix} \sigma_{read}^2)}}. \quad (6.6)$$

6.2.6 Simulations of HD189733b

As the first example we simulated transits of the hot Jupiter HD189733b. Unless otherwise noted, the planetary data in the following are taken from Wright et al. (2011, <http://exoplanets.org>). It has a minimum mass of $M \sin(i) = 1.14 M_J$. The orbit has a semi-major axis of 0.031 AU and a period of 2.2 days. The planet's radius is $1.14 r_J$.

The host star is a G5 type at 19.45 pc distance with a radius of $0.757 r_\odot$ (Torres et al., 2008). The magnitudes in J and K are 6.07 and 5.54 respectively, and in these bands it is too bright for NIRSpec. However, without knowing the L-band magnitude, we still tried simulations with the G395H grating. We used a Kurucz synthetic star spectrum adjusted to the star brightness⁵, shown in Figure 6.13.

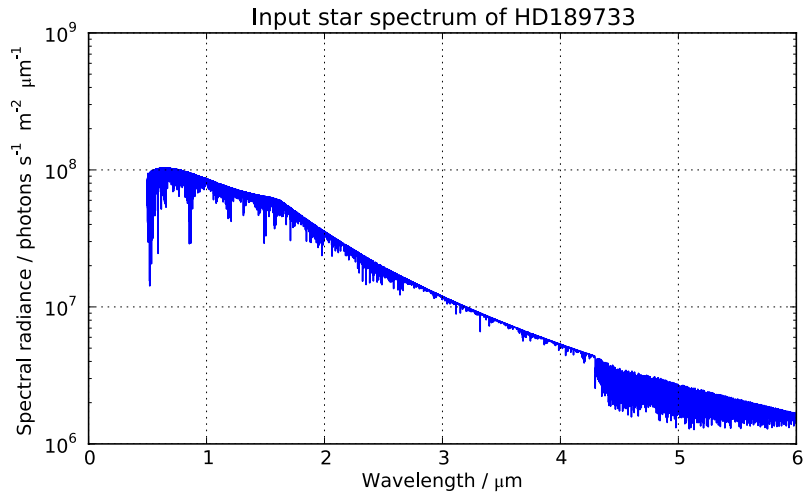


Figure 6.13: Synthetic Kurucz input spectrum for HD189733.

Observation parameters

With the detector subarray mode reading a 2048×32 pixel window, and a gain of $1.4 e^-/\text{ADU}$, the maximum allowed electron rate is $42,704 e^-/\text{s}$. To set the readout parameters, we determined the peak electron rate of the simulated exposure, shown in Figure 6.14. The oscillations are an effect of the local position of the spectrum in the detector column. If the PSF lands at exactly the boundary of two pixels, the core is spread over both, while when centered, it is concentrated on a single pixel. The exact shape of this pattern will depend on the final geometry in orbit, but we can predict the possible maximum rates by a smooth function following the spectrum peaks.

⁵J. Valenti, priv. comm.

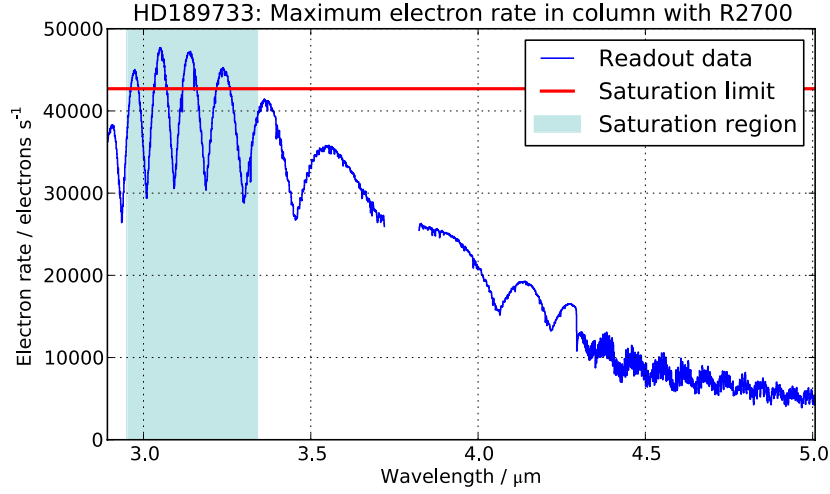


Figure 6.14: Maximum electron rate in the detector columns of an HD189733 observation. The oscillations depend on the PSF position on the pixels, and will move with the final instrument geometry. The saturation limit of $42,704 \text{ e}^-/\text{s}$ is crossed in $2.95\text{--}3.34 \mu\text{m}$.

As it can be seen, the saturation threshold is crossed in the range of about $2.95\text{--}3.34 \mu\text{m}$. Only judging from the peak electron rate, the exposure would be considered impossible. As the spectrum drops considerably towards longer wavelengths, at least these areas can be observed, along with narrow bands where the PSF is split over two detector pixels. We therefore set $n_g = 2$ and calculated the SNR data for different scenarios, ignoring the saturation effect.

Primary transit

The primary transit time was determined from data in Winn et al. (2007) to $t_{\text{trans}} = 1 \text{ h} = 3600 \text{ s}$. We neglected limb darkening and stellar variability in the simulation, and assumed a constant depth between second and third contact. At maximum we could fit $n_e = 1331$ exposures, giving a effective exposure time of $t_{\text{eff}} = 1200 \text{ s}$.

Sing et al. (2011) report HST measurements of planet/star radius ratios in the range of $r_{\text{Planet}}/r_{\text{Star}} \approx 0.156 \dots 0.16$. We calculated $d_p = r_{\text{Planet}}^2/r_{\text{Star}}^2$, and the SNR data in the according range for a single transit with Equation 6.4. The contours are shown in Figure 6.15. To improve the image clarity and reduce the oscillations in the stellar spectrum, the input rate has been filtered with a moving median over 11 pixels in the spectral direction.

Even in the R2700 mode, NIRSpec will be able to achieve very high SNR values by observing only a single transit event. Due to its massive photon collecting ability, the photon noise can be damped very quickly. The average wavelength step is 0.67 nm , and d_p could be determined with a SNR of $40\text{--}140$ in each bin.

To characterize the potential to detect an atmosphere, we examined the SNR levels

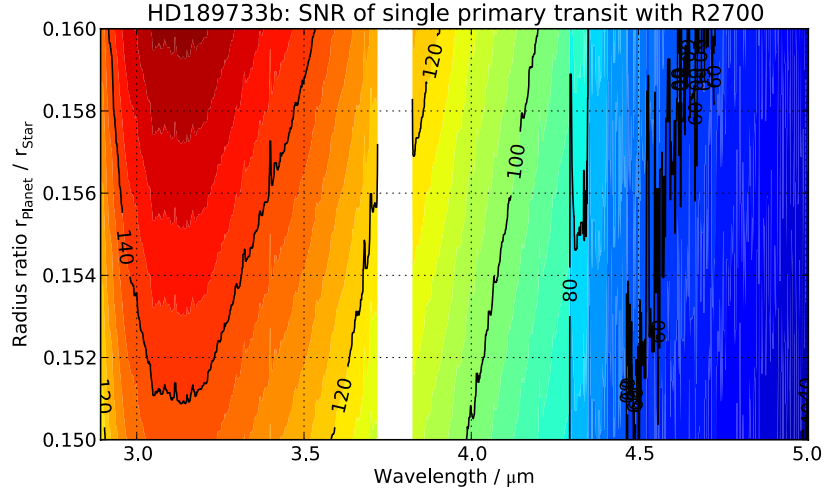


Figure 6.15: SNR of the planet/star ratio obtained from a single primary transit of HD189733b with R2700. The input data has been filtered with a moving median over 11 pixels in the spectral direction. The average wavelength step is 0.67 nm. SNR values of 40–140 are easily possible within each wavelength bin.

using Equation 6.6. We set the planet radius to $r_{\text{planet}} = 0.15463 r_{\text{star}}$ (Torres et al., 2008). Pont et al. (2008) show a simulated atmospheric spectrum with effective heights of $h = 0 \dots 3000$ km. The corresponding SNR contours are plotted in Figure 6.16. Again, the data has been filtered with a moving median over 11 pixels in the spectral direction.

Features equal to a height of 1500–2500 km are reliably detected in the full wavelength range. If the high resolution is not necessary, the fidelity can be increased by rebinning the data to large spectral bins, allowing the observation of even smaller scale heights.

Secondary eclipse

Recently, Waldmann et al. (2012) showed ground-based observations of the self-emitted flux of HD189733b in K and L-band. We simulated the corresponding NIRSpect data and their SNR with Equation 6.5 for a range of flux ratios $d_s = 0 \dots 0.012$. We determined the transit time to $t_{\text{trans}} = 3456$ s from data by Knutson et al. (2007). With $n_e = 1277$ exposures in the single phase, we obtained $t_{\text{eff}} = 1151$ s. The SNR data is shown in Figure 6.17, along with the measured points from Waldmann et al. (2012). Not only does NIRSpect deliver a vastly higher resolution, also the errors in single spectral bins are smaller than the ones of currently available data.

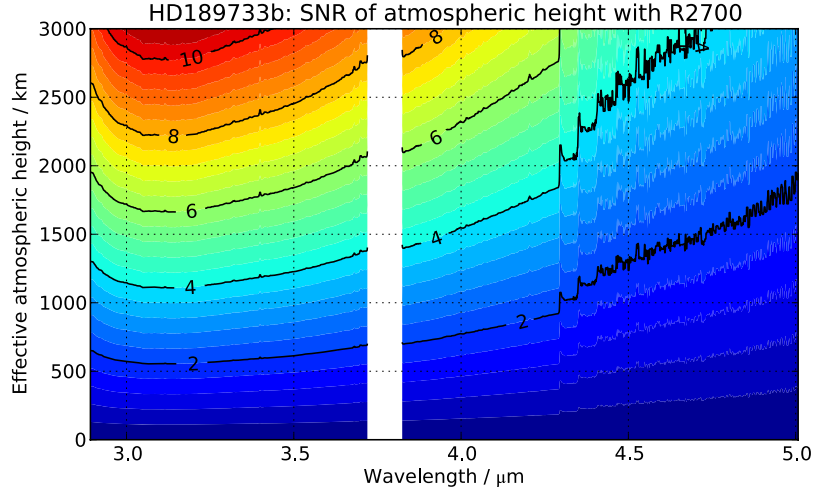


Figure 6.16: SNR of the effective atmospheric height obtained from a single primary transit of HD189733b with R2700. The input data has been filtered with a moving median over 11 pixels in the spectral direction. The average wavelength step is 0.67 nm. Scale heights of 1500–2500 km could be reliably detected with high resolution.

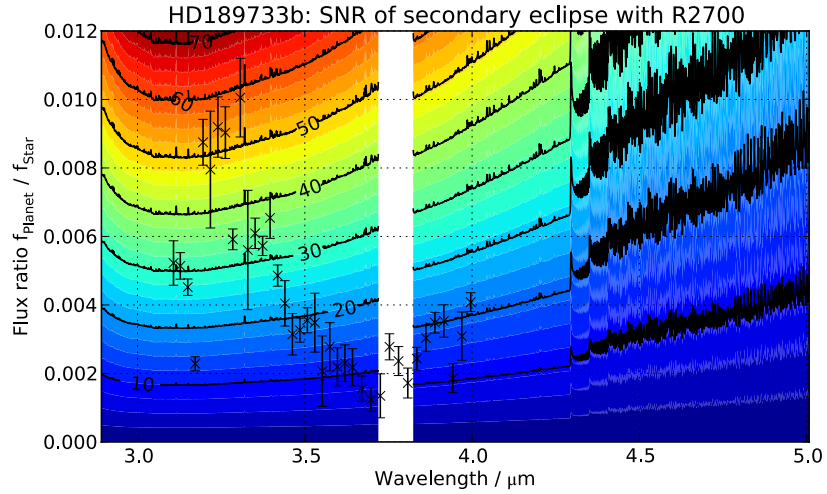


Figure 6.17: SNR of the planet/star flux ratio obtained from a single secondary eclipse of HD189733b with R2700. The average wavelength step is 0.67 nm. Even ratios down to 10^{-3} could be observed. Overplotted is the data from Waldmann et al. (2012). The NIRSpec results are much higher resolved and with a larger individual SNR.

6.2.7 Simulations of GJ1214b

The second planet in our simulations was GJ1214b with a mass of $M = 6.55 M_{\oplus}$ and a radius of $2.68 r_{\oplus}$ (Charbonneau et al., 2009). It is one of the first discovered

transiting exoplanets of the so-called super-Earth type, which is an intermediate class between Earth-sized planets and ice giants as Neptune and Uranus. It orbits the host star with a semi-major axis of 0.0143 AU and a period of 1.58 days.

The star itself is a M4.5 dwarf at 12.95 pc distance. Being that close, it has become a primary target to study the characteristics of super Earths with transit spectroscopy (Bean et al., 2010; Berta et al., 2011; Croll et al., 2011; Crossfield et al., 2011; de Mooij et al., 2012; Désert et al., 2011). The star has a radius of $0.2064 r_{\odot}$ (Berta et al., 2011) and an effective temperature of 3000 K. The J and K magnitudes are 9.75 and 8.78 respectively, indicating that an observation with NIRSpec is possible with R1000 and R2700. To cover the full spectral range of each band, we chose to simulate the R1000 exposures. As input for the IPS we used a NextGen synthetic spectrum adapted to the stellar parameters⁶, which is shown in Figure 6.18.

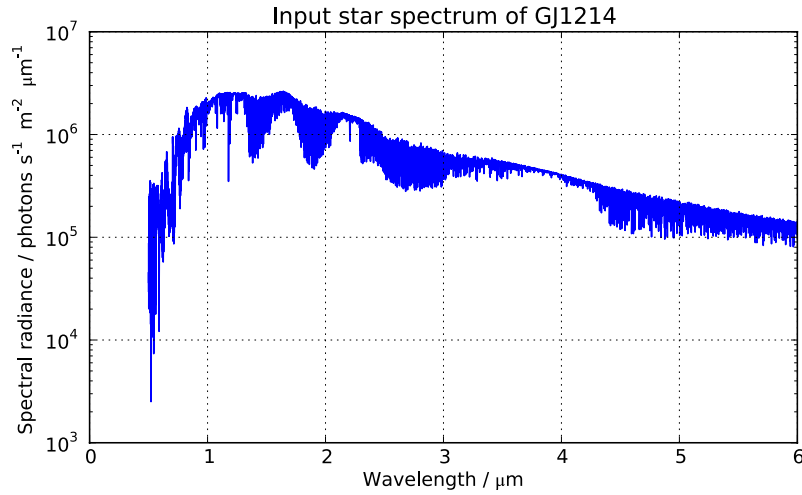


Figure 6.18: Synthetic NextGen input spectrum for GJ1214.

Observation parameters

From each exposure of the three bands, we determined the peak electron rate. The duration of the primary transit is given by Berta et al. (2011) with 40.1 minutes between the second and third contact, no limb darkening or stellar variability is assumed here. The planet/star radius ratio is stated with 0.1171. As before, we derived individual values for n_g and n_e , and the resulting effective exposure time (see Table 6.3). The star is somewhat fainter than HD189733, and we are able to fit more groups within one integration. This leads to a considerable improvement of the effective integration times. While in the previous case, $\frac{2}{3}$ of the transit time was lost, here we only miss 16–29%.

⁶J. Valenti, priv. comm.

Table 6.3: Exposure parameters for observations of GJ1214. Compared to the transit time $t_{\text{trans}} = 2406 \text{ s}$, the effective exposure times are smaller by 16–29%.

Disperser	$r_{\text{max}} / \text{e}^-/\text{s}$	n_g	n_e	$t_{\text{eff}} / \text{s}$
G140M	14269	6	381	1717
G235M	13945	6	381	1717
G395M	6806	12	205	2033

Atmosphere in primary transit

The high interest in observing GJ1214b is based on the potential of characterizing its atmospheric composition. It allows to learn more about this particular type of planets, whether it is similar to Earth, a water world, or an ice giant. To evaluate future possibilities with NIRSpec, we calculated the SNR level of atmospheric features. To compare with observations, Bean et al. (2010) showed model spectra varying by $0.15 r_{\oplus}$, which corresponds to 0–955 km. The combined data of a single transit with each of the three R1000 gratings is shown in Figure 6.19, smoothed with a 11 pixel moving median in spectral direction. To cover the full spectral range, in total three observations are necessary.

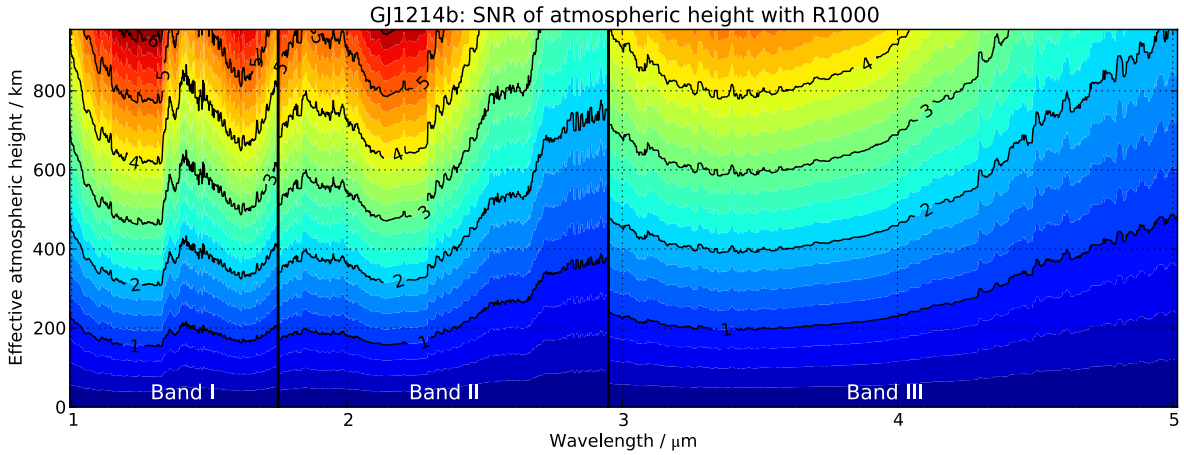


Figure 6.19: SNR of the effective atmospheric height obtained from a single primary transit of GJ1214b observed with each of the R1000 gratings. The input data has been filtered with a moving median over 11 pixels in the spectral direction. To cover the complete spectral range, three transits need to be observed. The border between the bands has been set to the center of the $0.1 \mu\text{m}$ wide overlaps. The average wavelength steps are 0.64 nm , 1.07 nm , and 1.8 nm respectively in each band. Atmospheric features with heights of 500–800 km could be detected with one transit observation at this resolution.

The three bands overlap by $0.1 \mu\text{m}$, therefore we set the boundary between two to the center of the overlap regions. Although the wavelength step increases from I to III by almost a factor of 3, the blue spectral range receives more photons, so that the SNR is approximately constant, only deteriorating at the very red end. Overall, we could reliably detect atmospheric features with equivalent heights of 500-800 km with only one transit observation in each mode. Again, to probe smaller scale heights, the data could be rebinned to larger spectral intervals.

6.2.8 Simulations of an Earth-sized planet in the habitable zone

The ultimate motivation to study planets around other stars is the question whether there are other lifeforms in the universe. In analogy to our own solar system, this would require the planets to be located in the Habitable Zone (HZ), where they could sustain an atmosphere and liquid water on the surface (Kasting et al., 1993).

Observing such a planet around a sun-like star turns out to be impossible with the current means. To detect very small atmospheric features, one would have to combine the data of several transits, which, in the case of Earth, would take decades. Besides, it also would be very unlikely that the planet is found at all, if the orbital periods are in the order of years, and transits occur with the same cadence.

It has become clear that late stellar types are better suited to look for potentially habitable planets (KT09). The distance of the HZ depends on the stellar surface temperature, which decreases towards K and M. Therefore the planets orbit closer to the star and with shorter orbital periods, yielding more transits within the same time.

Observation parameters

As an example of an Earth-sized planet with $r_{\text{Planet}} = r_{\oplus}$ around a M-dwarf, we simulated the observation of GJ1214 put at 10 pc distance. We determined the orbital semi-major axis of the planet as shown by KT09 to

$$a_{\text{Planet}} = \left(\frac{T_{\text{eff Star}}}{T_{\text{eff } \odot}} \right)^2 \cdot \frac{r_{\text{Star}}}{r_{\odot}} = 0.0558 \text{ AU},$$

and the orbital period P_{Planet} with Kepler's third law using GJ1214b as the second body in the planetary system, giving

$$P_{\text{Planet}} = \left(\frac{a_{\text{Planet}}}{a_{\text{GJ1214b}}} \right)^{3/2} \cdot P_{\text{GJ1214b}} = 12.2 \text{ days}.$$

The transit duration is then

$$t_{\text{trans}} = \frac{2r_{\text{Star}}}{2\pi a_{\text{Planet}}} \cdot P_{\text{Planet}} = 5766 \text{ s}.$$

We scaled the electron rates with $(12.95/10)^2$, and obtained the exposure parameters for all the gratings shown in Table 6.4. In the R1000 bands I and II, the effective exposure time is only about 50% of the transit time due to a fast detector saturation. Despite the higher resolution with the R2700 gratings, the actual SNR in a certain wavelength interval will be higher due to a considerably longer effective integration.

SNR of atmospheric features

To judge the habitability of a planet, the focus is on detecting absorption of molecules also present in Earth's atmosphere. We selected broad features of H_2O and CO_2 from KT09 whose center wavelengths λ_0 are in the NIRSpec range, and which have a large effective height h . For each we calculated the SNR values of a single transit SNR_A by integrating over the equivalent width in the spectrum $\Delta\lambda$, and using Equation 6.6 with the total electron rate and the equivalent readout noise of the included pixels.

As for no feature a reliable detection will be possible with only one transit, we assumed that the data of several events can be combined. We determined the number of orbits necessary to reach a SNR of 5 (N_5), and also the time this would take if each single event could be observed (t_5) respecting the orbital period. The selected molecules, their parameters, and the result are shown in Table 6.5.

As already expected, the data obtained with the R2700 dispersers has a higher SNR due to the longer effective integration time, especially in band II. No single molecule could be detected with only one transit observation, but large features are within reach during the mission when combining multiple transits.

This possibility has to be critically assessed. As explained by Gardner et al. (2006), JWST has only a small continuous viewing zone around the ecliptic poles. Other sky regions are partly accessible during a certain time of the year, and it will strongly depend on the star position, the planet orbit timing, and the overall observing

Table 6.4: Exposure parameters for observations of GJ1214 put at 10 pc distance with an Earth-sized planet in the habitable zone. Compared to $t_{\text{trans}} = 5766$ s, the effective exposure time is much shorter in the R1000 mode.

Disperser	$r_{\text{max}} / \text{e}^-/\text{s}$	n_g	n_e	$t_{\text{eff}} / \text{s}$
G140M	23930	3	1598	2881
G235M	23386	3	1598	2881
G395M	11414	7	799	4322
G140H	8501	10	581	4714
G235H	9178	9	639	4609
G395H	4561	18	336	5150

Table 6.5: SNR of atmospheric features of an Earth-sized planet in the habitable zone orbiting a M4.5 dwarf at 10 pc, and required iterations to achieve a SNR of 5. The values for the R2700 dispersers are higher due to a longer effective integration time.

Molecule	$\lambda_0 / \mu\text{m}$	$\Delta\lambda / \mu\text{m}$	h / km	Disperser	SNR_A	N_5	t_5 / years
H ₂ O	1.9	0.2	5	G235M	0.22	514.8	17.2
				G235H	0.30	278.7	9.30
CO ₂	2.8	0.1	20	G235M	0.32	242.1	8.10
				G235H	0.44	130.3	4.37
H ₂ O	3.3	0.25	20	G395M	0.83	35.9	1.20
				G395H	0.94	28.3	0.97
CO ₂	4.3	0.4	20	G395M	0.73	46.5	1.57
				G395H	0.84	35.8	1.20

schedule how many transits can be observed at all. Nevertheless, the number of events necessary for the water and CO₂ bands at 3.3 and 3.4 μm is 29–36, which appears possible throughout the mission lifetime of 5 years.

The option to combine multiple transits also requires stability of the instrument. However, if variations are only of relative nature and on timescales longer than a single transit, they will cancel out when processing the data individually for each event. This is likely the case for the wavefront error and the shape of the PSF. Also the change in GWA positioning between observations will lead to varying sampling of the spectra, but when integrating over a large spectral range, this effect is mitigated. Hence we conclude that given a suitable Earth-sized planet candidate is found until JWST is in operation, NIRSpec will be able to detect large atmospheric features in its transmission spectrum.

What I cannot create, I do not understand.

Richard Feynman

7

Conclusion and outlook

The initial goal of this thesis was to verify the functionality of the IPS, assemble and verify a realistic instrument model, and to perform first scientific simulations of NIRSpec observations.

When doing simulations with the IPS, we discovered errors that we were able to fix by revising the corresponding algorithms. Unfortunately, it will take more time and effort to eliminate the remaining problems leading to wrong count rates, and enabling the input of spatially resolved objects with complex spectra. Until then, we can create simulations for the other object types, and adjust the results manually to obtain correct electron rate levels.

To simplify the usage of the IPS for proper scientific exploitation, we developed additional software tools. For the data input we created an interface to set up observation scenes, and we presented a data reduction pipeline to extract spectra from count rate maps. Both applications turned out to be essential in the following work.

We also showed how we could verify the NIRSpec model with calibration data. We were able to calibrate the geometry of the spectrograph with high accuracy, despite only modifying low-order parameters. Including measurements with the MSA from the second cryogenic campaign, we expect to be able to reach at least the same accuracy in the full FOV, and extend the analysis to the FORE optics.

Besides, we verified the NIRSpec throughput. To reduce uncertainties it was advantageous to do relative comparisons of different parts, and avoid dependence on absolute data as far as possible. With the various instrument modes we could separate contributions from single subsystems, and were finally limited by the absolute knowledge of the calibration source.

Simulating typical science cases of NIRSpec, we presented the data for a spectroscopic deep field observation. Already during the preparation of the scene we found that the target selection and placement depends critically on object position, bright-

ness, and size. Evaluation of the extracted spectra revealed NIRSpec’s capabilities to observe high-redshift objects with deep sky exposures.

The second on-sky simulation dealt with the observation of exoplanetary transits. We assessed different sources of instrumental noise, and found only the readout noise being relevant for single transit events. Besides, we described how the host star brightness restricts the observability and impacts the SNR due to fast detector saturation. Simulating transit data for HD189733b and GJ1214b we saw that NIRSpec will provide remarkable results for near-IR spectra of hot Jupiters and super-Earths, surpassing the quality of all currently available data. When combining the output of multiple events, it will be able to detect large absorption features of Earth-sized planets in the habitable zone around close M-dwarfs.

Both scientific examples show the outstanding capabilities of NIRSpec and JWST. It will be a unique facility for discoveries in the early universe, and also unrivaled for exoplanet research until dedicated missions are launched. The IPS can be a key element in the science preparation for NIRSpec, and its simulations will help greatly to understand the planned observations, and their expected data.

The image is an image.
Lenny Kravitz



Additional images

A.1 Verification of the as-built optical model

A.1.1 Measured wavefront errors at the FPA

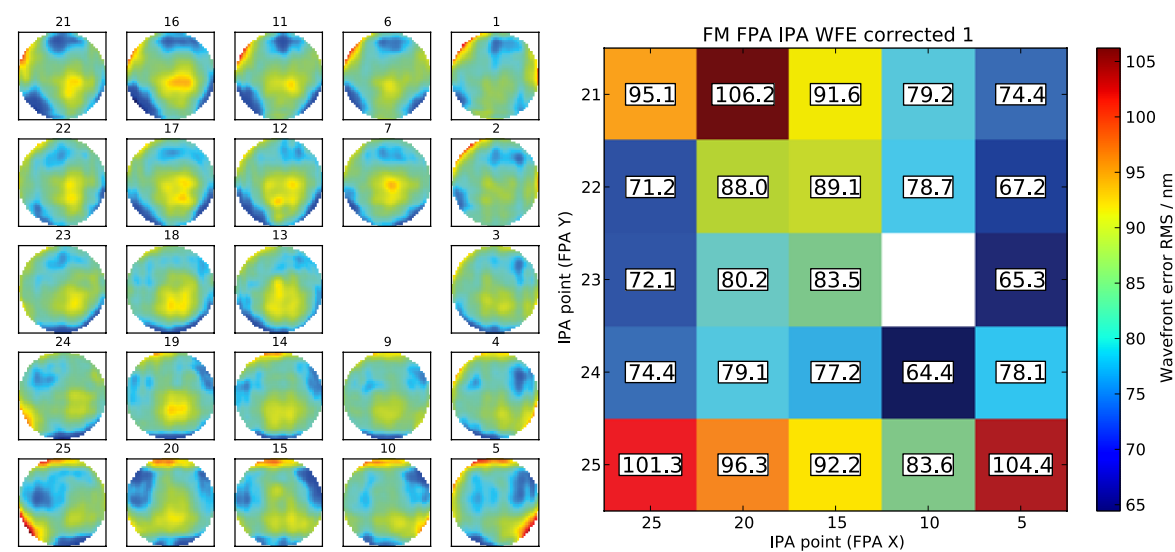


Figure A.1: Measured wavefront errors at the FPA plane at ambient, FPA center (step 1).
RMS mean: 83 ± 12 nm.

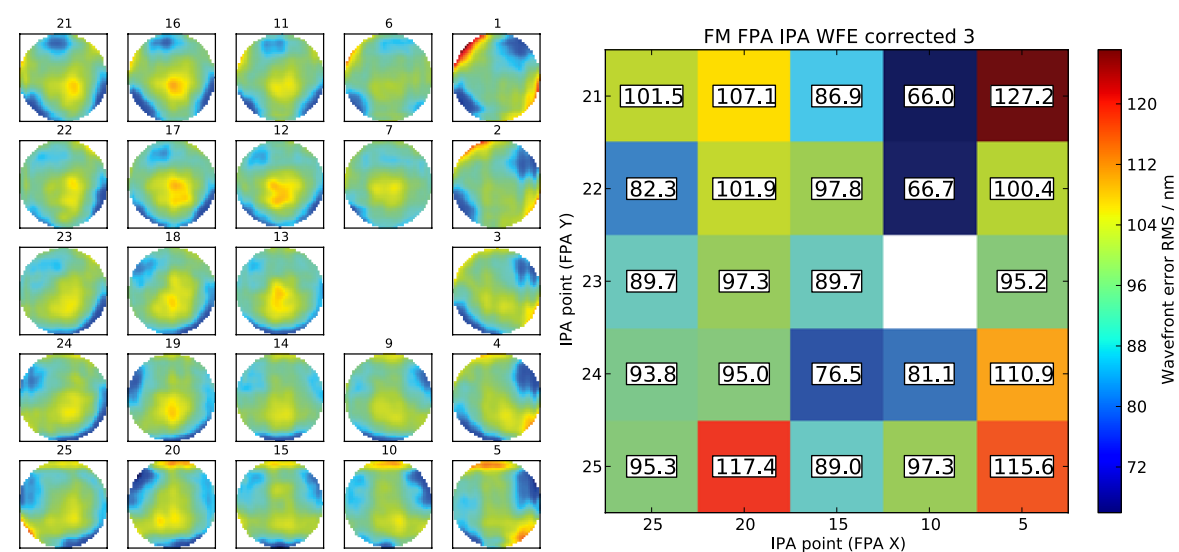


Figure A.2: Measured wavefront errors at the FPA plane at ambient, FPA +x-side (step 3).
RMS mean: 95 ± 14 nm.

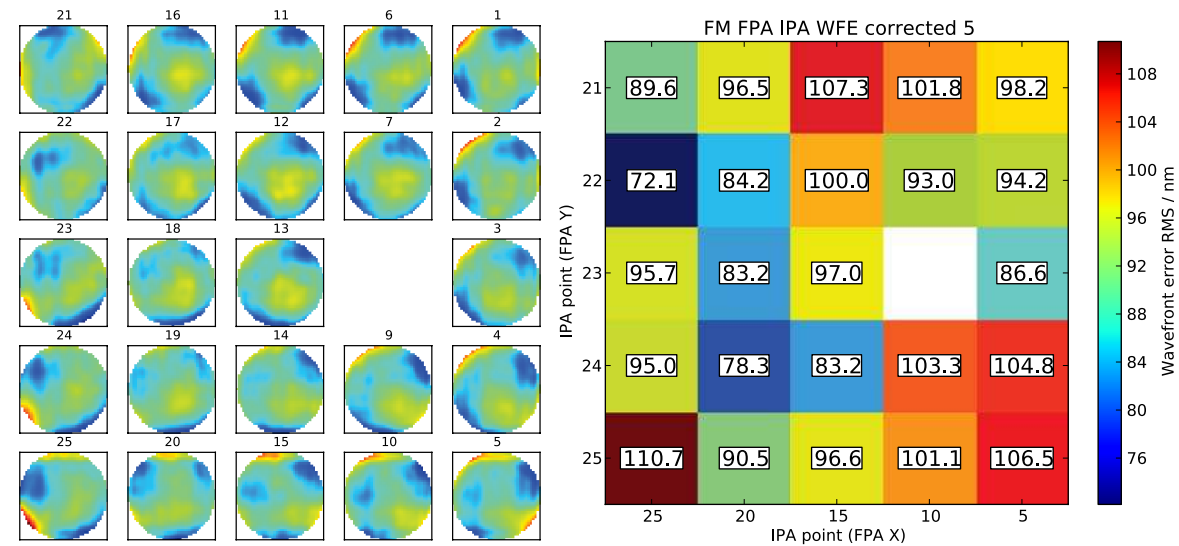


Figure A.3: Measured wavefront errors at the FPA plane at ambient, FPA -x-side (step 5).
RMS mean: 95.6 ± 9.4 nm.

A.1.2 Simulated wavefront errors at the FPA

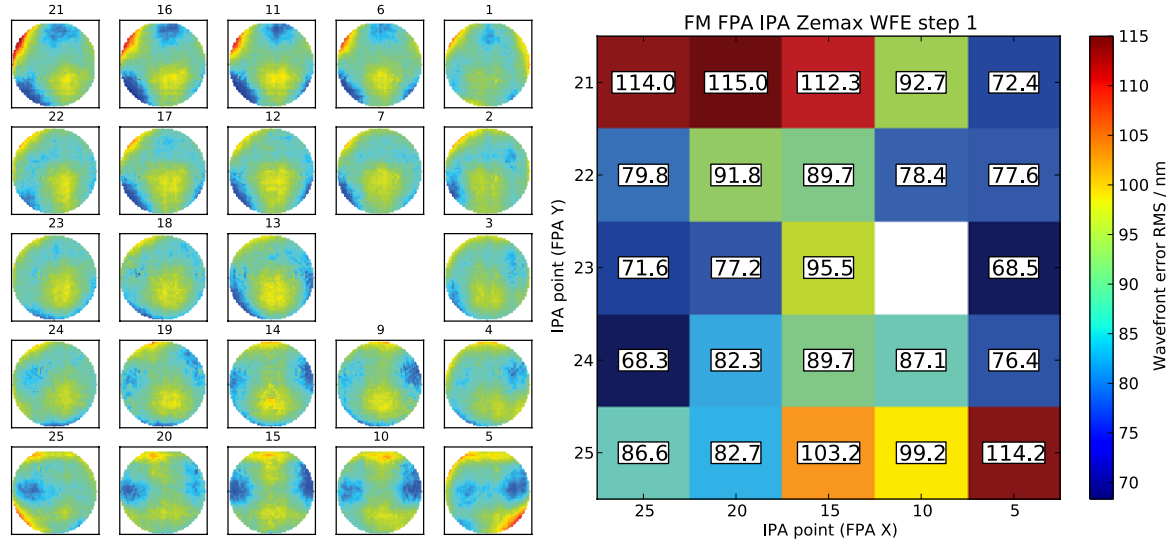


Figure A.4: Simulated wavefront errors at the FPA plane at ambient, FPA center (step 1).
RMS mean: 89 ± 14 nm.

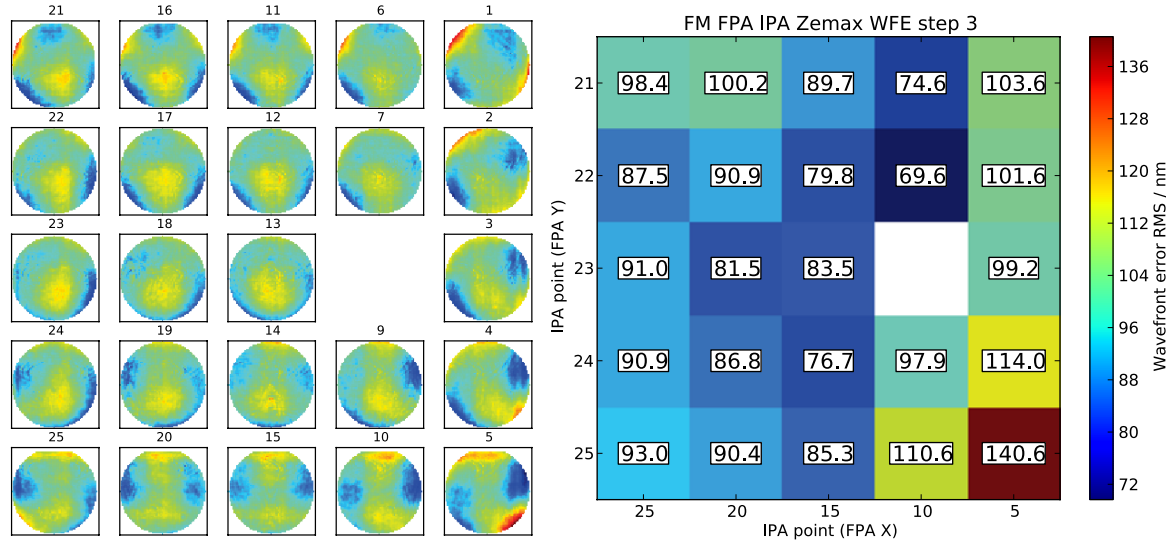


Figure A.5: Simulated wavefront errors at the FPA plane at ambient, FPA +x-side (step 3).
RMS mean: 93 ± 15 nm.

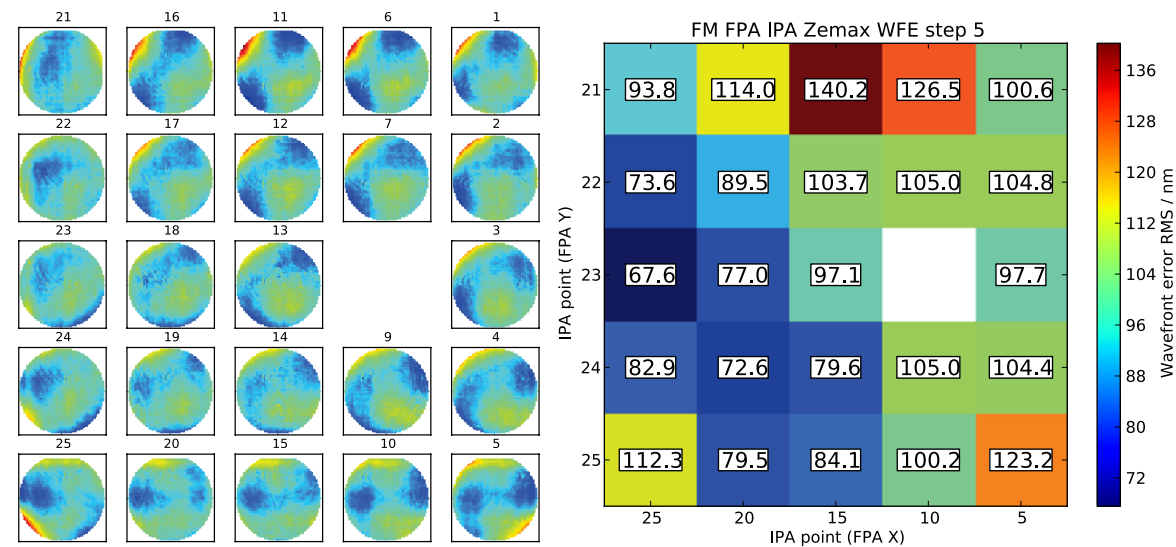


Figure A.6: Simulated wavefront errors at the FPA plane at ambient, FPA -x-side (step 5).
RMS mean: 97 ± 18 nm.

A.1.3 Wavefront error residuals at the FPA

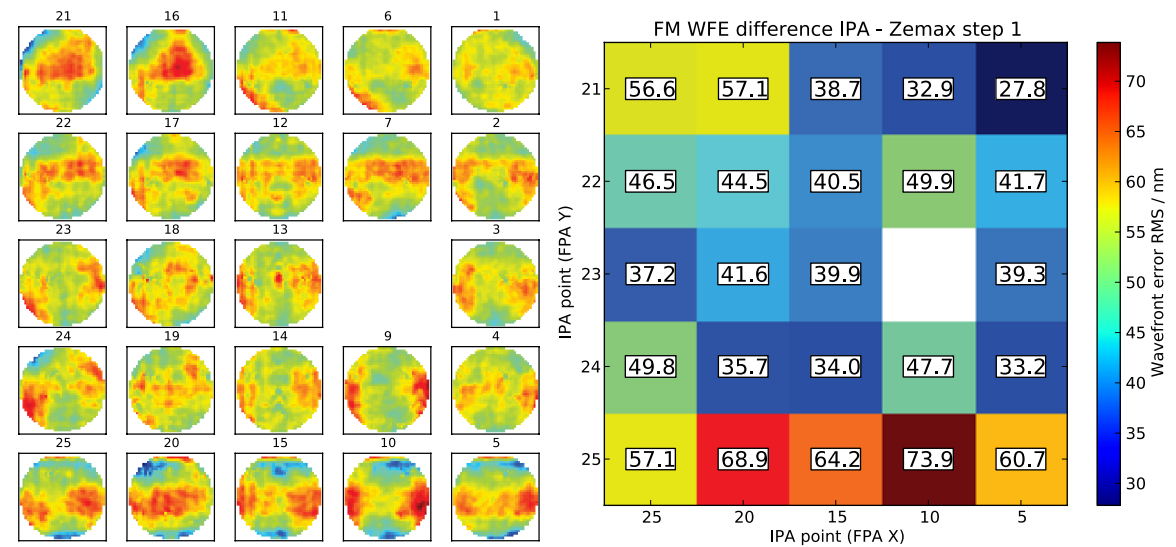


Figure A.7: Wavefront errors residuals at the FPA plane at ambient, FPA center (step 1).
RMS mean: 47 ± 12 nm.

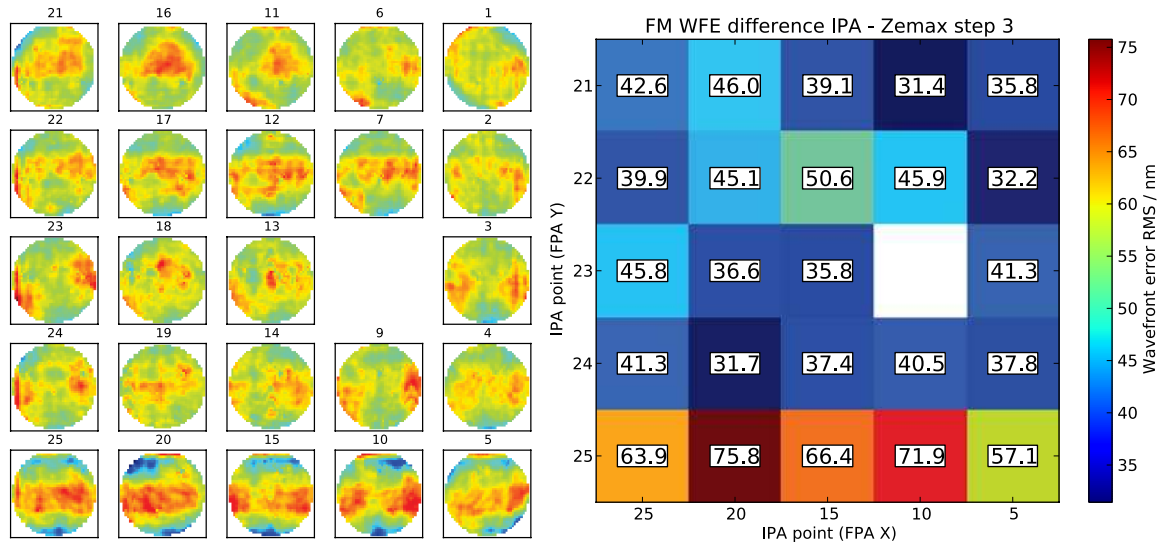


Figure A.8: Wavefront errors residuals at the FPA plane at ambient, FPA +x-side (step 3).
RMS mean: 46 ± 12 nm.

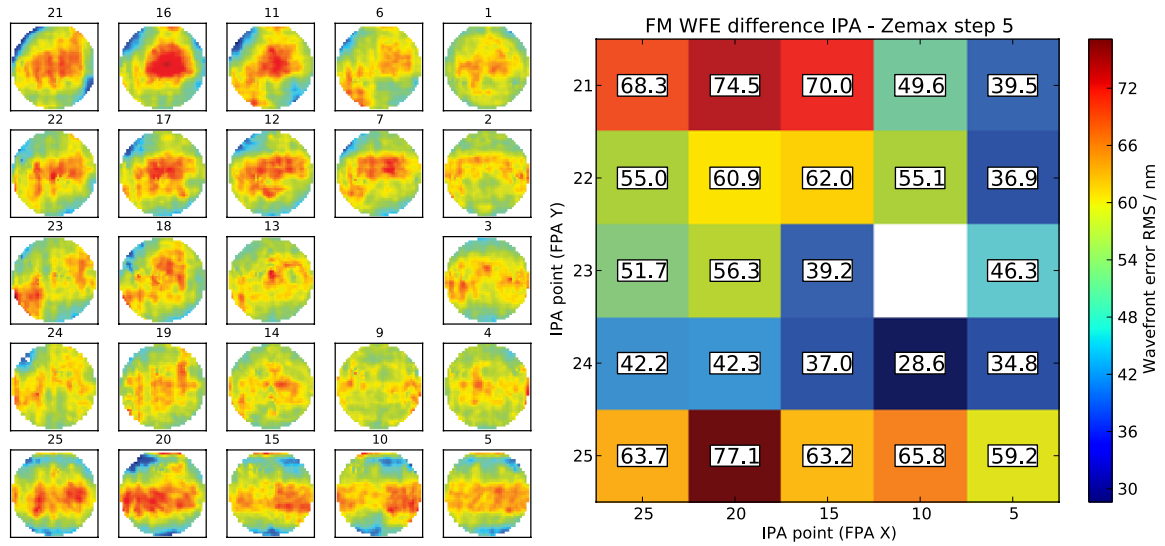


Figure A.9: Wavefront errors residuals at the FPA plane at ambient, FPA -x-side (step 5).
RMS mean: 53 ± 13 nm.

A.2 NIRSpec model data

A.2.1 Wavefront error maps

FORE and COL optics

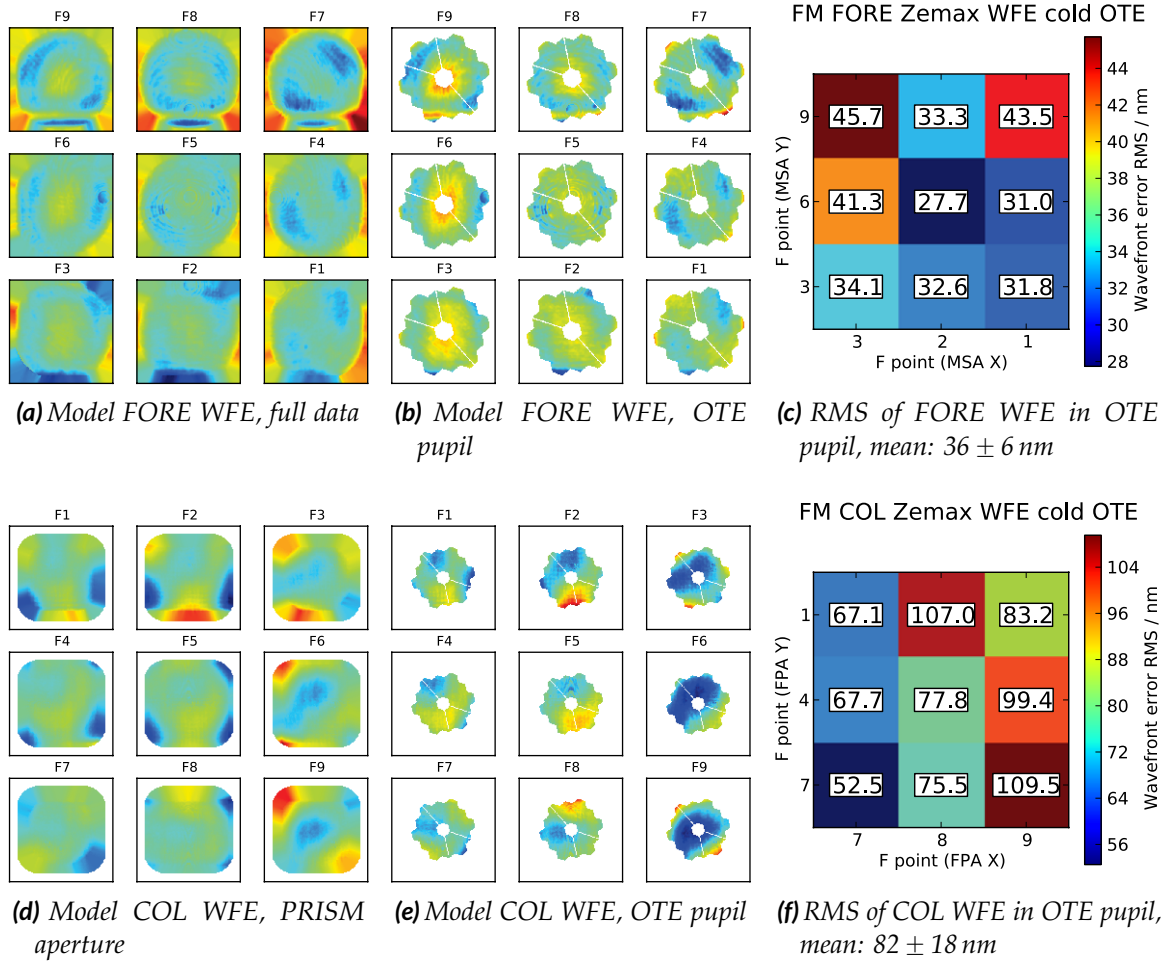


Figure A.10: (a)–(c): IPS model wavefront error of the FORE optics at the nominal field points F1–F9, arranged in the MSA coordinate system. (a): Fully extrapolated data. (b): Maps masked with projected OTE aperture stop. (c): RMS of the maps masked with projected OTE stop. (d)–(f): IPS model wavefront error of the COL optics at the nominal field points F1–F9, arranged in the FPA coordinate system. (d): Extrapolated data in PRISM aperture. (e): Maps in projected OTE aperture stop. (f): RMS of the maps masked with projected OTE stop.

Camera

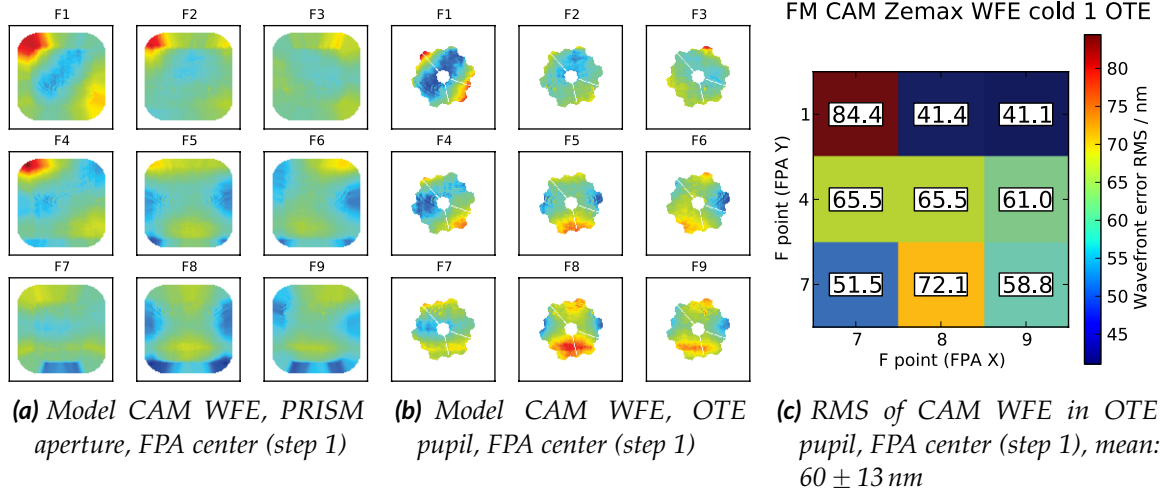


Figure A.11: IPS model wavefront error of the CAM optics at the nominal field points F1–F9 in the FPA center (step 1), arranged in the FPA coordinate system. (a): Extrapolated data in PRISM aperture. (b): Maps masked with projected aperture OTE stop. (c): RMS of the maps masked with projected OTE stop.

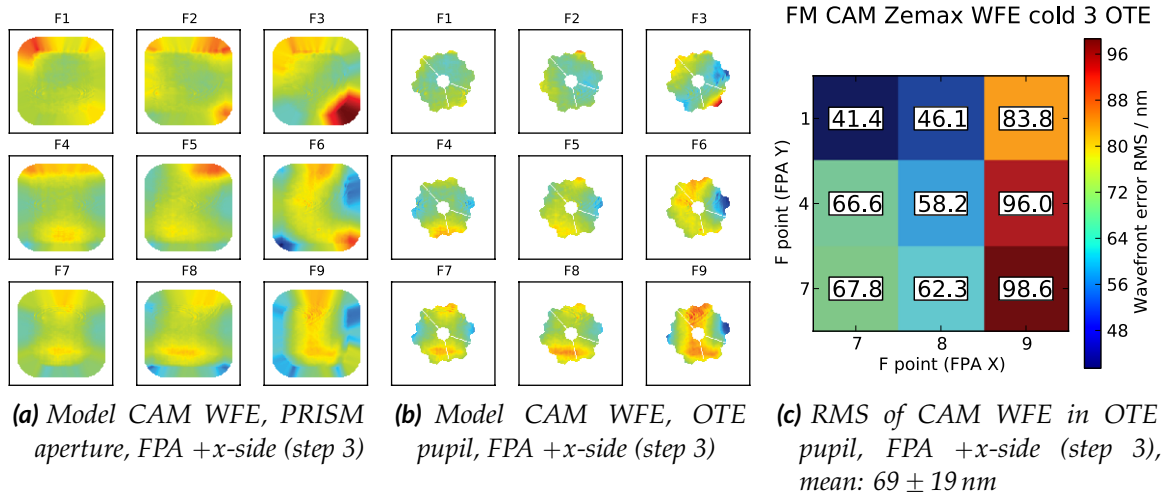


Figure A.12: IPS model wavefront error of the CAM optics at the nominal field points F1–F9 on the FPA +x-side (step 3), arranged in the FPA coordinate system. (a): Extrapolated data in PRISM aperture. (b): Maps masked with projected aperture OTE stop. (c): RMS of the maps masked with projected OTE stop.

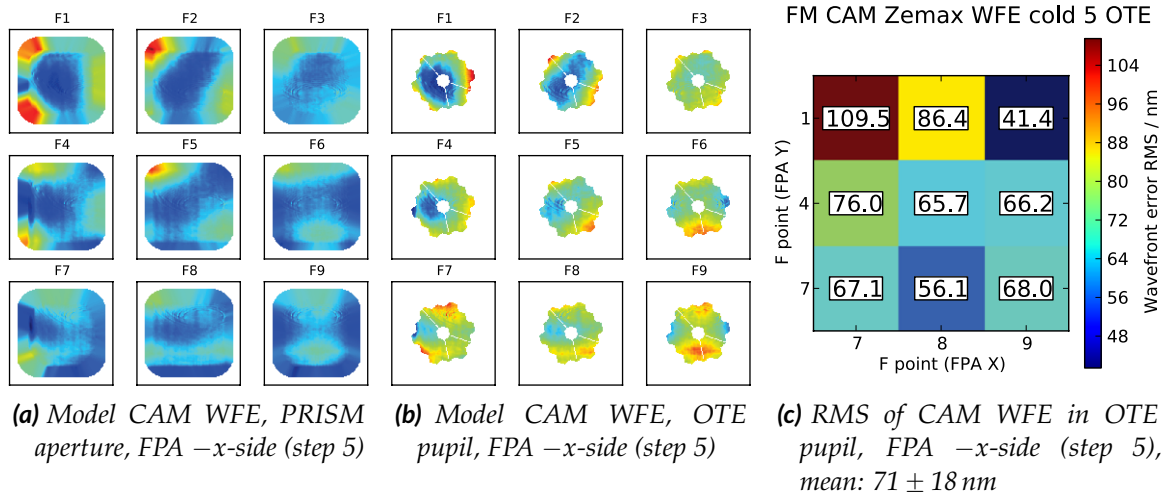


Figure A.13: IPS model wavefront error of the CAM optics at the nominal field points F1–F9 on the FPA –x-side (step 5), arranged in the FPA coordinate system. (a): Extrapolated data in PRISM aperture. (b): Maps masked with projected aperture OTE stop. (c): RMS of the maps masked with projected OTE stop.

A.2.2 Efficiencies

Mirrors

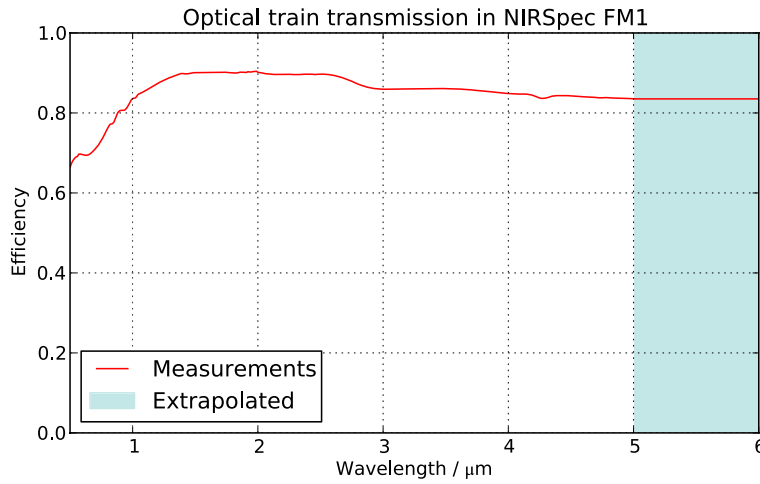


Figure A.14: Combined throughput of the mirrors in the FM1 optical train. The measurements cover the range 0.5–5 μm , and have been extrapolated to 6 μm .

FWA elements

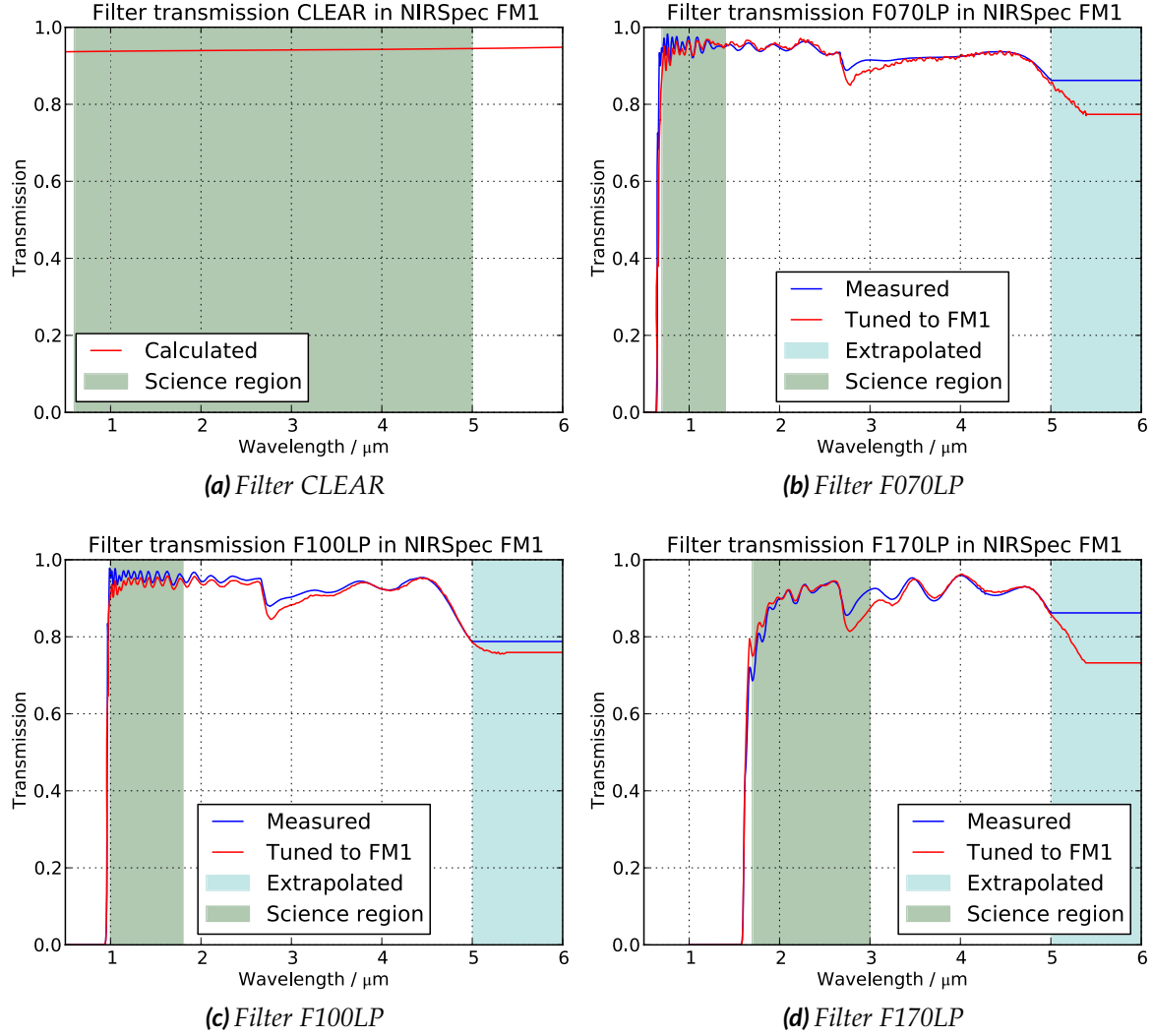


Figure A.15: Efficiencies of the elements on the FWA in the NIRSpec FM1 model, measured and tuned data where applicable, partly extrapolated to 6 μm . Continued on next page.

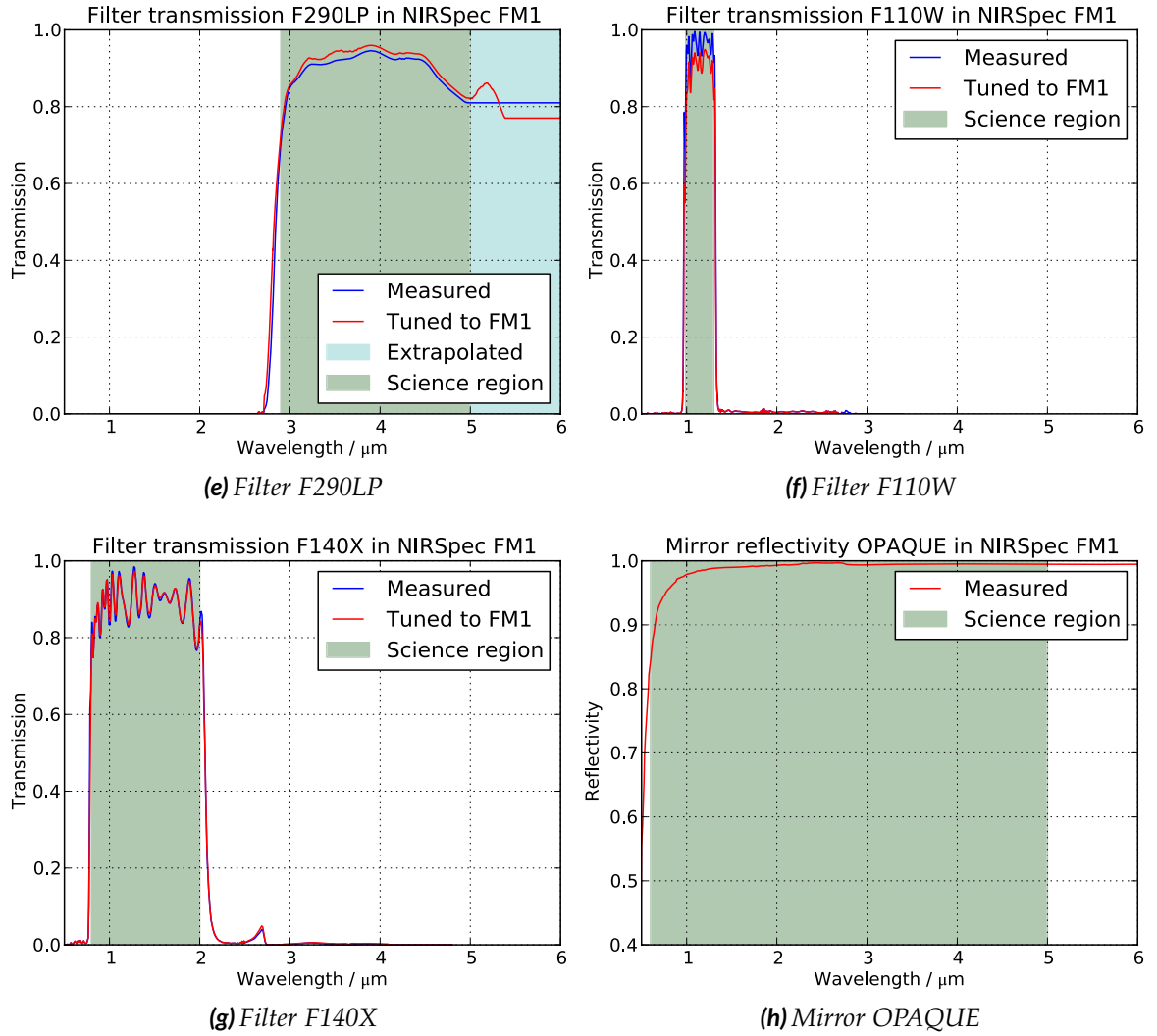


Figure A.15: Efficiencies of the elements on the FWA in the NIRSpec FM1 model, measured and tuned data where applicable, partly extrapolated to 6 μm .

GWA elements

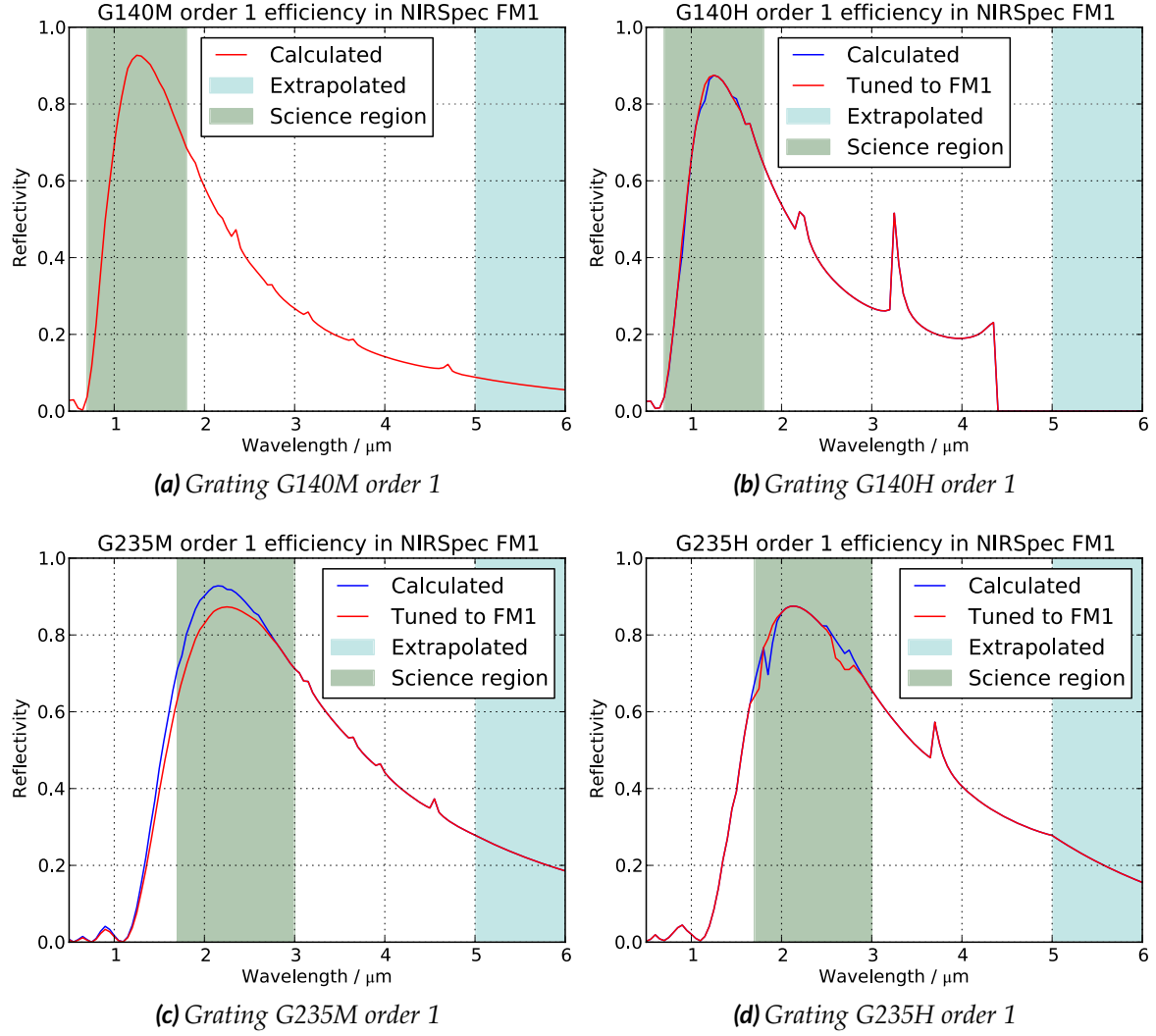


Figure A.16: Efficiencies of the elements on the GWA in the NIRSpec FM1 model, measured and tuned data where applicable, extrapolated to 6 μm . Continued on next page.

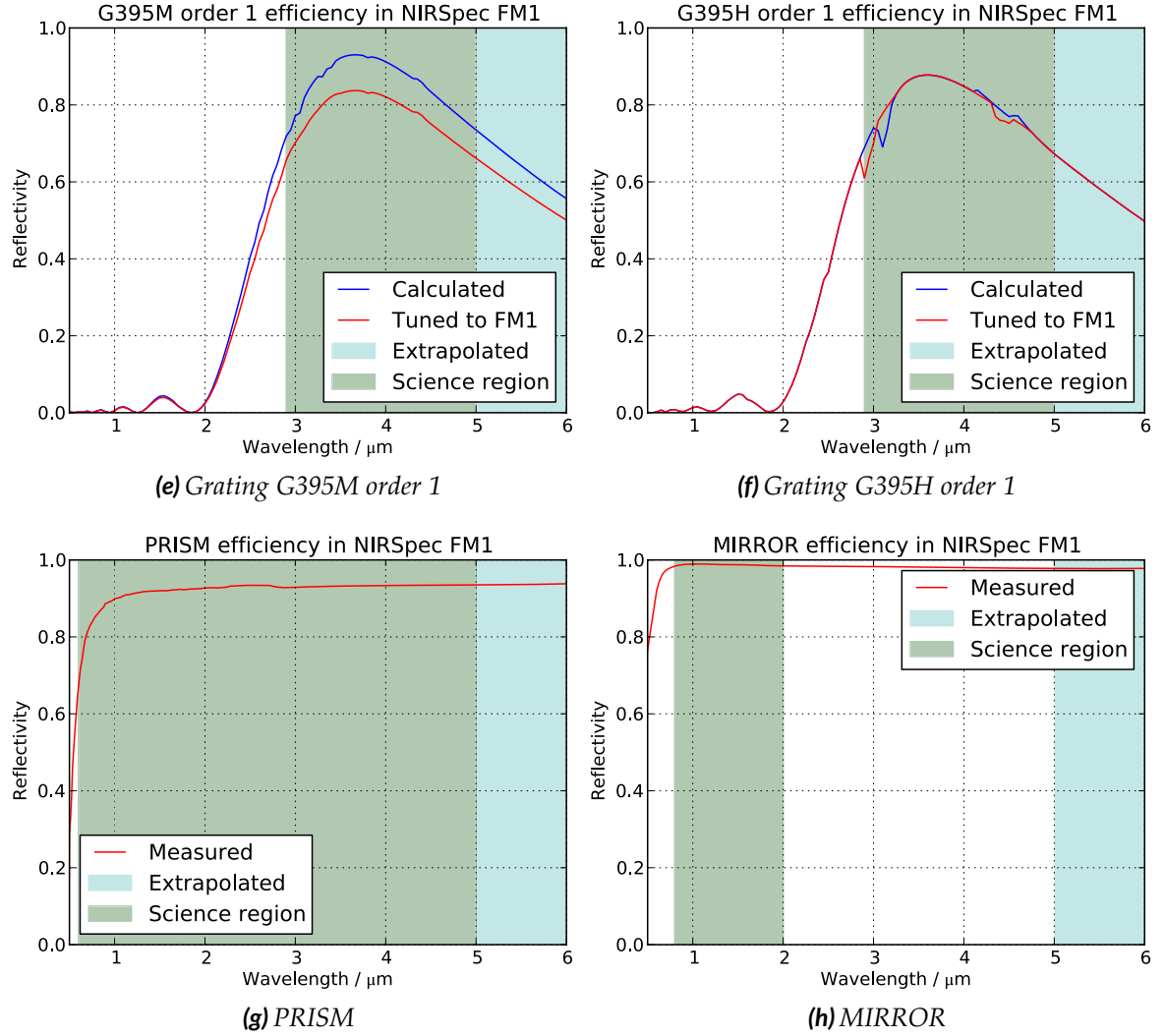


Figure A.16: Efficiencies of the elements on the GWA in the NIRSpec FM1 model, measured and tuned data where applicable, extrapolated to 6 μm .

Detector

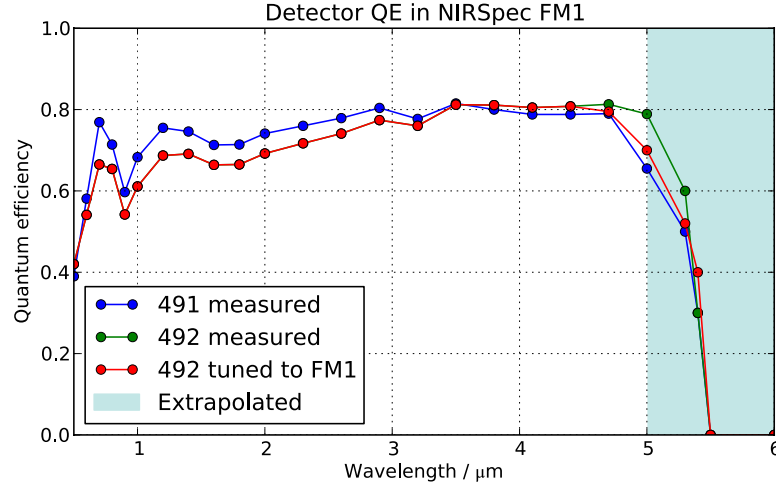


Figure A.17: Average NIRSpec FM1 detector quantum efficiency for the SCAs 491 and 492. The measurements cover the range 0.5–5 μm , and have been extrapolated to 6 μm with an artificial cutoff at 5.5 μm . At the red end, we tuned the values with FM1 calibration data.

IFU

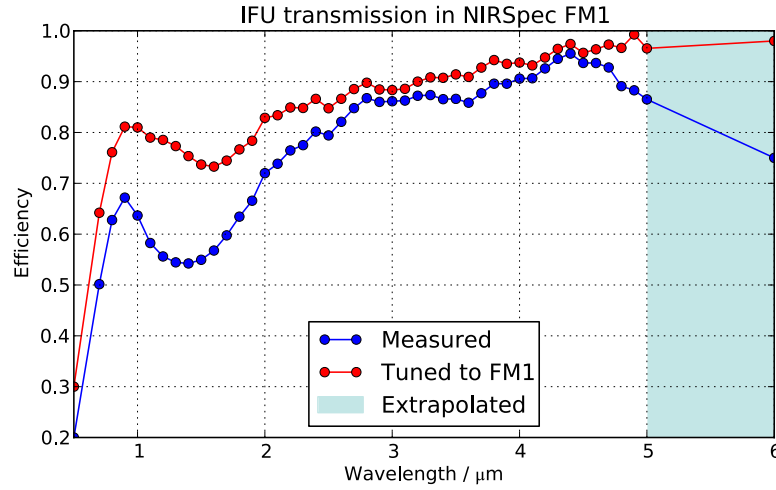


Figure A.18: Global end-to-end throughput of the FM1 IFU for all slices. The measurements cover the range 0.5–5 μm , and have been extrapolated to 6 μm . The data was tuned with measurements of the FM1 calibration campaign.

A little knowledge is the root of all evil.

Result of <http://proverb.gener.at/or/>

B

Publications

B.1 Overview

Parts of our work have been published in two conference proceedings. The first paper (Dorner et al., 2010) in section B.2 describes the analysis of the NIRSpec demonstration model calibration data. We extracted profiles and integrated intensities of pinhole images on the detector, and compared them to simulations with the IPS. We could successfully reproduce the measured data, but had to tune the input models by significant amounts. It turned out that likely the detector behavior was different between readout modes. However, we could partially verify the algorithms in the IPS, and conclude that simulations are worthless with imprecise input data.

The second paper (Dorner et al., 2011) in section B.3 shows our first simulation of a high-redshift galaxy along with the spectrum extraction. We briefly presented the IPS, the science input interface, and our extraction pipeline. In the end, we described the simulation of a galaxy spectrum at $z = 2$, and showed the obtained spectrum compared to the input.

Confronting the NIRSpec Instrument Performance Simulator outputs with results of the NIRSpec Demonstration Model calibration campaign

Bernhard Dorner^{*a}, Pierre Ferruit^a, Xavier Gnata^b, Stephan M. Birkmann^c, Torsten Böker^c, Guido de Marchi^c, Marco Sirianni^c, Werner J. Hupfer^b, Jess Köhler^b, Manfred-Georg Kolm^b, Ralf Ehrenwinkler^b, Laure Piqueras^a, Emeline Legros^a, Pierre-Jacques Legay^a, Arlette Pécontal-Rousset^a, Aurélien Jarno^a, Aurélien Pons^a

^aUniversité de Lyon, Lyon, F-69003, France; Université Lyon 1, Observatoire de Lyon, 9 Avenue Charles André, Saint-Genis Laval, F-69230; CNRS, UMR 5574, Centre de Recherche Astrophysique de Lyon; Ecole Normale Supérieure de Lyon, Lyon, F-69007, France

^bEADS Astrium GmbH, P.O., 81663 Munich, Germany

^cEuropean Space Agency, Dep. RSSD, Keplerlaan 1, 2200 AG Noordwijk, Netherlands

ABSTRACT

The James Webb Space Telescope (JWST) is the successor mission to the Hubble Space Telescope and will operate in the near- and mid-infrared wavelength ranges. One of the four science instruments on board the spacecraft is the multi-object spectrograph NIRSpec, currently developed by the European Space Agency (ESA) with EADS Astrium Germany GmbH as the prime contractor. NIRSpec will be able to measure the spectra of more than 100 objects simultaneously and will cover the near infrared wavelength range from 0.6 to 5.0 μm at various spectral resolutions. To verify the performance of NIRSpec and simulate future on-ground and in-orbit observations with this instrument, the Instrument Performance Simulator (IPS) software is developed at Centre de Recherche Astrophysique de Lyon (CRAL) as subcontractor to Astrium.

In early and mid-2009, the NIRSpec Demonstration Model (DM), fully representative up to the slit plane, underwent cryogenic tests and calibration runs. The detector was placed at the slit plane in case of the DM to measure specific optical performance aspects. A simplified version of the IPS was prepared, matching the DM configuration and also serving as a testbed for the final software for the flight model. In this paper, we first present the simulation approach used in the IPS, followed by results of the DM calibration campaign. Then, for the first time, simulation outputs are confronted with measured data to verify their validity.

Keywords: JWST, NIRSpec, Optical simulation, Instrument Performance Simulator, Infrared

1. INTRODUCTION

The future James Webb Space Telescope¹ (JWST), scheduled for launch in 2014, will be the successor observatory to the Hubble Space Telescope. The JWST will carry four science instruments for imaging and spectrographic observations between 0.6 and 27 μm . Among them, the Near-Infrared Spectrograph NIRSpec² is designed for low- and mid-resolution spectroscopy in the near-infrared from 0.6 to 5 μm . At the moment, assembly of the NIRSpec Flight Model (FM) is ongoing, and the instrument is nearing completion.³ As a part of the project, a team at Centre de Recherche Astrophysique de Lyon (CRAL) develops the Instrument Performance Simulator (IPS) software.⁴ It is used to explore and verify the instrument characteristics and to generate fake calibration and science exposures.

In mid-2009, the NIRSpec Demonstration Model (DM) successfully completed its calibration campaign.⁵ The goal was to validate the optical and mechanical behavior of the instrument, and to operate the test setup as a whole for the first time. The obtained set of real instrument data was also used to check the IPS input data and its output.

* E-mail: dorner@obs.univ-lyon1.fr; phone +33 4 78 86 85 26; fax +33 4 78 86 83 86

In this paper, at first the DM and its cryo measurement campaign is described in Section 2, followed by a presentation of the according IPS version and goals of the analysis in Section 3. The next Section 4 shows some of the results and observations of the measurements, while Section 5 contains the IPS simulations and comparisons to the real data. In the final Section 6, the conclusions from the DM campaign and the IPS verification are drawn and discussed.

2. DESCRIPTION OF THE DM AND THE TEST CAMPAIGN

The NIRSpec DM is a simplified edition of the final instrument. The optical train in the DM, in contrast to NIRSpec's nominal design,⁶ terminates at the focal plane of the Micro-Shutter Array (MSA), where the detector is placed. Besides, instead of a fully equipped filter wheel, a structural model with a single clear CaF₂ filter substrate is implemented, which has an oversized tri-contagon stop mimicking the edges of the JWST primary mirror. Apart from that, the optical elements up to this first image plane of the instrument are fully representative.

The detector subsystem is an Engineering Test Unit (ETU), consisting of two non-flight grade HAWAII-2RG arrays, but with the same fundamental parameters. Each HgTeCd-array has 2048×2048 pixels with a size of 18 μm. The platescale at the slit plane is about half as large as at real detector plane, therefore the detector area covers only about 50% of the NIRSpec field of view in the spatial direction, while still almost reaching out to the full extension in the spectral direction. The so-called Sensor Chip Assemblies (SCAs) are labeled 491 on the MSA $-x$ -side, and 492 on the $+x$ -side. Two SIDECAR-ASICs control the reset and readout, and convert the signals to Analog-Digital Units (ADUs). The readout is done non-destructively in a MULTIACCUM sampling-up-the-ramp scheme and takes about 10.6 s for one full frame.⁷

The test setup was similar as planned for the FM:⁸ It consisted of NIRSpec placed in a cryo chamber and cooled to operating temperature of about 38 K, a custom-built Calibration Light Source (CLS), and a cryo-mechanism to place either a Field Stop (FS) or a PinHole Mask (PHM) in the focal plane at the instrument entrance. Usage of the stop provided a flatfield illumination, while the PHM emulated point sources with the help of small holes. Due to manufacturing effects, their diameters varied from 1 to 18 μm, but only one pinhole

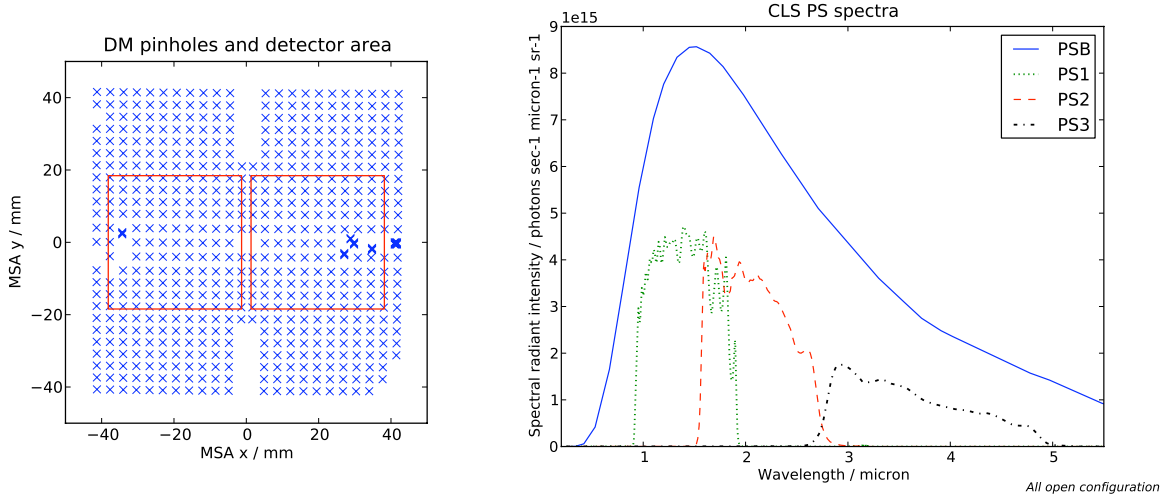


Figure 1. *Left*: Projected location of the pinholes in the MSA plane (blue crosses) and the DM detector field of view, SCA 491 left and SCA 492 right (red lines). The compact groups of pinholes are placed at the future locations of the fixed slits and the integral field unit entrance. The detector coverage is reduced due to the larger platescale at this image plane. *Right*: CLS spectra for the pinhole exposure modes at maximum intensity, data as provided by the manufacturer. Each of the three bandpass filters covers almost one wavelength octave.

was smaller than $3\mu\text{m}$, and 75% were in the range from 5 to $8\mu\text{m}$. The holes were distributed on a regular grid in the area of the microshutters, and some were placed at the projected locations of the fixed slits and the integral field unit entrance (Figure 1 left). The mounting mechanism allowed precise positioning of the PHM in three axes for different focal positions and sub-pixel steps for dithered images.

In the CLS for the DM, a filament light source provided the illumination. Various filters and attenuators mounted on four movable Filter Wheels (FW) allowed the adjustment of the flux level and spectral characteristics of the beam, before it was fed into a large integrating sphere. Elements on the wheels 1 and 2 could be combined to select different nominal light levels, wavelength bands, line filters and fine absorption spectra. The most important one for the DM pinhole exposures were the so-called PS-modes, providing either the full lamp spectrum (PSB), or three wavelength bands, approximately for each scientific region (PS1, PS2, and PS3). These four illuminations are displayed in Figure 1 right. It is obvious that each of the three bandpass filters covers almost one wavelength octave. Although the pinholes were spatially unresolved in the projection, their image was therefore only a broad-band Point Spread Function (PSF). FW number 3 contained 7 slits with different widths to adjust the intensity level by factors of 0.25–4 around the nominal position. It is worth noting that the bandpass filters have different diameters than the open PSB-element, therefore, simply for geometrical reasons, the attenuation factors of FW 3 were different for each mode.

The series of performance test was derived from the suite planned for the FM, but taking into account that the DM does not provide the spectrographic capabilities of the flight model, the amount of exposures was greatly reduced. Before the actual verification of NIRSpec, some preparatory exposures were taken to characterize the CLS intensities in the so-called "CLS" test sequence. One of the main goals of the campaign was to certify the ability of NIRSpec to adjust for varying focal positions at the entrance plane, therefore focal sweeps with the refocus mechanism were analyzed for different focus positions of the PHM. After retrieval of the nominal refocus position, the image geometry was measured with the pinhole images, using sub-pixel dithering to increase the spatial resolution. Finally, the source and instrument flatfield was recorded.

3. THE IPS VERSION FOR THE DM

Initially, to simulate exposures with the DM, an early release of the IPS was done (IPS-1). Unresolved issues in the software and progress on the edition for the FM (IPS-2 and IPS-3) led to the decision to abandon the IPS-1, but slightly modify the IPS-3 to match the simplified configuration of the DM. This offered the opportunity to test the algorithms of the FM version, instead of using a completely different software whose development had already stopped.

Fortunately, few adjustments were necessary. The spectrograph part was bypassed in imaging mode with ideal optics and a 1:1 coordinate transform, and the slit masks in the MSA plane were not applied. In addition, the procedure to generate flatfields was changed to cover the full detector instead of the nominal open MSA area only. All other computation modules could be used in the same way as coded for the FM but fed with data of the DM components.

Almost all IPS algorithms are straightforward applications of well-known physics, including Fourier and geometrical optics. As one exception, the modeling of the diffraction caused by the pinholes in the cryogenic test setup is uncertain. There is no theory describing the passage of light through an opening with roughly the same size as the wavelength itself. However, this diffraction determines the opening of the beam after the pinholes, the amount of light captured by the pupil stop, the throughput ratio in the pinhole exposures, and finally the electron rate recorded for each pinhole. So far, the diffraction effect has been calculated by simple application of standard formulas, which in principle are only valid for the short wavelength range. Now, the data taken allow a test of the calculations by comparing the signal levels in flatfield mode with the intensities of the pinholes. The pinhole images also offer a check of the Fourier propagation module and its data inputs by comparing the broad-band PSF shapes with calculated ones from the IPS. Even though a large part of the DM tests was dedicated to the focal sweeps, there is no comparison possible with the IPS, which is designed for in-focus case only and does not include the necessary near-field Fresnel propagation.

In the instrument model, the coordinate transforms are treated by a paraxial projection with rotations and scaling factors along two axes, and finally a 2D 5th order polynomial for the distortion. To accommodate for

the chromatic effect of the filter, the 25 polynomial coefficients are linearly fitted between data for different wavelengths. With the pinhole images, a precise determination of the distortion and coordinate transforms is possible.

4. DM CAMPAIGN RESULTS

4.1 General observations

In the measurement setup, a high thermal background of more than 100K was present, causing the detector to saturate too quickly to record a flatfield in full frame mode. Therefore the readout was done in window mode, which allowed much shorter exposure times. For the pinhole images, the mask blocked most of the background radiation, and full frame readouts were possible. To each exposure, a second one was taken with the illumination switched off. The pinhole signal level turned out to be rather weak compared to the background, therefore the CLS attenuation wheel 3 was usually set to its full-open position, unless noted otherwise.

The detectors turned out to be another critical point. Tuning of the ASIC microcode finally led to a system with readout noise levels only slightly higher than measured by the manufacturer. Nevertheless, a high reset level of about 10,000 ADUs limited the available dynamic range. It was further restricted to a maximum of 40,000 ADUs to avoid entering the non-linear regime, whose parameters were not well known. The gain was measured to be $1.35 \text{ e}^-/\text{ADU}$. Many dead or hot pixels, especially on chip 492, degraded the data quality. This was critical for the pinhole images, as bad pixels at the pinhole locations heavily disturbed the integrated electron rates or size measurements.

The processing of the raw data was done with the IQLAC software.⁹ After fitting the electron rates to exposures with the CLS signal on and off, the difference image was written into so-called "processed science" files, which contained the final extracted electron rate of the signal itself. Nevertheless, the data severely suffered from the additional photon noise introduced by the strong background, and it was difficult to detect very faint signal levels. The pixels were marked with quality flags, and only the ones without problems or with saturation at a late readout frame were taken into account in the data analysis.

4.2 CLS intensity levels

In the "CLS" test sequence, all available CLS modes were recorded with all FW 3 attenuations. Two different readout windows had been selected on the detectors trying to minimize the number of bad pixels inside. Best performance and FW 3 attenuation coverage was reached with the smallest window size of 32×32 pixels. Even so, the brightest CLS configurations (e.g. PSB) saturated too quickly, only an attenuation by the CLS wheel 3 could reduce the incident flux to measurable levels.

To extract the photon rate per pixel, the exposures were corrected for the Quantum Efficiency (QE) of the detector arrays. For each SCA, there were QE maps measured by the manufacturer at different wavelengths. The data fidelity was uncertain due to possible contamination in the setup. At first, the wavelengths at which the QE was extracted were set close to the maximum of the input spectra (Figure 1 right), but finally adjusted until the four windows on both chips approximately had the same photon rate. This based on the assumption of a perfectly flat illumination, but first simulations of the instrument did not indicate a strong dependence of the light level with field position. Low QE values were uncertain, and pixels with efficiencies smaller than 0.2 were flagged during the radiometry correction, and rejected later on to avoid an impact on the results. In all the processing, noisy pixels were excluded by a 4σ -clipping around the median, while the total number of valid pixels was monitored to guarantee proper statistics. The final images were checked for any inconsistencies, and the average value over both windows and detectors determined, as well as the standard deviation.

In order to compare with the pinhole intensities taken at maximum source level, it was necessary to know the flatfield PSB signal at the full open FW 3 position. As mentioned earlier, the FW 3 attenuations were different for each PS spectrum due to the filter sizes. By using the data for PS1, PS2, PS3, and four values for reduced PSB intensities, the filter diameters and the FW 3 slit sizes were fitted to a geometrical model. With its help, the attenuations of FW 3 for the PSB configuration were calculated and the photon rates for the three missing FW 3 settings extrapolated. The measured values along with the extrapolated PSB data are shown in Figure 2. The behavior of the curves is consistent with a monotone increase at low levels and a small kink at the 159

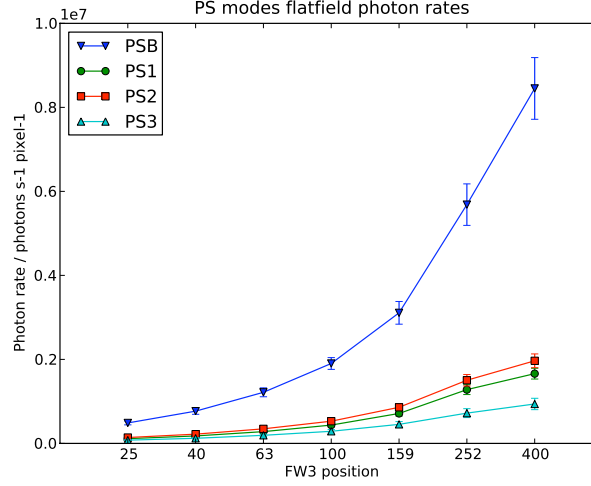


Figure 2. Flatfield photon rates per pixel of the CLS PS modes. All values are as measured, except PSB at 159, 252, and 400 which have been calculated with the filter geometries.

position. Evidently, due to their smaller diameter, the relative increase to the full open position for the band filters is less compared with PSB.

4.3 Pinhole images

After obtaining the nominal focus position, the PHM was used to examine point sources propagated through the NIRSpec re-imaging stage. The goal of sampling a PSF by 2.5 detector pixels in the Full Width - Half Maximum (FWHM) could only be reached from $3\mu\text{m}$ onwards. To increase the sampling and add precision in the position determination, the PHM was moved by 1/3-pixel steps to record a 3×3 dither pattern. Unfortunately, the rotation of the detector with respect to the axes of the cryo mechanism was not taken into account, therefore the dithering grid was tilted by 41.5° , eventually giving an irregular coverage.

To combine the non-uniformly dithered data, the Drizzle-algorithm¹⁰ was chosen, as it is able to cope with non-uniform samplings, increase the spatial resolution, and reject bad pixels, while preserving the surface flux. During the DM campaign, a first coordinate transform had been derived from a single pinhole image. It was used to calculate the position shifts on the detector and correctly place the dithered images on the output grid. In test runs, the optimal drizzle parameters were determined to $scale = 0.5$ and $pixfrac = 0.7$, yielding an output detector image oversampled by a factor 2, containing pixels equivalent to $9\mu\text{m}$ size. Drizzle is known to underestimate the noise, therefore the resulting variances of the pixels have been multiplied by 4 to give a more realistic estimation. The exposures were radiometrically corrected as described in subsection 4.2, and again only the pixels with good quality were selected; for drizzling, an inverse variance weighting was used.

In Figure 3, the pinholes for the fixed slit A_200_1 recorded in PSB on chip 492 are shown. The left image is the detector data in the center PHM position as processed by the IQLAC. Due to many bad pixels, a lot of data is missing, and the image shapes are degraded. The right image displays the same area from the drizzled data. The quality of the upper pinhole shape has improved dramatically, missing data could be filled by the other dither steps. Here, even the six-spoke-star diffraction pattern caused by the tri-contagon stop is partly visible. Nevertheless, drizzling can not do magic, so if too many pixels are missing in the input, as for the central and lower pinhole, then not even this advanced algorithm can recover the original image.

Figure 4 shows the full detector chips after drizzling for the PSB exposures. The pinhole grid pattern is clearly visible, as well as the four groups for the fixed slits. Upon closer inspection, some pinholes reveal a sickle-like feature caused by reflections on the rear side of the pinhole mask and coma like wings as seen in

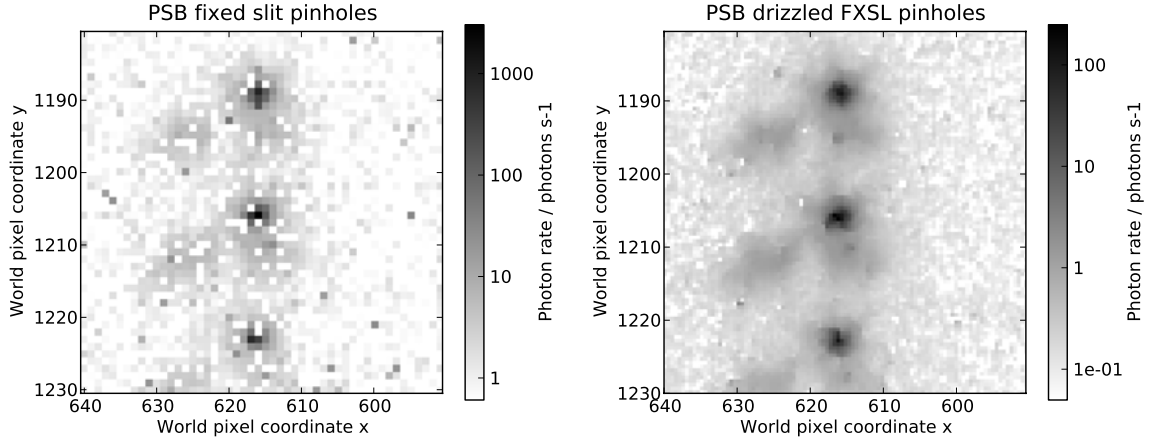


Figure 3. Images of the pinholes for the fixed slit A_200_1 in PSB mode on detector 492 in logarithmic scale. *Left*: Standard processed data in detector resolution with many bad pixels. *Right*: Result after drizzling of 9 dithered exposures in 0.5-pixel resolution. Regions of missing data could be filled, the diffraction pattern of the upper pinhole is partly visible. The tail-like feature extending to the lower left is caused by straylight. The peak photon rate is lower, because the spatial resolution is two times higher, while the surface flux is conserved.

Figure 3. Especially on SCA 491, there is also some straylight present, rising towards the top-left corner. The four triangles at the left and right edges are special fiducials attached to the field stop, which do not cancel out due to noise. Other notable features are the detector readout areas, which all have their own output channel. Four of them extend horizontally across the chips and obviously behave slightly different. Other missing patches result from non-operable or low-efficient pixels.

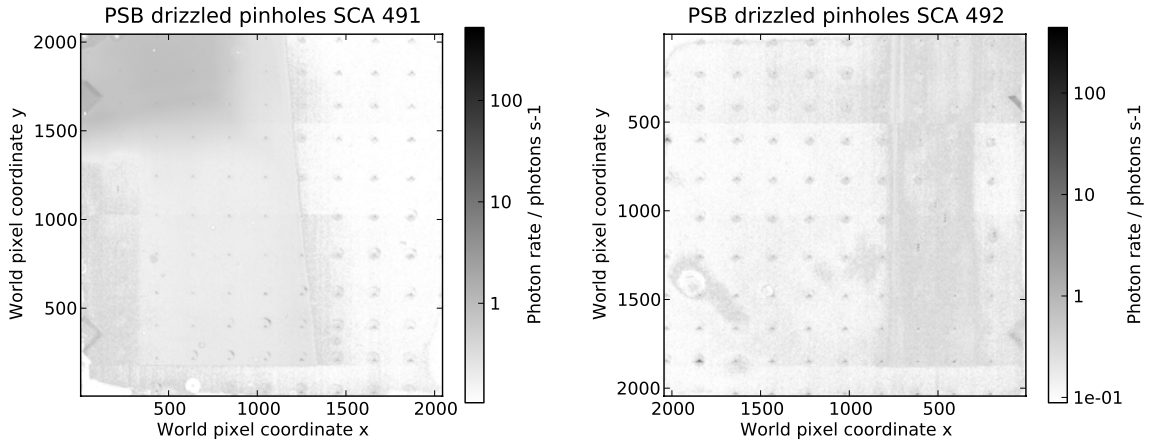


Figure 4. Images of the drizzled full frames in PSB mode of both detectors in logarithmic scale. The single pinholes are visible, as well as many detector defects and patches of straylight. See text for detailed explanation.

4.4 PSF photometry on the pinholes

Even though drizzling improved the quality of the pinhole images somewhat, straylight and bad pixels posed a problem to simple aperture photometry. In addition, for PS3, the photon rates were very low and barely above the background level. Therefore, a PSF photometry was performed.

At first, each pinhole position was predicted using the initially derived coordinate transform, and a 155 detector pixel large window was cut around it. A circular extraction area was defined with the radius corresponding to the second dark ring of an Airy-disc ($2.25 \lambda f\#$) with the wavelength $\lambda = 1.9 \mu\text{m}$ and the nominal F-number $f\# = 12.5$, yielding 2.97 detector pixels. This may seem large for the PS1 and small for PS3, but turned out to catch most of the pinhole intensity for all modes, while stopping before reaching the straylight and background-dominated area. In this extraction circle, the geometrical centroid was calculated and set for the new position of the pinhole image. For each of them, the background level was then measured as the median in an annulus 50–75 detector pixels around the centroid, values clipped at 4σ . The size was necessary to avoid the seckle-shapes reaching into this area, as well as having at maximum one pinhole inside when analyzing the groups for the fixed slits. The single windows were corrected for the individual background, and they were visually controlled to exclude pinholes in bad detector areas, or the ones that displayed an disturbed shape due to missing input pixels.

All the pinhole images were nearly radially symmetric, and two-dimensional Gauss ($A \exp(-r^2/\sigma^2/2)$), Lorentz ($A/(r^2/\sigma^2 + 1)$) and Moffat-functions ($A/(r^2/\sigma^2 + 1)^\beta$) were fitted to the data inside the circle, optimizing the function parameters as well as their center position. For all pinholes, none of the four different centers were separated more than 0.1 pixels, which equals $1.8 \mu\text{m}$, confirming the possibility to use either of them for a precise position measurement. In the left part of Figure 5, a radial plot is shown for the image in PS1 of pinhole 115, which has a diameter of $5.9 \mu\text{m}$. The Gauss fit generally underestimated the center and the wings, while being high on the slope. The Lorentz functions had the opposite problems. The Moffat functions with three free parameters could adjust best to the data. This is not surprising, because each image eventually consists of PSFs attenuated differently by the diffraction at the pinhole, and integrated over the CLS band. The bands were shown in Figure 1 right to be rather broad, and therefore one could not expect a pure diffraction PSF, as can be seen in the center of Figure 5. The residuals of the fits generally show no systematic pattern, therefore the radial symmetry can be confirmed, see Figure 5 right for an example.

The PSF photometry was done over all the pixels inside a box of 3 times the extraction radius. Figure 6 shows the integrated photon rates for each CLS band, PSB on top left, PS1 top right, PS2 bottom left, and PS3 bottom right. In all bands, a general trend for low rates at small diameters is evident. The absolute levels of

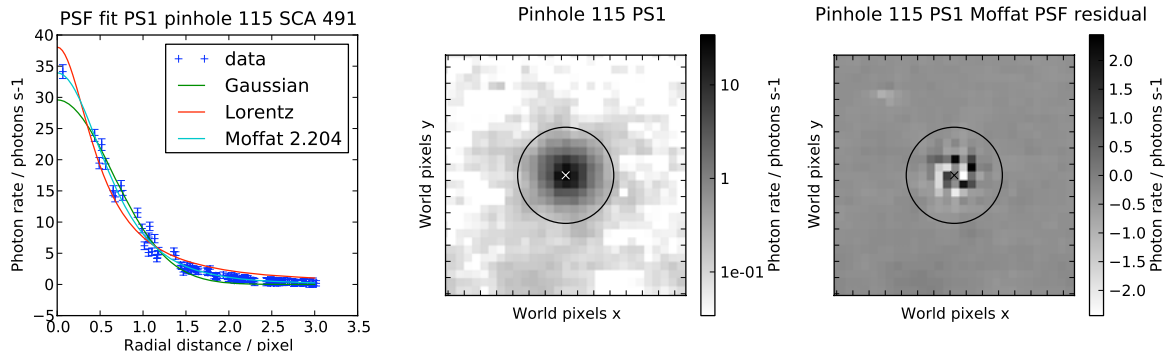


Figure 5. Exemplary results for the PSF fit for pinhole 115 with a diameter of $5.9 \mu\text{m}$, SCA 491 in band PS1. *Left*: Radial profile inside the extraction area with Gauss, Lorentz and Moffat fit curves. The Gauss is too flat in the center and the wings and high on the slope, the Lorentz overshoots the center and wings, while being too low on the slope. The Moffat with $\beta = 2.204$ matches best. *Center*: Image of the pinhole 115 in logarithmic scale. The fitted Moffat center is denoted with the 'x', the circle indicates the extraction radius used for the radial data. *Right*: The residual of the Moffat fit on pinhole 115. The values are considerably lower than the data, no systematic pattern is preset.

PS1 are about half of PSB, PS2 about 1/6. PS3 produced very faint images, the integrated rates are only about 1/30 of PSB, the peak values of many pinholes between 4–8 photons/s/detector pixel. Some data points are considerably lower than the general trend, especially the ones for diameters between 8 and 10 μm on SCA 492. This may be caused by wrong diameter data or non-circular pinhole shapes, increasing the diffraction losses. In the single data reduction steps, none of them posed problems or revealed abnormal features. It is also visible that the bluer bands PSB, PS1, and PS2 are stronger affected by the increasing diffraction towards smaller pinholes, while the flux is equally reduced for PS3 across all sizes.

4.5 Instrument geometry

Having improved the quality of the pinhole images, it was possible to derive more accurate coordinate transforms by simply using more pinholes, as well as taking advantage of the higher precision of the PSF fitting. Besides, the initial distortion fit was derived for one wavelength only. Now, for each band a separate set was available, from which the common pinholes were selected, leaving 149 in total. In spectral dimension, approximately the peak or center wavelength was used for the fit, that is 1.4, 1.5, 1.8, and 3.0 μm for PS1, PSB, PS2, and PS3 (compare with Figure 1 right).

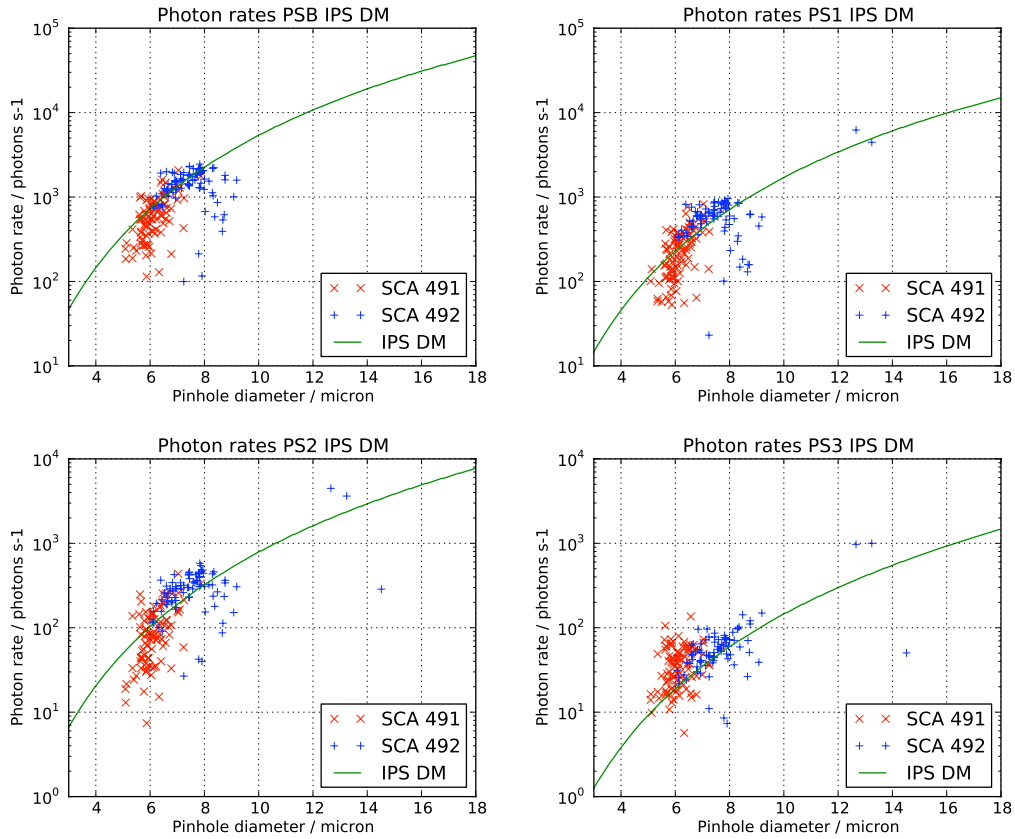


Figure 6. Integrated pinhole photon rates from Moffat PSF photometry in the four CLS PS bands (blue and red crosses). *Top left:* PSB, *top right:* PS1, *bottom left:* PS2, *bottom right:* PS3. Some of the pinholes seem to have either a wrong diameter, or a non-circular shape, which can lead to higher diffraction losses and lower the photon rate. Especially the values of the pinholes between 8 and 10 μm are questionable. The three large pinholes are missing in the PSB data due to pixel saturation and the value at 14.3 μm is clearly wrong in all bands. Values for diameters smaller than 6 μm are widely scattered. The green line is the final rate simulated by the IPS after tuning the inputs.

The exact geometry of the detector, especially the spacing of the two SCAs was not available before the test campaign. A wrong value of the distance between the chips introduces an error in the coordinate transform, which cannot be compensated either by a scaling factor or the polynomial, as the relative distances of the points on each array do not change. By introducing an artificial spacing in the input for the distortion fit and minimizing the residual, it was possible to retrieve a best-fit spacing. Eventually, this may not correspond to the real physical value, but the associated coordinate transform is optimal and simulations then match the measurements best. The final distortion residual, being the RMS of the differences of measured versus simulated points for the input data, is $1.5\mu\text{m}$ on average for all four wavelengths, which corresponds to $1/12^{\text{th}}$ of a detector pixel.

5. IPS SIMULATIONS AND VERIFICATION

5.1 IPS model data

The first step in using the IPS is the creation of the models, that include instrument parameters and data curves. The NIRSpec DM was described with: the total wavefront error of the instrument from ambient measurements (little change expected with temperature), reflectivities of the mirrors from ambient measurements with a simulated cryo-improvement, throughput of the CaF_2 -filter at cryo, pupil-stop shape from an as-built optical model, coordinate transform and detector geometry as derived above from the pinhole exposures, and a perfect detector with 100% quantum efficiency. The model of the CLS contained the source spectra as shown in Figure 1 right, multiplied with the measured reflectivity of a relay mirror inside the cryo chamber. The FW 3 attenuations were derived from the filter geometry and individually set for each PS band. The ideal detector is needed because the measurements to compare with are already radiometrically corrected. Besides, for simple radiometry simulations it is sufficient to only use photon rates, instead of full readouts which would have to be processed.

5.2 CLS flatfield rates

In contrast to the instrument data, the CLS spectra were uncertain concerning the spectral shape and the absolute level. For verification, a flatfield was simulated equal to the "CLS" test sequence. In the respective detector windows, the average photon rates were extracted and compared with the measured data. Various adjustments to the spectral shape and the band intensities were compared. The best match on average delivered the data already shown in Figure 1 right. Nevertheless, the overall absolute level was too low by a factor of 5.8. To rule out errors in the IPS, a simple calculation was done, exactly reproducing the simulations. Finally, to individually reach the measured values, the initial PS spectra were multiplied with 5.79, 5.89, 5.72, and 5.82 for PSB, PS1, PS2, and PS3.

The reason for this discrepancy is unclear. The most likely explanation is an error in the CLS data, especially as the output spectrum was not directly measured, but modeled to meet an integrated intensity, which had also only been determined in certain bands.

5.3 Pinhole intensities and images

Switching from flatfield to pinhole exposures required only a change of the cryo mask at the instrument entrance. Therefore, in the simulation, the purely geometrical throughput of the pupil stop is replaced with a spectral attenuation caused by the diffraction at the pinholes. This effect depends both on the diameter d and the wavelength λ , and is therefore different for each pinhole. In the approximation $d \gg \lambda$, it can be described as a 2D-convolution of the transmitted beam from the CLS by an Airy-function. The spectral throughput is then the ratio of the spectral flux captured by the pupil stop, and the total incoming spectral flux. The diffraction can be expressed as a function of the ratio pinhole diameter over wavelength $\gamma = d/\lambda$. To minimize calculation times in the IPS, in the last step of the model creation, the throughput is calculated for the range of γ necessary to cover the pinhole diameters and the spectra; The blue line in Figure 7 shows the data as predicted for the DM. Larger γ yield higher throughput, as less intensity is diffracted out of the pupil stop. When computing the electron rates for a pinhole, the spectrum is then attenuated with the corresponding values from this curve.

For the simulations, a fake pinhole mask was created containing 392 holes with diameters equally spaced from 1 to $18\mu\text{m}$. In combination with the CLS spectra, this corresponds to a range $0.167 \leq \gamma \leq 36$, while the measurements from the DM cover data for $0.9 \leq \gamma \leq 16$ with overlap between the single bands. The total

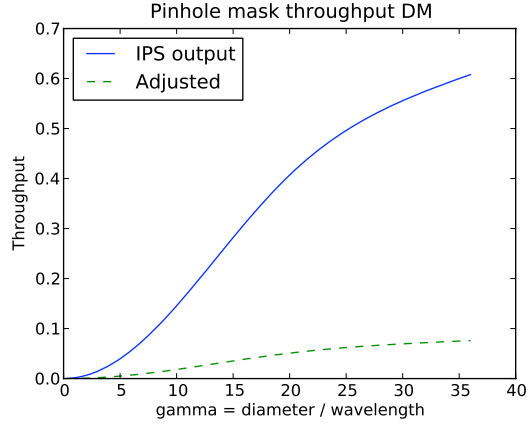


Figure 7. Pinhole diffraction throughput curve in dependence of $\gamma = d/\lambda$, calculated by the IPS (blue line) and adjusted to measurements (green dashed line). Large pinholes diffract less intensity out of the pupil stop, while the diffraction severely attenuates the spectra for small γ . The adjusted data is unrealistically low for large pinholes.

integrated photon rates were retrieved from the detector maps by summing over a box of 37×37 pixels at the pinhole locations, capturing all incoming photons.

A first simulation predicted far too high intensities across all bands and wavelengths. Again, to exclude mistakes in the IPS, the values were reproduced by simple calculations using the same throughput and spectra. To determine the correct curve, several fits to the measurements were done, but excluding the points falling off the general trend. In the end, a simple scaling of the pinhole throughput curve by $1/8$ was found to be best, while not tampering the diffraction curve for $\gamma > 14$. The adjusted curve is plotted in Figure 7 with the green dashed line. The simulated rates are shown in Figure 6 by the green lines. They are correct for the diameters from $6\text{--}8\text{ }\mu\text{m}$, which are the majority. The drop at small pinholes is reproduced worse, as well as the data for PS3 in general. On the other hand, this band is also the least reliable, as the signal there was very noisy and barely above the background. Considering the large scatter in these areas over one order of magnitude, the simulation is still of good quality, and the values for large diameters are well predicted.

To compare the shapes of the pinhole images, dithered exposures were generated similar to the DM test. Inter-pixel crosstalk was applied and synthetic noise calculated,⁷ derived from the photon rates, average measured

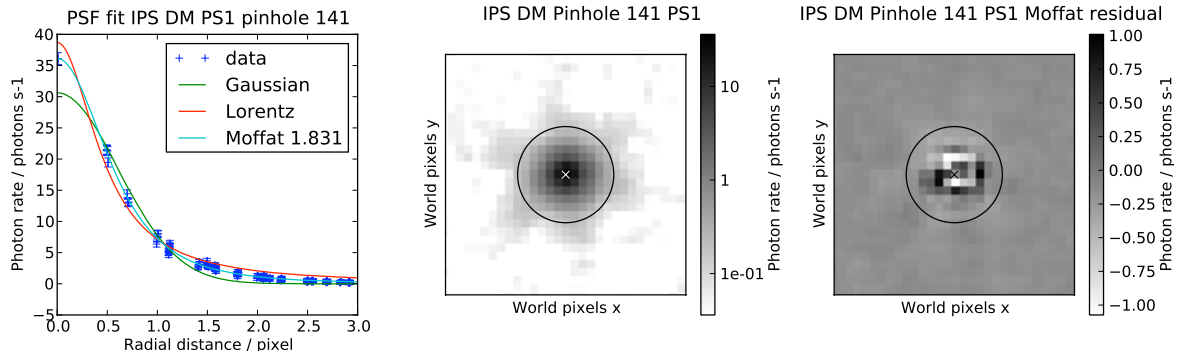


Figure 8. Data for a simulated dithered pinhole with $7.1\text{ }\mu\text{m}$ diameter, integrated photon rate similar to Figure 5. *Left:* Radial plot and fit curves. *Center:* Oversampled pinhole image after drizzling. *Right:* Residual after subtraction of the fitted Moffat PSF.

background, and readout noise. The data has been processed as described above. Figure 8 shows a fake pinhole with 7.1 μm diameter, but approximately the same integrated photon rate as the real 115 in Figure 5. The radial profile, shape and size match very well. Using a pinhole with the same diameter as for 115, gives an integrated rate reduced by a factor of 2, but still equal images. This rather points to a wrong diameter in the pinhole mask data than to errors in the IPS or processing, especially because the PSF photometry data of the simulations agreed with the noise-free photometry.

6. DISCUSSION AND CONCLUSION

The NIRSpec DM calibration campaign was finished successfully, all the requirements could be verified. It was the first time that the complete calibration setup was used, thus it is not surprising to discover points to improve. The largest issue was the high thermal background. This was analyzed afterwards and measures have been taken to optimize the cryo setup, resulting in a reduced background level by a factor of 7–8.

Deviations in the source levels and spectra could only be discovered by simulations, while the real spectral shapes remain vague. In the FM CLS, this problem has been resolved by calibrating spectra for defined operational modes in absolute levels. Another critical point was the quality of the detectors. Even if not expected to be flight-like, the large number of bad pixels made it difficult to extract meaningful information for the pinhole and focus exposures. This could only be compensated partially by the processing of dithered images. In addition, the available quantum efficiency data was shaky and had only a low spectral resolution. In combination with the high background, the rather small linear range led to problems in flatfield mode, as well as for very bright pinholes, which saturated early. All the points concerning the detectors are expected to be strongly improved in the FM, thanks to the better quality and level of characterization of the SCAs.

Verification of the IPS had to be done gradually. In the frame of the delivery to EADS/Astrium, the software is tested against standardized inputs; most of the algorithms are applications of standard phenomena, and were checked with simple calculations. Therefore, discrepancies in the flatfields could only result from the input data. After increasing the CLS levels by about a factor of 5.8, the pinhole intensities were far too high. By reducing the diffraction curve by a factor of 8, the simulations were matched the measurements, but the resulting throughput values for large pinholes became unrealistically low. Besides, the two scalings partly compensate each other: A simulation with non-modified data would produce pinhole intensities only about 1.3 times too high. The reason for the large discrepancy is unknown, likely it is an inconsistency between detector readouts in window mode and full frame, propagating directly into the source and pinhole diffraction in the presented analysis. Nevertheless, the simulations have been proven to produce PSFs as observed, and the pinhole diffraction may still be described sufficiently correct. Therefore, the IPS will be very helpful in the preparation of the FM test campaign.

To sum it up, the DM campaign was an important milestone in the development of NIRSpec. It revealed weaknesses in the test setup, data processing and test procedures, which can be taken care of in preparation for the FM calibration. It was also useful to compare the IPS output with real data for the first time, which confirmed the "garbage in, garbage out" principle. Specifically, without precise inputs for the models, the simulations are worthless for predictions and fidelity can only be achieved after comparison with measurements, if they are of good quality themselves. Despite limited knowledge of the behavior of key components in the test setup, the algorithms of the IPS could at least be partly verified.

ACKNOWLEDGMENTS

The authors want to thank all the people from EADS/Astrium, ESA, NASA, and IABG involved in the DM campaign for their support and contribution to the successful completion. The research leading to these results has received funding from the European Community's Seventh Framework Program (FP7/2007-2013) under grant agreement nr. PITN-GA-2008-214227 - ELIXIR.

REFERENCES

- [1] Gardner, J. P., Mather, J. C., Clampin, M., Doyon, R., Greenhouse, M. A., Hammel, H. B., Hutchings, J. B., Jakobsen, P., Lilly, S. J., Long, K. S., Lunine, J. I., McCaughrean, M. J., Mountain, M., Nella, J.,

- Rieke, G. H., Rieke, M. J., Rix, H., Smith, E. P., Sonneborn, G., Stiavelli, M., Stockman, H. S., Windhorst, R. A., and Wright, G. S., “The James Webb Space Telescope,” *Space Science Reviews* **123**, 485–606 (Apr. 2006).
- [2] Bagnasco, G., Kolm, M., Ferruit, P., Honnen, K., Köhler, J., Lemke, R., Maschmann, M., Melf, M., Noyer, G., Rumler, P., Salvignol, J., Strada, P., and Te Plate, M., “Overview of the near-infrared spectrograph (NIRSpec) instrument on-board the James Webb Space Telescope (JWST),” *Proc. SPIE* **6692** (2007).
- [3] Birkmann, S., Böker, T., Jakobsen, P., de Marchi, G., Sirianni, M., Bagnasco, G., Jensen, P., te Plate, M., Rumler, P., Salvignol, J., Strada, P., Kolm, M., Gnata, X., Honnen, K., Köhler, J., Lemke, R., Maschmann, M., Melf, M., Ferruit, P., and Dorner, B., “Status of the JWST NIRSpec instrument,” *Proc. SPIE* **7731** (2010).
- [4] Piqueras, L., Legros, E., Pons, A., Legay, P., Ferruit, P., Dorner, B., Pecontal-Rousset, A., Gnata, X., and Mosner, P., “The JWST/NIRSpec instrument performance simulator software,” *Proc. SPIE* **7738** (2010).
- [5] Boeker, T., Birkmann, S., de Marchi, G., Jakobsen, P., Sirianni, M., Ferruit, P., Gnata, X., Mosner, P., Ehrenwinkler, R., and Beck, T., “The NIRSpec Demonstration Model Test Campaign,” *Bulletin of the American Astronomical Society* **41**, 396 (Jan. 2010).
- [6] te Plate, M., Holota, W., Posselt, W., Koehler, J., Melf, M., Bagnasco, G., and Marenaci, P., “Opto-mechanical design of the near infrared spectrograph NIRSpec,” *Proc. SPIE* **5904**, 185–198 (2005).
- [7] Rauscher, B. J., Fox, O., Ferruit, P., Hill, R. J., Waczynski, A., Wen, Y., Xia-Serafino, W., Mott, B., Alexander, D., Brambora, C. K., Derro, R., Engler, C., Garrison, M. B., Johnson, T., Manthripragada, S. S., Marsh, J. M., Marshall, C., Martineau, R. J., Shakoorzadeh, K. B., Wilson, D., Roher, W. D., Smith, M., Cabelli, C., Garnett, J., Loose, M., Wong-Anglin, S., Zandian, M., Cheng, E., Ellis, T., Howe, B., Jurado, M., Lee, G., Nieznanski, J., Wallis, P., York, J., Regan, M. W., Hall, D. N. B., Hodapp, K. W., Böker, T., De Marchi, G., Jakobsen, P., and Strada, P., “Detectors for the James Webb Space Telescope Near-Infrared Spectrograph. I. Readout Mode, Noise Model, and Calibration Considerations,” *PASP* **119**, 768–786 (July 2007).
- [8] Bagnasco, G., Ferruit, P., Böker, T., Closs, M., Dorner, B., Gnata, X., Koehler, J., Kolm, M., Kuechel, C., Langenbach, H., Melf, M., Pittet, J., Te Plate, M., and Wetteman, T., “The on-ground calibration of the Near Infrared Spectrograph (NIRSpec) instrument on-board the James Webb Space Telescope (JWST),” *Proc. SPIE* **7010** (2008).
- [9] Gerssen, J., Janssen, K., Meeus, G., Hupfer, W., Gnata, X., Ferruit, P., Roth, M., Mosner, P., de Marchi, G., and Böker, T., “IQLAC: a data analysis system for the NIRSpec on-ground test campaign,” *Proc. SPIE* **7010** (2008).
- [10] Fruchter, A. S. and Hook, R. N., “Drizzle: A Method for the Linear Reconstruction of Undersampled Images,” *PASP* **114**, 144–152 (Feb. 2002).

Astronomical Data Analysis Software and Systems XX
ASP Conference Series, Vol. 442
Ian N. Evans, Alberto Accomazzi, Douglas J. Mink, and Arnold H. Rots, eds.
© 2011 Astronomical Society of the Pacific

First Simulation and Data Reduction of a JWST/NIRSpec Observation

Bernhard Dorner,¹ Pierre Ferruit,² Laure Piqueras,¹ Emeline Legros,¹
Arlette Pécontal,¹ Aurélien Jarno,¹ Aurélien Pons,¹ Xavier Gnata,³ and
Camilla Pacifici⁴

¹*Université de Lyon, Lyon, F-69003, France;*
Université Lyon 1, Observatoire de Lyon,
9 Avenue Charles André, Saint-Genis Laval, F-69230;
CNRS, UMR 5574, Centre de Recherche Astrophysique de Lyon;
Ecole Normale Supérieure de Lyon, Lyon, F-69007, France

²*European Space Agency, Dep. RSSD,*
Keplerlaan 1, 2200 AG Noordwijk, Netherlands

³*EADS Astrium GmbH, P.O., 81663 Munich, Germany*

⁴*Institut d'Astrophysique de Paris, 98bis Boulevard Arago, 75014 Paris, France*

Abstract. The James Webb Space Telescope (JWST), a joint project by NASA, ESA, and CSA, is the successor mission to the Hubble Space Telescope. One of the four science instruments of the observatory is the multi-object spectrograph NIRSpec. It will be able to measure the spectra of more than 100 objects simultaneously and will cover the near infrared wavelength range from 0.6 to 5.0 μm at various spectral resolutions. Due to the instrument complexity, it was seen as necessary to create an instrument simulator for studies of the instrument performance, optical and geometrical effects, as well as the creation of realistic calibration and science exposures to develop and test data analysis tools. The Centre de Recherche Astrophysique de Lyon (CRAL), as subcontractor to EADS Astrium GmbH, is developing this Instrument Performance Simulator (IPS) software for NIRSpec. One of the key objectives of the IPS is to generate realistic simulated JWST/NIRSpec exposures of astrophysical sources, providing a check of NIRSpec in-orbit performance and inputs for the definition of the best observation strategies. We briefly summarize how the different input data is used for the instrument model, and present a first spectral extraction pipeline tailored to the IPS. Following this, we show the simulated exposure of an observation of a typical NIRSpec target, a modeled redshifted galaxy, and compare the finally extracted spectrum with the input.

1. Introduction

The James Webb Space Telescope (JWST, Gardner et al. 2006), scheduled for launch in 2014, will be the successor observatory to the Hubble Space Telescope. One of the science instruments, the Near-Infrared Spectrograph NIRSpec (Bagnasco et al. 2007), is designed for low- and mid-resolution spectroscopy in the near-infrared from 0.6 to 5 μm . A team at the Centre de Recherche Astrophysique de Lyon (CRAL) is developing the NIRSpec Instrument Performance Simulator (IPS) software (Piqueras et al. 2010), which provides an end-to-end optical and performance simulation of the telescope and the instrument, including the detector readout. The software package is written in C/C++ and is close to delivery to EADS Astrium.

We defined a simple file interface to feed science target data into the IPS, and simulated a typical science case, a sample galaxy at redshift $z = 2$. In addition we created a first data processing pipeline for IPS output. The extracted spectrum of the exposure is compared with the input galaxy spectrum and is found to match very well.

2. IPS Sky Simulations

2.1. IPS Data Flow

The instrument model in the IPS is based on data from different subsystems, as the optics, microshutters and slits, dispersers, and detectors. The available light sources comprise ground and on-board calibration lamps and sources on the sky. Combining the instrument data with one of the source modules, an “IPS model” is created which describes the selected instrument mode. From the source description, a source file is computed and used in combination with the IPS model to calculate a noiseless electron count rate map, a first main simulation output. The tool to create the NIRSpec MULTIACCUM data cube with the sequential non-destructive readouts is a separate module. It uses the detector description and the selected readout parameters to generate a realistic raw data file from the electron rate maps.

2.2. Sky Scene Interface

The native IPS source file format is very general to accommodate various source types, but not well suited to exchange data with external users. Besides, the source placement for observations is only possible on the sky. In order to test the instrument performance in certain scenarios, it is more convenient to place the sources directly in shutters or slits. Therefore, we established a set of input FITS files that contain common data types: single spectra, an intensity image and a spectrum, and a data cube. Furthermore, we defined a scene description that allows users to place the sources relative to single shutters, slits, slices, or on the sky. A set of IDL scripts and Python classes were prepared, that also give examples how to construct exposure scenes from external data.

3. Data Processing and Results

3.1. Extraction Pipeline Workflow

The final IPS output is a FITS datacube with raw data. To ease the comparison with the input, we created a first processing pipeline for NIRSpec. It follows the classical approach of long-slit spectroscopy, adjusted to the multi-object capabilities of the instrument. The pipeline inputs are the fitted slopes from the readout cube, providing gain and linearity corrected electron rate, variance, and quality flags for each pixel. They can be generated from the readout simulation with external pre-processing software, or by adding analytic noise and pixel crosstalk to the electron rate maps.

Each target exposure is divided by a simulated flatfield taken with the same spectrograph configuration and the internal calibration lamp. The pipeline then uses the instrument model data from the IPS to predict the spectrum location and extract the traces for all the targets in the observation. It rectifies the spectra to a uniform spectral and spatial sampling, creates the target spectra, and subtracts the sky background.

For the absolute radiometric calibration, there is a set of simulated reference star exposures, probing the field of view and different positions inside shutters. These exposures are processed the same way as science targets and constitute the photometric reference spectrum set. For each observed target, the local calibration spectrum is interpolated from these reference spectra according to the position on sky and inside the slit. Applied to the background subtracted target spectrum, the final calibrated spectrum is obtained. Depending on the extraction parameters, this is a one- or two-dimensional spectrum with uniform wavelength sampling, containing the spectral photon rate, variance, and quality flags.

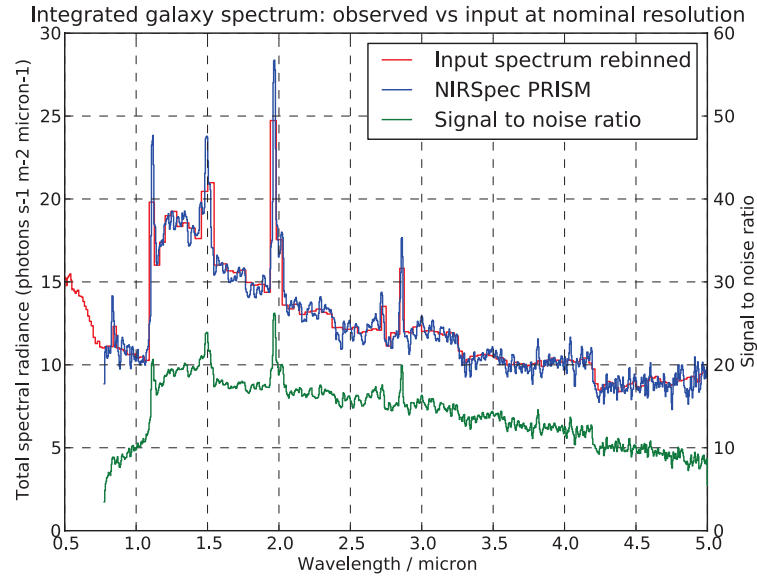


Figure 1. Comparison of a simulated and extracted NIRSpec spectrum (blue) and input galaxy spectrum (red) for the prism mode, including the derived signal to noise ratio (green).

3.2. Extraction Pipeline Framework

All the spectrum extraction has been coded in Python in a very modular approach. The main class encompasses the top-level methods of the pipeline, as determination of the exposure parameters, data extraction and processing, data file I/O, and logging. These methods make use of classes for single pipeline models, which contain characterization data of the instrument modules read from the IPS database. Those classes again use low-level classes from the framework to handle the IPS input data. They offer methods to read IPS data files and for basic calculations directly related to the instrument module. In addition, there is a set of data file classes for the different data products (count rate maps and spectra), providing file I/O, data arithmetic, and graphical output. All the pipeline classes use a dedicated calculation library that provides generic mathematical functions, partly extended to handle pixel quality flags. Scripting the pipeline is therefore possible on a high level using the main class' methods only.

3.3. Example Simulation

One of the major science cases of NIRSpec is the multi-object observation of high-redshift galaxies. We used a simulated galaxy spectrum at redshift $z = 2$ (Pacifci et al., in prep.), and put it as a point source at the center of a minislit (1×3 shutters). In addition, we set an average Zodiacal spectrum as a background source covering the complete field of view. The observation was simulated with the prism at a spectral resolution of $R \approx 100$. We added synthetic noise to the electron rates corresponding to a standard exposure duration of 902 s. With the same spectrograph configuration we also simulated a flatfield exposure with the internal calibration light source.

The spectrum was processed as described in subsection 3.1 and finally collapsed in the spatial dimension. We rebinned the input galaxy spectrum to the nominal spectral resolution of the instrument to compare it with the simulated data. Figure 1 shows the plot of the extracted spectrum (blue) and the rebinned input spectrum (red). Both curves match very well. The obtained result is slightly better resolved, as the spectral resolution element of a point source is smaller than the nominal 2.2 detector pixels. The signal to noise ratio was determined from the

propagated variances in each pixel and is plotted in the green curve, confirming a good spectrum quality beyond wavelengths of $1.1\ \mu\text{m}$.

4. Conclusion and Outlook

The IPS provides a realistic simulation of NIRSpec of in-orbit observations. We designed a simple data interface for astronomical users and started the first on-sky simulations with as-built instrument models. In addition, we created a spectrum extraction pipeline for IPS output. So far, point sources have been successfully extracted and the pipeline is now extended to other sources and instrument modes. The software will also be used during the upcoming instrument cryo tests and can serve as a testbed for different extraction techniques.

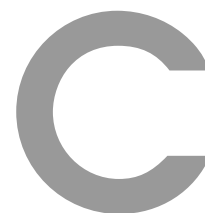
Acknowledgments. BD and CP are funded by the European Community's Seventh Framework Program (FP7/2007-2013) under grant agreement PITN-GA-2008-214227 - ELIXIR, and thank Stephane Charlot for the network lead and all the encouragement. All authors would like to thank the engineers at EADS Astrium and the ESA JWST science team members for the great cooperation and inspiring discussions.

References

- Bagnasco, G., et al. 2007, in *Cryogenic Optical Systems and Instruments XII*, edited by J. B. Heaney, & L. G. Burrieschi (Bellingham, WA: SPIE), vol. 6692 of Proc. SPIE, 66920M
- Gardner, J. P., et al. 2006, *Space Sci. Rev.*, 123, 485
- Piqueras, L., et al. 2010, in *Modeling, Systems Engineering, and Project Management for Astronomy IV*, edited by G. Z. Angeli, & P. Dierickx (Bellingham, WA: SPIE), vol. 7738 of Proc. SPIE, 773812

<Oasis> brb
 <passi> ok
 <Oasis> re
 <passi> wb
 <Oasis> thx
 <passi> np
 <Oasis> cs?
 <passi> ip?
 <spanky> ihr spinnt doch

<http://german-bash.org/11488>



Acronyms

Acronym	Expression
ADC	Analog-Digital Converter
ADU	Analog-Digital Unit
arcmin	arcminutes
arcsec	arcsecond
ATP	Acceptance Test Procedure
CAA	CALibration Assembly
CAL	CALibration optics
CAM	CAMera optics
CDS	Correlated Double Sampling
CLS	Calibration Light Source
COL	COLlimator optics
CRAL	Centre de Recherche Astrophysique de Lyon
CSA	Canadian Space Agency
DM	Demonstration Model
ESA	European Space Agency
FFT	Fast Fourier Transform
FGS	Fine Guidance Sensor
FM1	Flight Model 1
FPA	Focal Plane Array
FS	Field Stop
FSM	Field Stop Mask
FW	Filter Wheel <i>[in CLS]</i>
FWA	Filter Wheel Assembly
FWHM	Full Width at Half Maximum

Continued on next page...

Acronym	Expression
FXSL	FiXed SLits
GWA	Grating Wheel Assembly
HST	Hubble Space Telescope
HZ	Habitable Zone
iFFT	inverse Fast Fourier Transform
IFU	Integral Field Unit
IPS	Instrument Performance Simulator
IR	InfraRed
ISIM	Integrated Science Instrument Module
JWST	James Webb Space Telescope
mas	milliarcsecond
MSA	MicroShutter Assembly
NASA	National Aeronautics and Space Administration
NIPPLS	NIRSpec IPS Pipeline Software
NIRCam	Near-InfraRed Camera
NIRISS	Near-InfraRed Imaging Spectrograph
NIRSpec	Near-InfraRed Spectrograph
MIRI	Mid-InfraRed Instrument
OTE	Optical Telescope Element
OTEIP	OTE Image Plane
PHM	PinHole Mask
PSF	Point Spread Function
RMA	Refocusing Mirror Assembly
RMS	Root Mean-Square
RSS	Root of the Sum of the Squares
SCA	Sensor Chip Assembly
SHS	Shack-Hartmann Sensor
SiC	Silicon Carbide
SNR	Signal to Noise Ratio
TMA	Three-Mirror Anastigmat
UDF	Ultra-Deep Field
WFE	WaveFront Error

Bibliography

- G. Bagnasco, M. Kolm, P. Ferruit, K. Honnen, J. Köhler, R. Lemke, M. Maschmann, M. Melf, G. Noyer, P. Rumler, J.-C. Salvignol, P. Strada, and M. Te Plate. Overview of the near-infrared spectrograph (NIRSpec) instrument on-board the James Webb Space Telescope (JWST). In *Society of Photo-Optical Instrumentation Engineers (SPIE) Conference Series*, volume 6692, 2007. doi: 10.1117/12.735602.
- G. Bagnasco, P. Ferruit, T. Böker, M. Closs, B. Dorner, X. Gnata, J. Köhler, M. Kolm, C. Kuechel, H. Langenbach, M. Melf, J.-F. Pittet, M. Te Plate, and T. Wetteman. The on-ground calibration of the Near Infrared Spectrograph (NIRSpec) instrument on-board the James Webb Space Telescope (JWST). In *Society of Photo-Optical Instrumentation Engineers (SPIE) Conference Series*, volume 7010, 2008. doi: 10.1117/12.788172.
- J. L. Bean, E. Miller-Ricci Kempton, and D. Homeier. A ground-based transmission spectrum of the super-Earth exoplanet GJ 1214b. *Nature*, 468:669–672, December 2010. doi: 10.1038/nature09596.
- T. Beck. STScI NIRSpec Calibration Pipeline Processing Description. Technical Report JWST-STScI-001859, SM-12, Space Telescope Science Institute, 2009.
- S. V. W. Beckwith, M. Stiavelli, A. M. Koekemoer, J. A. R. Caldwell, H. C. Ferguson, R. Hook, R. A. Lucas, L. E. Bergeron, M. Corbin, S. Jogee, N. Panagia, M. Robberto, P. Royle, R. S. Somerville, and M. Sosey. The Hubble Ultra Deep Field. *AJ*, 132: 1729–1755, November 2006. doi: 10.1086/507302.
- Z. K. Berta, D. Charbonneau, J. Bean, J. Irwin, C. J. Burke, J.-M. Désert, P. Nutzman, and E. E. Falco. The GJ1214 Super-Earth System: Stellar Variability, New Transits, and a Search for Additional Planets. *ApJ*, 736:12, July 2011. doi: 10.1088/0004-637X/736/1/12.
- S. M. Birkmann, T. Böker, P. Ferruit, G. Giardino, P. Jakobsen, G. de Marchi, M. Sirianni, M. B. J. Te Plate, J.-C. Savignol, X. Gnata, T. Wettemann, B. Dorner, G. Cresci, F. Rosales-Ortega, M. Stuhlinger, R. Cole, J. Tandy, and C. Brockley-Blatt. Wavelength calibration of the JWST near-infrared spectrograph (NIRSpec). In *Society of Photo-Optical Instrumentation Engineers (SPIE) Conference Series*, volume 8150, September 2011. doi: 10.1117/12.893896.

- L. Blackmore, E. Murray, D. P. Scharf, M. Aung, D. Bayard, P. Brugarolas, F. Hadaegh, A. Lee, M. Milman, and B. Sirlin, S. Kang. Instrument pointing capabilities: past, present, and future. In *AAS Guidance and Control Conference*. Jet Propulsion Laboratory, National Aeronautics and Space Administration, February 2011. URL <http://hdl.handle.net/2014/41915>.
- T. Böker, S. Birkmann, G. de Marchi, P. Jakobsen, M. Sirianni, P. Ferruit, X. Gnata, P. Mosner, R. Ehrenwinkler, and T. Beck. The NIRSpec Demonstration Model Test Campaign. In *American Astronomical Society Meeting Abstracts #215*, volume 42 of *Bulletin of the American Astronomical Society*, page #439.06, January 2010.
- A. J. Bunker, S. Wilkins, R. S. Ellis, D. P. Stark, S. Lorenzoni, K. Chiu, M. Lacy, M. J. Jarvis, and S. Hickey. The contribution of high-redshift galaxies to cosmic reionization: new results from deep WFC3 imaging of the Hubble Ultra Deep Field. *MNRAS*, 409:855–866, December 2010. doi: 10.1111/j.1365-2966.2010.17350.x.
- D. Charbonneau, T. M. Brown, R. W. Noyes, and R. L. Gilliland. Detection of an Extrasolar Planet Atmosphere. *ApJ*, 568:377–384, March 2002. doi: 10.1086/338770.
- D. Charbonneau, L. E. Allen, S. T. Megeath, G. Torres, R. Alonso, T. M. Brown, R. L. Gilliland, D. W. Latham, G. Mandushev, F. T. O’Donovan, and A. Sozzetti. Detection of Thermal Emission from an Extrasolar Planet. *ApJ*, 626:523–529, June 2005. doi: 10.1086/429991.
- D. Charbonneau, Z. K. Berta, J. Irwin, C. J. Burke, P. Nutzman, L. A. Buchhave, C. Lovis, X. Bonfils, D. W. Latham, S. Udry, R. A. Murray-Clay, M. J. Holman, E. E. Falco, J. N. Winn, D. Queloz, F. Pepe, M. Mayor, X. Delfosse, and T. Forveille. A super-Earth transiting a nearby low-mass star. *Nature*, 462:891–894, December 2009. doi: 10.1038/nature08679.
- M. F. Closs, P. Ferruit, D. R. Lobb, W. R. Preuss, S. Rolt, and R. G. Talbot. The Integral Field Unit on the James Webb Space Telescope’s Near-Infrared Spectrograph. In *Society of Photo-Optical Instrumentation Engineers (SPIE) Conference Series*, volume 7010, 2008. doi: 10.1117/12.788820.
- D. Coe, N. Benítez, S. F. Sánchez, M. Jee, R. Bouwens, and H. Ford. Galaxies in the Hubble Ultra Deep Field. I. Detection, Multiband Photometry, Photometric Redshifts, and Morphology. *AJ*, 132:926–959, August 2006. doi: 10.1086/505530.
- B. Croll, L. Albert, R. Jayawardhana, E. Miller-Ricci Kempton, J. J. Fortney, N. Murray, and H. Neilson. Broadband Transmission Spectroscopy of the Super-Earth GJ 1214b Suggests a Low Mean Molecular Weight Atmosphere. *ApJ*, 736:78, August 2011. doi: 10.1088/0004-637X/736/2/78.

- I. J. M. Crossfield, T. Barman, and B. M. S. Hansen. High-resolution, Differential, Near-infrared Transmission Spectroscopy of GJ 1214b. *ApJ*, 736:132, August 2011. doi: 10.1088/0004-637X/736/2/132.
- G. de Marchi, M. B. J. Te Plate, S. M. Birkmann, T. Böker, P. Ferruit, G. Giardino, P. Jakobsen, M. Sirianni, J.-C. Savignol, X. Gnata, R. Barho, M. Kosse, P. Mosner, B. Dorner, G. Cresci, F. Rosales-Ortega, M. Stuhlinger, T. Gross, and T. Leikert. Calibrating the position of images and spectra in the NIRSpec instrument for the James Webb Space Telescope. In *Society of Photo-Optical Instrumentation Engineers (SPIE) Conference Series*, volume 8150, September 2011. doi: 10.1117/12.893914.
- E. J. W. de Mooij, M. Brogi, R. J. de Kok, J. Koppenhoefer, S. V. Nefs, I. A. G. Snellen, J. Greiner, J. Hanse, R. C. Heinsbroek, C. H. Lee, and P. P. van der Werf. Optical to near-infrared transit observations of super-Earth GJ 1214b: water-world or mini-Neptune? *A&A*, 538:A46, February 2012. doi: 10.1051/0004-6361/201117205.
- J.-M. Désert, J. Bean, E. Miller-Ricci Kempton, Z. K. Berta, D. Charbonneau, J. Irwin, J. Fortney, C. J. Burke, and P. Nutzman. Observational Evidence for a Metal-rich Atmosphere on the Super-Earth GJ1214b. *ApJ*, 731:L40, April 2011. doi: 10.1088/2041-8205/731/2/L40.
- B. Dorner, P. Ferruit, X. Gnata, S. M. Birkmann, T. Böker, G. de Marchi, M. Sirianni, W. J. Hupfer, J. Köhler, M.-G. Kolm, R. Ehrenwinkler, L. Piqueras, E. Legros, P.-J. Legay, A. Pécontal-Rousset, A. Jarno, and A. Pons. Confronting the NIRSpec instrument performance simulator outputs with results of the NIRSpec demonstration model calibration campaign. In *Society of Photo-Optical Instrumentation Engineers (SPIE) Conference Series*, volume 7738, July 2010. doi: 10.1117/12.856623.
- B. Dorner, P. Ferruit, L. Piqueras, E. Legros, A. Pécontal, A. Jarno, A. Pons, X. Gnata, and C. Pacifici. First Simulation and Data Reduction of a JWST/NIRSpec Observation. In I. N. Evans, A. Accomazzi, D. J. Mink, & A. H. Rots, editor, *Astronomical Data Analysis Software and Systems XX*, volume 442 of *Astronomical Society of the Pacific Conference Series*, page 343, July 2011.
- R. Doyon, J. Hutchings, N. Rowlands, C. E. Evans, E. Greenberg, C. Haley, A. D. Scott, D. Touahri, M. Beaulieu, D. Lafrenière, R. Abraham, E. Barton, P. Chayer, L. Ferrarese, A. W. Fullerton, R. Jayawardhana, D. Johnstone, A. Martel, A. W. M. R. Meyer, J. Pipher, K. Saad, M. Sawicki, A. Sivaramakrishnan, and K. Volk. The JWST tunable filter imager (TFI). In *Society of Photo-Optical Instrumentation Engineers (SPIE) Conference Series*, volume 7731, July 2010. doi: 10.1117/12.857382.
- A. S. Fruchter and R. N. Hook. Drizzle: A Method for the Linear Reconstruction of Undersampled Images. *PASP*, 114:144–152, February 2002. doi: 10.1086/338393.

- J. P. Gardner, J. C. Mather, M. Clampin, R. Doyon, M. A. Greenhouse, H. B. Hammel, J. B. Hutchings, P. Jakobsen, S. J. Lilly, K. S. Long, J. I. Lunine, M. J. McCaughrean, M. Mountain, J. Nella, G. H. Rieke, M. J. Rieke, H.-W. Rix, E. P. Smith, G. Sonneborn, M. Stiavelli, H. S. Stockman, R. A. Windhorst, and G. S. Wright. The James Webb Space Telescope. *Space Sci. Rev.*, 123:485–606, April 2006. doi: 10.1007/s11214-006-8315-7.
- J. Gerssen, K. Janssen, G. Meeus, W. Hupfer, X. Gnata, P. Ferruit, M. Roth, P. Mosner, G. de Marchi, and T. Böker. IQLAC: a data analysis system for the NIRSpec on-ground test campaign. In *Society of Photo-Optical Instrumentation Engineers (SPIE) Conference Series*, volume 7010, 2008. doi: 10.1117/12.787973.
- X. Gnata. *Développement d'un simulateur de performances pour le spectrographe NIRSpec du futur télescope spatial JWST*. PhD thesis, Université Claude Bernard - Lyon 1, 2007.
- J. W. Goodman. *Introduction to Fourier Optics*. McGraw-Hill, 2nd edition, 1996.
- S. D. Horner and M. J. Rieke. The near-infrared camera (NIRCam) for the James Webb Space Telescope (JWST). In J. C. Mather, editor, *Society of Photo-Optical Instrumentation Engineers (SPIE) Conference Series*, volume 5487, pages 628–634, October 2004. doi: 10.1117/12.552281.
- L. Kaltenegger and W. A. Traub. Transits of Earth-like Planets. *ApJ*, 698:519–527, June 2009. doi: 10.1088/0004-637X/698/1/519.
- J. F. Kasting, D. P. Whitmire, and R. T. Reynolds. Habitable Zones around Main Sequence Stars. *Icarus*, 101:108–128, January 1993. doi: 10.1006/icar.1993.1010.
- H. A. Knutson, D. Charbonneau, L. E. Allen, J. J. Fortney, E. Agol, N. B. Cowan, A. P. Showman, C. S. Cooper, and S. T. Megeath. A map of the day-night contrast of the extrasolar planet HD 189733b. *Nature*, 447:183–186, May 2007. doi: 10.1038/nature05782.
- E. Komatsu, K. M. Smith, J. Dunkley, C. L. Bennett, B. Gold, G. Hinshaw, N. Jarosik, D. Larson, M. R. Nolte, L. Page, D. N. Spergel, M. Halpern, R. S. Hill, A. Kogut, M. Limon, S. S. Meyer, N. Odegard, G. S. Tucker, J. L. Weiland, E. Wollack, and E. L. Wright. Seven-year Wilkinson Microwave Anisotropy Probe (WMAP) Observations: Cosmological Interpretation. *ApJS*, 192:18, February 2011. doi: 10.1088/0067-0049/192/2/18.
- A. S. Kuttyrev, N. Collins, J. Chambers, S. H. Moseley, and D. Rapchun. Microshutter arrays: high contrast programmable field masks for JWST NIRSpec. In *Society of Photo-Optical Instrumentation Engineers (SPIE) Conference Series*, volume 7010, 2008. doi: 10.1117/12.790192.

- P. A. Lightsey, A. A. Barto, and J. Contreras. Optical performance for the James Webb Space Telescope. In J. C. Mather, editor, *Society of Photo-Optical Instrumentation Engineers (SPIE) Conference Series*, volume 5487, pages 825–832, October 2004. doi: 10.1117/12.550091.
- P. A. Oesch, R. J. Bouwens, C. M. Carollo, G. D. Illingworth, M. Trenti, M. Stiavelli, D. Magee, I. Labbé, and M. Franx. Structure and Morphologies of $z \sim 7$ -8 Galaxies from Ultra-deep WFC3/IR Imaging of the Hubble Ultra-deep Field. *ApJ*, 709: L21–L25, January 2010. doi: 10.1088/2041-8205/709/1/L21.
- C. Pacifici, S. Charlot, J. Blaizot, and J. Brinchmann. Relative merits of different types of rest-frame optical observations to constrain galaxy physical parameters. *MNRAS*, page 2451, February 2012. doi: 10.1111/j.1365-2966.2012.20431.x.
- C. Palmer. *Diffraction Grating Handbook*. Newport Corporation, 6th edition, 2005.
- L. Piqueras, P.-J. Legay, E. Legros, P. Ferruit, A. Pécontal, X. Gnata, and P. Mosner. The JWST/NIRSpec instrument performance simulator. In *Society of Photo-Optical Instrumentation Engineers (SPIE) Conference Series*, volume 7017, 2008. doi: 10.1117/12.789056.
- L. Piqueras, E. Legros, A. Pons, P.-J. Legay, P. Ferruit, B. Dorner, A. Pécontal, X. Gnata, and P. Mosner. The JWST/NIRSpec instrument performance simulator software. In *Society of Photo-Optical Instrumentation Engineers (SPIE) Conference Series*, volume 7738, July 2010. doi: 10.1117/12.856860.
- F. Pont, H. Knutson, R. L. Gilliland, C. Moutou, and D. Charbonneau. Detection of atmospheric haze on an extrasolar planet: the 0.55-1.05 μm transmission spectrum of HD 189733b with the HubbleSpaceTelescope. *MNRAS*, 385:109–118, March 2008. doi: 10.1111/j.1365-2966.2008.12852.x.
- B. J. Rauscher, O. Fox, P. Ferruit, R. J. Hill, A. Waczynski, Y. Wen, W. Xia-Serafino, B. Mott, D. Alexander, C. K. Brambora, R. Derro, C. Engler, M. B. Garrison, T. Johnson, S. S. Manthripragada, J. M. Marsh, C. Marshall, R. J. Martineau, K. B. Shakoorzadeh, D. Wilson, W. D. Roher, M. Smith, C. Cabelli, J. Garnett, M. Loose, S. Wong-Anglin, M. Zandian, E. Cheng, T. Ellis, B. Howe, M. Jurado, G. Lee, J. Nieznanski, P. Wallis, J. York, M. W. Regan, D. N. B. Hall, K. W. Hodapp, T. Böker, G. De Marchi, P. Jakobsen, and P. Strada. Detectors for the James Webb Space Telescope Near-Infrared Spectrograph. I. Readout Mode, Noise Model, and Calibration Considerations. *PASP*, 119:768–786, July 2007. doi: 10.1086/520887.
- J. Schmoll, A. G. Basden, D. G. Bramall, P. Clark, R. E. Cole, G. N. Dodsworth, S. J. Goodsell, A. McCalden, G. J. Murray, R. M. Myers, R. M. Sharples, J. A. Tandy,

- and P. Thomas. Optical ground support equipment for the alignment of JWST-NIRSpec. In *Society of Photo-Optical Instrumentation Engineers (SPIE) Conference Series*, volume 7010, 2008. doi: 10.1117/12.789521.
- D. J. Schroeder. *Astronomical Optics*. San Diego: Academic Press, 2nd edition, 2000.
- D. K. Sing, F. Pont, S. Aigrain, D. Charbonneau, J.-M. Désert, N. Gibson, R. Gilliland, W. Hayek, G. Henry, H. Knutson, A. Lecavelier Des Etangs, T. Mazeh, and A. Shporer. Hubble Space Telescope transmission spectroscopy of the exoplanet HD 189733b: high-altitude atmospheric haze in the optical and near-ultraviolet with STIS. *MNRAS*, 416:1443–1455, September 2011. doi: 10.1111/j.1365-2966.2011.19142.x.
- M. te Plate, W. Holota, W. Posselt, J. Köhler, M. Melf, G. Bagnasco, and P. Marenaci. Opto-mechanical design of the near infrared spectrograph NIRSpec. In *Society of Photo-Optical Instrumentation Engineers (SPIE) Conference Series*, volume 5904, pages 185–198, 2005. doi: 10.1117/12.620772.
- M. te Plate, J. L. Alvarez, P.-A. Frugier, and P. Marenaci. Physical optics model for simulating the optical performance of the NIRSpec. In *Society of Photo-Optical Instrumentation Engineers (SPIE) Conference Series*, volume 6692, 2007. doi: 10.1117/12.734088.
- R. I. Thompson, G. Illingworth, R. Bouwens, M. Dickinson, D. Eisenstein, X. Fan, M. Franx, A. Riess, M. J. Rieke, G. Schneider, E. Stobie, S. Toft, and P. van Dokkum. The Near-Infrared Camera and Multi-Object Spectrometer Ultra Deep Field: Observations, Data Reduction, and Galaxy Photometry. *AJ*, 130:1–12, July 2005. doi: 10.1086/430528.
- G. Torres, J. N. Winn, and M. J. Holman. Improved Parameters for Extrasolar Transiting Planets. *ApJ*, 677:1324–1342, 2008. doi: 10.1086/529429.
- I. P. Waldmann, G. Tinetti, P. Drossart, M. R. Swain, P. Deroo, and C. A. Griffith. Ground-based Near-infrared Emission Spectroscopy of HD 189733b. *ApJ*, 744:35, January 2012. doi: 10.1088/0004-637X/744/1/35.
- E. W. Weisstein. "Statistical Median." From MathWorld—A Wolfram Web Resource. URL <http://mathworld.wolfram.com/StatisticalMedian.html>.
- J. N. Winn, M. J. Holman, G. W. Henry, A. Roussanova, K. Enya, Y. Yoshii, A. Shporer, T. Mazeh, J. A. Johnson, N. Narita, and Y. Suto. The Transit Light Curve Project. V. System Parameters and Stellar Rotation Period of HD 189733. *AJ*, 133:1828–1835, April 2007. doi: 10.1086/512159.

- G. S. Wright, G. Rieke, T. Böker, L. Colina, E. van Dishoeck, P. Driggers, S. Friedman, A. Glasse, G. Goodson, T. Greene, M. Guedel, T. Henning, P.-O. Lagage, J. Lorenzo-Alvarez, M. Meixner, H. Norgaard-Nielsen, G. Olofsson, T. Ray, M. Ressler, K. Sukhatme, J. Thatcher, C. Waelkens, and D. Wright. Progress with the design and development of MIRI, the mid-IR instrument for JWST. In *Society of Photo-Optical Instrumentation Engineers (SPIE) Conference Series*, volume 7731, July 2010. doi: 10.1117/12.857262.
- J. T. Wright, O. Fakhouri, G. W. Marcy, E. Han, Y. Feng, J. A. Johnson, A. W. Howard, D. A. Fischer, J. A. Valenti, J. Anderson, and N. Piskunov. The Exoplanet Orbit Database. *PASP*, 123:412–422, April 2011. doi: 10.1086/659427.